frontiers | Research Topics

Surface processes and morphodynamics related to climate and human impacts

Edited by
María Fernandez, Jesús Rodrigo-Comino, Ataollah Kavian
and Yang Yu

Published in
Frontiers in Earth Science
Frontiers in Environmental Science

ISSN 1664-8714
ISBN 978-2-83250-925-8
DOI 10.3389/978-2-83250-925-8

About Frontiers

Frontiers is more than just an open access publisher of scholarly articles: it is a pioneering approach to the world of academia, radically improving the way scholarly research is managed. The grand vision of Frontiers is a world where all people have an equal opportunity to seek, share and generate knowledge. Frontiers provides immediate and permanent online open access to all its publications, but this alone is not enough to realize our grand goals.

Frontiers journal series

The Frontiers journal series is a multi-tier and interdisciplinary set of open-access, online journals, promising a paradigm shift from the current review, selection and dissemination processes in academic publishing. All Frontiers journals are driven by researchers for researchers; therefore, they constitute a service to the scholarly community. At the same time, the *Frontiers journal series* operates on a revolutionary invention, the tiered publishing system, initially addressing specific communities of scholars, and gradually climbing up to broader public understanding, thus serving the interests of the lay society, too.

Dedication to quality

Each Frontiers article is a landmark of the highest quality, thanks to genuinely collaborative interactions between authors and review editors, who include some of the world's best academicians. Research must be certified by peers before entering a stream of knowledge that may eventually reach the public - and shape society; therefore, Frontiers only applies the most rigorous and unbiased reviews. Frontiers revolutionizes research publishing by freely delivering the most outstanding research, evaluated with no bias from both the academic and social point of view. By applying the most advanced information technologies, Frontiers is catapulting scholarly publishing into a new generation.

What are Frontiers Research Topics?

Frontiers Research Topics are very popular trademarks of the *Frontiers journals series*: they are collections of at least ten articles, all centered on a particular subject. With their unique mix of varied contributions from Original Research to Review Articles, Frontiers Research Topics unify the most influential researchers, the latest key findings and historical advances in a hot research area.

Find out more on how to host your own Frontiers Research Topic or contribute to one as an author by contacting the Frontiers editorial office: frontiersin.org/about/contact

Surface processes and morphodynamics related to climate and human impacts

Topic editors
María Fernandez — Universidad de León, Spain
Jesús Rodrigo-Comino — University of Granada, Spain
Ataollah Kavian — Sari Agricultural Sciences and Natural Resources University, Iran
Yang Yu — Beijing Forestry University, China

Citation
Fernandez, M., Rodrigo-Comino, J., Kavian, A., Yu, Y., eds. (2022). *Surface processes and morphodynamics related to climate and human impacts*. Lausanne: Frontiers Media SA. doi: 10.3389/978-2-83250-925-8

Table of contents

frontiers | Frontiers in Earth Science

TYPE Editorial
PUBLISHED 21 November 2022
DOI 10.3389/feart.2022.1082090

OPEN ACCESS

EDITED AND REVIEWED BY
Zhenliang Yin,
Northwest Institute of Eco-Environment and Resources (CAS),
China

*CORRESPONDENCE
María Fernández-Raga,
maria.raga@unileon.es

SPECIALTY SECTION
This article was submitted to Hydrosphere,
a section of the journal
Frontiers in Earth Science

RECEIVED 27 October 2022
ACCEPTED 04 November 2022
PUBLISHED 21 November 2022

CITATION
Fernández-Raga M, Kavian A, Yu Y and Rodrigo-Comino J (2022), Editorial: Surface processes and morphodynamics related to climate and human impacts.
Front. Earth Sci. 10:1082090.
doi: 10.3389/feart.2022.1082090

Editorial: Surface processes and morphodynamics related to climate and human impacts

María Fernández-Raga[1]*, Ataollah Kavian[2], Yang Yu[3] and Jesús Rodrigo-Comino[4]

[1]Department of Applied Physics, University of León, León, Spain, [2]Faculty of Natural Resources, Sari Agricultural Sciences and Natural Resources University, Sari, Iran, [3]School of Soil and Water Conservation, Jixian National Forest Ecosystem Research Network Station, CNERN, Beijing Forestry University, Beijing, China, [4]Departamento de Análisis Geográfico Regional y Geografía Física, University of Granada, Granada, Spain

KEYWORDS

Earth surface processes, land degradation, erosion, land sustainability, control measures

Editorial on the Research Topic
Surface processes and morphodynamics related to climate and human impacts

The variation of climate conditions and the rapid increase in human activities such as non-sustainable agricultural or forestry or urban management shape the landscape, sometimes causing negative impacts. Recent scientific literature has been highlighting abundant study cases where Earth's surface morphologies are suffering from exploitation of natural resources (mining, wood, water, etc.), wildfires, or non-controlled urban sprawl. One of the main consequences is an irreparable damage of soil quality. These changes are also affected by an imminent climate change with responses varying dependent on scale, from the pedon to the hillslopes, catchments, or regions. Depending on how fast and intense these modifications of Earth's surface conditions progress, land productivity, water quality, and biomass should be studied.

Due to the unknown dynamics of climate change and the speed with which human population and activities increase, the scientific community is daily seeking new models, designing field measurements, and applying diverse control measures to estimate, quantify, and reduce the possible negative impacts.

Land degradation processes are shaping the Earth's surface, but for scientists, stakeholders, and policymakers it is not a new concept. In this Research Topic, the environmental and dynamic processes that modify the most sensible spheres of the land surface are discussed: bio-, hydro-, and pedospheres. Therefore, it is indispensable that humankind pay attention and raise awareness of the factors, causes, consequences, and possible control measures of soil processes with negative impacts on natural and anthropogenic ecosystems. Moreover, the increasing awareness of the critical role of climate change related to temperature, precipitation patterns, and wind characteristics is discussed. It is demonstrated that climate change could introduce new trends to the current known surface processes, despite the continuous advances in observational techniques and more comprehensive laboratory and field monitoring programs and application of new models that aim to decipher the interactions between soil, water, and atmosphere. This Research Topic grouped novel investigations, providing a much better understanding of the physical environment and human interventions and new methodologies developed to study erosion using models, sensors, photogrammetry, field research, *in situ* observations, qualitative assessments, etc.

A total of eleven manuscripts have been accepted, including nine studies from China, one on the Tibetan ecosystem, and another one on the Antarctic continent. They aimed to represent the different approaches to erosion, using new techniques and applying novel tools applicable under both natural and human-made processes affected by climatic change. Wang et al. highlighted the determination of the natural processes happening in areas that are likely to determine the fate of terrestrial environments, focusing on the increase in erosion because of the interaction of rainfall intensity and defrosting depth. Their results improved the understanding of the response of freeze/thaw/compound water erosion to hydraulic conditions. Another article explored soil water migration characteristics of two typical vegetation types at the Loess Plateau during seasonal freezing and thawing processes using bare lands (BL) as control plots. It provides a scientific basis for vegetation restoration in arid and semi-arid areas, useful for other countries too. Sun et al. measured the soil water content and mineral composition for 87 different soil profiles distributed along three transects to show that textural layered soils were patchily but extensively distributed throughout a study area in China. Liu et al. demonstrated the combined effects of ridge direction and width on surface runoff and soil losses from hillslopes cultivated with croplands, indicating that ridge direction had significant effects on runoff and sediment yield ($p < 0.05$), although ridge width had no influence. Cross tillage is advised for soil and water conservation on sloping croplands in arid and semi-arid regions of China.

Readers can find two other interesting manuscripts that focused on how the vegetation communities affect aspects such as the redistribution of carbon or the water content, analyzing the influence of micro-dunes in plant adaptation modus considering water-limited environments. Wang et al. used stable isotopes to analyze the variability in water sources of the native species during the growing season in an alpine semi-arid desert on the Qinghai–Tibet Plateau, China. Liang et al., meanwhile, assessed three different environments: naturally regenerating forests (NF), artificial black locust plantation (BP), and a corn field (CK). They found that vegetation restoration of NF slowed migration and homogenized organic carbon distribution.

Other investigations published in this Research Topic were based on the use of robust models to forecast future conditions. For example, Li et al. coupled a model to determine inflow in an ungauged stream and assembled an empirical mode decomposition (EEMD) to group runoff series into several stationary components and a trend. All of them were combined with the long short-term memory (LSTM) model used to build the prediction model for each sub-series. To verify these last two models, Yuan et al. designed the MI method and the Radial Basis Function (RBF) model, which are basics for the decision-making of starting water transfer process, and designed compensation roles of hydrological characteristics and storage capacities of multi-reservoirs to maximize the utilization efficiency of water resources. On the other, Cai et al. in the Datong-Huangshui area, analyzed the composition of the inter-basin water transfer system, and constructed a dispatching rule extraction model including water transfer, water diversion, and water supply rules. In a similar Research Topic, Xu et al. described the main factors influencing the change in temporal stability of soil water content in different seasons such as elevation, root density, and sand content. This allowed the design of scientific guidance for monitoring this hydrological property.

Last but not least, Kreczmer et al. published novel research about the Antarctic continent, in which they identified, mapped, and quantified terrestrial glacial and periglacial landforms developed in front of windy glaciers with the help of digital images and elevation maps elaborated during a UAV BVLOS photogrammetric survey in 2016, Google Earth Pro images from 2006, and maps from 1978/1979.

Author contributions

All authors listed have made a substantial, direct, and intellectual contribution to the work and approved it for publication.

Acknowledgments

The guest editors would like to express our sincere thanks to all authors who submitted their studies, irrespective of being accepted or not to this particular Research Topic. We also appreciate all reviewers, editors, and the Editor-in-Chief for their continuous assistance in making this Research Topic a success.

Conflict of interest

The authors declare that the research was conducted in the absence of any commercial or financial relationships that could be construed as a potential conflict of interest.

Publisher's note

frontiers
in Environmental Science

ORIGINAL RESEARCH
published: 09 December 2020
doi: 10.3389/fenvs.2020.609594

Experimental Study of Freeze-Thaw/Water Compound Erosion and Hydraulic Conditions as Affected by Thawed Depth on Loessal Slope

Wei Wang[1], Zhanbin Li[1,2], Rui Yang[3], Tian Wang[1]* and Peng Li[1,2]

[1] State Key Laboratory of Eco-hydraulics in Northwest Arid Region of China, Xi'an University of Technology, Xi'an, China, [2] Key Laboratory of National Forestry Administration on Ecological Hydrology and Disaster Prevention in Arid Regions, Xi'an University of Technology, Xi'an, China, [3] College of Architecture and Civil Engineering, Yan'an University, Yan'an, China

Freeze-thaw cycles have significant influences on slope erosion processes. In this study, simulated rainfall laboratory experiments were implemented to investigate erosion processes and the relationship between the soil loss rate and hydraulics conditions under different thawed depths and rainfall intensities. The results indicated that linear regression could be used to describe the relationship between the soil loss rate and runoff time. Soil loss rate, as measured by the curve slope *k* (represented the increase rate in the soil loss rate), generally increased with runoff time over different thawed depths across all rainfall intensities. The *k* values generally increased with rainfall intensity from 0.6 to 1.2 mm/min, with the exception of the 4 cm thawed slope, for which the *k* values initially increased before decreasing with rainfall intensity from 0.6 to 1.2 mm/min. The mean soil loss rate and range also increased with thawed depth under the same rainfall intensity. Finally, the interaction of rainfall intensity and thawed depth had the greatest effect on soil loss rate, while stream erosion power was the hydraulic parameter that exhibited the best soil loss rate prediction performance. The results presented herein improve the understanding of the response of freeze-thaw/water compound erosion to hydraulic conditions.

Keywords: freeze-thaw, rainfall, thawed depth, compound erosion, hydraulic conditions

Edited by:
Ataollah Kavian,
Sari Agricultural Sciences and Natural Resources University, Iran

Reviewed by:
Bingbing Zhu,
Shaanxi Normal University, China
Fengbao Zhang,
Northwest A&F University, China

***Correspondence:**
Tian Wang
t.wang@xaut.edu.cn

Specialty section:
This article was submitted to Soil Processes, a section of the journal Frontiers in Environmental Science

Received: *23 September 2020*
Accepted: *17 November 2020*
Published: *09 December 2020*

Citation:
Wang W, Li Z, Yang R, Wang T and Li P (2020) Experimental Study of Freeze-Thaw/Water Compound Erosion and Hydraulic Conditions as Affected by Thawed Depth on Loessal Slope. Front. Environ. Sci. 8:609594. doi: 10.3389/fenvs.2020.609594

INTRODUCTION

Soil erosion is one of the main environmental problems facing the world (Batista et al., 2019; Dazzi and Papa, 2019; Shi et al., 2020), and this is especially true in the Loess Plateau of China (Shi et al., 2019; Guo et al., 2020; Yu et al., 2020; Yue et al., 2020). However, research in this region has focused on hydraulic erosion and wind erosion, while comparatively little is known about freeze-thaw precipitation compound erosion (Xu et al., 2015a,b; Zhang B.J. et al., 2019; Zhang J. et al., 2019; Zhang W. et al., 2019).

Seasonal freeze-thaw (FT) influences soil physical characteristics, such as soil bulk density (Li et al., 2013; Li and Fan, 2014), erodibility (Wang et al., 2017; Cheng et al., 2018), aggregates (Edwards, 2013; Xiao et al., 2019), and water content (Ala et al., 2016; Wang et al., 2019), which make the soil more susceptible to erosion under compound forces (Edwards, 2013; Li and Fan, 2014). As more snow and glaciers melt due to global warming, soil erosion is continually worsening (Ragettli et al., 2015; Wang et al., 2020). Most mid-latitude regions also suffer from seasonal FT erosion (Ragettli et al., 2015; Wang et al., 2019). Depending on Second National Soil Erosion Remote Sensing Survey in China, 13.23% of national territorial area is in danger of FT erosion (Fan et al., 2009). In the loess hilly-gully region of Loess Plateau, there are around 105–125 d with average temperatures below 0°C, and the average annual rainfall is 300–600 mm, which meets the basic conditions necessary for FT erosion (Wang et al., 2019, 2020). Soil erosion during the thawing period is a unique erosion form known as FT-hydraulic compound erosion.

Previous laboratory rainfall experiments on frozen slopes have shown contrasting patterns. Using control FT-water combined erosion experiments, Wang et al. (2019) found that the total sediment yield of a FT slope exhibited increased soil erosion compared to a control slope (Wang et al., 2019). Wang et al. (2020) found that frozen slopes displayed higher sediment yield capacity at equal flow rates when compared with shallow-thawed and unfrozen slopes. However, Zhou et al. (2009) investigated the effects of the thawed depth on black soil erosion under simulated rainfall and found that the erosion amount decreased with increasing thawed depth under lower soil water content. Wei et al. (2015) studied the impacts of FT cycles on runoff and sediment yield of slope land and found that FT cycles greatly increased the sediment yield intensity. In contrast, Ban et al. (2017) found that shallower thawed depths delivered more sediments than deeper thawed depths of high altitude and latitude regions. However, few studies have investigated the effects of thawed depth on soil erosion processes in loess slopes under simulated rainfall.

Generally, hydraulic parameters are essential to describing erosion processes and understanding the hydrodynamic mechanisms of slope erosion (Cuomo et al., 2016; Zi et al., 2016; Xiao et al., 2017; Mirzaee and Ghorbanidashtaki, 2018; Luo et al., 2019). Foster and Meyer (1972) showed that erosion has a positive relationship with shear stress. Govers (1990) found that unit stream power was the best parameter for describing erosion processes. Nearing et al. (1999) and Cai (1995) found stream power to be better than other hydraulic parameters for describing erosion processes. Lu et al. (2009) put forward the stream erosion power concept and established the relationship between soil loss rate and stream erosion power. Wang et al. (2020) found that runoff energy loss could predict thawed soil erosion processes under concentrated flow well. Govers (1992) determined that no existing formula could perform efficiently over the entire range of available data. Soil loss by shallow flows is more closely correlated with flow energy than shear stress (Zhang et al., 2002). Some studies have indicated that stream power is better than shear stress for Dc prediction (Knapen et al., 2007; Cao et al., 2009); however, it is still not clear which parameters are suitable for the prediction of FT precipitation compound erosion under simulated rainfall.

Here, we used laboratory experiments of three rainfall intensities to survey erosion processes and assess the relationship between soil loss rate and various hydraulics parameters under four thawed depths and three gradient rainfall intensities. The specific objectives of this study were to (i) assess erosion processes with runoff time under different thawed depths, and (ii) determine the relationships between soil loss rate and hydraulic parameters.

MATERIALS AND METHODS

Experimental Materials and Design

We used loessal soil collected from the Wangmaogou catchment (37°34′13″–37°36′03″ N and 110°20′26″–110°22′ 46″ E) in Shaanxi Province, China. The collected soil was air-dried and sieved (10 mm) to remove roots, stones, and other debris. The soil particle with 2 mm distribution was then measured using a Mastersizer2000 particle size analyzer (Malvern Instruments, Malvern, United Kingdom), which showed the mechanical composition of the original soil was 0.02 ± 0.003% clay, 65.28 ± 0.43% silt, and 34.7 ± 0.21% sand depending on USDA classification system of soil texture. We then increased the soil water content to 15% by gravity and kept it indoors for 24 h while covered with plastic.

The experimental soil flume was 2 m long, 0.75 m wide, and 0.3 m deep (**Figure 1A**). The skeleton of the soil flume was made of angle steel, and the wall (0.4 m high) was made from wood to reduce heat exchange so that the soil thawed vertically. The bottom of the flume was filled 0.05 m deep with sand to maintain water permeability. Next, experimental soil was added to a depth of 25 cm in 5 cm layers. Quantitative experimental soil for each layer was obtained depending on the soil dry bulk (1.3 g/cm3), soil water content (15%), and volume of each layer. The surface topography on two sides was raised to an experimental slope of 15°. The area of slope farmland less than 15° accounts for 43.65% of the total area of slope farmland, and the slope gradient 15° is a relative threshold of soil erosion modulus.

A FT system, 4.5 m long × 2.5 m wide × 2.5 m high, was used to freeze the experimental soil layer. The FT system could produce temperatures of −40 to 30°C with an accuracy of ±1°C. To ensure the soil was completely frozen, the filled soil flume was placed in the FT system for 24 h at −18 to −22°C. We investigated four thawed depths: 0, 2, 4, and 6 cm. The completely frozen soil-filled flume was then placed at room temperature for thawing, during which time a needle was used to measure the thawed depth every 15 min to meet the requirement of thawed depth during the thawing period. The filled soil flume was then divided into 12 grid cells for testing points of thawed depth. We subjected the slope to three rainfall intensities (0.6, 0.9, and 1.2 mm/min) and set a runoff duration of 60 min for each experiment from the rainfall simulator (**Figures 1B,C**). Each experiment was repeated two times to give a total of 36 experiments and the results were averaged.

The slope was divided into four transects between 0–0.5, 0.5–1.0, 1.0–1.5, and 1.5–2.0 m. The surface flow velocity of the four transects was measured at 1 min intervals using the $KMnO_4$ tracer method (**Figure 1D**). We multiplied the measured

FIGURE 1 | The experimental soil flume **(A)**, calibration rainfall intensity **(B)**, rainfall simulator **(C)** and runoff over the flume **(D)**.

surface flow velocities by a correction factor of 0.65 to obtain the mean flow velocity (Luk and Merz, 1992). The flow widths were measured on the four transects using a ruler at 1-min intervals.

The soil flume bottom was constructed with convergence equipment to collect runoff and sediment at 1 min intervals. The runoff volume was measured in each gathered bucket, and the weight of sediment was recorded after drying in an oven at 105°C for >24 h.

Methods

The soil loss rate was calculated as the erosion amount per unit area per second:

$$S_r = \frac{e_r}{lwt} \tag{1}$$

where S_r is the soil loss rate (g/m^2/s); e_r is the mass of soil loss during the observation time (g); l and w are the length and width of the experimental flume (m), respectively; and t is the observation time (s).

Shear stress, which is related to soil particle detachment and transport, was calculated as follows (Xiao et al., 2017):

$$\tau = \gamma_m gRJ \tag{2}$$

where τ is the shear stress (Pa); γ_m is the muddy water density (kg/m^3); g is the gravitational acceleration (m/s^2); J is the slope gradient (m/m); and R is the hydraulic radius, which was considered equal to the flow depth under overland flow conditions (m).

It was difficult to directly measure flow depth because the flow depth was shallow and the bed elevation changed with erosion. We calculated flow depth as follows:

$$h = \frac{Q}{VWt} \tag{3}$$

where h is the flow depth (m); Q is the runoff volume (m^3); W is the water width (m); t is the time (s); and V is the mean flow velocity (m/s).

The stream power, which represents power consumed by water flow per unit area, was calculated as previously described (Cao et al., 2009):

$$\omega = \tau V \tag{4}$$

where ω is the stream power (N/m/s); τ is the shear stress (Pa); V is the mean flow velocity (m/s).

The unit stream power, which describes the rate of change of potential energy per unit water mass with time, was calculated as follows (Zhang et al., 2002):

$$P = VJ \tag{5}$$

where P is the unit stream power (m/s); J is the slope gradient (m/m); V is the mean flow velocity (m/s).

The stream erosion power, which comprehensively expresses the efficiency of runoff erosion and sediment transport, was calculated as described by Lu et al. (2009):

$$E = Q'_m H \tag{6}$$

where E is the stream erosion power [$\mathrm{m^4/(s{\cdot}m^2)}$]; Q'_m is the runoff peak modulus [$\mathrm{m^3/(s{\cdot}m^2)}$], which is equal to the runoff peak divided by the experimental soil flume area; and H is the mean flow depth (m).

Data Analysis

The regression analyses and associated figures were drawn using OriginPro 8.5 (OriginLab Inc, Northampton, MA, United States), statistical analyses were conducted with SPSS 16.0 (SPSS Inc, Chicago, IL, United States).

RESULTS

Soil Loss Rate Variation With Runoff Time Under Different Thawed Depths

As shown in **Figure 2**, linear regression was used to describe the relationship between the soil loss rate and runoff time. The determination coefficient (R^2) was used to elevate the regression equation (**Table 1**). Soil loss rate, as measured by the curve slope k (represented the increase rate in the soil loss rate), generally increased with runoff time over different thawed depths across all rainfall intensities (**Figure 2** and **Table 1**), although it plateaued or slightly decreased after 30 min in some trials (e.g., **Figure 2C**, 4 cm depth).

The R^2 values were greater than 0.82 for all tests under 0.6 mm/min intensity. The value of k became greater with deeper thawed depth under 0.6 mm/min intensity and increased to two times when the thawed depth increased from 2 to 4 cm under 0.6 mm/min intensity (**Table 1**). The value of k was 2.17 times greater at a thawed depth of 4 cm than at 2 cm under 0.6 mm/min

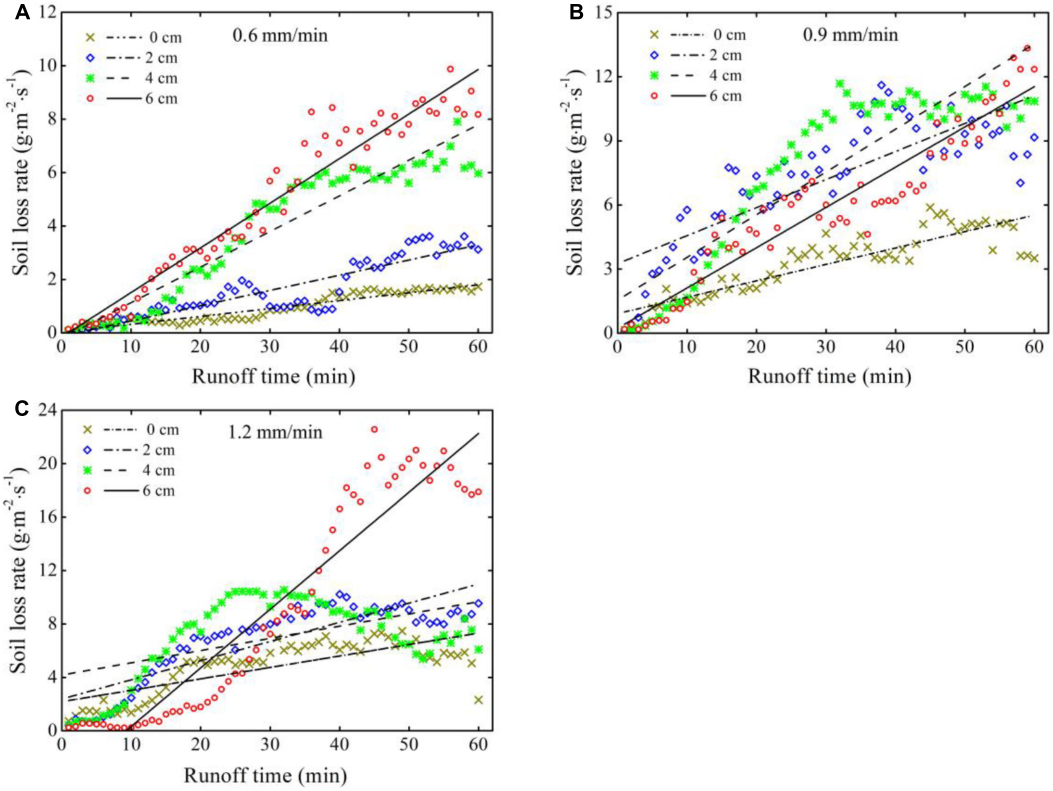

FIGURE 2 | The relationship between soil loss rate and runoff time over different thawed depth at 0.6 mm/min **(A)**, 0.9 mm/min **(B)**, and 1.2 mm/min **(C)**.

TABLE 1 | Regression parameters of erosion processes under different thawed depth and rain intensity.

Thawed depth (cm)	Curve slope (*k*)			Determination coefficients (R^2)		
	0.6 mm/min	0.9 mm/min	1.2 mm/min	0.6 mm/min	0.9 mm/min	1.2 mm/min
0	0.03	0.08	0.09	0.90	0.77	0.56
2	0.06	0.13	0.14	0.82	0.66	0.73
4	0.13	0.20	0.09	0.91	0.79	0.26
6	0.17	0.19	0.44	0.94	0.90	0.90

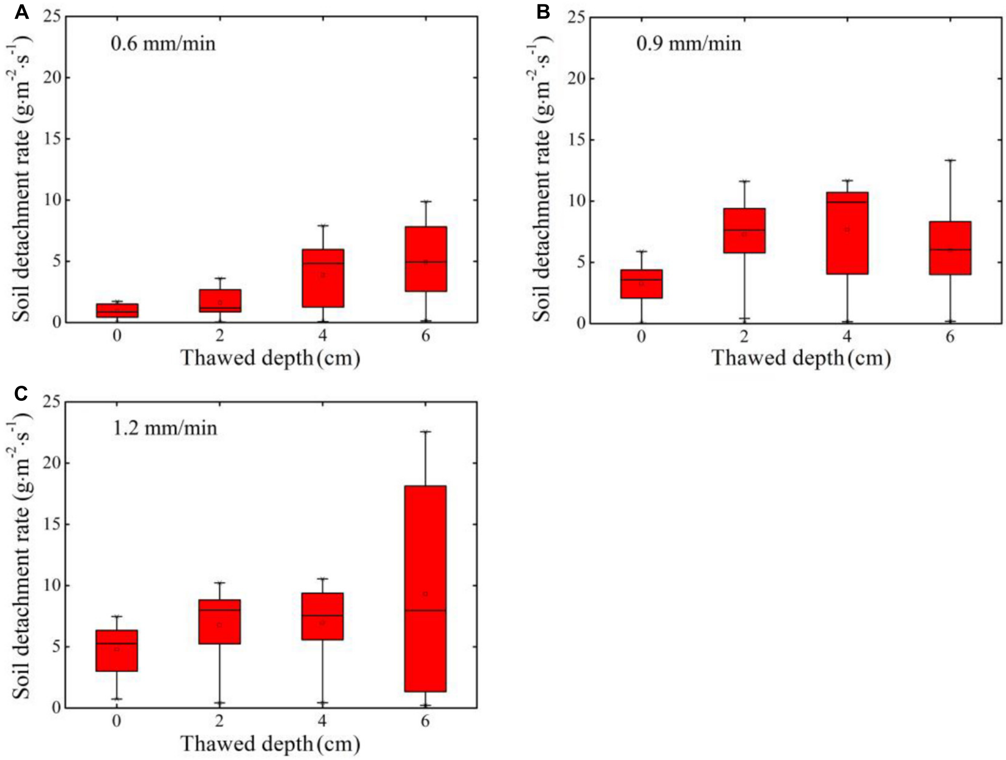

FIGURE 3 | The box plot of soil loss rate under different thawed depth at 0.6 mm/min **(A)**, 0.9 mm/min **(B)**, and 1.2 mm/min **(C)**.

intensity (**Table 1**). As the thawed depth increased from 4 to 6 cm, the value of *k* increased to 1.31 times under 0.6 mm/min intensity (**Table 1**).

The R^2 values were greater than 0.66 for all tests under 0.9 mm/min intensity (**Table 1**). The value of *k* became greater as the thawed depth increased from 0 to 4 cm under 0.9 mm/min intensity (**Table 1**), while it decreased slightly as the thawed depth increased from 4 to 6 cm under 0.9 mm/min intensity (**Table 1**). The value of *k* increased by 1.63 times when the thawed depth increased from 0 to 2 cm under 0.9 mm/min intensity (**Table 1**), while it was 1.54 times greater at a thawed depth of 4 cm than 2 cm under 0.9 mm/min intensity (**Table 1**).

The R^2 values were 0.56, 0.73 and 0.90 at the thawed depths of 0, 2, and 6 cm under 1.2 mm/min. However, the R^2 was 0.26 at a thawed depth of 4 cm under 1.2 mm/min. Except for the thawed depth of 4 cm, the values of *k* tended to increase as the thawed depth increased from 0 to 6 cm. As the thawed depth increased from 0 to 2 cm, the value of *k* increased by 1.56 times under 1.2 mm/min intensity (**Table 1**). Additionally, the value of *k* was 3.14 times greater at a thawed depth of 6 cm than 2 cm under 1.2 mm/min intensity (**Table 1**).

For the 0, 2, and 6 cm thawed depths, the values of *k* increased with increasing rainfall intensity from 0.6 to 1.2 mm/min. The values of *k* also increased when rainfall intensity increased from 0.6 to 0.9 mm/min for the thawed depth of 4 cm. However, the value of *k* tended to decrease when the rainfall intensity increased from 0.9 to 1.2 mm/min for the thawed depth of 4 cm.

Statistical Analysis of Soil Loss Rate Under Different Thawed Depths

Figure 3 shows a box plot of soil loss rate under four thawed depths at rainfall intensities of 0.6 mm/min (a), 0.9 mm/min (b), and 1.2 mm/min (c). The data used to create **Figure 3** are summarized in **Table 2**.

TABLE 2 | The statistics of soil loss rate for different thawed depth under changing rainfall intensity.

Thawed depth (cm)	0.6 mm/min			0.9 mm/min			1.2 mm/min		
	Range	Median	Mean	Range	Median	Mean	Range	Median	Mean
0	1.72	0.85	0.93	5.86	3.57	3.26	6.73	5.26	4.79
2	3.57	1.18	1.62	11.52	7.64	7.26	9.80	7.99	6.76
4	7.84	4.83	3.86	11.53	9.91	7.65	10.11	7.54	6.97
6	9.74	4.94	4.93	13.15	6.03	5.98	22.34	7.96	9.32

TABLE 3 | Relationships between soil loss rate and hydraulic conditions.

Hydraulic conditions	Equation	R^2	Significance level (P)
Shear stress	$S_r = 172.31(\tau - 0.66)$	0.52	<0.01
Mean stream power	$S_r = 784.18\omega^{0.61}$	0.60	<0.01
Mean unit stream power	$S_r = 8873.4(P - 0.011)$	0.57	<0.01
Stream erosion power	$S_r = 583.02E^{0.52}$	0.68	<0.01

The mean soil loss rate increased as thawed depth increased under the same rainfall intensity (**Figure 3**). A similar phenomenon was also observed for the 1.2 mm/min rainfall intensity except at the thawed depth of 6 cm (**Figure 3**). At a thawed depth of 0 and 6 cm, the mean soil loss rate increased as rainfall intensity increased. At thawed depths of 2 and 4 cm, the mean soil loss rate increased when the rainfall intensity increased from 0.6 to 0.9 mm/min (**Figure 3** and **Table 3**). However, the mean soil loss rate decreased when the rainfall intensity increased from 0.9 to 1.2 mm/min (**Figure 3** and **Table 2**).

As shown in **Figure 3**, the median values increased as the thawed depth increased under rainfall intensities of 0.6 and 0.9 mm/min (**Table 2**). For the 1.2 mm/min rainfall intensity, the median values tended to increase as the thawed depth increased from 0 to 4 cm (**Table 2**). However, decreases in the median value were observed at a rainfall intensity of 0.9 mm/min when the thawed depth was from 4 to 6 cm (**Table 2**). Moreover, the median value increased with increasing rainfall intensity at thawed depths of 0, 2, and 6 cm (**Table 2**). For a thawed depth of 4 cm, the median value increased as rainfall intensity increased from 0.6 to 0.9 mm/min (**Table 2**). However, the median value was lower under 0.9 mm/min than under 1.2 mm/min (**Table 2**).

The range was used to describe the variation in soil loss rate for individual groups (**Table 2**). The range increased as thawed depth increased under the same rainfall intensity (**Table 2**). For thawed depths of 0 and 6 cm, the range values also increased as rainfall intensity increased from 0.6 to 1.2 mm/min (**Table 2**). For thawed depths of 2 and 4 cm, the ranges also increased as rainfall intensity increased from 0.6 to 0.9 mm/min (**Table 2**); however, the ranges decreased as rainfall intensity increased from 0.9 to 1.2 mm/min (**Table 2**).

Relationships Between Soil Loss Rate and Hydraulic Conditions

Figure 4 shows the relationship between soil loss rate and shear stress (a), mean stream power (b), mean unit stream power (c), and stream erosion power (d). All the mean hydraulics conditions were found to have a positive relationship with soil loss rate (**Figure 4**).

Soil loss rate can be linearly described via mean shear stress (**Figure 4A** and **Table 3**). The determination coefficient (R^2) is 0.52 and the probabilities test was less than the significance level of 0.01. The erodibility value based on the mean shear stress was 0.17 s/m and the critical shear stress was 0.66 Pa.

The soil loss rate can be fitted to mean stream power with the following power function (**Figure 4B** and **Table 3**). The R^2 was 0.60 and the probabilities test was less than the significance level of 0.01. The erodibility value based on the mean stream power was 0.78 s^2/m^2 and the power was 0.61.

The soil loss rate showed a linear increase as the mean unit stream power increased, and the relationship could be fitted with the linear expression (**Figure 4C** and **Table 3**). The R^2 of Eq. (3) is 0.57 and the probabilities test was less than the significance level of 0.01. The erodibility value based on the mean unit stream power was 0.78 kg/m^3 and the critical unit stream power was 0.1 cm/s.

The power function below effectively described the relationship between the soil loss rate and stream erosion power (**Figure 4D** and **Table 3**). The R^2 value of Eq. (4) was 0.68 and the probabilities test was less than the significance level of 0.01. The erodibility value based on the mean stream power was 0.58 kg/L^4 and the power was 0.52.

DISCUSSION

The Effect of Rainfall Intensity and Thawed Depth on Soil Loss Rate

Under different rainfall intensities, the *k* differed with increasing thawed depth. The soil loss rate is determined by hydrodynamic and erosion material conditions. In this study, the hydrodynamic was determined by the rainfall intensity and the soil utilized. For the same rainfall intensity, the *k* value increased up to a thawed depth of 4 cm. This was likely because shallower thawed soil layers (0 and 2 cm) have slower thawing rates due to heat conduction because the frozen layer will decrease the infiltration ability (Sharratt et al., 2000; Zheng et al., 2001; Wang et al., 2020). As a result, the erodible soil was in short supply, leading to a lower erosion rate. As thawed depth increased (4 and 6 cm), more erodible soil was supplied compared the shallower thawed depths, leading to greater erosion rates. However, the limited hydrodynamic conditions at these depths resulted in decelerating erosion rates. For the 1.2 mm/min rainfall intensity, the erodible soil was still limited for 0 and 2 cm thawed depths.

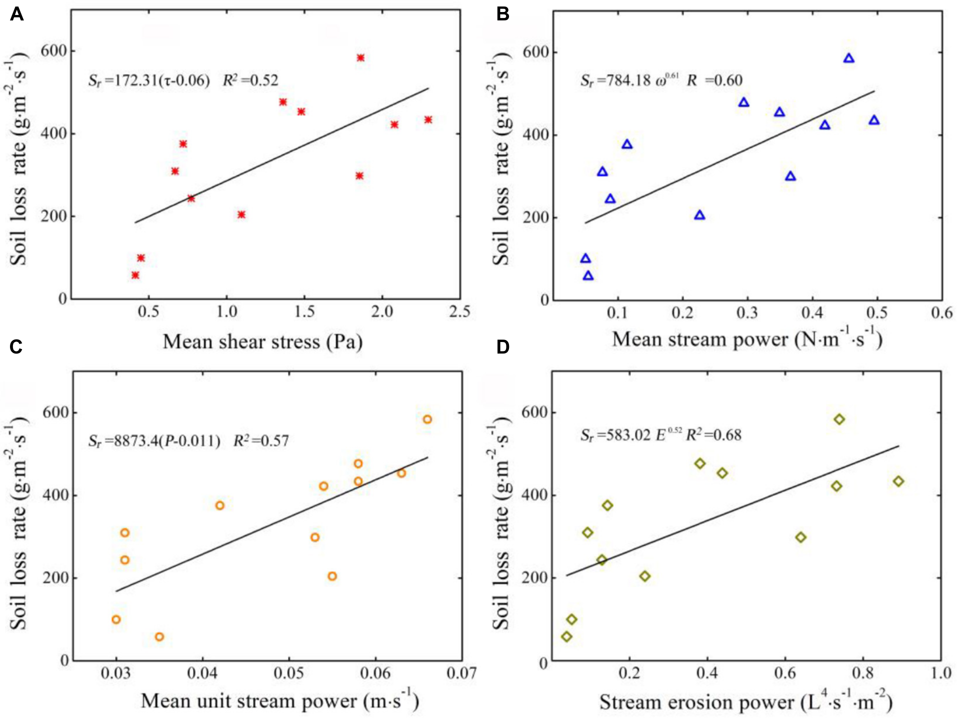

FIGURE 4 | The relationships between the soil loss rate and the mean shear stress **(A)**, mean stream power **(B)**, mean unit stream power **(C)** and stream erosion power **(D)**.

TABLE 4 | Correlation coefficients between soil loss rate with coupling effects of rainfall intensity and initial thawed depth.

Factor	*I*	*H*	*I*H*
Correlation coefficient	0.694**	0.575**	0.763**

*I, rainfall intensity; H, thawed depth; I*H, rainfall-thawed depth; **P < 0.01.*

The 4 cm thawed depth showed a unique trend under high intensity rainfall. Specifically, the soil loss rate began to decrease after 30 min of rainfall, which led to the lowest *k* value in that trial. The soil loss rate decreased because frozen soil melted slowly in the final 30 min of rainfall, but the soil loss rate was still higher than at thawed depths of 0 and 2 cm.

To clarify the correlation of rainfall intensity and thawed depth, the correlations between soil loss rate and rainfall, thawed depth and rainfall intensity-thawed depth were analyzed. As shown in **Table 4**, soil loss rate was significantly correlated with rainfall intensity, thawed depth, and rainfall intensity-thawed depth in the following order: $I^*H > I > H$. These findings indicate that interaction of rainfall intensity and thawed depth has the most important effect on soil loss rate.

Response of Soil Loss Rate to Hydraulics Conditions

In this study, the soil loss rate could be robustly predicted as linear functions of previously identified hydraulic conditions, which is similar to the results of previous studies (Laflen et al., 1991; Nearing et al., 1999; Zhang et al., 2003, 2015). However, we found lower erodibility values than some previous investigations, where erodibility ranged from 8.18×10^{-4} to 8.4×10^{-3} s/m (He et al., 2003; Zhang et al., 2013). Additionally, the critical shear stress was only 10% that obtained from a recent laboratory study (Cao et al., 2009). Zhang et al. (2015) found that the critical shear stress was 12.8 Pa under a steep slope accumulation yield experiment (30∼50°), while we found that critical shear stress was almost 20 times greater than that obtained in their study at 15°. Together, these results suggest that FTed soil has a greater erodibility and is less resistant to erosion (Li and Fan, 2014; Ban et al., 2017; Wang et al., 2020).

In addition, the mean stream power coefficient was larger and the power exponent was smaller than in previous studies (Zhang et al., 2008; Mirzaee and Ghorbanidashtaki, 2018; Wang et al., 2018). The larger coefficient mainly resulted from thawed soil having increased susceptibility to provide sediment sources (Wang et al., 2018, 2020). The smaller power exponent indicated that the increasing amplitude of the loss rate decreased with increased stream power because more energy was used to transport the sediment while the loss energy increased (Zhang et al., 2009; Shen et al., 2016; Xiao et al., 2017).

The erodibility value of unit stream power was larger and the critical unit stream power value was smaller than for previously conducted studies (Wang et al., 2017, 2020). This can be attributed to freeze-thawed soil being more easily eroded (Cuomo et al., 2016; Zi et al., 2016). Many erosion models based on processes utilize stream power to establish transport capacity.

In our experiments, stream power could not predict loss rate well, similar to the results of previous studies (Nearing et al., 1999; Zhang et al., 2002, 2003; Wang et al., 2016).

The probabilities test ($P < 0.01$) indicate that all the hydraulics conditions examined could be used to describe the changes in soil loss rate. However, based on the R^2 values, stream erosion power best described the relationship between the soil loss rate and the hydraulic conditions, followed by stream power, unit stream power and shear stress. Flow energy has been shown to be more closely related to soil loss rate than shear stress, as well as to be a useful indicator for describing soil loss rate (Nearing et al., 1999; Zhang et al., 2002; Wang et al., 2016; Xiao et al., 2017). Shear stress is mainly related to slope and flow depth, and thus reflects the response of eroded slope surfaces to concentrated flow. However, water depth is determined by dividing the runoff by the average water width. As a result, the horizontal and vertical evolution of the rill network cause increased inaccuracy of the measured water width. Hence, shear stress was not good predictive parameter in this study. For mean stream power and unit stream power, flow velocity, which was measured by $KMnO_4$ tracking, was the crucial parameter. The flow velocity is the average of different rill velocities resulting from eroded surfaces; thus, flow velocity error increases with rill amount. As a result, hydraulic conditions based on flow velocity will also become less robust. However, the predictive power of soil loss rate from stream or unit stream power was still better than that of shear stress. Finally, stream erosion power is calculated from the flow peak and average flow depth. The average flow depth can be obtained from total runoff amount divided by the underlayer area, which has lower measurement error. Thus, stream erosion power is a better hydraulic parameter for predicting soil loss rate.

CONCLUSION

In this study, experimental investigations of erosion processes of different thawed depth loessal slopes were conducted under different rainfall intensities. The results indicated that linear regression could be used to describe the relationship between the soil loss rate and runoff time. The k values increased as rainfall intensity increased from 0.6 to 1.2 mm/min except for the 4 cm thawed depth slope. For the 4 cm thawed depth, the values of k increased first, then decreased as the rainfall intensity increased from 0.6 to 1.2 mm/min. In general, the mean soil loss rate increased with thawed depth under each rainfall intensity. Additionally, the range increased as thawed depth increased under the same rainfall intensity. We observed a significant relationship between soil loss rate and rainfall intensity, thawed depth, and their interaction, and their interaction was found to have the most important effects on soil loss rate. After testing multiple hydraulic conditions, stream erosion power was found to be the best predictor of soil loss rate.

DATA AVAILABILITY STATEMENT

The raw data supporting the conclusions of this article will be made available by the authors, without undue reservation.

AUTHOR CONTRIBUTIONS

WW and TW conceived the main idea of this manuscript. ZL, RY, and PL designed and performed the experiment. WW wrote the manuscript and all authors contributed to improving the manuscript.

FUNDING

This research was supported by the National Key Research and Development Program of China (No. 2017YFC0504704), the National Natural Science Foundation of China (52009104 and 51779204), the Project of Ecological Restoration and Environmental Protection in the Upper and Middle Watershed of the Yellow River (QNZX-2019-03), the Shaanxi Province Innovation Talent Promotion Plan Project Technology Innovation Team (Nos. 2018TD-037 and 2020TD-023).

ACKNOWLEDGMENTS

We thank the reviewers for their useful comments and suggestions.

REFERENCES

Ala, M., Liu, Y., Wang, A. Z., and Niu, C. Y. (2016). Characteristics of soil freeze-thaw cycles and their effects on water enrichment in the rhizosphere. *Geoderma* 264, 132–139. doi: 10.1016/j.geoderma.2015.10.008

Ban, Y. Y., Lei, T. W., Chen, C., Yin, Z., and Qian, D. F. (2017). Meltwater erosion process of frozen soil as affected by thawed depth under concentrated flow in high altitude and cold regions. *Earth Surf. Process. Landf.* 42, 2139–2146. doi: 10.1002/esp.4173

Batista, P. V., Davies, J., Silva, M. L., and Quinton, J. N. (2019). On the evaluation of soil erosion models: are we doing enough? *Earth Sci. Rev.* 197:102898. doi: 10.1016/j.earscirev.2019.102898

Cai Guoqiang (1995). *Small Watershed Runoff Process Model. The Second Session of National Fundamental Theories of Sediment Transport Research Symposium*. Beijing: China Water Power Press, 233-238.

Cao, L. X., Zhang, K. L., Dai, H. L., and Guo, Z. L. (2009). Modeling soil detachment on unpaved road surfaces on the loess plateau. *Trans. ASABE* 54, 1377–1384. doi: 10.13031/2013.39039

Cheng, Y., Li, P., Xu, G., Li, Z., Wang, T., Cheng, S., et al. (2018). The effect of soil water content and erodibility on losses of available nitrogen and phosphorus in simulated freeze-thaw conditions. *Catena* 166, 21–33. doi: 10.1016/j.catena.2018.03.015

Cuomo, S., Della Sala, M., and Pierri, M. (2016). Experimental evidences and numerical modelling of runoff and soil erosion in flume tests. *Catena* 147, 61–70. doi: 10.1016/j.catena.2016.06.044

Dazzi, C., and Papa, G. L. (2019). Soil genetic erosion: new conceptual developments in soil security. *Int. Soil Water Conserv. Res.* 7, 317–324. doi: 10.1016/j.iswcr.2019.08.001

Edwards, L. M. (2013). The effects of soil freeze—thaw on soil aggregate breakdown and concomitant sediment flow in Prince Edward Island: a review. *Can. J. Soil Sci.* 93, 459–472. doi: 10.4141/cjss2012-059

Fan, H. M., Zhang, R. F., Zhou, L. L., Wu, M., and Liu, Y. H. (2009). Impact of climate change on freeze-thaw function and freeze-thaw erosion in black soil region of Northeast of China. *J. Arid Land Res. Environ.* 23, 48–53.

Foster, G. R., and Meyer, L. D. (1972). Transport of soil particles by shallow flow. *Trans. ASAE* 15, 99–102. doi: 10.13031/2013.37840

Govers, G. (1990). Empirical relationships for the transport capacity of overland flow: erosion, transport, and deposition process. *LAHS Publ.* 1, 45–63.

Govers, G. (1992). Relationship between discharge, velocity, and flow area for rills eroding loose, non–layered materials. *Earth Surf. Process. Landf.* 17, 515–528. doi: 10.1002/esp.3290170510

Guo, M., Wang, W., Li, J., Bai, Y., Kang, H., and Yang, B. (2020). Runoff characteristics and soil erosion dynamic processes on four typical engineered landforms of coalfields: an in-situ simulated rainfall experimental study. *Geomorphology* 349:106869. doi: 10.1016/j.geomorph.2019.106896

He, X. W., Zhang, G. H., and Liu, B. Y. (2003). Soil detachment by shallow flow on slopes. *Trans. CSAE* 19, 52–55.

Knapen, A., Poesen, J., and De Baets, S. (2007). Seasonal variations in soil erosion resistance during concentrated flow for a loess-derived soil under two contrasting tillage practices. *Soil Tillage Res.* 94, 425–440. doi: 10.1016/j.still.2006.09.005

Laflen, J. M., Elliot, W. J., Simanton, J. R., Holzhey, C. S., and Kohl, K. D. (1991). WEPP: soil erodibility experiments for rangeland and cropland soils. *J. Soil Water Conserv.* 46, 39–44.

Li, G. Y., and Fan, H. M. (2014). Effect of freeze-thaw on water stability of aggregates in a black soil of northeast China. *Pedosphere* 24, 285–290. doi: 10.1016/S1002-0160(14)60015-1

Li, Q., Liu, G. B., Xu, M. X., Sun, H., Zhang, Z., and Gao, L. Q. (2013). Effect of seasonal freeze-thaw on soil anti-scouribility and its related physical property in hilly loess plateau. *Trans. Chin. Soc. Agric. Eng.* 29, 105–112.

Lu, K. X., Li, Z. B., and Ju, H. (2009). Application of runoff erosion power in the calculation of soil erosion and sediment yield on hillslopes. *J. Water Resour. Water Eng.* 20, 70–73.

Luk, S. H., and Merz, W. (1992). Use of the salt tracing technique to determine the velocity of overland flow. *Soil Technol.* 5, 289–301.

Luo, J., Zheng, Z., Li, T., and He, S. (2019). The changing dynamics of rill erosion on sloping farmland during the different growth stages of a maize crop. *Hydrol. Process.* 33, 76–85. doi: 10.1002/hyp.13312

Mirzaee, S., and Ghorbanidashtaki, S. (2018). Deriving and evaluating hydraulics and detachment models of rill erosion for some calcareous soils. *Catena* 164, 107–115. doi: 10.1016/j.catena.2018.01.016

Nearing, M. A., Simanton, J. R., Norton, L. D., Bulygin, S. J., and Stone, J. J. (1999). Soil erosion by surface water flow on a stony, semiarid hillslope. *Earth Surf. Process. Landf.* 24, 677–686. doi: 10.1002/(SICI)1096-9837(199908)24:8<677::AID-ESP981>3.0.CO;2-1

Ragettli, S., Pellicciotti, F., Immerzeel, W. W., Miles, E. S., Petersen, L., Heynen, M., et al. (2015). Unraveling the hydrology of a Himalayan catchment through integration of high resolution in situ data and remote sensing with an advanced simulation model. *Adv. Water Resour.* 78, 94–111. doi: 10.1016/j.advwatres.2015.01.013

Sharratt, B. S., Lindstrom, M. J., Benoit, G. R., Young, R. A., and Wilts, A. (2000). Runoff and soil erosion during spring thaw in the northern US Corn Belt. *J. Soil Water Conserv.* 55, 487–494.

Shen, N., Wang, Z. L., and Wang, S. (2016). Flume experiment to verify WEPP rill erosion equation performances using loess material. *J. Soils Sediments* 16, 2275–2285. doi: 10.1007/s11368-016-1408-3

Shi, P., Feng, Z. H., Gao, H. D., Li, P., Zhang, X. M., Zhu, T. T., et al. (2020). Has "Grain for Green" threaten food security on the Loess Plateau of China? *Ecosyst. Health Sustainabil.* 6:1709560. doi: 10.1080/20964129.2019.1709560

Shi, P., Zhang, Y., Li, P., Li, Z. B., Yu, K. X., Ren, Z. P., et al. (2019). Distribution of soil organic carbon impacted by land-use changes in a hilly watershed of the Loess Plateau, China. *Sci. Total Environ.* 652, 505–512. doi: 10.1016/j.scitotenv.2018.10.172

Wang, D. D., Wang, Z. L., Shen, N., and Chen, H. (2016). Modeling soil detachment capacity by rill flow using hydraulic parameters. *J. Hydrol.* 535, 437–479. doi: 10.1016/j.jhydrol.2016.02.013

Wang, T., Li, P., Hou, J., Li, Z., Ren, Z., Cheng, S., et al. (2018). Response of the meltwater erosion to runoff energy consumption on loessal slopes. *Water* 10:1522. doi: 10.3390/w10111522

Wang, T., Li, P., Li, Z., Hou, J., Xiao, L., Ren, Z., et al. (2019). The effects of freeze–thaw process on soil water migration in dam and slope farmland on the Loess Plateau, China. *Sci. Total Environ.* 666, 721–730. doi: 10.1016/j.scitotenv.2019.02.284

Wang, T., Li, P., Liu, Y., Hou, J., Li, Z., Ren, Z., et al. (2020). Experimental investigation of freeze-thaw meltwater compound erosion and runoff energy consumption on loessal slopes. *Catena* 185:104310. doi: 10.1016/j.catena.2019.104310

Wang, T., Li, P., Ren, Z., Xu, G., Li, Z., Yang, Y., et al. (2017). Effects of freeze-thaw on soil erosion processes and sediment selectivity under simulated rainfall. *J. Arid Land* 9, 234–243. doi: 10.1007/s40333-017-0009-3

Wei, X., Li, X. G., and Huang, C. H. (2015). Impacts of freeze-thaw cycles on runoff and sediment yield of slope land. *Trans. Chin. Soc. Agric. Eng.* 31, 157–163.

Xiao, H., Liu, G., Liu, P., Zheng, F., Zhang, J., and Hu, F. (2017). Response of soil erosion rate to the hydraulic conditions of concentrated flow on steep loessial slopes on the Loess Plateau of China. *Hydrol. Process.* 31, 2613–2621. doi: 10.1002/hyp.11210

Xiao, L., Zhang, Y., Li, P., Xu, G., Shi, P., and Zhang, Y. (2019). Effects of freeze-thaw cycles on aggregate-associated organic carbon and glomalin-related soil protein in natural succession grassland and Chinese pine forest on the Loess Plateau. *Geoderma* 334, 1–8. doi: 10.1016/j.geoderma.2018.07.043

Xu, X., Liu, Z. Y., Xiao, P. Q., Guo, W., Zhang, H., Zhao, C., et al. (2015a). Gravity erosion on the steep loess slope: behavior, trigger and sensitivity. *Catena* 135, 231–239. doi: 10.1016/j.catena.2015.08.005

Xu, X., Zhang, H., Wang, W., Zhao, C., and Yan, Q. (2015b). Quantitative monitoring of gravity erosion using a novel 3D surface measuring technique: validation and case study. *Nat. Hazards* 75, 1927–1939. doi: 10.1007/s11069-014-1405-z

Yu, Y., Zhao, W., Martinez-Murillo, J., and Pereira, P. (2020). Loess Plateau: from degradation to restoration. *Sci. Total Environ.* 738:140206. doi: 10.1016/j.scitotenv.2020.140206

Yue, L., Juying, J., Bingzhe, T., Binting, C., and Hang, L. (2020). Response of runoff and soil erosion to erosive rainstorm events and vegetation restoration on abandoned slope farmland in the Loess Plateau region, China. *J. Hydrol.* 584:124694. doi: 10.1016/j.jhydrol.2020.124694

Zhang, B. J., Zhang, G., Yang, H., and Wang, H. (2019). Soil resistance to flowing water erosion of seven typical plant communities on steep gully slopes on the Loess Plateau of China. *Catena* 173, 375–383. doi: 10.1016/j.catena.2018.10.036

Zhang, G. H., Liu, B. Y., Nearing, M. A., Huang, C. H., and Zhang, K. L. (2002). Soil detachment by shallow flow. *Trans. ASABE* 45, 351–357. doi: 10.13031/2013.8527

Zhang, J., Yang, M., Deng, X., Liu, Z., and Zhang, F. (2019). The effects of tillage on sheet erosion on sloping fields in the wind-water erosion crisscross region of the Chinese loess plateau. *Soil Tillage Res.* 187, 235–245. doi: 10.1016/j.still.2018.12.014

Zhang, W., Xing, S., and Hou, X. (2019). Evaluation of soil erosion and ecological rehabilitation in Loess Plateau region in Northwest China using plutonium isotopes. *Soil Tillage Res.* 191, 162–170. doi: 10.1016/j.still.2019.04.004

Zhang, G. H., Liu, B. Y., Liu, G. B., He, X. W., and Nearing, M. A. (2003). Detachment of undisturbed soil by shallow flow. *Soil Sci. Soc. Am. J.* 67, 713–719. doi: 10.2136/sssaj2003.7130

Zhang, G. H., Liu, G. B., Tang, K. M., and Zhang, X. C. (2008). Flow detachment of soils under different land uses in the Loess Plateau of China. *Trans. Am. Soc. Agric. Biol. Eng.* 51, 883–890. doi: 10.13031/2013.24527

Zhang, G. H., Liu, Y. M., Han, Y. F., and Zhang, X. C. (2009). Sediment transport and soil detachment on steep slopes: II. Sediment feedback relationship. *Soil Sci. Soc. Am. J.* 73, 1298–1304. doi: 10.2136/sssaj2009.0074

Zhang, L., Gao, Z., Yang, S., Li, Y., and Tian, H. (2015). Dynamic processes of soil erosion by runoff on engineered landforms derived from expressway construction: a case study of typical steep spoil heap. *Catena* 128, 108–121. doi: 10.1016/j.catena.2015.01.020

Zhang, Y. D., Wu, S. F., Feng, H., and Huo, Y. Y. (2013). Experimental study of rill dynamic development process and its critical dynamic conditions on loess slope. *J. Sediment Res.* 2, 25–32.

Zheng, X., Van Liew, M. W., and Flerchinger, G. N. (2001). Experimental study of the infiltration into a bean stubble field during seasonal freeze-thaw period. *Soil Sci.* 166, 3–10. doi: 10.1097/00010694-200101000-00002

Zhou, L. L., Wang, T. L., Fan, H. M., Wu, M., Chai, Y., Liu, J., et al. (2009). Effects of incompletely thawed layer on black soil slope rainfall erosion. *J. Soil Water Conserv.* 23, 1–5.

Zi, T., Kumar, M., Kiely, G., Lewis, C., and Albertson, J. (2016). Simulating the spatio-temporal dynamics of soil erosion, deposition, and yield using a coupled sediment dynamic and 3d distributed hydrologic model. *Environ. Model. Softw.* 83, 310–325. doi: 10.1016/j.envsoft.2016.06.004

Conflict of Interest: The authors declare that the research was conducted in the absence of any commercial or financial relationships that could be construed as a potential conflict of interest.

frontiers
in Environmental Science

ORIGINAL RESEARCH
published: 27 January 2021
doi: 10.3389/fenvs.2020.614761

Vegetation Restoration Alleviated the Soil Surface Organic Carbon Redistribution in the Hillslope Scale on the Loess Plateau, China

Yipeng Liang[1,2], *Xiang Li*[1,2], *Tonggang Zha*[1,2,3]* and *Xiaoxia Zhang*[1,4]

[1]*School of Soil and Water Conservation, Beijing Forestry University, Beijing, China,* [2]*Key Laboratory of Soil and Water Conservation and Desertification Combating, State Forestry and Grassland Administration, Beijing Forestry University, Beijing, China,* [3]*Jixian National Forest Ecosystem Research Network Station, CNERN, Beijing Forestry University, Beijing, China,* [4]*The Third Construction Co., Ltd. of China Construction First Group, Beijing, China*

The redistribution of soil organic carbon (SOC) in response to soil erosion along the loess slope, China, plays an important role in understanding the mechanisms that underlie SOC's spatial distribution and turnover. Consequently, SOC redistribution is key to understanding the global carbon cycle. Vegetation restoration has been identified as an effective method to alleviate soil erosion on the Loess Plateau; however, little research has addressed vegetation restoration's effect on the SOC redistribution processes, particularly SOC's spatial distribution and stability. This study quantified the SOC stock and pool distribution on slopes along geomorphic gradients in naturally regenerating forests (NF) and an artificial black locust plantation (BP) and used a corn field as a control (CK). The following results were obtained: 1) vegetation restoration, particularly NF, slowed the migration of SOC and reduced the heterogeneity of its distribution effectively. The topsoil SOC ratios of the sedimentary area to the stable area were 109%, 143%, and 210% for NF, BP, and CK, respectively; 2) during migration, vegetation restoration decreased the loss of labile organic carbon by alleviating the loss of dissolved organic carbon (DOC) and easily oxidized organic carbon (EOC). The DOC/SOC in the BP and NF increased significantly and was 13.14 and 17.57 times higher, respectively, than that in the CK ($p < 0.05$), while the EOC/SOC in the BP and NF was slightly higher than that in the CK. A relevant schematic diagram of SOC cycle patterns and redistribution along the loess slope was drawn under vegetation restoration. The results suggest that vegetation restoration in the loess slope, NF in particular, is an effective means to alleviate the redistribution and spatial heterogeneity of SOC and reduce soil erosion.

Keywords: vegetation restoration, soil organic carbon stability, hillslope, soil erosion, Loess Plateau (China)

Edited by:
Jesús Rodrigo-Comino,
Universität Trier, Germany

Reviewed by:
Mahboobeh Kiani-harchegani,
Yazd University, Iran
Safwan Mohammed,
University of Debrecen, Hungary

***Correspondence:**
Tonggang Zha
zhtg73@bjfu.edu.cn

Specialty section:
This article was submitted to Soil Processes,
a section of the journal
Frontiers in Environmental Science

Received: *07 October 2020*
Accepted: *18 December 2020*
Published: *27 January 2021*

Citation:
Liang Y, Li X, Zha T and Zhang X (2021) Vegetation Restoration Alleviated the Soil Surface Organic Carbon Redistribution in the Hillslope Scale on the Loess Plateau, China.
Front. Environ. Sci. 8:614761.
doi: 10.3389/fenvs.2020.614761

INTRODUCTION

Soil is considered the most significant terrestrial carbon sink. It is a critical factor in the regulation of the global carbon cycle, as well as in the supply of pivotal ecosystem services (Muñoz-Rojas et al., 2016; Pereira et al., 2018; Brevik et al., 2020). Soil organic carbon (SOC) is the amount of organic carbon contained in the soil fraction and contributes to a variety of important biological, physical, and chemical functions (Muñoz-Rojas et al., 2016; Willaarts et al., 2016; Wiesmeier et al., 2019;

Pereira et al., 2020). SOC's depletion has a negative influence on water storage capacity, soil fertility, and the supply of other significant ecosystem services, such as climate regulation, and is therefore a major factor that leads to soil degradation (Kiani-Harchegani and Sadeghi, 2020). In water-limited ecosystems, vegetation restoration is one of the options to prevent land degradation and soil erosion (Yu et al., 2016; Shi et al., 2019a). Ongoing vegetation restoration and climate change processes are having a far-reaching effect on soil carbon stocks, which creates an imbalance in carbon input/output ratios and results frequently in net releases back into the atmosphere (Haigh et al., 2019; Petrakis et al., 2020; van der Bank and Karsten, 2020). SOC is the most susceptible to changes in site conditions and is therefore the target of most evaluations (García-Díaz et al., 2016; Yeasmin et al., 2020).

In past years, numerous estimates of SOC stocks have been conducted at multiple scales (from slope to watershed, regional and global), using different approaches (Abdalla et al., 2018; Álvaro-Fuentes et al., 2014; Grebliunas et al., 2016; García-Díaz et al., 2018; Shi et al., 2019b; Rodrigo-Comino et al., 2020). Quantitative assessments of the redistribution of SOC along geomorphic gradients and the processes involved have become increasingly important in a changing climate (Bloom et al., 2016; Yu et al., 2019a; Olson and Gennadiev, 2020). At the same time, the storage of SOC showed significant differences within ecological units because of the effect of such local factors as soil properties, topographic conditions, soil depth, and land use and management (Novara et al., 2019). Among these, topography is one of the five major soil surface formation factors (Jenny, 1994). Topography affects soil erosion and thus affects SOC's spatial distribution either directly or indirectly (Sun et al., 2010; Rodrigo-Comino et al., 2016, 2017; Cagnarini et al., 2019; Cerdà and Rodrigo-Comino, 2020). Several studies have demonstrated the effects of topography and soil erosion on SOC's distribution (Beguería et al., 2015). For example, a previous study reported a close relationship between soil erosion and SOC content and indicated further that the SOC content is generally higher in a slope's middle and lower reach than in the upper reach (Sanderman and Chappell, 2013; Hancock et al., 2019). A typical hill slope can be divided into a stable area, eroding area, and sedimentary area according to its position and gradient on the slope (Wang et al., 2014a; Wang et al., 2017). Topography affects the stable area less, but the SOC in the eroding area will continue to migrate toward the sedimentary area, where it will accumulate (Doetterl et al., 2016). At the same time, the slope system also affects the composition and stability of SOC (Wang et al., 2014b; Wiaux et al., 2014). In some simulations in hillslope plots, the distribution of labile organic carbon varied markedly along slopes (Berhe and Torn, 2017), and most followed the trend: sedimentary area > stable area > eroded area (Doetterl et al., 2012; Patton et al., 2019; Wang et al., 2019). However, current research on the distribution of the SOC in the extension of slopes focuses primarily on agricultural land or grassland (Kirkels et al., 2014; Doetterl et al., 2016; Li et al., 2019). Vegetation restoration is recognized widely as an effective way to enhance SOC content and control soil erosion (Kim and Kirschbaum, 2015; Xin et al., 2016; Hancock et al.,2019). Therefore, it seems likely that vegetation restoration may also affect the SOC redistribution process in areas with complex terrain.

The Chinese Loess Plateau covers approximately 64 × 10^4 km^2, lies in the semiarid zone of China, and is characterized by thick (50–300 m), yet highly erodible soil (Feng et al., 2013). Hundreds of years of intensive cultivation and severe erosion have incised the plateau and thus fragmented the vast flat area into tableland and slopes, with notable depositions in valley bottoms (Wang et al., 2017; Yu et al., 2019b). To alleviate soil erosion, large-scale ecological restoration efforts have been implemented in the Loess Plateau, the most notable example of which is the Grain for Green Project (GGP) that was initiated in the 1980s (Feng et al., 2013; Yu et al., 2020a). These projects have improved vegetation restoration greatly and affected SOC sequences and the carbon cycle on the Loess Plateau (Chang et al.,2011; Ran et al., 2013; Wang et al., 2017). However, systematic investigations of the results of vegetation restoration on SOC redistribution and its stability have not been reported to date. Particularly, the topographic positions of SOC in the hilly-gully region on the fragmented Loess Plateau remain unknown.

To offer new insights to fill this gap, hillslope positions and vegetation-induced changes in SOC in the first 0–30 cm were investigated on three different hillslopes of the loess hilly watershed where farmland has been transformed into forestland. Accordingly, this study's primary goals were to 1) detect changes in SOC at different soil depths (0–10, 10–20, and 20–30 cm) and different vegetation types at the hillslope scale and 2) assess the effects of vegetation species and topography on soil carbon stability during ecological restoration. Our study hypothesized that vegetation restoration alleviates the spatial heterogeneity of SOC by increasing organic input and decreasing soil erosion and the slow SOC mineralization or loss of unstable carbon.

MATERIALS AND METHODS

Study Area

As a typical loess gully area, the Caijiachuan Watershed ($110^0 27'$-$111^0 07'$E, $35^0 53'$-$36^0 21'$ N, elevation 868–1553 m) is located on the Loess Plateau in Ji County, Shanxi province, China (**Figure 1**). This area has a warm, temperate continental climate with an average mean temperature of 10°C, a mean duration of 2,563 h of sunshine, a frost-free period of 172 days, and a mean annual precipitation of 575.9 mm. The precipitation varies greatly between years and seasons and is concentrated largely between June and September of each year (Zhou et al., 2013). The study area is characterized by a deeply incised hilly-gully loess landscape. The soils are the result of a high wind-deposited loess process and can be classified as Haplic Luvisols (IUSS Working Group, 2006).

In general, soils are characterized by a high content of sand (45–60%) and silt (36–55%) material with certain variations depending on the hillslope position and previous land uses (Zhang et al., 2013b). The soil bulk density is approximately 1.15–1.30 g cm^{-3}, with a low organic matter content (5–15 g kg^{-1}). The principal forest types are naturally regenerating forests (NF) dominated by aspens (*Populus davidiana*) and oaks (*Quercus liaotungesis*) and reforested areas of black locust (*Robinia pseudoacacia*), Chinese pine (*Pinus

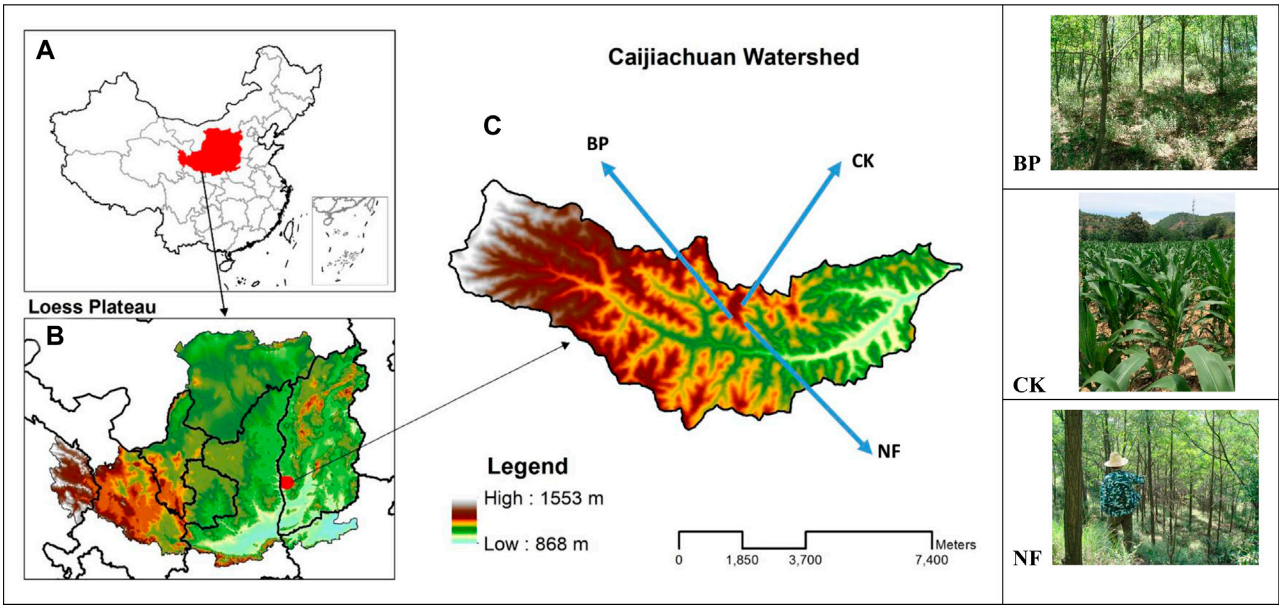

FIGURE 1 | Locations of the research sites (a: China, b: Shanxi Province, and c the Caijiachuan Watershed). NF is the naturally regenerating forest, BP is the black locust plantation, and CK is the cropland as control.

TABLE 1 | Basic information on the research site (Caijiachuan catchment, Shanxi Province, North China). DBH = diameter at breast height; canopy density is provided for the forested sites and coverage is provided for the corn farmland; "–" = not measured. The values presented are the means and SD in brackets.

Vegetation type	Slope length (m)	Slope angle $(^{0})$	Slope aspect	Altitude (m)	DBH (cm)	Tree height (m)	Tree density (hm^{-2})	Canopy density/coverage (%)
Black locust plantation	281	19	South	1 120	11.48 (0.26)	8.39 (0.40)	1864 (12)	84.6 (2.3)
Natural recovery forest	302	20	Southeast	1 040	10.96 (0.35)	6.68 (0.22)	1942 (15)	87.3 (5.1)
Corn farmland	278	18	South	1 120	–	–	–	84.5 (1.6)

tabulaeformis), and cypresses (*Platycladus orientalis*). All forests were planted in 1990 as part of the GGP.

Experimental Design

Three typical hillslopes characterized by similar landforms (considering the gradient, aspect, and length fully) and different vegetation types (**Table 1**) were selected, representing 1) a black locust plantation (BP), 2) NF, and 3) a corn field as a control (CK). Both the BP and NF were converted from corn filed in 1990, and the main tree species in the NF was secondary *Quercus aliena* Bl. Both the BP and CK are located in the same gully at similar elevations (1120 m a.s.l.). The NF is located in an area affected by a gully of approximately 4 km southeast and an elevation of approximately 1040 m a.s.l. Corn fields in this area adopt the traditional cultivation model with few management measures, such as ploughing and fertilization.

In this study, the hillslopes were divided into three erosional areas based on the slope gradient and soil erosion conditions (**Figure 2**). Specifically, the stable area was defined as the area at the shoulder of a slope with a low gradient (<50) and light soil erosion marks. The eroding area was defined as the area in the backslope with a steeper gradient (>100) and clearer soil erosion signs. Finally, the sedimentary area was defined as the area at the footslope with a lower gradient (<50). Because the eroded material from the eroding areas is used to accumulate in the sedimentary parts, the soils therein consist largely of a mixture of sediment setting on loess parent materials in deeper layers (Doetterl et al., 2012; Doetterl et al., 2016; Wang et al., 2017).

Field Sampling

In mid-August, 2017, three plots of 10 × 10 m (separated by at least 10 m) were established representing the typical erosional area of each typical hillslope. Detailed site conditions (including elevation, slope length, angle, and aspect), as well as a vegetation inventory, were conducted in each plot. Five sampling points were set randomly and soil samples were collected at 10 cm intervals from a depth of 0–30 cm using a cylindrical soil driller (4 cm diameter and 20 cm long). Soil from corresponding layers was mixed to form one soil composite

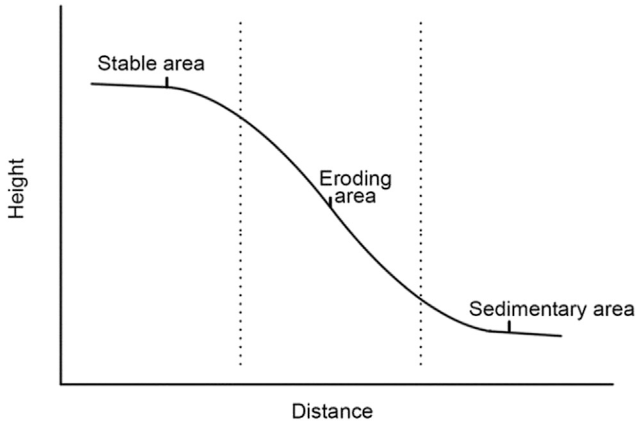

FIGURE 2 | Topographical transect showing stable, eroding, and sedimentary areas. The stable area is on the top of the slope and has a small gradient (<5^0) and little erosion. The eroding area is in the middle of the slope and has a steep gradient (>10^0) and strong soil erosion. The sedimentary area is at the bottom of a slope and has a small gradient (<5^0) and notable sediment deposit.

sample. Five replicate soil samples were collected in each plot, and 135 soil samples were collected in total. Each soil sample was divided evenly into two parts after visible roots and other impurities were removed, and one was naturally air-dried, while the other was refrigerated at 4°C until further use.

Laboratory Analysis

The air-dried soil was passed through a 0.2 mm sieve to ensure complete removal of gravel. The SOC content was determined by the potassium dichromate external heating method (Bao, 2000). The dissolved organic carbon (DOC) content was analyzed as follows: 10 g of a soil sample was added to a triangular flask with 40 ml of distilled water. The sample was shocked and leached for approximately 30 min at room temperature after 10 min of high-velocity centrifugation (6000 r/min at 4°C). The supernatant obtained was filtered through a 0.45 μm filter into separate vials and the extracts were analyzed for DOC using a total organic carbon analyzer (Multi N/C 3100, Analytik Jena AG, Thuringia, Germany). The level of easily oxidized organic carbon (EOC) in the organic phases was measured using 333 mmol/L of $KMnO_4$ by shaking for 1 h, centrifugation for 5 min at 4000 g, diluting 10 times with deionized water, and using a spectrophotometer (AQ8100, Thermo Scientific™, MA) to measure the absorbance at 565 nm (Von Lützow et al., 2007). The $KMnO_4$ standard curve and calculation method were based on Blaire et al. (1995) report.

Statistical Analysis

An analysis of variance (ANOVA) was used to analyze vegetation restoration's effects on SOC content, DOC/SOC, and EOC/SOC between forest types, slope areas, and soil depth ($p < 0.05$). The means for each vegetation type in **Table 1** were calculated by averaging the values of nine plots within the same slope, and the means in the figures for each area were calculated by averaging the values from three replicated plots in the corresponding soil layers. All data analyses were performed using SPSS v. 23.0 (SPSS Inc. 2016; NC) and R software v. 3.6 (R Development Core Team, 2012; R Project for Statistical Computing, Vienna, Austria).

RESULTS

Effect of Vegetation Restoration on SOC Content

Figure 3 shows that the SOC content increased significantly in response to vegetation restoration ($p < 0.05$). For the BP, the average SOC content was 6.85 g/kg, 1.38 times higher than that of the CK. For NF, the average SOC content was 14.28 g/kg, 2.88 times higher than that of the CK. The SOC content in the same area decreased significantly with increasing soil depth ($p < 0.05$).

The SOC content followed the same distributions throughout the three vegetation types: sedimentary area > stable area > eroding area. However, the range of the changes observed was smaller after vegetation restoration. The ratio of the SOC content in the sedimentary to eroding areas in the CK was 247.0%, which decreased to 158.4% and 129.3% in response to the BP and NF, respectively. The change in the SOC distribution along the slope was most obvious in the 0–10 cm soil layer following vegetation recovery. In BP and CK, the SOC content in the deposition area was significantly higher than that in both the stable and eroding areas ($p < 0.05$). However, in NF, no significant difference was found in the surface soil between the three areas tested ($p < 0.05$). In the 20–30 cm soil layer, the SOC contents of NF, BP, and CK were all significantly higher in the deposition area than in the stable area and the content in the stable area was significantly higher than that in the eroding area ($p < 0.05$).

Effects of Vegetation Restoration on SOC Stability

Effects on Dissolved Organic Carbon

The proportion of DOC in SOC increased significantly ($p < 0.05$) after vegetation restoration (**Figure 4**). The DOC/SOC of the BP and NF was 0.92% and 1.23%, respectively, 13.14 times and 17.57 times higher, respectively, compared to the CK

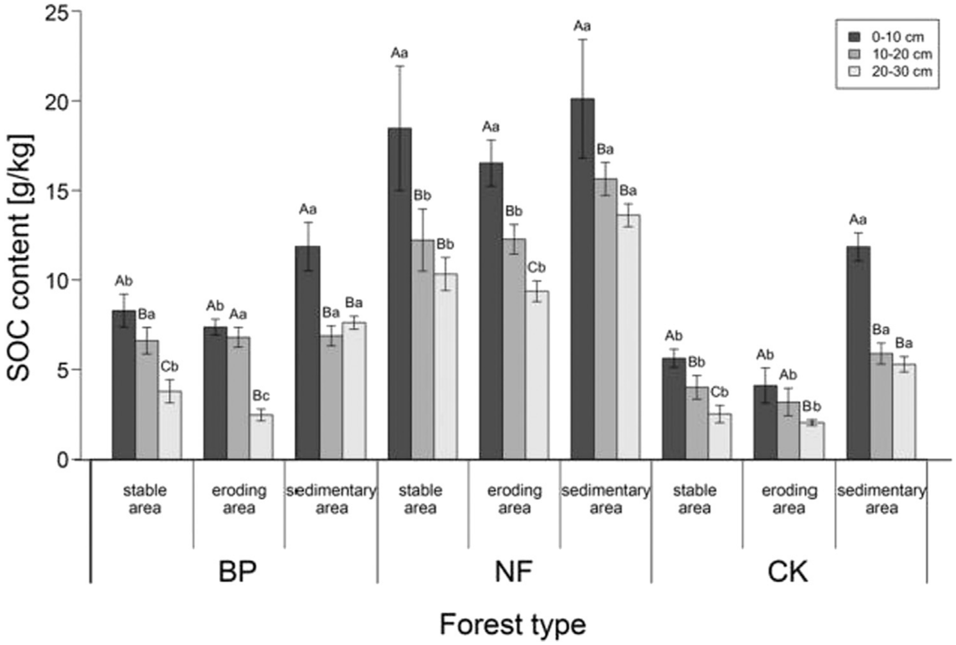

FIGURE 3 | Soil organic carbon content of the 0–30 cm soil layer (in 10 cm intervals) in the three areas defined in **Figure 2** under naturally regenerating forests (NF), black locust plantation (BP), and the corn field as the control (CK). Vertical bars represent the standard deviations of five replicated soil samples. Different capital letters for the same areas indicate significant differences at $p < 0.05$ of soil layers, while different lowercase letters for the same soil layers indicate significant differences at $p < 0.05$ of different regions.

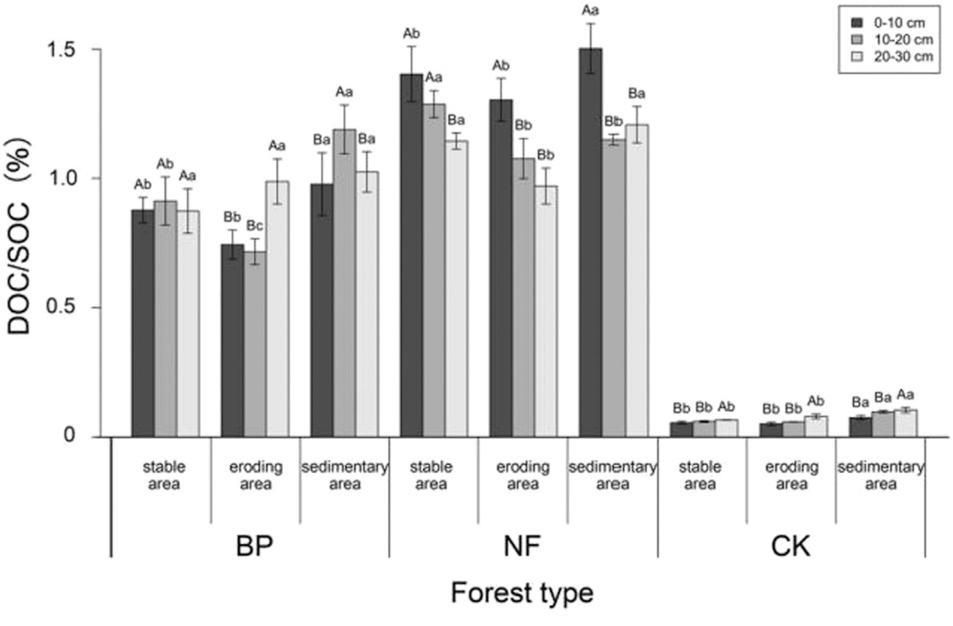

FIGURE 4 | Ratio of dissolved organic carbon (DOC) to total soil organic carbon (SOC) of the 0–30 cm soil layer (in 10 cm intervals) in three areas under different forest types. Vertical bars represent the standard deviations of five replicated soil samples. Different capital letters for the same areas indicate significant differences at $p < 0.05$ of soil layers, while different lowercase letters for the same soil layers indicate significant differences at $p < 0.05$ of different regions.

(0.07%). The DOC/SOC differed significantly in different soil layers; however, no consistent pattern of change was identified ($p < 0.05$). In the BP, the DOC fluctuated with the soil layer, but without apparent regularity; in the same area of NF, DOC/SOC decreased with increasing soil depth but increased in the CK.

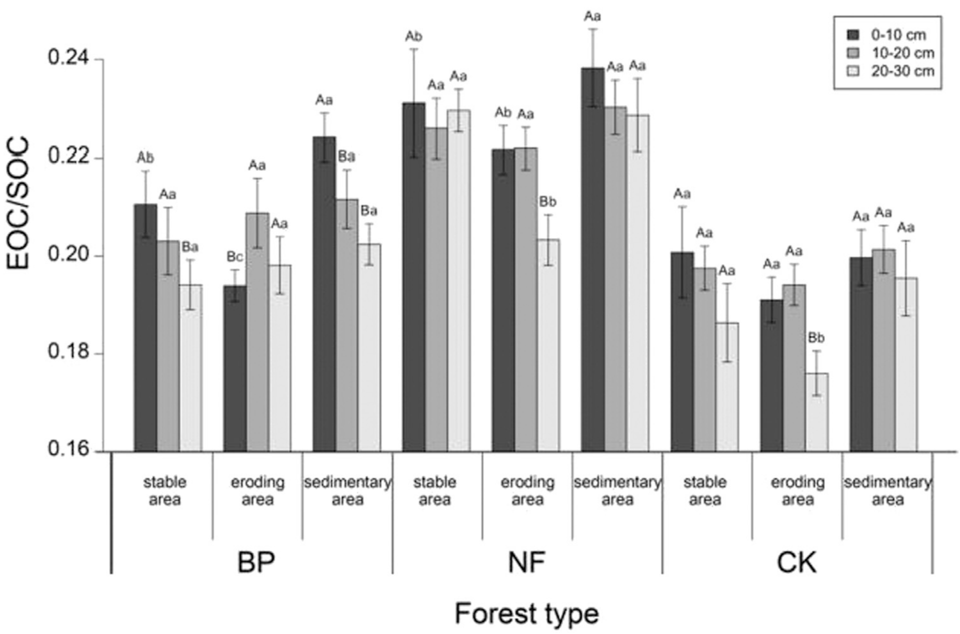

FIGURE 5 | Ratio of easily oxidized organic carbon (EOC) to SOC of the 0–30 cm soil layer (in 10 cm intervals) in the three areas under different forest types. Vertical bars represent the standard deviations of five replicated soil samples. Different capital letters for the same areas indicate significant difference at $p < 0.05$ of soil layers, while different lowercase letters of the same soil layers indicate significant differences at $p < 0.05$ of different regions.

Compared to the CK, the increasing extent of DOC/SOC in the sedimentary area decreased significantly after vegetation restoration ($p < 0.05$). In the BP, NF, and CK, the ratios of DOC/SOC in the deposition areas were 1.29, 1.15, and 1.50 times that in the eroding area. For the BP, the DOC/SOC in the sedimentary area in the 0–10 cm and 10–20 cm soil layers was significantly higher than that in the stable and eroding areas ($p < 0.05$). However, in the 20–30 cm soil layer, no significant difference was found between the deposition and eroding areas ($p < 0.05$), and in NF, no significant erosion or accumulation of DOC in a specific area was observed ($p < 0.05$). In the CK, the DOC/SOC of each soil layer in the deposition area was significantly higher than that in both the stable and eroding areas ($p < 0.05$).

Effects on the Easily Oxidized Organic Carbon

Figure 5 shows that the increase in EOC/SOC following vegetation restoration was not significant ($p < 0.05$). The average EOC/SOC values of the BP and NF were 20.52% and 22.56%, respectively, approximately 1.06 and 1.16 times higher than that of the CK (19.38%). The EOC/SOC in both the stable and sedimentary areas decreased with increasing soil depth; however, no regular change was identified in the eroding area. No significant difference was found between different soil layers in any of the three regions ($p < 0.05$).

Among the three vegetation types, the EOC/SOC ratio was slightly, but not significantly, lower in the eroding area than the stable area, and the EOC/SOC in the deposition area was identical to that in the stable area ($p < 0.05$). Vegetation restoration did not affect this result significantly ($p < 0.05$). The ratios of EOC/SOC in the sedimentary areas of the BP, NF, and CK were 1.06, 1.08, and 1.06 times higher, respectively, than that in the eroding area. The EOC/SOC of the 0–10 cm layer in the BP and NF was significantly higher than that in the eroding area ($p < 0.05$); however, in the 10–20 cm and the 20–30 cm soil layers, there were no significant ($p < 0.05$) differences among the three areas. The CK showed no significant difference between soil layers ($p < 0.05$).

DISCUSSION

Effect of Vegetation Restoration on SOC Migration at the Soil Surface (0–30 cm)

Soil erosion and SOC deposition along hillslopes can lead to spatial redistribution of SOC, i.e., the removal of soils that are rich in organic carbon from source hillslopes (shoulder and backslope) and their accumulation at the footslope (Wang et al., 2017). It has been confirmed that the SOC content in the cultivated areas of the Loess Plateau had the following distribution pattern: sedimentary area > stable area > eroded area (Wang et al., 2014a; Li et al., 2019). In our study, considering the first 30 cm, the SOC distribution along the hillslope after vegetation restoration followed a similar trend. However, the ratio of SOC content in the sedimentary area to the eroded area decreased significantly ($p < 0.05$). This could indicate that vegetation restoration reduced the migration of SOC effectively in some areas. Further, while vegetation recovery increased the SOC input, it decreased soil erosion effectively (Wang et al., 2011; Qin et al., 2014). This could also explain the fact that the SOC among these three areas of the 0–10 cm soil layer after vegetation recovery decreased significantly; at the same time, the change was not significant in the 20–30 cm soil layer ($p < 0.05$). Further, in NF, the surface SOC did not differ

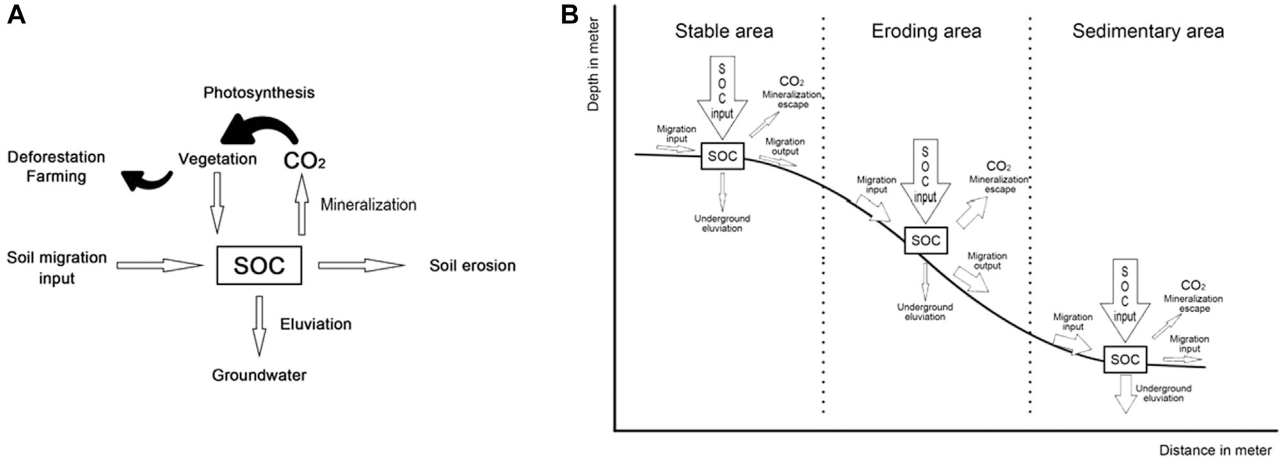

FIGURE 6 | (A) SOC cycle pattern. SOC reserves depend mainly on a dynamic balance between input and output. For SOC in a certain area, SOC input includes largely soil migration input because of soil erosion and organic carbon contained in the vegetation litter; SOC output includes largely soil migration output because of soil erosion, mineralization, and dissolution of active parts of SOC. The carbon dioxide (CO_2) in the atmosphere is fixed by photosynthesis to achieve carbon circulation. **(B)** SOC migration pattern in stable, eroding, and sedimentary areas along the slopes in response to vegetation restoration. The thickness of the arrows indicates the amount of SOC migration.

significantly between different areas, and thus, NF could be considered to perform better in reducing SOC heterogeneity. This could be the case because the BP vegetation types were relatively simple over time and their diversity recovery was slower than that of NF (Zhang et al., 2017). This led indirectly to a low root density in the surface soil and a small cumulative amount of litter on the surface (Ceccon et al., 2011; Vos et al., 2019). Therefore, the resulting soil erosion-inhibiting effects were weaker in the BP than in NF.

With respect to the sampling depth, we cannot assume that the SOC concentration below 30 cm was unimportant. Therefore, future research should be devoted to assessing the effects that the tree roots, root secretions, and the microorganisms associated with them may affect, which, subsequently, enrich the SOC pool themselves. Secondly, it would be possible to observe whether dissolved SOC migrates deep into the soil. Finally, soil organisms have a very large effect (direct and indirect) on the distribution of SOM in soil (also at a depth of over 30 cm). This is particularly common in soils developed on loess and is associated particularly with earthworms (anecic earthworms) (Lavelle, 1988).

Effect of Vegetation Restoration on the Stability of SOC on Hillslopes

It is accepted generally that DOC, microbial biomass carbon, EOC, and particulate organic carbon are the most active parts of SOC (Von Lützow et al., 2007; Wang et al., 2014b). These indices reflect small changes in the soil before it experiences changes in the total organic carbon (Bloom et al., 2016; Yu et al., 2020b). EOC and DOC were considered the most sensitive indicators of labile organic carbon in response to changes in vegetation areas (Haynes, 2005; Zhang et al., 2013a). Hence, EOC/SOC and DOC/SOC were chosen to evaluate vegetation restoration's effects on SOC stability.

Generally, DOC originates from plant litter, microbial decomposition, and root exudation (Franzluebbers, 2002). Although the DOC content is very low, it has strong mobility in the soil and therefore is considered one of the main forms of soil nutrient loss (Perakis and Hedin, 2002; Zhang et al., 2003). In this study, the increment in DOC/SOC in the sedimentary area was significantly lower in response to vegetation restoration, particularly for NF compared to the CK ($p < 0.05$). This showed that vegetation restoration could slow the migration of DOC to some extent. This could be because of the higher litter inputs in NF and BP than that in the CK, and decomposed litter add DOC to the surface soil. Moreover, litter's runoff interception function can reduce the migration of DOC (Ma et al., 2016b). EOC refers to the part of SOC that can be oxidized by 330 mmol/L potassium permanganate (Neff and Asner, 2001; Von Lützow et al., 2007). In NF, BP, and CK, the distribution trends of EOC/SOC along the slopes were fundamentally identical: EOC/SOC was identical in the stable and sedimentary areas and slightly exceeded that in the eroded area. No significant ($p < 0.05$) enrichment trend in EOC was found in the sedimentary area, which Doetterl et al. (2012) also reported for cropland in central Belgium. It has been suggested that most of the EOC may have been mineralized during the migration process (Zhou et al., 2005; Ma et al., 2016a). In the 0–10 cm layer in both NF and BP, the EOC/SOC ratios in the stable and the sedimentary areas were significantly higher ($p < 0.05$) than that in the eroded area. However, there was no significant difference among the three areas in the CK ($p < 0.05$). This indicated that vegetation restoration could reduce topsoil mineralization during erosion to some extent.

Several studies have concluded that the SOC is more active in the foothills than in other areas (Doetterl et al., 2012; Zhang et al., 2019), although naturally, anthropogenic effects can introduce some variability in this final result. However, this study did not find any significant enrichment of labile organic carbon in the sedimentary area. This may be because the active components in organic carbon have been mineralized already during the migration process, or they may have migrated to deeper soil layers because of leaching (Wang et al., 2015; Kelleway et al., 2016).

This research concerns soil, and therefore in the future, more aspects related to the lack of clear information about the way soil properties affect (strongly in some cases) the process of soil organic matter (SOM) mineralization and its transformation should be included. For example, the potential presence of redox traces in soil (which is likely in soils at the bottom part of the slope) would indicate the contribution to the SOM mineralization of conditions other than simply erosion or vegetation. Another soil process could be related to soil oxygenation conditions and thus the conditions for SOM mineralization as well. In this research, we did not include information about the activity of soil fauna, but it could be an interesting line of future research because even earthworms can change the distribution of SOM (and also SOC) in soil significantly.

Schematic Diagram of SOC Cycle Patterns on Hillslopes

Since Doetterl et al. (2012); Doetterl et al. (2016) proposed agricultural land slopes' effect on SOC content and its stability explicitly, several models and regional organic carbon estimates have introduced topographic factors (Bloom et al., 2016; Fissore et al., 2017; Patton et al., 2019). Therefore, a model for the process of SOC migration on the slope was proposed in this study. SOC reserves depend mainly on a dynamic balance between input and output (Bloom et al., 2016; Vos et al., 2019), as indicated in **Figure 6A**. According to the findings of this study, SOC also migrated and redistributed within the soil slope system, as shown in **Figure 6B**. In stable areas, topographic factors affected SOC less and the input and output along the slope were both very small. In the vertical direction, the litter vegetation produced increased the SOC input and improved the SOC activity to some extent. The activated SOC was mineralized and then either degassed in the form of carbon dioxide or continued to migrate to lower layers because of leaching. However, stable organic carbon is stored in the soil for a long period. In the eroded area, SOC will migrate downward together with the eroded soil because of the slope. Therefore, for a specific area, SOC input and output will increase simultaneously. In the vertical direction, the vegetation-induced organic carbon input remains largely the same as in the stable area; however, soil erosion will intensify the labile organic carbon's mineralization and leaching, thus causing organic carbon to decrease continuously during its downward migration. In the sedimentary area, the eroded soil is deposited and the SOC content increases in response. However, the primary component is stable organic carbon. The reason may be that most of the labile organic carbon either has been mineralized during the migration process or could not be enriched in the sedimentary area because of leaching. However, the CK's slope migration and conversion process differed notably from that of the BP and NF. On the one hand, the SOC input on arable land is relatively small and crop yield increases the SOC output, thus decreasing the total SOC on the slope (Von Lützow et al., 2006; Vos et al., 2019). On the other hand, because of the decreased coverage with surface litter and low content of labile organic carbon, a large amount of SOC migrates downward from the eroded area because of soil erosion and finally deposits in the sedimentary area.

Finally, we agree strongly that erosion changes the soil and affects its morphology, properties, and taxonomic position. It cannot be assumed that the same soil will be everywhere, but we consider that although other soils occur in each of the transect sections studied, which is attributable to erosion and other processes in the past, as well as different water-air conditions in the soil, our results correspond to the most representative possible patterns according to the number of soil surface samples and low variability.

CONCLUSION

To examine vegetation restoration's effects on SOC redistribution along a loessial hillslope, soil samples were collected from stable, eroding, and sedimentary areas of typical hillslopes with different vegetation types in the hilly-gully loess area of China. Our results demonstrated that, compared to croplands, the differences in SOC content among these three areas decreased in NF and the BP, and the proportion of labile carbon to total SOC increased significantly for DOC/COC, but not for EOC/DOC. We conclude that this could indicate that vegetation restoration in the typical Loess Plateau hillslopes (NF in particular) is an effective measure to alleviate SOC's redistribution and spatial heterogeneity and reduce soil erosion, which directly affects other ecosystem services. Therefore, the effect of vegetation recovery considering the vegetation type should be taken into account to better estimate the soil carbon storage and evaluate ecosystem services in the sloping areas of the Loess Plateau in China.

DATA AVAILABILITY STATEMENT

The original contributions presented in the study are included in the article/Supplementary Material; further inquiries can be directed to the corresponding author.

AUTHOR CONTRIBUTIONS

YL finished the data curation and formal analysis and wrote the original draft. TZ played a guiding role in conceptualizing the field experiment, review, and editing the manuscript. XL and XZ assisted in data analysis and sample collection.

FUNDING

This work was supported by the state-supporting technology project in the 12th Five Year Plan (2015BAD07B030302).

ACKNOWLEDGMENTS

Special thanks go to *Editor World LLC* for English language editing. The authors thank the editor and the anonymous reviewers for helpful comments and suggestions during the review process.

REFERENCES

Álvaro-Fuentes, J., Plaza-Bonilla, D., Arrúe, J. L., Lampurlanés, J., and Cantero-Martínez, C. (2014). Soil organic carbon storage in a no-tillage chronosequence under Mediterranean conditions. *Plant Soil* 376, 31–41. doi:10.1007/s11104-012-1167-x

Abdalla, M., Hastings, A., Chadwick, D. R., Jones, D. L., Evans, C. D., Jones, M. B., et al. (2018). Critical review of the impacts of grazing intensity on SOC storage and other soil quality indicators in extensively managed grasslands. *Agric. Ecosyst. Environ.* 253, 62–81. doi:10.1016/j.agee.2017.10.023

Bao, S. (2000). *Soil Agrochemical analysis*. Beijing: China Agriculture Press.

Beguería, S., Angulo-Martínez, M., Gaspar, L., and Navas, A. (2015). Detachment of SOC by rainfall splash: experimental assessment on three agricultural soils of Spain. *Geoderma* 245–246, 21–30. doi:10.1016/j.geoderma.2015.01.010

Berhe, A. A., and Torn, M. S. (2017). Erosional redistribution of topsoil controls soil nitrogen dynamics. *Biogeochemistry* 132, 37–54. doi:10.1007/s10533-016-0286-5

Blaire, G. J., Lefroy, R. D., and Lisle, L. (1995). Soil carbon fractions based on their degree of oxidation, and the development of a carbon management index for agricultural systems. *Crop Pasture Sci.* 46, 1459–1466. doi:10.1071/AR9951459

Bloom, A. A., Exbrayat, J., van der Velde, I. R., Feng, L., and Williams, M. (2016). The decadal state of the terrestrial carbon cycle: global retrievals of terrestrial carbon allocation, pools, and residence times. *Proc. Natl. Acad. Sci. Unit. States Am.* 113, 1285–1290. doi:10.1073/pnas.1515160113

Brevik, E. C., Slaughter, L., Singh, B. R., Steffan, J. J., Collier, D., Barnhart, P., et al. (2020). Soil and human health: current status and future needs. *Air Soil. Water Res.* 13, 1178622120934441. doi:10.1177/1178622120934441

Cagnarini, C., Blyth, E., Emmett, B. A., Evans, C. D., Griffiths, R. I., and Keith, A. (2019). Zones of influence for soil organic matter dynamics: a conceptual framework for data and models. *Global Change Biol.* 25, 3996–4007. doi:10.1111/gcb.14787

Ceccon, C., Panzacchi, P., Scandellari, F., Prandi, L., Ventura, M., Russo, B., et al. (2011). Spatial and temporal effects of soil temperature and moisture and the relation to fine root density on root and soil respiration in a mature apple orchard. *Plant Soil* 342, 195–206. doi:10.1007/s11104-010-0684-8

Cerdà, A., and Rodrigo-Comino, J. (2020). Is the hillslope position relevant for runoff and soil loss activation under high rainfall conditions in vineyards? *Ecohydrol. Hydrobiol.* 20, 59–72. doi:10.1016/j.ecohyd.2019.05.006

Chang, R., Fu, B., Liu, G., and Liu, S. (2011). Soil carbon sequestration potential for “Grain for green” project in Loess Plateau, China. *Environ. Manage.* 48, 1158–1172. doi:10.1007/s00267-011-9682-8

Doetterl, S., Berhe, A. A., Nadeu, E., Wang, Z., Sommer, M., and Fiener, P. (2016). Erosion, deposition and soil carbon: a review of process-level controls, experimental tools and models to address C cycling in dynamic landscapes. *Earth Sci. Rev.* 154, 102–122. doi:10.1016/j.earscirev.2015.12.005

Doetterl, S., Six, J., Wesemael, B. V., and Van Oost, K. (2012). Carbon cycling in eroding landscapes: geomorphic controls on soil organic C pool composition and C stabilization. *Global Change Biol.* 18, 2218–2232. doi:10.1111/j.1365-2486.2012.02680.x

Feng, X., Fu, B., and Lu, N. (2013). How ecological restoration alters ecosystem services: an analysis of carbon sequestration in China’s Loess Plateau. *Sci. Rep.* 3, 2846. doi:10.1038/srep02846

Fissore, C., Dalzell, B. J., Berhe, A. A., Voegtle, M., Evans, M., and Wu, A. (2017). Influence of topography on soil organic carbon dynamics in a Southern California grassland. *Catena* 149, 140–149. doi:10.1016/j.catena.2016.09.016

Franzluebbers, A. J. (2002). Soil organic matter stratification ratio as an indicator of soil quality. *Soil Res.* 66, 95–106. doi:10.1016/S0167-1987(02)00018-1

García-Díaz, A., Allas, R. B., Gristina, L., Cerdà, A., Pereira, P., and Novara, A. (2016). Carbon input threshold for soil carbon budget optimization in eroding vineyards. *Geoderma* 271, 144–149. doi:10.1016/j.geoderma.2016.02.020

García-Díaz, A., Marqués, M. J., Sastre, B., and Bienes, R. (2018). Labile and stable soil organic carbon and physical improvements using groundcovers in vineyards from central Spain. *Sci. Total Environ.* 621, 387–397. doi:10.1016/j.scitotenv.2017.11.240

Grebliunas, B. D., Armstrong, S. D., and Perry, W. L. (2016). Changes in water-extractable organic carbon with cover crop planting under continuous corn silage production. *Air Soil. Water Res.* 9, 45. doi:10.4137/aswr.s30708

Haigh, M., Desai, M., Cullis, M., D’Aucourt, M., Sansom, B., Wilding, G., et al. (2019). Composted municipal green waste enhances tree success in opencast coal land reclamation in Wales. *Air Soil. Water Res.* 12, 1178622119877837. doi:10.1177/1178622119877837

Hancock, G. R., Kunkel, V., Wells, T., and Martinez, C. (2019). Soil organic carbon and soil erosion–Understanding change at the large catchment scale. *Geoderma* 343, 60–71. doi:10.1016/j.geoderma.2019.02.012

Haynes, R. J. (2005). Labile organic matter fractions as central components of the quality of agricultural soil: an overview. *Adv. Agron.* 85, 221–268. doi:10.1016/S0065-2113(04)85005-3

IUSS Working Group (2006). *World reference Base for soil Resources. World soil resources reports No. 103*, Rome: The International Union of Soil Science.

Jenny, H. (1994). *Factors of soil formation. A system of quantitative pedology*. New York: Dover Publications.

Kelleway, J. J., Saintilan, N., Macreadie, P. I., and Ralph, P. J. (2016). Sedimentary factors are key predictors of carbon storage in SE Australian Saltmarshes. *Ecosystems* 19, 865–880. doi:10.1007/s10021-016-9972-3

Kiani-Harchegani, M., and Sadeghi, S. H. (2020). Practicing land degradation neutrality (LDN) approach in the Shazand Watershed, Iran. *Sci. Total Environ.* 698, 134319. doi:10.1016/j.scitotenv.2019.134319

Kim, D., and Kirschbaum, M. U. F. (2015). The effect of land-use-change on the net exchange rates of greenhouse gases: a compilation of estimates. *Agric. Ecosyst. Environ.* 208, 114–126. doi:10.1016/j.agee.2015.04.026

Kirkels, F. M. S. A., Cammeraat, L. H., and Kuhn, N. J. (2014). The fate of soil organic carbon upon erosion, transport and deposition in agricultural landscapes–A review of different concepts. *Geomorphology* 226, 94–105. doi:10.1016/j.geomorph.2014.07.023

Lavelle, P. (1988). Earthworm activities and the soil system. *Biol. Fert. Soils* 6, 237–259. doi:10.1007/BF00260820

Li, T., Zhang, H., Wang, X., Cheng, S., Fang, H., and Liu, G. (2019). Soil erosion affects variations of soil organic carbon and soil respiration along a slope in Northeast China. *Ecol. Processes* 8, 28. doi:10.1186/s13717-019-0184-6

Ma, H., Yang, X., Guo, Q., Zhang, X., and Zhou, C. (2016a). Soil organic carbon pool along different altitudinal level in the Sygera Mountains, Tibetan Plateau. *J. Mt. Sci.* 13, 476–483. doi:10.1007/s11629-014-3421-6

Ma, W., Li, Z., Ding, K., Huang, B., Nie, X., and Lu, Y. (2016b). Soil erosion, organic carbon and nitrogen dynamics in planted forests: a case study in a hilly catchment of Hunan Province, China. *Soil Res.* 155, 69–77. doi:10.1016/j.still.2015.07.007

Muñoz-Rojas, M., Erickson, T. E., Dixon, K. W., and Merritt, D. J. (2016). Soil quality indicators to assess functionality of restored soils in degraded semiarid ecosystems. *Restor. Ecol.* 24, S43–S52. doi:10.1111/rec.12368

Neff, C. N., and Asner, G. P. (2001). Dissolved organic carbon in terrestrial ecosystems: synthesis and a model. *Ecosystems* 4, 29–48. doi:10.1007/s100210000058

Novara, A., Pulido, M., Rodrigo-Comino, J., Prima, S. D., Smith, P., Gristina, L., et al. (2019). Long-term organic farming on a citrus plantation results in soil organic carbon recovery. *Cuadernos de Investigación Geográfica* 45, 271–286. doi:10.18172/cig.3794

Olson, K. R., and Gennadiev, A. N. (2020). Dynamics of soil organic carbon storage and erosion due to land use change (Illinois, USA). *Eurasian Soil Sci.* 53, 436–445. doi:10.1134/S1064229320040122

Patton, N. R., Lohse, K. A., Seyfried, M. S., Godsey, S. E., and Parsons, S. B., (2019). Topographic controls of soil organic carbon on soil-mantled landscapes. *Sci. Rep.* 9,6390. doi:10.1038/s41598-019-42556-5

Perakis, S. S., and Hedin, L. O. (2002). Nitrogen loss from unpolluted South American forests mainly via dissolved organic compounds. *Nature* 416–419. doi:10.1038/415416a

Pereira, P., Barcelo, D., and Panagos, P. (2020). Soil and water threats in a changing environment. *Environ. Res.* 186, 109501. doi:10.1016/j.envres.2020.109501

Pereira, P., Bogunovic, I., Munoz-Rojas, M., and Brevik, E. (2018). Soil ecosystem services, sustainability, valuation and management. *Curr. Opin. Environ. Sci. Heal.* 5, 7–13. doi:10.1016/j.coesh.2017.12.003

Petrakis, R. E., Norman, L. M., Lysaght, O., Sherrouse, B. C., Semmens, D., Bagstad, K. J., et al. (2020). Mapping perceived social values to support a respondent-defined restoration economy: case study in Southeastern Arizona, USA. *Air Soil. Water Res.* 13, 1178622120913318. doi:10.1177/1178622120913318

Qin, Y., Xin, Z., Yu, X., and Xiao, Y. (2014). Influence of vegetation restoration on topsoil organic carbon in a small catchment of the Loess Hilly Region, China. *PloS One* 9 (6), e94489. doi:10.1371/journal.pone.0094489

Ran, L., Lu, X., and Xu, J. (2013). Effects of vegetation restoration on soil conservation and sediment loads in China: a critical review. *Crit. Rev. Environ. Sci. Technol.* 43, 1384–1415. doi:10.1080/10643389.2011.644225

Rodrigo-Comino, J., López-Vicente, M., Kumar, V., Rodríguez-Seijo, A., Valkó, O., Rojas, C., et al. (2020). Soil science challenges in a new era: a transdisciplinary overview of relevant topics. *Air Soil. Water Res.* 13, 1178622120977491. doi:10.1177/1178622120977491

Rodrigo-Comino, J., Ruiz Sinoga, J. D., Senciales González, J. M., Guerra-Merchán, A., Seeger, M., and Ries, J. B. (2016). High variability of soil erosion and hydrological processes in Mediterranean hillslope vineyards (Montes de Málaga, Spain). *Catena* 145, 274–284. doi:10.1016/j.catena.2016.06.012

Rodrigo-Comino, J., Senciales, J. M., Ramos, M. C., Martínez-Casasnovas, J. A., Lasanta, T., Brevik, E. C., et al. (2017). Understanding soil erosion processes in Mediterranean sloping vineyards (Montes de Málaga, Spain). *Geoderma* 296, 47–59. doi:10.1016/j.geoderma.2017.02.021

Sanderman, J., and Chappell, A. (2013). Uncertainty in soil carbon accounting because of unrecognized soil erosion. *Global Change Biol.* 19, 264–272. doi:10.1111/gcb.12030

Shi, P., Zhang, Y., Li, P., Li, Z., Yu, K., Ren, Z., et al. (2019a). Distribution of soil organic carbon impacted by land-use changes in a hilly watershed of the loess plateau, China. *Sci. Total Environ.* 652, 505–512. doi:10.1016/j.scitotenv.2018.10.172

Shi, P., Zhang, Y., Yu, Y., Li, P., Li, Z., Xiao, L., et al. (2019b). Land-use types and slope topography affect the soil labile carbon fractions in the loess hilly-gully area of Shaanxi, China. *Arch. Agron. Soil Sci.* 66, 638–650. doi:10.1080/03650340.2019.1630824

Sun, W., Guo, S., and Song, X. (2010). Effects of topography and land use on spatial distribution of topsoil organic carbon in loess hilly-gully region. *J. Nat. Resour.* 3, 443–453. doi:10.1016/S1875-2780(09)60057-2

van der Bank, M., and Karsten, J. (2020). Climate change and South Africa: a critical analysis of the earthlife and the drive for concrete climate practices. *Air Soil. Water Res.* 13, 1178622119885372. doi:10.1177/1178622119885372

Von Lützow, M., Kögel-knabner, I., Ekschmitt, K., Flessa, H., Guggengerger, G., Matzner, E., et al. (2007). SOM fractionation methods: relevance to functional pools and to stabilization mechanisms. *Soil Biol. Biochem.* 39, 2183–2207. doi:10.1016/j.soilbio.2007.03.007

Von Lützow, M., Kögel-knabner, I., Ekschmitt, K., Matzner, E., Guggengerger, G., Marschner, B., et al. (2006). Stabilization of organic matter in temperate soils: mechanisms and their relevance under different soil conditions–A review. *Eur. J. Soil Sci.* 57, 426–445. doi:10.1111/j.1365-2389.2006.00809.x

Vos, C., Don, A., Hobley, F. U., Prietz, R., Heidkamp, M., and Freibauer, A. (2019). Factors controlling the variation in organic carbon stocks in agricultural soils of Germany. *Eur. J. Soil Sci.* 70, 550–564. doi:10.1111/ejss.12787

Wang, X., Cammeraat, E. L. H., Cerli, C., and Kalbitz, K. (2014b). Soil aggregation and the stabilization of organic carbon as affected by erosion and deposition. *Soil Biol. Biochem.* 72, 55–65. doi:10.1016/j.soilbio.2014.01.018

Wang, X., Cammeraat, E. L. H., Romeijn, P., and Kalbitz, K. (2014a). Soil organic carbon redistribution by water erosion–the role of CO_2 emissions for the carbon budget. *PloS One* 9, e96299. doi:10.1371/journal.pone.0096299

Wang, X., Jelinski, N. A., Toner, B., and Yoo, K. (2019). Long-term agricultural management and erosion change soil organic matter chemistry and association with minerals. *Sci. Total Environ.* 648, 1500–1510. doi:10.1016/j.scitotenv.2018.08.110

Wang, Y., Fu, B., Lü, Y., and Chen, L. (2011). Effects of vegetation restoration on soil organic carbon sequestration at multiple scales in semi-arid Loess Plateau, China. *Catena* 85, 58–66. doi:10.1016/j.catena.2010.12.003

Wang, Y., Shao, M., Zhang, C., Liu, Z., Zou, J., and Xiao, J. (2015). Soil organic carbon in deep profiles under Chinese continental monsoon climate and its relations with land uses. *Ecol. Eng.* 361–367. doi:10.1016/j.ecoleng.2015.05.004

Wang, Z., Hu, Y., Wang, R., Guo, S., Du, L., and Zhao, M. (2017). Soil organic carbon on the fragmented Chinese Loess Plateau: combining effects of vegetation types and topographic positions. *Soil Res.* 174, 1–5. doi:10.1016/j.still.2017.05.005

Wiaux, F., Cornelis, J. T., Cao, W., Vanclooster, M., and Van Oost, K. (2014). Combined effect of geomorphic and pedogenic processes on the distribution of soil organic carbon quality along an eroding hillslope on loess soil. *Geoderma* 216, 36–47. doi:10.1016/j.geoderma.2013.10.013

Wiesmeier, M., Urbanski, L., Hobley, E., Lang, B., von Lützow, M., Marin-Spiotta, E., et al. (2019). Soil organic carbon storage as a key function of soils-a review of drivers and indicators at various scales. *Geoderma* 333, 149–162. doi:10.1016/j.geoderma.2018.07.026

Willaarts, B. A., Oyonarte, C., Muñoz-Rojas, M., Ibáñez, J. J., and Aguilera, P. A. (2016). Environmental factors controlling soil organic carbon stocks in two contrasting Mediterranean climatic areas of southern Spain. *Land Degrad. Dev.* 27, 603–611. doi:10.1002/ldr.2417

Xin, Z., Qin, Y., and Yu, X. (2016). Spatial variability in soil organic carbon and its influencing factors in a hilly watershed of the Loess Plateau, China. *Catena* 137, 660–669. doi:10.1016/j.catena.2015.01.028

Yeasmin, S., Jahan, E., Molla, M., Islam, A. K. M., Anwar, M., Or Rashid, M., et al. (2020). Effect of land use on organic carbon storage potential of soils with contrasting native organic matter content. *International Journal of Agronomy* 2020, 1–9. doi:10.1155/2020/8042961

Yu, H., Zha, T., Zhang, X., and Ma, L. (2019a). Vertical distribution and influencing factors of soil organic carbon in the Loess Plateau, China. *Sci. Total Environ.* 693, 133632. doi:10.1016/j.scitotenv.2019.133632

Yu, Y., Wei, W., Chen, L., Feng, T., and Daryanto, S. (2019b). Quantifying the effects of precipitation, vegetation, and land preparation techniques on runoff and soil erosion in a Loess watershed of China. *Sci. Total Environ.* 625, 755–764. doi:10.1016/j.scitotenv.2018.10.255

Yu, H., Zha, T., Zhang, X., Nie, L., Ma, L., and Pan, Y. (2020a). Spatial distribution of soil organic carbon may be predominantly regulated by topography in a small revegetated watershed. *Catena* 188, 104459. doi:10.1016/j.catena.2020.104459

Yu, Y., Zhao, W., Martinez-Murillo, J. F., and Pereira, P. (2020b). Loess Plateau: from degradation to restoration. *Sci. Total Environ.* 738, 140206. doi:10.1016/j.scitotenv.2020.140206

Yu, Y., Wei, W., Chen, L., Feng, T., Daryanto, S., and Wang, L. (2016). Land preparation and vegetation type jointly determine soil conditions after long-term land stabilization measures in a typical hilly catchment, Loess Plateau of China. *J. Soils Sediments* 17, 144–156. doi:10.1007/s11368-016-1494-2

Zhang, C., Liu, G., Xue, S., and Sun, C. (2013a). Soil organic carbon and total nitrogen storage as affected by land use in a small watershed of the Loess Plateau, China. *Eur. J. Soil Biol.* 54, 16–24. doi:10.1016/j.ejsobi.2012.10.007

Zhang, S., Zhang, A., Meng, X., and Yin, H. (2013b). Evaluation of soil erosion sensitivity in Jixian County, Shanxi Province based on ecological immigrants. *Soil Water Conser. China* 8, 61–63. doi:10.14123/j.cnki.swcc.2013.08.023

Zhang, H., Huang, Y., An, S., and Xin, X. (2003). Soil active organic carbon under forest communities in the Loess Plateau. *Res. Soil Water Conser.* 3, 65–70.

Zhang, X., Yang, Z., Zha, T., Zhang, Z., Wang, G., Zhu, Y., et al. (2017). Changes in the physical properties of soil in forestlands after 22 years under the influence of the Conversion of Cropland into Farmland Project in Loess region, Western Shanxi Province. *Acta Ecol. Sin.* 37 (2), 416–424. doi:10.5846/stxb201507291596

Zhang, Y., Li, P., Lie, X., Zhao, B., and Peng, S. (2019). Effects of topography and land use on soil organic carbon in hilly region of Loess Plateau. *Acta Pedol. Sin.* 56 (5) 1140–1149. doi:10.11766/trxb201901220367

Zhou, L., Li, B., and Zhou, G. (2005). Advances in controlling factors of soil organic carbon. *Adv. Earth Sci.* 20, 99–105.

Zhou, Z., Zhang, Z., Zha, T., Luo, Z., Zheng, J., and Sun, O. (2013). Predicting soil respiration using carbon stock in roots, litter and soil organic matter in forests of Loess Plateau in China. *Soil Biol. Biochem.* 57, 135–143. doi:10.1016/j.soilbio.2012.08.010

Conflict of Interest: Author XZ was employed by company The Third Construction Co., Ltd. of China Construction First Group.

The remaining authors declare that the research was conducted in the absence of any commercial or financial relationships that could be construed as a potential conflict of interest.

frontiers in Earth Science

ORIGINAL RESEARCH
published: 03 February 2021
doi: 10.3389/feart.2021.627500

Effects of Textural Layering on Water Regimes in Sandy Soils in a Desert-Oasis Ecotone, Northwestern China

Chengpeng Sun[1,2,3]*, Wenzhi Zhao*[1,2]**, Hu Liu*[1,2]*, Yongyong Zhang*[1,2] *and Hong Zhou*[4]

[1]Key Laboratory of Ecohydrology and River Basin Science, Northwest Institute of Eco-environment and Resources, Chinese Academy of Sciences, Lanzhou, China, [2]Linze Inland River Basin Research Station, Chinese Ecosystem Research Network, Lanzhou, China, [3]College of Resources and Environment, University of Chinese Academy of Sciences, Beijing, China, [4]Tourism College, Northwest Normal University, Lanzhou, China

Textural layering of soil plays an important role in distributing and regulating resources for plants in many semiarid and arid landscapes. However, the spatial patterns of textural layering and the potential effects on soil hydrology and water regimes are poorly understood, especially in arid sandy soil environments like the desert-oasis ecotones in northwestern China. This work aims to determine the distribution of textural layered soils, analyze the effects of different soil-textural configurations on water regimes, and evaluate which factors affect soil water infiltration and retention characteristics in such a desert-oasis ecotone. We measured soil water content and mineral composition in 87 soil profiles distributed along three transects in the study area. Constant-head infiltration experiments were conducted at 9 of the soil profiles with different texture configurations. The results showed that textural layered soils were patchily but extensively distributed throughout the study area (with a combined surface area percentage of about 84%). Soil water content in the profiles ranged from 0.002 to 0.27 g/cm^3 during the investigation period, and significantly and positively correlated with the thickness of a medium-textured (silt or silt loam) layer ($p < 0.001$). The occurrence of a medium-textured layer increased field capacity and wilting point and decreased available water-holding capacity in soil profiles. Burial depth of the medium-textured layer had no clear effects on water retention properties, but the layer thickness tended to. In textural layered soils, smaller water infiltration rate and cumulative infiltration, and shallower depths of wetting fronts were detected, compared with homogeneous sand profiles. The thickness and burial depth of medium-textured layers had obvious effects on infiltration, but the magnitude of the effects depended on soil texture configuration. The revealed patterns of soil textural layering and the potential effects on water regimes may provide new insight into the sustainable management of rainfed vegetation in the desert-oasis ecotones of arid northwestern China and other regions with similar environments around the world.

Keywords: Textural layering, Soil hydrology, Water retention, Water infiltration, Water regimes

OPEN ACCESS

Edited by:
Yang Yu,
Beijing Forestry University, China

Reviewed by:
Changbin Li,
Lanzhou University, China
Li Guo,
Sichuan University, China

****Correspondence:***
Wenzhi Zhao
zhaowzh@lzb.ac.cn

Specialty section:
This article was submitted to Hydrosphere, a section of the journal Frontiers in Earth Science

Received: *09 November 2020*
Accepted: *04 January 2021*
Published: *03 February 2021*

Citation:
Sun C, Zhao W, Liu H, Zhang Y and Zhou H (2021) Effects of Textural Layering on Water Regimes in Sandy Soils in a Desert-Oasis Ecotone, Northwestern China. Front. Earth Sci. 9:627500. doi: 10.3389/feart.2021.627500

Abbreviations: BD, Bulk density; TP, Total porosity; VWC, Volumetric water content; SWC, Soil water content; FC, Field capacity; WP, Wilting point; AWC, Available water content; SSA, Surface specific area; GD, Grain diameter.

INTRODUCTION

Textural layered soils are soils with textural contrasts, or duplex soils with subsoil in which the clay content is at least one and a half times that of the overlying layer (Northcote, 1971). These include abrupt textural-change soils (Hill and Parlange, 1972; Bockheim, 2016) characterized by a clear, abrupt, or sharp boundary between the surface and the underlying horizon, and soils with a considerable increase in clay content within a very short vertical distance (Hardie, et al., 2012; Bockheim and Hartemink, 2013). Commonly, soil texture in these soils ranges from sandy to medium or medium-heavy clay soils (Hardie, et al., 2013). The formation of textural layered soils is a complex process resulting from a number of factors, such as translocation via eluviation-illuviation, bioturbation, erosion, deposition, and artificial reclamation (Phillips, 2001; Alfnes, et al., 2004). Textural layered soils are ubiquitous in the natural world, in places like southwestern Australia (Tennant, et al., 1992), the southwestern United States (Munson, et al., 2016), and western Canada (Selim, 2011). In China, similar textural layered soils have been found in the wind-water erosion crisscross region of the Loess Plateau (Zhang, et al., 2017a), and in the desert-oasis ecotone of northwestern China (Zhou, et al., 2016).

The desert-oasis ecotone of northwestern China is an ecologically fragile region currently experiencing significant desertification (Yu, et al., 2020). Since the mid-1970s, native sand-adapted shrubs have been widely planted, in order to curb desertification and alleviate its influence on crops, pasture, and human life (Zhou, et al., 2017). In regions with low precipitation, water is a basic condition on which vegetation relies for survival (Noy-Meir, 1973). Soil texture can affect quantity and availability of plant water as an important determinant of soil hydrological properties and processes, e.g., water retention, infiltration and drainage. There is evidence that discontinuity of subsurface soil horizons is a common feature in arid regions, and causes spatial heterogeneity of soil texture (Pahlavan-Rad and Akbarimoghaddam, 2018; Regmi and Rasmussen, 2018), which in turn leads to high heterogeneity of water reserves. To accommodate such conditions, plants have changed foraging mechanisms by modifying root distribution patterns (Hamerlynck, et al., 2002; Zou, et al., 2005). Additional studies suggest that the root increases in some plants (e.g., deeply rooted shrubs) are dampened on textural layered soils (Browning, et al., 2008; Duniway, et al., 2018), due to the clay-rich subsurface soil horizons, which can inhibit root growth and elongation (Zhou, et al., 2019). Through these responses, textural layered soils can influence vegetation dynamics and landscape evolution (Hamerlynck, et al., 2002; Sperry and Hacke, 2002; Macinnis-Ng, et al., 2010), which in turn influences local ecological stability. Understanding the effects of textural layering on soil hydrological properties and processes in arid ecosystems will be helpful for predicting the patterns and self-organizing processes of rainfed vegetation in desert-oasis ecotones.

Textural layered soils are generally regarded as a natural isolation layer (de Jong van Lier and Wendroth, 2016), influencing flow behaviors and temporal availability of soil water (McAuliffe, 1994). Many studies have explored the impact of textural layering on soil hydrological properties, and results have suggested that textural variability can increase soil water storage (Ityel, et al., 2011; Zettl, et al., 2011; Mancarella, et al., 2012). However, previous studies have provided inconsistent results on the associations between soil water availability and textural variability (Huang, et al., 2013; Fensham, et al., 2015). The influence of textural layered soils on water infiltration have also been widely investigated. Textural layered soils often impede infiltration (Ma, et al., 2011; Li, et al., 2014) due to a capillary and hydraulic barrier resulting from the discontinuity of hydraulic properties (Ross, 1990; Miyazaki, et al., 1993). Generally, a capillary barrier develops when a coarse-textured layer is found beneath a fine-textured layer (Stormont and Anderson, 1999). Factors affecting the efficiency of a capillary barrier include soil texture (Yang, et al., 2004), thickness of the overlying layer (Qian, et al., 2010), and the size of the interfaces between soil horizons (Si, et al., 2011). A hydraulic barrier develops when a coarse-textured layer covers a fine-textured layer (Thompson, et al., 2010), and the barrier is mainly affected by precipitation characteristics (Chu and Mariño, 2005), thickness of the coarse layer (Zhang, et al., 2017a), and disparities in permeability between surface soil and subsoil (Mohammadzadeh-Habili and Heidarpour, 2015). Water infiltration can be extremely complex under the condition of the simultaneous presence of two flow barriers—for example, a soil profile with a contrast-textured interlayer. Most studies suggest that infiltration is inhibited in these conditions, and the effect varies by the number, position and soil texture of the interlayers (Gvirtzman, et al., 2008; Ng, et al., 2015; Wang, et al., 2018; Hou, et al., 2019). However, further studies have suggested that textural layered soils do not obstruct water flow (Rimon, et al., 2007), and even in some cases (e.g., under dry soil conditions), facilitate infiltration (Hardie, et al., 2011; Wang, et al., 2014). These controversial findings need to be further investigated.

Many approaches have been proposed for analyzing the characteristics of infiltration processes in textural layered soils. Common methods for acquiring soil hydrological processes include laboratory tests (Al-Maktoumi, et al., 2015), field experiments (Rimon, et al., 2007; Gvirtzman, et al., 2008), and simulations by current commercially available soil water models such as HYDRUS 1D or 2D (Wang, et al., 2017; Wang, et al., 2018), and theoretical models such as the Green-Ampt model (Mohammadzadeh-Habili and Heidarpour, 2015; Deng and Zhu, 2016). Preferential flow is a common phenomenon in the desert-oasis ecotone (Yan and Zhao, 2016; Zhang, et al., 2017b), however, HYDRUS failed to simulate the complexity of flow processes observed in dry soils, specifically confounding preferential flow (Hardie, et al., 2013). Taking the complexity of textural layering effects into consideration, we chose *in-situ* infiltration testing in this study.

The primary objectives of this study were to: 1) examine the distribution and structures of textural layered soils; 2) identify the role of textural layered soils in soil water content (*SWC*) and hydrological properties (water-holding capacities) and processes (water infiltration); and 3) discuss the potential implications of textural layered soils for vegetation conservation in the study region.

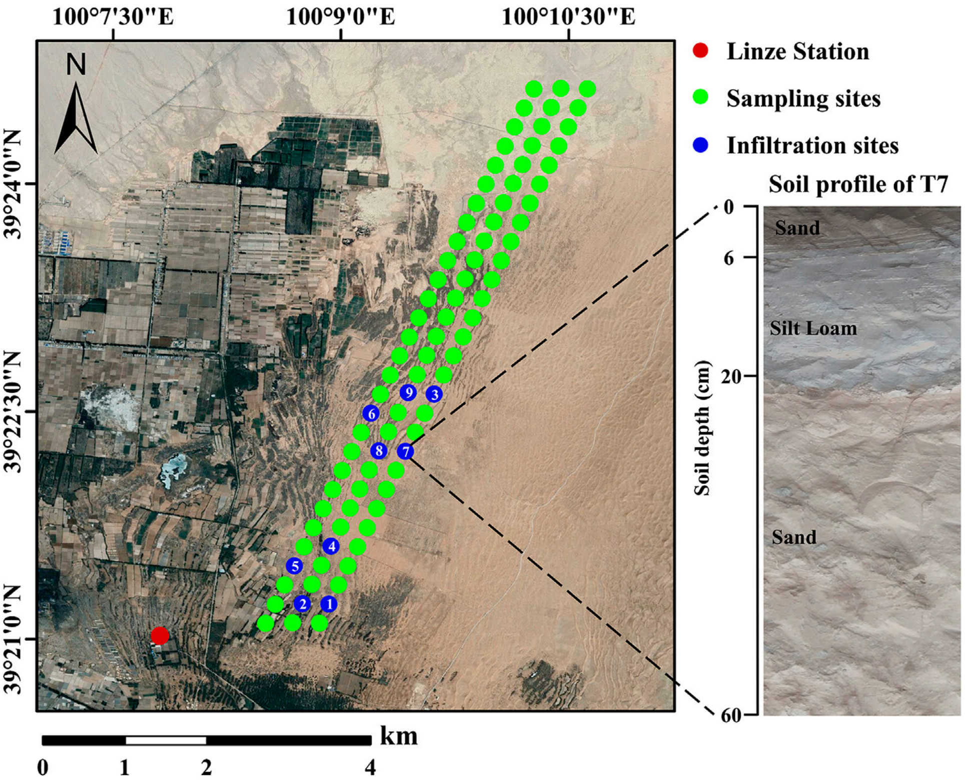

FIGURE 1 | Location of the sampling and infiltration sites. Note: Numbers from 1 to 9 at the blue points indicate the infiltration sites from T1 to T9, and the size of blue symbols does not represent the sampling range.

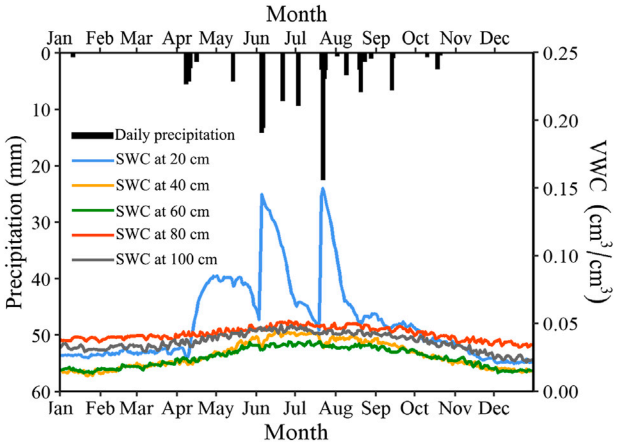

FIGURE 2 | Dynamics of precipitation and soil moisture (2017) in the study area.

MATERIALS AND METHODS

Study Area

The study was carried out in the Linze desert–oasis ecotone, located in the middle of the Heihe River Basin in northwestern China (39° 21′-39° 25′ N, 100° 08′-100° 11′ E). The area is about 3.5 km^2 and is surrounded by the Beishan Mountain to the northwest, the Heihe River to the south, and the Badain Jaran Desert to the east (**Figure 1**). The climate is continental, with cold winters and hot summers. Mean annual precipitation is about 116.8 mm, with rainfall maximum during the summer period from May to September. Mean annual temperature and evaporation were 7.6°C (−27.3–39.1°C) and 2,390 mm, respectively, for the 1987–2017 period (Liu, et al., 2018). The dominant soil types are Aridisol, Plaggept and Psamments (Liu, et al., 2011) in the margin of the oasis, owing to long-term alluvial deposits and eolian processes forming a special type of texture-contrast soil (Zhang and Zhao, 2015). The major landscape types include the peripheral desert, desert-oasis ecotone, and central oasis (Zhang, et al., 2018). Dominant plant species include natural native vegetation such as *Nitraria sphaerocarpa*, *Nitraria tangutorum* and *Calligonum mongolicum*, and planted *Haloxylon ammodendron.*

In the study area, *H. ammodendron* was planted at various times (2010, 2005, 1995, and 1975) using one-year-old seedlings in rows at about 2.0 m × 2.5 m spacing (Zhou, et al., 2017). Precipitation and volumetric water content (*VWC*) data collected by the Linze Inland River Basin Research Station of the Chinese Academy of Sciences indicated that single precipitation events did not usually recharge the soil below 20–30 cm. Clustered rain events could infiltrate into deeper layers, and wetting front fluctuations were mostly constrained to within 60 cm of the surface (**Figure 2**), as in deeper soils no impact of specific rain events was observed. Therefore, a key factor determining infiltration patterns in these soils involves the physical properties at 0–60 cm depth.

Soil Sampling

We set up three sampling transects 250 m apart. Along each transect, 29 sites were chosen at a distance of 250 m apart (**Figure 1**). The advantage of such sampling design was that it allowed us to assess the spatial distribution of medium-textured layers at the fringe of the oasis, and to evaluate potential impacts of medium-textured layers on soil water content. We sampled these 87 representative soil sites during the months of August and September 2018. At each site, we collected soil samples at intervals of 10 cm from 0 to 300 cm profiles with a hand-held soil auger (5 cm in diameter). Longitude and latitude at each site were obtained with a hand-held GPS. Land-use type and plant species were also noted. Sampling was paused for 7 days after a precipitation event to avoid confounding soil water content with direct precipitation inputs.

Infiltration Experiments and Observation Methods

To estimate the influence of textural layered soils on infiltration features, ponded infiltration measurements *in situ* were carried out on nine soil profiles with a medium-textured layer. The nine sites were selected from the 87 sites according to the following criteria (except for one control site): the presence of medium-textured layers in soils to 60 cm depth, and representative variations in soil texture configurations and burial depth of the medium-textured layers; these sites were named T1 to T9. The nine sites were divided into five categories based on the position and number of medium-textured layers: homogeneous soil profile (T1), soil profiles in which medium-textured layers covered the coarser layer (T2 and T3), soil profiles in which medium-textured layers lay beneath the coarser layer (T4 and T5), soil profiles with medium-textured soil interlaid within a coarser profile (T6 and T7), and soil profiles with multiple medium-texture layers (T8 and T9), as shown in **Table 1**.

A 20 cm inside-diameter ring was used to conduct infiltration tests, taking into consideration edge effects and disturbance of the sampled soil volume (Bagarello and Sgroi, 2004). A 100 cm-deep and 250 cm-wide soil profile was excavated with the central line of the ring as the axis in each site. The ring was carefully driven into soil 3 cm away from the excavated profile to a depth of 3 cm using a rubber hammer; surface vegetation was first removed, while the roots remained. To prevent extra seepage, we gently firmed the soil surface around the inside edges with a finger. The surface of the soil was padded with filter papers to prevent disturbance when adding water. A Mariotte bottle with an inner diameter of 40 cm and a height of 100 cm was used for the water supply. A 3 cm constant head of ponding was established in the ring, taking into consideration the effect of head of ponding on gravity potential and the maneuverability of the experiments (Touma, et al., 2007). The fall of the water level in the bottle was monitored to calculate the cumulative infiltration and the infiltration rate. The infiltration time was 450 min. The depth and breadth of the wetting front movement were obtained by observing the strong color contrast between wet and dry soil along the dug soil profile; only the right side of the horizontal wetting front was used, since the sides were nearly symmetrical. The dug profiles were covered with plastic to prevent evaporation. After infiltration, undisturbed soil samples were collected with steel cores (about 110 cm^3) at intervals of 10 cm from 0 to 60 cm profiles.

Soil Properties

Soil particle size was analyzed using a particle-size analyzer (Mastersizer 3,000, Malvern Instruments, Malvern, England) after being air-dried and sieved to < 2 mm. The components were clay (<0.002 mm), silt (0.002–0.05 mm), and sand (0.05–2 mm). According to USDA soil taxonomy, the texture of the sediments in the pan belonged to the medium-texture category (clay 0–40%, sand 0–52%). *SWC* was measured by the oven-drying method (105°C, 12 h). Some of the soil samples collected with stainless steel cylinders at the infiltration sites were dried in an oven at 105°C for 48 h to calculate bulk density (*BD*). Other soil samples were allowed to be saturated for 72 h, and were then centrifuged (H-1400 pF centrifuge for soil, Kokusan Corporation, Japan). The centrifuge was operated using 12 matric potentials as follows:

TABLE 1 | Soil texture configurations for infiltration measurements.

Site	Soil texture configuration	Soil texture of layers			Thickness of layers		
		L_1	L_2	L_3	L_1 (cm)	L_2 (cm)	L_3 (cm)
T1	HS	Sand	\	\	60	\	\
T2	MC	Silt	Sand	\	10	50	\
T3		Silt loam	Sand	\	55	5	\
T4	CM	Sand	Silt loam	\	13	47	\
T5		Sand	Silt loam	Sand	30	30	\
T6	CMC	Sand	Silt loam	Sand	17.5	21.5	21
T7		Sand	Silt loam	Sand	6	14	40
T8	MM	Sand	Silt loam	Loam	10	20	30
T9		Sand	Silt loam	Loam	26	20	14

[a]HS, MC, CM, CMC, and MM indicate homogeneous soil profile, soil profile in which medium-textured layers cover the coarser layer, soil profile in which medium-textured layers lie beneath the coarser layer, soil profile with medium-textured soil interlaid within coarser profile, and soil profile with multiple medium-textured layers, respectively.

[b]L_1, L_2, and L_3 represent the first layer, the second layer, and the third layer, respectively. Soil layers were categorized according to soil texture.

[c]"\" indicates no corresponding soil layer.

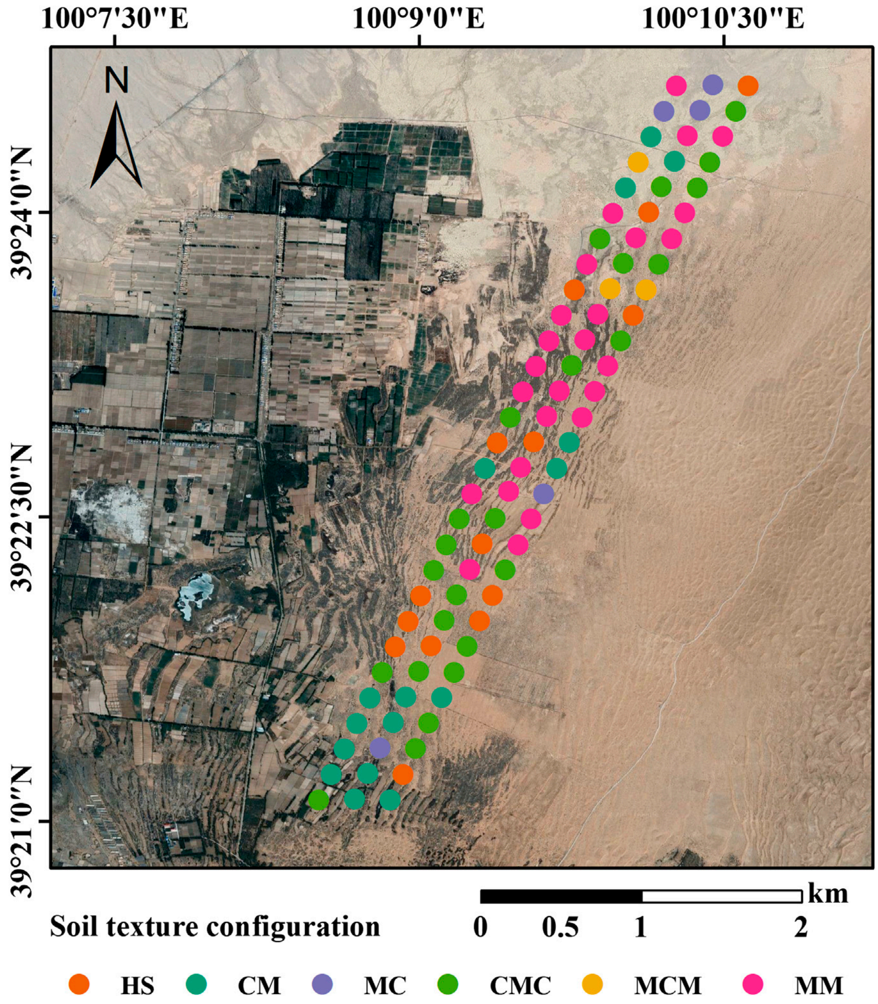

FIGURE 3 | Distribution map of different texture-configuration soils. HS, CM, MC, CMC, MCM, and MM represent homogeneous soil profile, soil profile in which medium-textured layers lie beneath the coarser layer, soil profile in which medium-textured layers cover the coarser layer, soil profile with medium-textured soil interlaid within a coarser profile, soil profile with coarser texture interlaid within a medium-textured profile, and soil profile with multiple medium-textured layers, respectively. Note: The size of circle symbols dose not represent the sampling range.

−0.001, −0.005, −0.01, −0.02, −0.04, −0.06, −0.08, −0.1, −0.2, −0.5, −1, and −1.5 MPa. The mass water content of each soil sample at a given pressure head was recorded individually. Water-holding capacity was measured using field capacity (*FC*), wilting point (*WP*), and available water content (*AWC*). In practice, *WP* is generally considered to be the soil water content at −1.5 MPa. *FC* for coarse- and medium-textured soils are measured more consistently at −0.01 MPa and −0.02 MPa, respectively, (Gijsman, et al., 2007). *AWC* represents the difference between *FC* and *WP* (Ren, et al., 2017). Therefore, *SWC* refers to mass water content, in this work.

Statistical Analyses

Statistical analyses were conducted with SPSS 22.0 (SPSS, Chicago, IL, United States). Because most of the soil property distributions failed the test of normality, a nonparametric Kruskal-Wallis ANOVA test could be used by comparing the differences in soil properties among the nine infiltration sites. We used linear regression to analyze the relationships between soil water content and textural size fractions of soil profiles, thickness, and burial depth of the medium-textured layers at the 87 sites. Correlation analysis was performed using Spearman's correlation coefficients to evaluate the relationships between water retention properties and soil properties at the nine infiltration sites.

RESULTS

Textural Layering and Soil-Structure Interactions

Textural layered soils displayed large variability in the sampled landscape. Overall, approximately 84% of soil profiles in the study area were textual layering soils, and the soils had a patchy distribution (**Figure 3**). Based on the position and number of

TABLE 2 | Median (Standard Error) of soil physical properties at the nine infiltration sites (0–60 cm).

Site	Soil texture configuration	Particle size distribution			SWC (g/cm3)	BD (g/cm3)	TP (%)	*SSA* (m^2/kg)	*GD* (*μm*)
		Sand (%)	Silt (%)	Clay (%)					
T1	HS	93.91 (0.17) a	4.49 (0.12) b	1.60 (0.05) b	0.03 (0.01) a	1.48 (0.01) a	44.28 (0.01) a	96.53 (8.63) a	62.20 (3.41) b
T2	MC	71.76 (16.00) ab	25.19 (14.29) ab	3.05 (1.72) ab	0.03 (0.03) a	1.43 (0.04) a	46.13 (0.02) a	127.30 (215.61) a	47.10 (26.43) b
T3	MC	19.94 (10.88) b	69.14 (9.58) a	10.93 (1.60) a	0.12 (0.03) b	1.31 (0.02) a	50.71 (0.01) a	1,443.00 (174.04) b	4.16 (6.13) a
T4	CM	28.63 (14.35) b	61.16 (12.25) a	10.21 (2.15) ab	0.16 (0.04) c	1.32 (0.03) a	50.25 (0.01) a	1,528.00 (244.55) b	3.93 (8.01) a
T5	CM	64.63 (13.26) ab	30.16 (11.55) ab	5.21 (1.71) ab	0.08 (0.07) abc	1.43 (0.04) a	46.17 (0.01) a	187.90 (245.98) a	31.90 (8.41) b
T6	CMC	49.08 (16.17) ab	44.77 (14.31) ab	6.15 (1.94) ab	0.09 (0.06) abc	1.40 (0.03) a	47.74 (0.01) a	662.65 (236.80) a	15.31 (7.06) b
T7	CMC	59.04 (16.45) ab	35.19 (14.11) ab	5.77 (2.38) ab	0.04 (0.03) a	1.41 (0.05) a	46.73 (0.02) a	200.85 (276.27) ab	30.25 (8.67) b
T8	MM	52.41 (11.44) ab	39.61 (9.71) ab	8.04 (1.82) ab	0.12 (0.05) abc	1.25 (0.05) a	52.80 (0.02) a	945.60 (219.85) a	6.35 (7.01) ab
T9	MM	49.44 (11.26) ab	41.18 (9.53) ab	9.37 (2.13) ab	0.09 (0.03) ab	1.32 (0.04) a	50.02 (0.02) a	1,257.00 (249.34) ab	4.77 (7.11) ab

HS, MC, CM, CMC, and MM represent homogeneous soil profile, soil profile in which medium-textured layers cover the coarser layer, soil profile in which medium-textured layers lie beneath the coarser layer, soil profile with medium-textured soil interlaid within a coarser profile, and soil profile with multiple medium-textured layers, respectively. Different lowercase letters indicate significant differences at $p < 0.05$.

medium-textured layers, the 87 sampling sites were separated into six classes: soil profile with multiple medium-textured layers (MM), soil profile with medium-textured soil interlaid within a coarser profile (CMC), soil profile in which medium-textured layers lay beneath the coarser layer (CM), homogeneous soil profile (HS), soil profile in which medium-textured layers covered the coarser layer (MC), and soil profile with coarser texture interlaid within a medium-textured profile (MCM); these accounted for 28.74 27.59, 18.39, 16.08, 5.75, and 3.45% of the samples, respectively.

Clay and silt concentrations (**Figure 4A** and **Figure 4B**) and *SWC* (**Figure 4D**) at the 87 sites were not normally distributed, but showed a strong tendency toward low values. Sand content data exhibited an opposite trend with >45% of soil profiles having sand content >90% (**Figure 4C**). Thickness of the medium-textured layer produced general unimodal distribution (**Figure 4F**), with >65% of medium-textured layers ranging in thickness from 0 to 90 cm. Distribution of burial depth was characterized by a single well-expressed maximum at 210–240 cm, with a second, less well-expressed maximum at 0–30 cm (**Figure 4E**).

Similarly, soil physical properties at the nine infiltration sites exhibited prominent differences (**Table 2** and **Figure 5**). The differences in *SWC*, surface specific area (*SSA*), and grain diameter (*GD*) between T1, T3, and T4 were significant ($p <$ 0.05). As the thickness of the medium-textured layer increased, *SWC* increased from 0.03 g/cm^3 for T1 to 0.12 g/cm^3 for T3 to the maximum (0.16 g/cm^3) for T4. *SSA* was substantially greater in T3 and T4 than in T1, and increased from 96.53 (m^2/kg) for T1 to 1,443.00 (m^2/kg) for T3 to 1,528.00 (m^2/kg) for T4. *GD* at T1 was approximately 15 times larger than that at T3 and T4. *SWC*, *SSA*, and *GD* had no remarkable variation in the same texture configuration profile other than soil profiles in which medium-textured layers covered the coarser layer (T2 and T3) and soil profiles in which medium-textured layers lay beneath the coarser layer (T4 and T5). *BD* and *TP* did not differ in the effects of soil textural layering. The distribution of clay, silt, and sand in the T1 profile was uniform, whereas textural size fractions were exceptionally heterogeneous in T2 to T9, with the medium-textured layers stratified horizontally thereby forming sharp textural interfaces. Specifically, *FC* and *WP* were much lower in subsurface medium-textured layers than in sites with the medium-textured layers on the surface (average of 0.21 and 0.13 g/cm^3, average of 0.24 and 0.16 g/cm^3, respectively, for *FC* and *WP*). Notably, there was no significant effect of burial depth of the medium-textured layer on water-holding capacity; *FC* and *WP* for sand layers overlying medium-textured layers were 0.14 and 0.04 g/cm^3, respectively, and the values for subsurface sand layers were 0.14 and 0.03 g/cm^3, respectively. Conversely, *AWC* exhibited no significant difference between overlying silt loam layers and subsurface silt loam layers (0.08 and 0.09 g/cm^3, respectively); *AWC* was higher in surface sand layers than in sand layers beneath the silt loam layers (0.11 and 0.09 g/cm^3, respectively). In general, the *FC* and *WP* of sand layers were lower than those of medium-textured layers, including silt loam and loam layers, and the *AWC* of sand layers was higher than that of medium-textured layers.

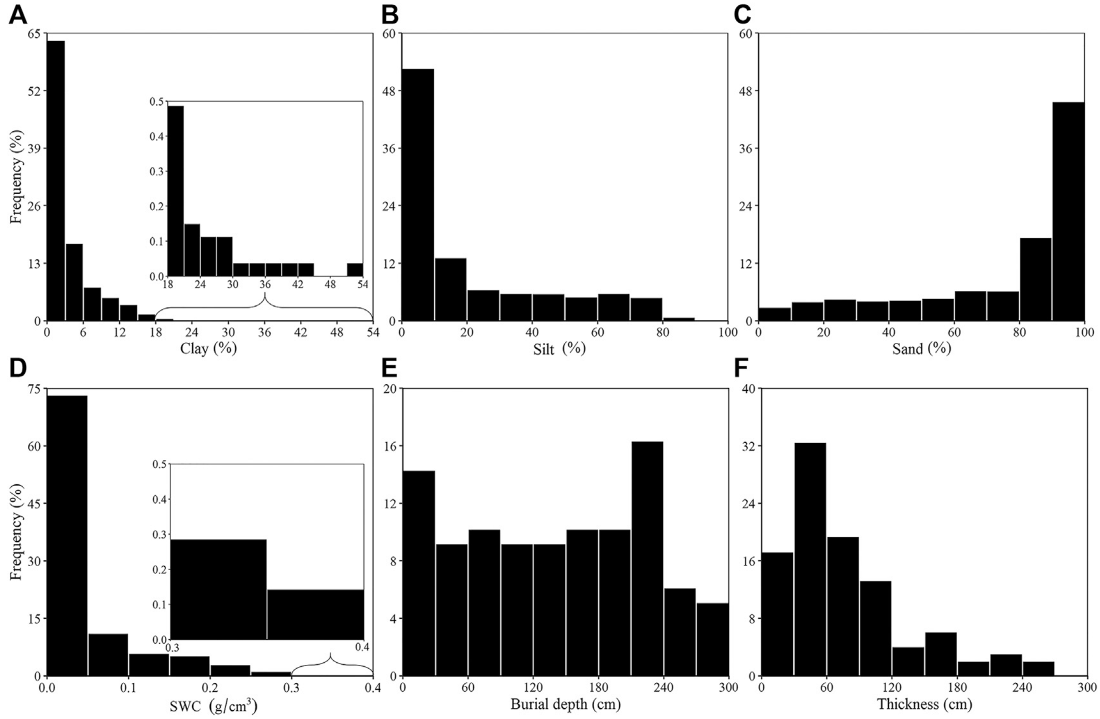

FIGURE 4 | Histograms of frequency distribution of values for soil texture fractions, soil water content, and thickness and burial depth of medium-textured layers at the 87 sites.

Soil Infiltration Features Affected by Textural Layering

The water infiltration rate was high at the beginning of the experiment, decreased significantly with time, and then slowed down, finally stabilizing in most sites, such as T1, T2, T3, T8, and T9 (**Figure 6**). However, the infiltration rate for T4 and T5 first began to increase, then decreased slowly compared with T1 (between 20 and −100 min), and thereafter stabilized; a special condition was detected at T5 and T6, where the infiltration rates declined linearly after 245 and 255 min, respectively. In addition, the infiltration rate curve for T7 fluctuated until 285 min. In general, the average infiltration rate fell in the order T1> T5> T9> T4> T6> T8> T7> T3> T2.

The cumulative infiltration curves rose gradually during the infiltration period (**Figure 6**). The cumulative infiltration at other sites was lower than that at T1 (709.89 cm); those of the average of soil profiles in which medium-textured layers covered the coarser layer (T2 and T3, 63.66 cm), of soil profiles with medium-textured soil interlaid within a coarser profile (T6 and T7, 196.58 cm), of soil profiles with multiple medium-textured layers (T8 and T9, 334.69 cm), and of soil profiles in which medium-textured layers lay beneath the coarser layer (T4 and T5, 408.14 cm) decreased by 91, 72, 53, and 43%, respectively. Interestingly, two turning points (the first at 120 min and the second at 255 min) were observed in the cumulative infiltration curve at T7, after which soil water infiltration decreased. However, this phenomenon was not as notable at other sites.

The horizontal and vertical wetting front initially advanced very fast and then slowed down until finally the rate of the wetting front became constant (**Figure 7**). The wetting zone for T1 was larger than that of the other sites, especially in the vertical direction. There were substantial reductions in the vertical wetting front at T2 to T9 compared with T1; the decreases were 74.5, 79.5, 72, 55, 74, 57, 73.5, and 50.3 cm, respectively. Meanwhile, the order of advancement in the horizontal direction for the same test duration was: T1, T5, T6, T8, T9, T4, T7, T2, and T3. The times when the wetting fronts of T4 to T9 first arrived at the interface were 20, 45, 4, 20, 15, and 35 min, respectively. The process of water penetration created an onion-shaped wetting front at T3 that propagated very slowly, in both vertical and horizontal directions. Likewise, the vertical and horizontal wetting distances at T2 and T7 were similar.

Water Regimes Affected by Textural Layering

A correlation analysis between *SWC* and soil properties among the 87 sites is shown in **Figure 8** and **Figure 9**. Significant positive correlations were found for *SWC* and silt ($r = 0.78$, $p < 0.001$, **Figure 8B**) and clay concentrations ($r = 0.73$, $p < 0.001$, **Figure 8C**) in soil depth to 300 cm, while *SWC* was highly significantly negatively correlated with sand concentration and an r value of 0.78 ($p < 0.001$, **Figure 8A**). And there was a significant negative correlation between *SWC* and burial depth of the medium-textured layers ($r = -0.25$, $p < 0.05$, **Figure 9A**), whereas the thickness of the layers was positively correlated with *SWC* ($r = 0.57$, $p < 0.001$, **Figure 9B**).

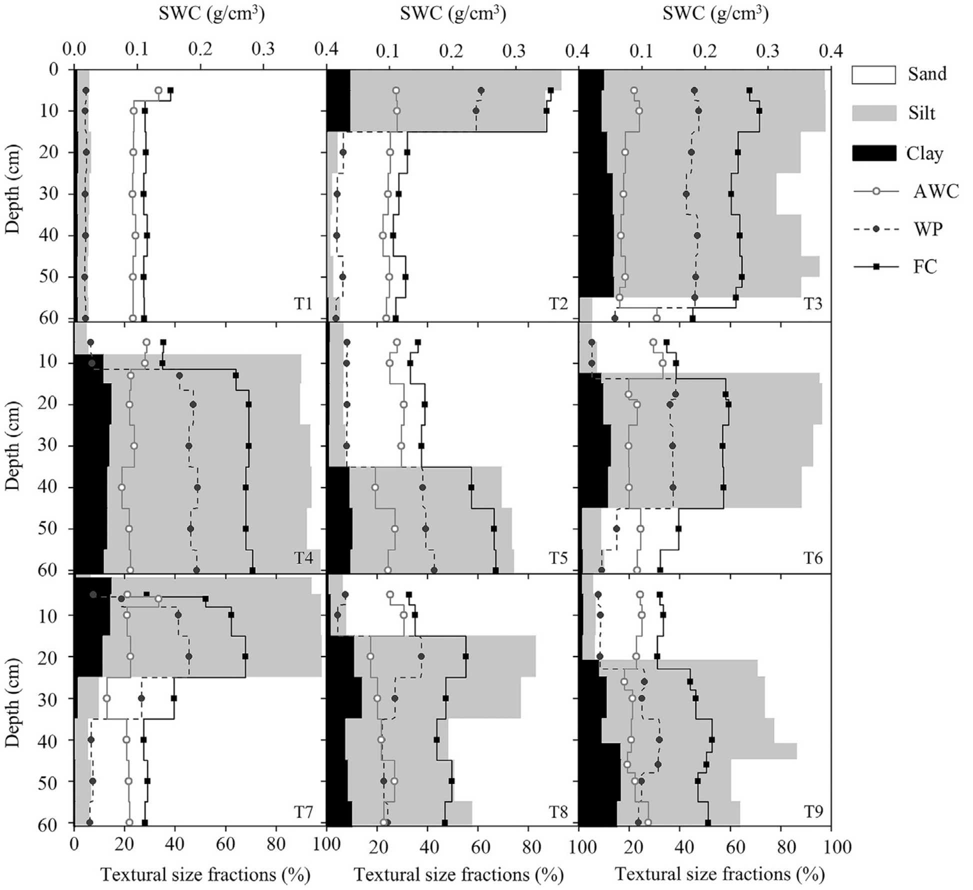

FIGURE 5 | Textural size fractions and water-holding capacities of different soil texture configurations.

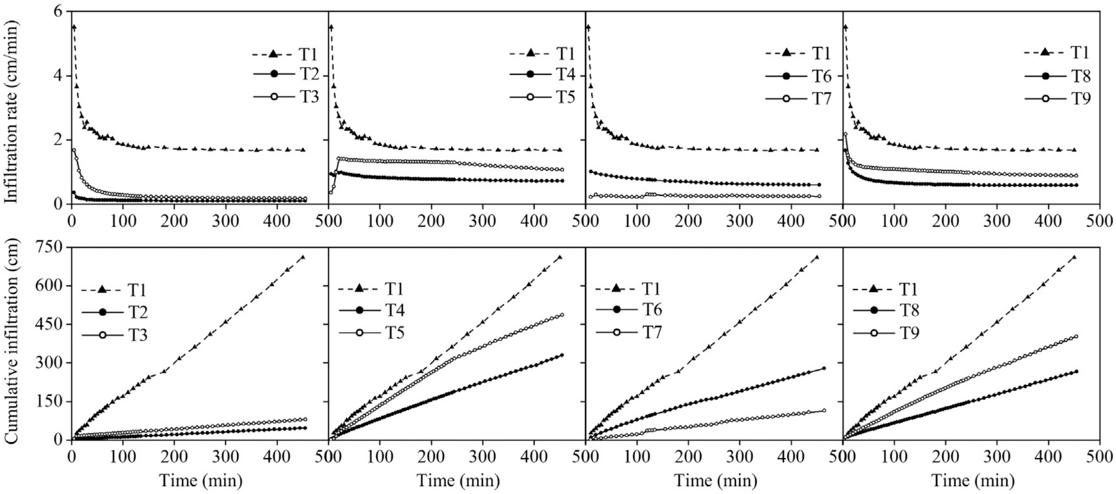

FIGURE 6 | Infiltration rate and cumulative infiltration with different texture configurations.

A correlation analysis between soil water retention and infiltration parameters and soil properties among the nine infiltration sites is shown in **Figure 10**. Water retention capacities (*FC*, *WP* and *AWC*) were significantly correlated with soil physical properties (*SWC*, sand, silt and clay concentrations, *BD*, and *TP*). A positive relationship with the thickness of the medium-textured layers was found for *FC* and *WP*, but not for *AWC*. The infiltration rate at 450 min (i_{450}) and cumulative infiltration at 450 min (I_{450}) were significantly positively correlated with sand concentration, *BD*, and the burial depth of the medium-textured layers, but significantly negatively correlated with silt concentration and *TP*. WFW_{450} and wetting front depth at 450 min (WFD_{450}) were significantly negatively correlated with the thickness of the medium-textured layers. Moreover, *SWC* was associated with the thickness of the medium-textured layers but not with the burial depth of these layers.

DISCUSSION

How Does Textural Layering Affect Soil Hydrological Properties and Processes?

Textural layering could increase water retention capacities both directly and indirectly. We had evidence that textural layering increased *FC*, *WP* and *AWC* of the surface sand layers (**Figure 5**), indicating the possibility of high water-storage capacity. These results were likely related to the increases in silt and clay content and *TP* of the surface sand layers and the thickness of the medium-textured layers, irrespective of the burial depth of those layers (**Figure 10**), because the thickness of the medium-textured layers is used as an indicator of silt and clay content, and increases in silt and clay content and *TP* can cause an increase in the abundance of small pore spaces where most water is retained (Sperry and Hacke, 2002). Our study also found that the correlation coefficients of soil texture with *FC* and *WP* were higher compared with those of *TP*, *BD* and the thickness. Any inconsistency might be caused by a discrepancy in initial soil water content, which can indirectly reflect matric potential. At high matric potentials, the impact of soil structure and physical properties on water-holding capacity would overrule the effect of clay content (Petersen, et al., 1996). Nevertheless, silt and clay contents become major contributors to water-holding capacity at low matric potentials (Banin and Amiel, 1970; Arthur, et al., 2013). In our study, low soil water content corresponded to low matric potential, and the concentrations of silt and clay were the major factors.

Although the burial depth of the medium-textured layers played minor roles in *FC*, *WP* and *AWC* compared with soil physical properties and the thickness of medium-textured layers (**Figure 10**), burial depth might be relevant for hydrological processes along with the texture configuration. In textural layering soils, the finer-textured layers act as barriers to infiltration (Li, et al., 2014), making burial depth an important factor in the infiltration process (Leconte and Brissette, 2001). Our study found that textural layering soil infiltration increased with the burial depth of the medium-textured layer, although it was less in the 17.5 cm treatment (T6) than in the 13 cm treatment (T4). A similar finding was reported by Wang *et al.* (Wang, et al., 2018), who found that the infiltration reduction effect was more pronounced in the 10 cm burial depth treatment than in the 5 cm treatment when the finer-textured layer was wettable. This result was also reported by Zhang *et al.* (Zhang, et al., 2017b), who indicated that infiltration increased as the burial depth of finer-textured layers increased from 0.5 to 25 cm, although the 10 cm treatment was an exception. They further found that burial depth hardly influenced infiltration process when the depth increased from 15 to 25 cm. Clearly, the impact of burial depth of the medium-textured layer on infiltration is complicated. On the other hand, our work revealed that textural layering soils had an infiltration-reduction effect, promoting the partition of water into lateral flows; these effects decreased in the order: MC, CMC, MM, and CM. This result is powerful evidence that the finer-textured layer governs the infiltration process (Kale and Sahoo, 2011). Infiltration is affected not only by the textural layering configurations and the burial depth of the finer-textured layers, but also by the thickness of the layers. For the MC scenario, the soil infiltrability of T2 was weaker than that of T3. There was no pronounced flow barrier effect in T3 resulting from the thickness of the overlying medium-textured layer when it greatly exceeded WFD_{450}. Therefore, the 450 min infiltration process in T3 could be regarded as active in the medium-textured layer alone. Generally, a homogenous coarse layer has the fastest infiltration, while a fine homogenous layer has the slowest infiltration (Deng and Zhu, 2016). One explanation for these opposing results is that the finer-textured layer had a low hydraulic conductivity and more water was needed to break the capillary barrier when it was dry (McCartney and Zornberg, 2010; Si, et al., 2011). Therefore, when a finer-textured layer overlies a sand layer, a flow barrier can form when the thickness of the finer-textured layers does not exceed the response length.

Overall, these findings suggested a role for textural layering in soil hydrological processes. Textural layering could increase the content of silt and clay and of soil porosity, resulting in increasing surface sand layer water retention. Soil texture configuration, burial depth and thickness of the medium-textured layers influenced flow barriers indirectly, thus impacting the infiltration process. Moreover, these results contribute to a better understanding of infiltration characteristics in soils with different textural configurations, and provide data for validating and developing infiltration models and preferential flow modeling.

How Does Textural Layering Control Water Regimes?

Data from the infiltration sites showed that textural layering significantly altered sand, silt and clay concentrations, and increased *SWC*, compared with HS (**Table 2**). There was significant correlation between *SWC* and soil texture (**Figure 8** and **Figure 10**). These results agreed with earlier findings, demonstrating that the effect of soil composition on *SWC* was inversely proportional to sand concentration and directly proportional to silt and clay concentrations (Gómez-Plaza, et al., 2001; Kokulan, et al., 2018). This trend was attributed to a higher absorption capacity with variations in the *SSA* with medium and fine particles (Petersen, et al., 1996), a result consistent with our findings (**Table 2**). Soil texture configuration could affect the thickness and burial depth of medium-textured layers and thus acted as another determining element of *SWC* (**Figure 9**). The thickness and burial depth of medium-textured layers were other

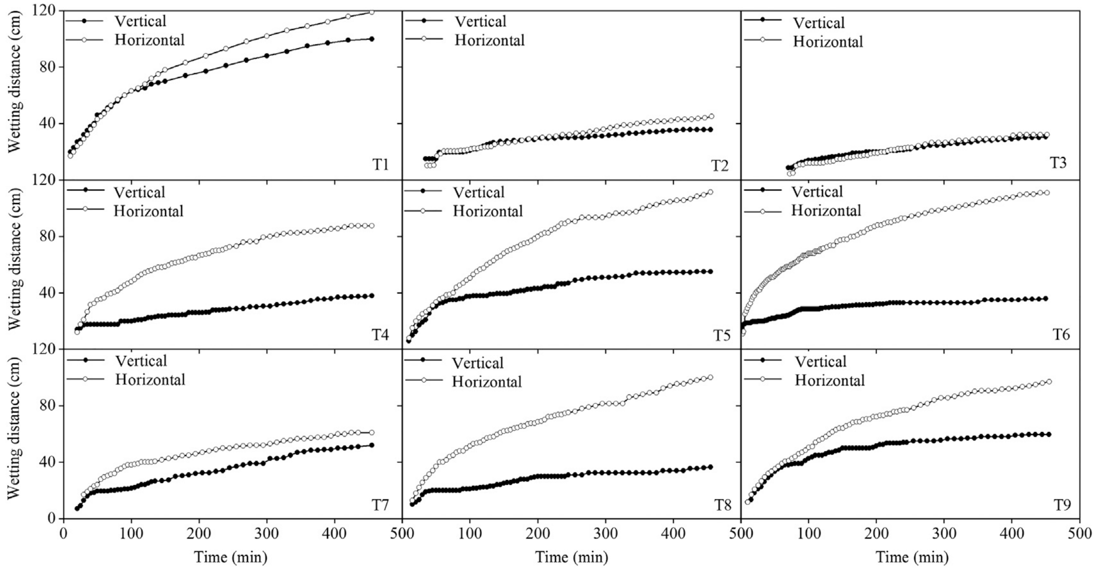

FIGURE 7 | Advance of the wetting front in horizontal and vertical directions, with time.

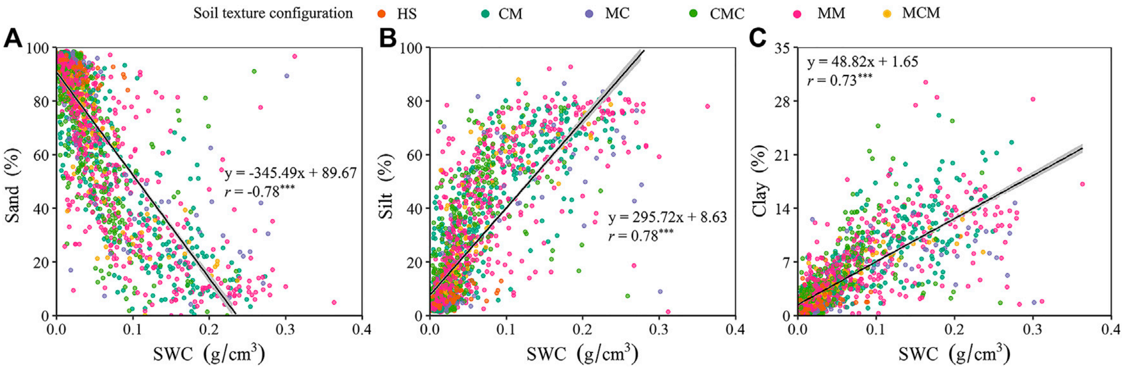

FIGURE 8 | Relationships between *SWC* and sand concentration (A), silt concentration (B) and clay concentration (C) in soils to 300 cm depth; *** significant at $p < 0.001$.

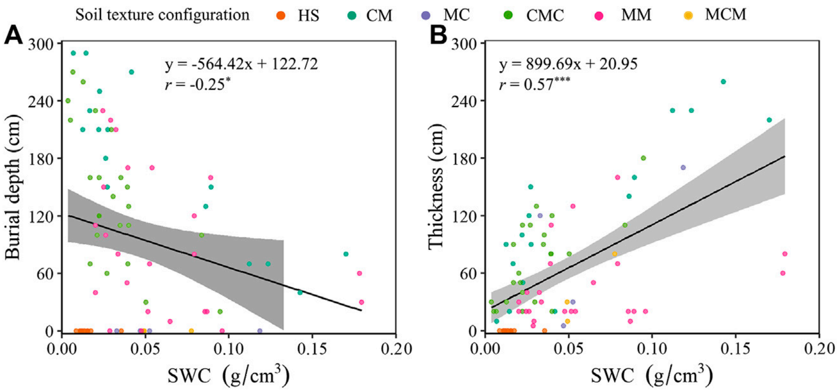

FIGURE 9 | Relationships between *SWC* and burial depth (A) and thickness (B) of medium-textured layers in soils to 300 cm depth; *** significant at $p < 0.001$, * significant at $p < 0.05$.

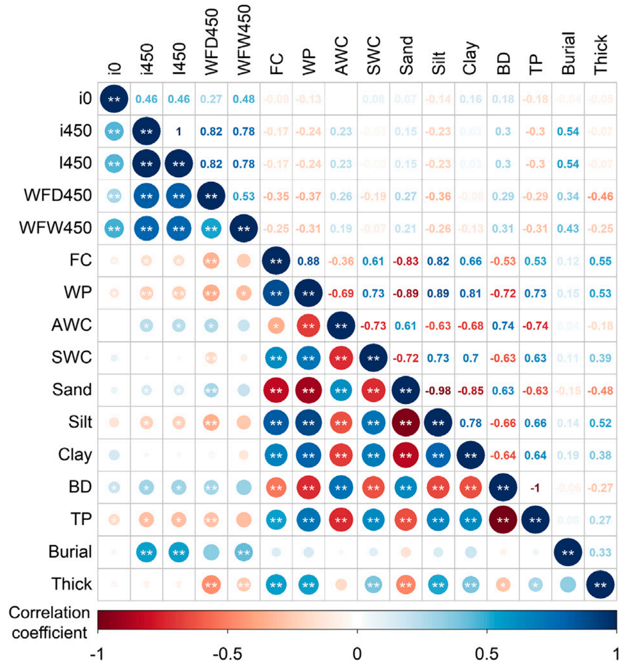

FIGURE 10 | Correlation matrix among soil properties and water-holding capacities and infiltration parameters. Note: i_0, i_{450}, I_{450}, WFW_{450} and WFD_{450} represent initial infiltration rate (cm/min), infiltration rate at 450 min (cm/min), cumulative infiltration at 450 min (cm), wetting front width at 450 min (cm) and wetting front depth at 450 min (cm), respectively; *FC*, *WP*, *AWC* and *SWC* represent fielding capacity (g/cm^3), wilting point (g/cm^3), available soil water content (g/cm^3) and soil water content (g/cm^3), respectively; *BD* and *TP* represent bulk density (g/cm^3) and total porosity (%), respectively; Burial and Thick represent the burial depth and thickness of the medium-textured layers (cm).

determining elements of *SWC*. The thickness of the medium-textured layers could be regarded as an indicator of silt and clay concentrations, and as a consequence, there was significant positive correlation between *SWC* and the thickness of medium-textured layers (**Figure 9** and **Figure 10**). On the other hand, there was little relationship between *SWC* and burial depth of the medium-textured layers (**Figure 9** and **Figure 10**). In the previous section, we discussed the complex relationship between burial depth and soil hydrological processes. This relationship further explains why the burial depth of the medium-textured layer had a negligible effect on soil water content, and in part accounted for the low *r* value (0.39) between the thickness of a medium-textured layer and *SWC* in this study (**Figure 10**). In general, because precipitation could be captured by medium-textured layers but not penetrate into subsurface soil, the effects of small precipitation pulses could accumulate to produce a larger response pulse (Noy-Meir, 1973), which, coupled with increased water-holding capacity, resulted in increased *SWC*.

Implications for Regional Vegetation Conservation

Arid ecosystems, where rainfall is uneven and long drought periods are recurrent (Fernández-Raga, et al., 2017), are characterized by a high sensitivity of vegetation to the plant-available water in the soil. Therefore, the sustainable management of rainfed vegetation is critical for the stability of the ecosystem in arid regions. We have proved that textural layering increased soil water quantity by extending the timescale of precipitation pulses and changing soil hydrological processes, and increased the *AWC* of surface sand layers (**Figure 4** and **Table 2**). This could presumably benefit perennial grasses as they are shallow-rooted and experience large fluctuations in water availability in the upper soil profile (Munson, et al., 2016). However, most studies have shown that woody plants dampened increases on textural layered soils because soil water was effectively inaccessible to plants for long periods, possibly limiting root growth (Fensham, et al., 2015). A recent study revealed that the interaction between rainfall and soil texture may change resources and recruitment strategies available to *Haloxylon ammodendron* (Liu, et al., 2020a). Due to the limited range of the soil layers, the results of this study were insufficient to confirm or refute the previous findings relating to woody plants. Aside from the effect of textural layering configurations on vegetation, the adaptation of plants to hydrology should also be taken into account (Liu, et al., 2020b). Therefore, further work is still needed to identify the potential effects of textural layered soils on eco-hydrological effectiveness and to determine whether textural layering should be considered a potential adverse factor for rainfed vegetation in the desert-oasis ecotones of arid northwestern China, especially as the ecological health of this ecotone is essential for regional ecosystem functioning and services.

CONCLUSION

Based on soil sampling and *in-situ* infiltration tests, this study examined the heterogeneity of textural layering soils and the effects of textural layering on soil water content, hydrological properties and processes. The main research results demonstrate that textural layered soils are widespread and the distribution of medium-textured layers shows discontinuity in the desert-oasis ecotone; and that the presence of medium-textured layers plays a critical role in soil water content, water storage and infiltration in sandy soils. Textural layering can increase soil water content in sandy soils both above and beneath medium-textured layers; and soil water content depends largely on the soil texture configurations, the thickness of medium-textured layers, and silt and clay concentrations. Medium-textured layers significantly increase soil porosity, and higher soil porosity results in increased water retention in surface sand layers. Meanwhile, medium-textured layers generate flow barriers in soil profiles-barriers that could capture and retain water for substantial periods of time relative to sandy soils. The infiltration process is mainly determined by soil texture configuration, and by the burial depth and thickness of medium-textured layers. The present study has only examined textural layering effects on soil water content and hydrological properties and processes. Textural layering effects on vegetation dynamics deserve further attention to improve sand-fixing vegetation in desert-oasis ecotones.

DATA AVAILABILITY STATEMENT

The original contributions presented in the study are included in the article/Supplementary Material, further inquiries can be directed to the corresponding author.

AUTHOR CONTRIBUTIONS

All authors listed have made a substantial, direct, and intellectual contribution to the work and approved it for publication.

FUNDING

This research was jointly supported by the National Natural Science Foundation of China (41630861) and the West Light Foundation of the Chinese Academy of Sciences (2019–2021, awarded to Hu Liu).

ACKNOWLEDGMENTS

We thank Qiyue Yang for his kind assistance in conducting the laboratory tests for this study.

REFERENCES

Al-Maktoumi, A., Kacimov, A., Al-Ismaily, S., Al-Busaidi, H., and Al-Saqri, S. (2015). Infiltration into two-layered soil: the Green–Ampt and averyanov models revisited. *Tran. Porous Med.* 109 (1), 169–193. doi:10.1007/s11242-015-0507-8

Alfnes, E., Kinzelbach, W., and Aagaard, P. (2004). Investigation of hydrogeologic processes in a dipping layer structure: 1. The flow barrier effect. *J. Contam. Hydrol.* 69 (3–4), 157–172. doi:10.1016/j.jconhyd.2003.08.005

Arthur, E., Tuller, M., Moldrup, P., Resurreccion, A. C., Meding, M. S., Kawamoto, K., et al. (2013). Soil specific surface area and non-singularity of soil-water retention at low saturations. *Soil Sci. Soc. Am. J.* 77 (1), 43–53. doi:10.2136/sssaj2012.0262

Bagarello, V., and Sgroi, A. (2004). Using the single-ring infiltrometer method to detect temporal changes in surface soil field-saturated hydraulic conductivity. *Soil Tillage Res.* 76 (1), 13–24. doi:10.1016/j.still.2003.08.008

Banin, A., and Amiel, A. (1970). A correlative study of the chemical and physical properties of a group of natural soils of Israel. *Geoderma* 3 (3), 185–198. doi:10.1016/0016-7061(70)90018-2

Bockheim, J. G. (2016). Genesis of soils with an abrupt textural contrast in the United States. *Catena* 137, 422–431. doi:10.1016/j.catena.2015.10.011

Bockheim, J. G., and Hartemink, A. E. (2013). Distribution and classification of soils with clay-enriched horizons in the United States. *Geoderma* 209–210, 153–160. doi:10.1016/j.geoderma.2013.06.009

Browning, D. M., Archer, S. R., Asner, G. P., McClaran, M. P., and Wessman, C. A. (2008). Woody plants in grasslands: post-encroachment stand dynamics. *Ecol. Appl.* 18 (4), 928–944. doi:10.1890/07-1559.1

Chu, X. F., and Mariño, M. A. (2005). Determination of ponding condition and infiltration into layered soils under unsteady rainfall. *J. Hydrol.* 313 (3–4), 195–207. doi:10.1016/j.jhydrol.2005.03.002

de Jong van Lier, Q., and Wendroth, O. (2016). Reexamination of the field capacity concept in a Brazilian Orison. *Soil Sci. Soc. Am. J.* 80 (2), 264–274. doi:10.2136/sssaj2015.01.0035

Deng, P., and Zhu, J. (2016). Analysis of effective Green–Ampt hydraulic parameters for vertically layered soils. *J. Hydrol.* 538, 705–712. doi:10.1016/j.jhydrol.2016.04.059

Duniway, M. C., Petrie, M. D., Peters, D. P., Anderson, J. P., Crossland, K., and Herrick, J. E. (2018). Soil water dynamics at 15 locations distributed across a desert landscape: insights from a 27-yr dataset. *Ecosphere* 9 (7), e02335. doi:10.1002/ecs2.2335

Fensham, R. J., Butler, D. W., and Foley, J. (2015). How does clay constrain woody biomass in dryland?. *Global Ecol. Biogeogr.* 24 (8), 950–958. doi:10.1111/geb.12319

Fernández-Raga, M., Palencia, C., Keesstra, S., Jordán, A., Fraile, R., Angulo-Martínez, M., et al. (2017). Splash erosion: a review with unanswered questions. *Earth Sci. Rev.* 171, 463–477. doi:10.1016/j.earscirev.2017.06.009

Gijsman, A. J., Thornton, P. K., and Hoogenboom, G. (2007). Using the WISE database to parameterize soil inputs for crop simulation models. *Comput. Electron. Agric.* 56 (2), 85–100. doi:10.1016/j.compag.2007.01.001

Gómez-Plaza, A., Martınez-Mena, M., Albaladejo, J., and Castillo, V. M. (2001). Factors regulating spatial distribution of soil water content in small semiarid catchments. *J. Hydrol.* 253 (1–4), 211–226. doi:10.1016/S0022-1694(01)00483-8

Gvirtzman, H., Shalev, E., Dahan, O., and Hatzor, Y. H. (2008). Large-scale infiltration experiments into unsaturated stratified loess sediments: monitoring and modeling. *J. Hydrol.* 349 (1–2), 214–229. doi:10.1016/j.jhydrol.2007.11.002

Hamerlynck, E. P., McAuliffe, J. R., McDonald, E. V., and Smith, S. D. (2002). Ecological responses of two Mojave Desert shrubs to soil horizon development and soil water dynamics. *Ecology* 83 (3), 768–779. doi:10.1890/0012-9658(2002)083[0768:EROTMD]2.0.CO;2

Hardie, M. A., Cotching, W. E., Doyle, R. B., Holz, G., Lisson, S., and Mattern, K. (2011). Effect of antecedent soil moisture on preferential flow in a texture-contrast soil. *J. Hydrol.* 398 (3–4), 191–201. doi:10.1016/j.jhydrol.2010.12.008

Hardie, M. A., Doyle, R. B., Cotching, W. E., and Lisson, S. (2012). Subsurface lateral flow in texture-contrast (duplex) soils and catchments with shallow bedrock. *Appl. Environ. Soil Sci.* 2012 (5), 10. doi:10.1155/2012/861358

Hardie, M. A., Doyle, R., Cotching, W., Holz, G., and Lisson, S. (2013). Hydrogeology and preferential flow in the Tasmanian texture-contrast soils. *Vadose Zone J.* 12 (4). doi:10.2136/vzj2013.03.0051

Hill, D. E., and Parlange, J. Y. (1972). Wetting front instability in layered soils. *Soil Sci. Soc. Am. J.* 36 (5), 697–702. doi:10.2136/sssaj1972.03615995003600050010x

Hou, X. K., Li, T. L., Vanapalli, S. K., and Xi, Y. (2019). Water percolation in a thick unsaturated loess layer considering the ground-atmosphere interaction. *Hydrol. Process.* 33, 794–802. doi:10.1002/hyp.13364

Huang, M., Zettl, J. D., Barbour, S. L., Elshorbagy, A., and Si, B. C. (2013). The impact of soil moisture availability on forest growth indices for variably layered coarse-textured soils. *Ecohydrology* 6 (2), 214–227. doi:10.1002/eco.1260

Ityel, E., Lazarovitch, N., Silberbush, M., and Ben-Gal, A. (2011). An artificial capillary barrier to improve root zone conditions for horticultural crops: physical effects on water content. *Irrigat. Sci.* 29 (2), 171–180. doi:10.1007/s00271-010-0227-3

Kale, R. V., and Sahoo, B. (2011). Green-Ampt infiltration models for varied field conditions: a revisit. *Water Resour. Manag.* 25 (14), 3505–3536. doi:10.1007/s11269-011-9868-0

Kokulan, V., Akinremi, O., Moulin, A. P., and Kumaragamage, D. (2018). Importance of terrain attributes in relation to the spatial distribution of soil properties at the micro scale: a case study. *Can. J. Soil Sci.* 98 (2), 292–305. doi:10.1016/j.scitotenv.2017.01.062

Leconte, R., and Brissette, F. P. (2001). Soil moisture profile model for two-layered soil based on sharp wetting front approach. *J. Hydrol. Eng.* 6 (2), 141–149. doi:10.1061/(Asce)1084-0699(2001)6:2(141)

Li, X. P., Chang, S. X., and Salifu, K. F. (2014). Soil texture and layering effects on water and salt dynamics in the presence of a water table: a review. *Environ. Rev.* 22 (1), 41–50. doi:10.1139/er-2013-0035

Liu, H., Wu, C. D., Yu, Y., Zhao, W. Z., Yang, Q. Y., Wang, S. J., et al. (2020b). Modeling the physiological responses of a desert shrub to rainfall pulses in an arid environment in northwestern China. *J. Arid Environ.* 183, 104277. doi:10.1016/j.jaridenv.2020.104277

Liu, H., Yu, Y., Zhao, W. Z., Guo, L., Liu, J. T., and Yang, Q. Y. (2020a). Inferring subsurface preferential flow features from a wavelet analysis of hydrological signals in the shale hills catchment. *Water Resour. Res.* 56 (11), e2019WR026668. doi:10.1029/2019wr026668

Liu, J. L., Ren, W., Zhao, W. Z., and Li, F. R. (2018). Cropping systems alter the biodiversity of ground- and soil-dwelling herbivorous and predatory arthropods in a desert agroecosystem: implications for pest biocontrol. *Agric. Ecosyst. Environ.* 266, 109–121. doi:10.1016/j.agee.2018.07.023

Liu, W. J., Su, Y. Z., Yang, R., Yang, Q., and Fan, G. P. (2011). Temporal and spatial variability of soil organic matter and total nitrogen in a typical oasis cropland ecosystem in arid region of Northwest China. *Environ. Earth Sci.* 64 (8), 2247–2257. doi:10.1007/s12665-011-1053-5

Ma, Y., Feng, S. Y., Zhan, H. B., Liu, X. D., Su, D. Y., Kang, S. Z., et al. (2011). Water infiltration in layered soils with air entrapment: modified Green-Ampt model and experimental validation. *J. Hydrol. Eng.* 16 (8), 628–638. doi:10.1061/(asce)he.1943-5584.0000360

Macinnis-Ng, C. M. O., Fuentes, S., O'Grady, A. P., Palmer, A. R., Taylor, D., Whitley, R. J., et al. (2010). Root biomass distribution and soil properties of an open woodland on a duplex soil. *Plant Soil* 327 (1–2), 377–388. doi:10.1007/s11104-009-0061-7

Mancarella, D., Doglioni, A., and Simeone, V. (2012). On capillary barrier effects and debris slide triggering in unsaturated layered covers. *Eng. Geol.* 147-148, 14–27. doi:10.1016/j.enggeo.2012.07.003

McAuliffe, J. R. (1994). Landscape evolution, soil formation, and ecological patterns and processes in Sonoran Desert bajadas. *Ecol. Monogr.* 64 (2), 111–148. doi:10.2307/2937038

McCartney, J. S., and Zornberg, J. G. (2010). Effects of infiltration and evaporation on geosynthetic capillary barrier performance. *Can. Geotech. J.* 47 (11), 1201–1213. doi:10.1139/t10-024

Miyazaki, T., Hasegawa, S., and Kasubuchi, T. (1993). Water flow in soils. New York: Marcel Dekker, Inc.

Mohammadzadeh-Habili, J., and Heidarpour, M. (2015). Application of the Green–Ampt model for infiltration into layered soils. *J. Hydrol.* 527, 824–832. doi:10.1016/j.jhydrol.2015.05.052

Munson, S. M., Sankey, T. T., Xian, G., Villarreal, M. L., and Homer, C. G. (2016). Decadal shifts in grass and woody plant cover are driven by prolonged drying and modified by topo-edaphic properties. *Ecol. Appl.* 26 (8), 2480–2494. doi:10.1002/eap.1389

Ng, C. W., Liu, J., Chen, R., and Xu, J. (2015). Physical and numerical modeling of an inclined three-layer (silt/gravelly sand/clay) capillary barrier cover system under extreme rainfall. *Waste Manag.* 38, 210–221. doi:10.1016/j.wasman.2014.12.013

Noy-Meir, I. (1973). Desert ecosystems: environment and producers. *Annu. Rev. Ecol. Evol.* 4 (1), 25–51. doi:10.1146/annurev.es.04.110173.000325

Pahlavan-Rad, M. R., and Akbarimoghaddam, A. (2018). Spatial variability of soil texture fractions and pH in a flood plain (case study from eastern Iran). *Catena* 160, 275–281. doi:10.1016/j.catena.2017.10.002

Petersen, L. W., Moldrup, P., Jacobsen, O. H., and Rolston, D. E. (1996). Relations between specific surface area and soil physical and chemical properties. *Soil Sci.* 161 (1), 9–21. doi:10.1097/00010694-199601000-00003

Phillips, J. D. (2001). Contingency and generalization in pedology, as exemplified by texture-contrast soils. *Geoderma* 102 (3–4), 347–370. doi:10.1016/S0016-7061(01)00041-6

Qian, T. W., Huo, L. J., and Zhao, D. Y. (2010). Laboratory investigation into factors affecting performance of capillary barrier system in unsaturated soil. *Water Air Soil Pollut.* 206 (1–4), 295–306. doi:10.1007/s11270-009-0106-9

Regmi, N. R., and Rasmussen, C. (2018). Predictive mapping of soil-landscape relationships in the arid Southwest United States. *Catena* 165, 473–486. doi:10.1016/j.catena.2018.02.031

Ren, H., Xu, Z., Isbell, F., Huang, J., Han, X., Wan, S., et al. (2017). Exacerbated nitrogen limitation ends transient stimulation of grassland productivity by increased precipitation. *Ecol. Monogr.* 87 (3), 457–469. doi:10.1002/ecm.1262

Rimon, Y., Dahan, O., Nativ, R., and Geyer, S. (2007). Water percolation through the deep vadose zone and groundwater recharge: preliminary results based on a new vadose zone monitoring system. *Water Resour. Res.* 43 (5), W05402. doi:10.1029/2006wr004855

Selim, H. M. (1993). water and solute transport. Dordrecht: Springer Netherlands.

Ross, B. (1990). The diversion capacity of capillary barriers. *Water Resour. Res.* 26 (10), 2625–2629. doi:10.1029/WR026i010p02625

Si, B., Dyck, M., and Parkin, G. W. (2011). Flow and transport in layered soils. *Can. J. Soil Sci.* 91 (2), 127–132. doi:10.4141/cjss11501

Sperry, J. S., and Hacke, U. G. (2002). Desert shrub water relations with respect to soil characteristics and plant functional type. *Funct. Ecol.* 16 (3), 367–378. doi:10.1046/j.1365-2435.2002.00628.x

Stormont, J. C., and Anderson, C. E. (1999). Capillary barrier effect from underlying coarser soil layer. *J. Geotech. Geoenviron.* 125 (8), 641–648. doi:10.1061/(ASCE)1090-0241.19991258641

Tennant, D., Scholz, G., Dixon, J., and Purdie, B. (1992). Physical and chemical characteristics of duplex soils and their distribution in the south-west of Western Australia. *Aust. J. Exp. Agric.* 32 (7), 827–843. doi:10.1071/EA9920827

Thompson, A., Nimmer, M., and Misra, D. (2010). Effects of variations in hydrogeological parameters on water-table mounding in sandy loam and loamy sand soils beneath stormwater infiltration basins. *Hydrogeol. J.* 18 (2), 501–508. doi:10.1007/s10040-009-0532-1

Touma, J., Voltz, M., and Albergel, J. (2007). Determining soil saturated hydraulic conductivity and sorptivity from single ring infiltration tests. *Eur. J. Soil Sci.* 58 (1), 229–238. doi:10.1111/j.1365-2389.2006.00830.x

Wang, C., Mao, X., and Hatano, R. (2014). Modeling ponded infiltration in fine textured soils with coarse interlayer. *Soil Sci. Soc. Am. J.* 78 (3), 745–753. doi:10.2136/sssaj2013.12.0535

Wang, J., Huang, Y., Long, H., Hou, S., Xing, A., and Sun, Z. (2017). Simulations of water movement and solute transport through different soil texture configurations under negative-pressure irrigation. *Hydrol. Process.* 31 (14), 2599–2612. doi:10.1002/hyp.11209

Wang, X., Li, Y., Si, B., Ren, X., and Chen, J. (2018). Simulation of water movement in layered water-repellent soils using HYDRUS-1D. *Soil Sci. Soc. Am. J.* 82 (5), 1101–1112. doi:10.2136/sssaj2018.01.0056

Yan, J., and Zhao, W. (2016). Characteristics of preferential flow during simulated rainfall events in an arid region of China. *Environ. Earth Sci.* 75 (7), 566. doi:10.1007/s12665-015-5101-4

Yang, H., Rahardjo, H., Leong, E. C., and Fredlund, D. G. (2004). A study of infiltration on three sand capillary barriers. *Can. Geotech. J.* 41 (4), 629–643. doi:10.1139/t04-021

Yu, Y., Zhao, W., Martinez-Murillo, J. F., and Pereira, P. (2020). Loess Plateau: from degradation to restoration. *Sci. Total Environ.* 738, 140206. doi:10.1016/j.scitotenv.2020.140206

Zettl, J., Lee Barbour, S., Huang, M., Si, B., and Leskiw, L. A. (2011). Influence of textural layering on field capacity of coarse soils. *Can. J. Soil Sci.* 91 (2), 133–147. doi:10.4141/cjss09117

Zhang, F. B., Bai, Y. J., Xie, L. Y., Yang, M. Y., Li, Z. B., and Wu, X. R. (2017a). Runoff and soil loss characteristics on loess slopes covered with aeolian sand layers of different thicknesses under simulated rainfall. *J. Hydrol.* 549, 244–251. doi:10.1016/j.jhydrol.2017.04.002

Zhang, Y., Zhao, W., and Fu, L. (2017b). Soil macropore characteristics following conversion of native desert soils to irrigated croplands in a desert-oasis ecotone, Northwest China. *Soil Till. Res.* 168, 176–186. doi:10.1016/j.still.2017.01.004

Zhang, Y., Zhao, W., He, J., and Fu, L. (2018). Soil susceptibility to macropore flow across a desert-oasis ecotone of the Hexi Corridor, Northwest China. *Water Resour. Res.* 54 (2), 1281–1294. doi:10.1002/2017wr021462

Zhang, Y., and Zhao, W. (2015). Vegetation and soil property response of short-time fencing in temperate desert of the Hexi Corridor, northwestern China. *Catena* 133, 43–51. doi:10.1016/j.catena.2015.04.019

Zhou, H., Zhao, W. Z., and Yang, Q. Y. (2016). Root biomass distribution of planted haloxylon ammodendron in a duplex soil in an oasis:desert boundary area. *Ecol. Res.* 31, 673–681. doi:10.1007/s11284-016-1376-5

Zhou, H., Zhao, W. Z., and Zhang, G. F. (2017). Varying water utilization of Haloxylon ammodendron plantations in a desert-oasis ecotone. *Hydrol. Process.* 31 (4), 825–835. doi:10.1002/hyp.11060

Zhou, Y., Watts, S. E., Boutton, T. W., and Archer, S. R. (2019). Root density distribution and biomass allocation of co-occurring woody plants on contrasting soils in a subtropical savanna parkland. *Plant Soil* 438 (1–2), 263–279. doi:10.1007/s11104-019-04018-9

Zou, C. B., Barnes, P. W., Archer, S., and McMurtry, C. R. (2005). Soil moisture redistribution as a mechanism of facilitation in savanna tree-shrub clusters. *Oecologia* 145 (1), 32–40. doi:10.1007/s00442-005-0110-8

Conflict of Interest: The authors declare that the research was conducted in the absence of any commercial or financial relationships that could be construed as a potential conflict of interest.

frontiers in Earth Science

ORIGINAL RESEARCH
published: 11 March 2021
doi: 10.3389/feart.2021.629826

Soil Moisture Estimation and Its Influencing Factors Based on Temporal Stability on a Semiarid Sloped Forestland

Mingzhu Xu[1], *Guoce Xu*[1]*, *Yuting Cheng*[2]*, *Zhiqiang Min*[3], *Peng Li*[1], *Binhua Zhao*[1], *Peng Shi*[1] *and Lie Xiao*[1]

[1] *Key Laboratory of National Forestry Administration on Ecological Hydrology and Disaster Prevention in Arid Regions, Xi'an University of Technology, Xi'an, China,* [2] *College of Life Sciences, Yan'an University, Yan'an, China,* [3] *Northwest Surveying, Planning and Designing Institute of National Forestry and Grassland Administration, Xi'an, China*

Soil water content (SWC) plays a crucial role in the hydrological cycle and ecological restoration in arid and semi-arid areas. Studying the temporal stability of SWC spatial distribution is a requirement for the dynamic monitoring of SWC and the optimization of water resource management. The SWC in a *Pinus tabulaeformis* Carr. forest on the slope of the Loess Plateau of China were analyzed in five soil layers (0–100 cm with an interval of 20 cm) in the rainy and dry seasons from July 2014 to November 2017. The mean SWC was estimated and the main factors affecting the temporal stability of the SWC were further analyzed. Results showed that the SWC had strong temporal stability during the two seasons for several consecutive years. The temporal stability of SWC and the number of representative locations varied with season and depth. The elevation, soil total phosphorus (STP), clay, silt, or sand content of the representative locations approached the corresponding mean value of the study area. A single representative location accurately represented the mean SWC for the five depths in the rainy and dry seasons (RMSE <2%; rainy season: $0.81 < R^2 < 0.94$; dry season: $0.63 < R^2 < 0.83$; $p < 0.01$). The mean relative difference (MRD) and the relative difference standard deviation (SDRD) changed with the seasons and were significantly correlated with elevation, root density, and sand and silt content in two seasons ($p < 0.05$). Elevation, root density, and sand content were the main factors influencing the change of SWC temporal stability in different seasons. The results provide scientific guidance to monitor SWC by using a small number of locations and enrich our understanding of the factors affecting the temporal stability of SWC in the rainy and dry seasons of the Loess Plateau of China.

Keywords: soil water content, temporal stability, influencing factors, representative location, season, spatial distribution pattern, soil particle size

Edited by:
Ataollah Kavian,
Sari Agricultural Sciences and Natural Resources University, Iran

Reviewed by:
Abdolreza Bahremand,
Gorgan University of Agricultural Sciences and Natural Resources, Iran
María J. Polo,
University of Cordoba, Spain

***Correspondence:**
Guoce Xu
xuguoce_x@163.com
Yuting Cheng
chengyutingstar@163.com

Specialty section:
This article was submitted to Hydrosphere, a section of the journal Frontiers in Earth Science

Received: *16 November 2020*
Accepted: *20 January 2021*
Published: *11 March 2021*

Citation:
Xu M, Xu G, Cheng Y, Min Z, Li P, Zhao B, Shi P and Xiao L (2021) Soil Moisture Estimation and Its Influencing Factors Based on Temporal Stability on a Semiarid Sloped Forestland. Front. Earth Sci. 9:629826. doi: 10.3389/feart.2021.629826

INTRODUCTION

Soil water content (SWC) is an important or even dominant influencing factor for the hydrological cycle, and vegetation and ecological restoration in arid and semi-arid ecosystems. SWC is also the key carrier of material transport in soil and an important driving force for energy transport (Brocca et al., 2009; Heathman et al., 2012; Penna et al., 2013; Zhao et al., 2019; Cheng et al., 2021). However, It is very difficult to obtain SWC data on large areas quickly and accurately. Besides, owing to the influence of topography, rainfall, soil characteristics, vegetation, and human activities, SWC shows high variations at different spatial and temporal scales (Western and Blöschl, 1999; Gómez-Plaza et al., 2001; Zhao et al., 2010; Biswas and Cheng Si, 2011; Hu and Si, 2016), which also increases the difficulty in obtaining reliable SWC data. SWC also had a major influential role in the processes of rainfall infiltration, evaporation, solute transport, runoff and sediment yield, plant photosynthesis, and groundwater recharge (de Souza et al., 2011; Duan et al., 2016; Wang et al., 2019; Xiao et al., 2020). Therefore, it is very important to understand the dynamic characteristics of SWC for vegetation protection, ecological restoration, and water resources management in arid and semi-arid areas.

Although the SWC displays high variability in time and space. However, in 1985, Vachaud first discovered that the high and low rank order of SWC at sample locations presented relative stability phenomenon with time and defined the concept of SWC temporal stability for the first time. He defined "temporal stability" as "the time-invariant association between spatial location and classical statistical parameters of a given soil property". The method of SWC temporal stability is based on point-scale observations and considers that the SWC at certain locations can represent the mean SWC of a region over a period of time. The temporal stability concept at different spatial scales (e.g., slope, watershed, field, landscape-scale), different land-use types (e.g., rangeland, grass, pasture, agricultural land, shrub, forest), different terrain conditions (e.g., rolling, gentle sloping, complex terrains) and different climate zones (e.g., semi-arid, semi-humid, humid, semiarid) has been widely noticed and verified (Kachanoski and De Jong, 1988; Williams et al., 2009; Jacobs et al., 2010; Liu and Shao, 2014). At present, SWC temporal stability is widely used to interpolate missing SWC data and establish hydrological models (Pachepsky et al., 2005; Penna et al., 2013), and verify or correct remote sensing SWC data affected by resolution, vegetation, ground roughness, and topography (Mohanty and Skaggs, 2001; Jacobs et al., 2004; Vivoni et al., 2008; Wang et al., 2020). Besides, rapidly identifying the representative locations of SWC and use of these locations to directly or indirectly estimate the mean SWC is an important application of the concept of SWC temporal stability (Duan et al., 2017; He et al., 2019). The advantage of using the SWC representative location to obtain large-area SWC is that can reduce measurement costs and shorten the measurement cycle compared with traditional random multi-sample methods (Jacobs et al., 2004; Xu et al., 2017b). Direct or indirect estimation of the spatial mean SWC at different scales through the most temporally stable location or representative locations is very effective and feasible with accurate estimation results. (Grayson and Western, 1998; Guber et al., 2008; Hu and Si, 2014; Li et al., 2015; He et al., 2019). It is also able to accurately estimate the multi-year average SWC within the allowed error range (Schneider et al., 2008; Liu and Shao, 2014). Since 1999, the Chinese government has implemented a wide-ranging project of returning farmland to forests and grasslands to improve the ecological environment and reduce soil erosion of the Loess Plateau (Shi et al., 2020; Yu et al., 2020). However, soil water consumption increases with the increase of vegetation cover, which exacerbates the water shortage problem in the vegetation restoration process of the Loess Plateau (Liu and Shao, 2015), and causes the changes of SWC dependent on soil depth (Yaseef et al., 2010; Gao et al., 2011; Jian et al., 2015). Therefore, it is necessary to study the temporal stability patterns of SWC in different seasons over consecutive years to understand the dynamics of soil SWC and the effect of vegetation restoration on SWC changes in the Loess Plateau. No studies have yet focused on the temporal stability of SWC, and the factors affecting this temporal stability, in the dry and rainy seasons on the Loess Plateau for several consecutive years.

Many studies have been performed to determine the factors influencing SWC temporal stability, and many results have shown that SWC temporal stability depends on soil properties, topography, vegetation, climate, observation period, and scale of the study area (Vachaud et al., 1985; Gómez-Plaza et al., 2000; Heathman et al., 2009; Hu et al., 2009; Pan and Wang, 2009; Martinez et al., 2013; Liu et al., 2020; Xu et al., 2021). Soil texture and topography are considered to be some of the most dominant influencing factors. Vachaud et al. (1985) reported that the clay content contributes more to the temporal stability of SWC than other relevant factors, consistent with Mohanty and Skaggs (2001). However, Mohanty and Skaggs (2001) found that sandy soils exhibited stronger and more remarkable temporal stability contrasted with silty soils. Jacobs et al. (2004) studied various terrains of the Walnut Creek watershed in an Iowa depression (hilltop, steep slope, and mild slope), and pointed that the optimal time stable locations were those on a mild slope having moderate or above moderate clay content. Gao et al. (2011) also reported that those time-stable locations should have some identical or similar characteristics with locations of comparatively high clay content, comparatively mild slope, and comparatively planar surface for the 0–60 cm SWC in semi-arid jujube. This confirmed the results of Jacobs et al. (2004). Hu et al. (2009) study showed that land use did not affect the SWC spatial variability and temporal stability, but soil particle size and organic matter content were the main key factors of SWC temporal stability. Studies have confirmed that vegetation also has an important effect on the stability of SWC (Gómez-Plaza et al., 2001), the normalized difference vegetation index value in the most stable location was the moderate and above level (Jacobs et al., 2010). Jia et al. (2013) found that SWC shortage was mainly caused by vegetation restoration and depended on plant species, while vegetation cover and aboveground biomass were the main factors affecting SWC temporal stability. He et al. (2019) reported that vegetation characteristics such as leaf area index, soil bulk density, and canopy interception losses had an obvious effect on the temporal stability of high-elevation forests SWC. Besides, the temporal stability of SWC varied with the seasons and was stronger with the increase of vertical soil depth (Pachepsky et al., 2005; Guber et al., 2008; Xu et al., 2017a). Vanderlinden et al. (2012) found that a combination of topography, soil, vegetation, and climate have close interaction and comprehensive influence on SWC stability, rather than a

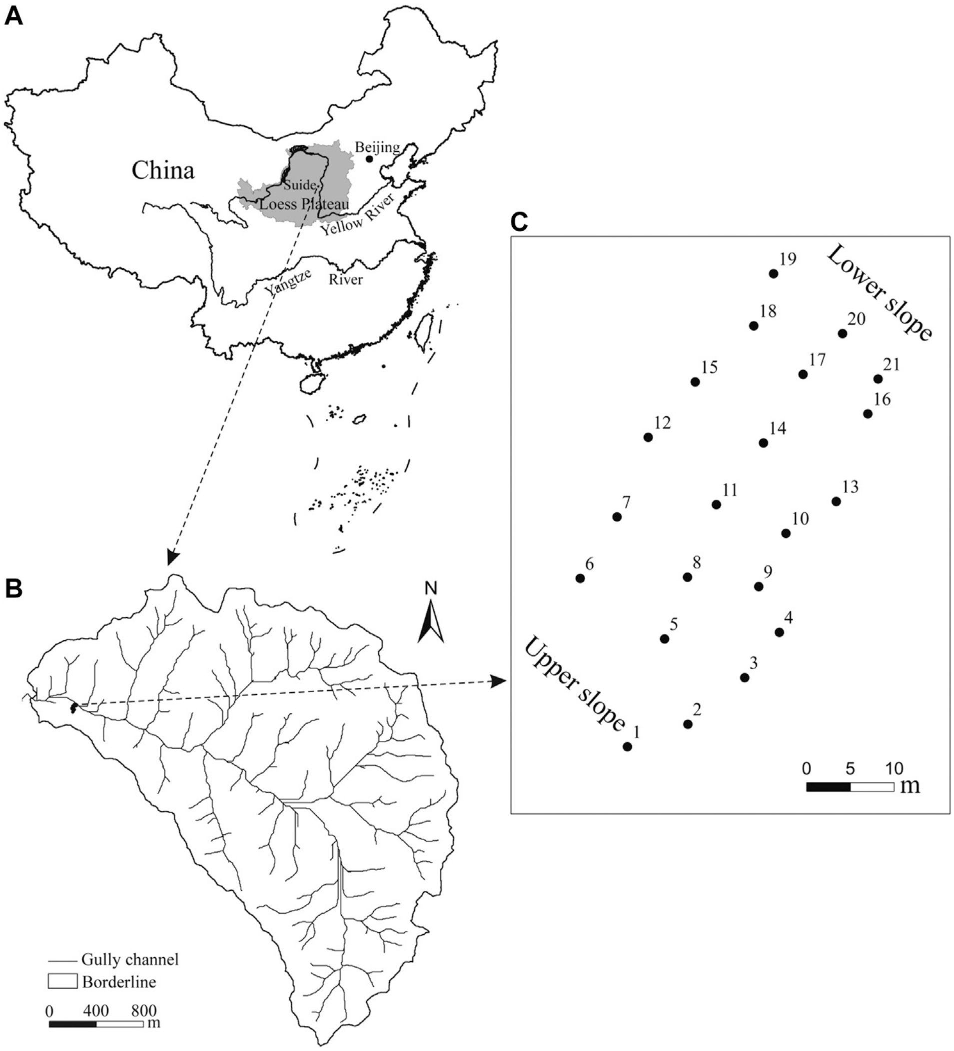

FIGURE 1 | The distribution of the 21 tube locations across the hillslope **(C)** located in the Wangmaogou watershed **(B)** on the Loess Plateau, China **(A)**.

single dominant factor. Therefore, it is difficult to reach a consensus on the factors that affect the temporal stability of SWC. Further understanding of the influence of these factors on the temporal stability of SWC would be helpful for the rapid and accurate identification of representative locations, the prediction and estimation of SWC at different scales, and the establishment of SWC models.

This study was based on the measured data of SWC from July 2014 to November 2017 in 21 monitoring locations on a slope afforested with *Pinus tabulaeformis* Carr. The objectives of this study were: 1) to evaluate the spatial distribution and temporal stability of SWC at different depths during the dry and rainy seasons for several consecutive years; 2) to estimate the mean SWC at different depths in two periods using a single representative location; and 3) to further identify the dominant factors that influence the temporal stability of SWC in different seasons.

MATERIALS AND METHODS

Study Area

The study was conducted in Wangmaogou watershed (110°20′26″–110°22′46″E, 37°34′13″–37°36′03″N). This 5.97 km^2 area is located in Suide county, Shaanxi province, China (**Figure 1**). The watershed belongs to the typical gully region of the Loess Plateau, a central area of hydraulic erosion. The area of the upland and gully region in the watershed is 2.97 km^2, accounting for 46.7% of the total watershed area. The elevation ranging is from 940 to 1200 m and the mean gradient is 28°. The region is dominated by a continental monsoon climate and has a mean temperature of 10.2°C. The annual mean evaporation and precipitation are 1,519 mm and 513 mm, respectively. Precipitation is unevenly distributed throughout the year, with more than 73.1% rainfall occurring between July and October. **Figure 2** shows the precipitation distribution in the

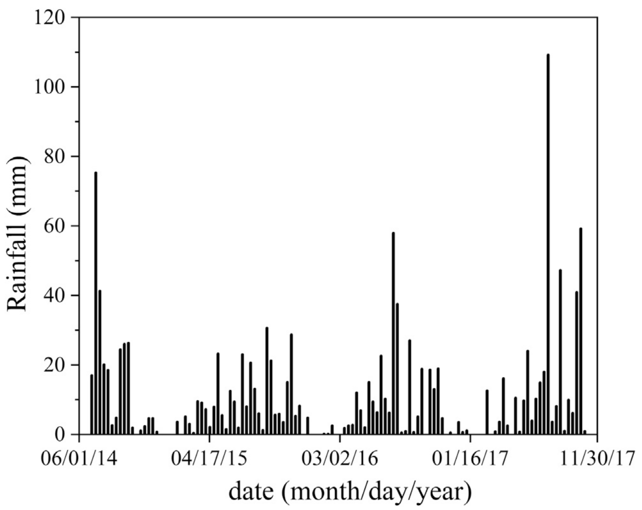

FIGURE 2 | Evolution of daily rainfall for the study area from 2014 to 2017.

study area from June 2014 to November 2017. The typical soil type in the study area is loessial soil and the bulk density of surface soil ranges from 1.1 to 1.3 g/cm^3. The soil in the watershed is made of over 60% fine sand and silt. The land use is dammed land (6.24%), forest land (9.5%), slope farmland (22.32%), terrace (25.78%), and grassland (36.51%). More information about the soil properties for the studied slope is shown in **Table 1**. *Pinus tabulaeformis* Carr. is one of the main tree species in the vegetation restoration process of Loess Plateau, so we chose typically sloped forestland covered by *Pinus tabulaeformis* Carr. to study. The selected slope is a slope and gully system with a small proportion of 1/5 of the whole slope, and the *Pinus tabulaeformis* Carr. is mainly distributed on the gully slope. The sample locations were placed in an approximate grid pattern along with the entire Pinus tabulaeformis Carr. forestland (**Figure 1C**). The mean plant spacing is 1.95 m and the stand age is 30 years.

Soil Sampling and Measurement

We chose 21 sampling locations on the hillslope, at elevations ranging from 964 to 997 m, and placed a 2 m long polycarbonate

TABLE 1 | Statistical characteristics of soil properties at different depths.

Properties	Depth (cm)	Min (%)	Max (%)	Mean (%)	SE (%)	SD (%)	CV (%)
SOC (g/kg)	H1	8.88	19.45	14.36	0.59	2.69	19
	H2	7.58	17.01	13.18	0.66	2.87	22
	H3	5.32	16.72	11.54	0.73	3.35	29
	H4	6.61	16.66	12.41	0.58	2.67	22
	H5	6.02	17.23	12.11	0.55	2.54	21
STN (g/kg)	H1	0.13	1.06	0.52	0.05	0.23	44
	H2	0.00	0.85	0.46	0.05	0.22	40
	H3	0.08	0.95	0.43	0.05	0.22	52
	H4	0.13	1.37	0.46	0.05	0.25	55
	H5	0.10	1.07	0.48	0.06	0.26	52
STP (g/kg)	H1	2.50	5.06	3.53	0.13	0.62	18
	H2	1.46	5.20	3.41	0.15	0.69	20
	H3	0.12	4.52	3.38	0.21	0.93	28
	H4	2.02	6.76	3.53	0.21	0.96	27
	H5	1.86	4.44	3.28	0.13	0.61	19
Clay (%)	H1	0.15	0.35	0.24	0.01	0.07	28
	H2	0.12	0.36	0.22	0.01	0.06	26
	H3	0.02	0.43	0.20	0.02	0.08	40
	H4	0.04	0.37	0.20	0.01	0.07	35
	H5	0.12	0.31	0.20	0.01	0.05	26
Silt (%)	H1	61.89	72.51	66.61	0.63	2.90	4
	H2	59.97	71.78	67.15	0.77	3.46	5
	H3	49.75	75.41	65.28	1.23	5.65	9
	H4	50.91	83.30	65.78	1.43	6.55	10
	H5	56.22	82.42	65.69	1.38	6.35	10
Sand (%)	H1	27.14	37.95	33.14	0.64	2.93	9
	H2	27.99	39.79	32.63	0.78	3.48	11
	H3	24.32	50.09	34.52	1.24	5.66	16
	H4	16.36	48.86	34.02	1.44	6.58	19
	H5	17.28	43.55	34.11	1.39	6.36	19
Root density (cm/cm^3)	H1	0.12	1.43	0.46	0.06	0.29	63
	H2	0.05	0.77	0.28	0.04	0.16	58
	H3	0.03	0.39	0.17	0.02	0.10	58
	H4	0.03	0.55	0.15	0.03	0.12	76
	H5	0.02	0.30	0.12	0.02	0.08	70

SOC, soil organic carbon; STP, soil total phosphorus; STN, soil total nitrogen; H1,0–20 cm;H2,20–40 cm;H3,40–60 cm;H4,60–80 cm;H5,80–100 cm.

TABLE 2 | Statistical characteristics of SWC at different soil depths during rainy and dry seasons.

Statistics	Rainy season					Dry season				
Depth (cm)	H1	H2	H3	H4	H5	H1	H2	H3	H4	H5
Mean (%)	9.69	13.13	14.49	13.21	12.11	6.60	10.2	11.63	10.9	10.53
Min (%)	0.30	0.46	1.10	5.81	6.60	0.27	0.34	0.33	6.45	6.27
Max (%)	26.1	28.78	28.26	28.93	28.97	21.07	23.34	27.02	27.02	25.34
SE (%)	0.18	0.21	0.19	0.17	0.15	0.15	0.20	0.16	0.14	0.13
CV (%)	51	44	35	34	33	50	42	30	28	26
SD (%)	4.92	5.76	5.02	4.53	4.04	3.27	4.25	3.43	3.06	2.70

SE, standard error; CV, coefficient of variation; SD, standard deviation. H1,0–20 cm;H2,20–40 cm;H3,40–60 cm;H4,60–80 cm;H5,80–100 cm.

(PC) tube with an inner diameter of 44 mm at those locations (**Figure 1C**). The mean horizontal distance between adjacent PC tubes was about 10 m. Soil samples with roots were gathered at each sampling location at 20 cm intervals, and each sample was taken back to the laboratory for testing and analysis of its soil organic carbon content (SOC), soil total phosphorus (STP), soil total nitrogen (STN), soil particle size and root density (**Table 1**). N/C3100 analyzer (Analytik Jena AG, Germany) was applied to measure SOC. Foss 8400 analyzer and Auto Discrete analyzer (ADA, CleverChem 200, Germany) were employed to analyze the content of STN and STP. The WinRHIZO 2013 image analyzer system (Regent Instruments Inc., Quebec, Canada) was employed to scan root samples that were previously rinsed to acquire root length and diameter. The Mastersizer 2000 particle size analyzer (Malvern Instruments, Malvern, United Kingdom) was applied to measure soil particle composition which was sorted according to clay (<0.002 mm), silt (0.002–0.05 mm), and sand (0.05–2.0 mm) by the percentage of the soil particle distribution.

Volumetric SWC (%, V/V) was obtained by a time domain reflectometry (TDR) system (TRIME-PICO IPH, Ettlingen, Germany) at each location at soil depths of 0–20, 20–40, 40–60, 60–80 and 80–100 cm. The mean values of 3 measurements were taken as the final SWC at each tube location and each depth. The SWC was generally recorded twice a month (at least once a month) for a total of 57 measurement events from July 2014 to November 2017. During the rainy season from June to November, 35 measurement events took place in total, and during the dry season from December to May of the following year, 22 measurement events took place in total. In all 21 sampling locations, SWC was recorded by TDR during the rainy season and the dry season. The five soil layers at a soil depth of 0–100 cm at 20 cm intervals were designated as H1, H2, H3, H4, and H5, respectively.

Method of Data Analysis

The following methods were used to analyze the SWC temporal stability and the representativeness of the estimation results at H1, H2, H3, H4, and H5 depths. The Spearman's rank correlation coefficient, *rs*, was used to reflect the temporal stability and consistency of SWC rank changes with time at different sampling locations. Furthermore, *rs* = 1 indicated that soil the spatial distribution of SWC had strong temporal stability in spatial distribution during different periods (Douaik et al., 2006). The relative difference method was originally proposed by Vachaud et al. (1985). The mean relative difference (MRD) and the relative difference standard deviation (SDRD) were adopted to describe the SWC temporal stability and find the representative locations. A location can be regarded as the SWC representative location when the MRD of the sampling location ranged from −0.05 to 0.05, and the corresponding SDRD was lower than the mean value for SDRD (Jacobs et al., 2004; Xu et al., 2015). The SWC at representative locations can predict or estimate the mean SWC in the study area. A *t*-test can be used to test whether there was a significant difference between the SWC of representative locations

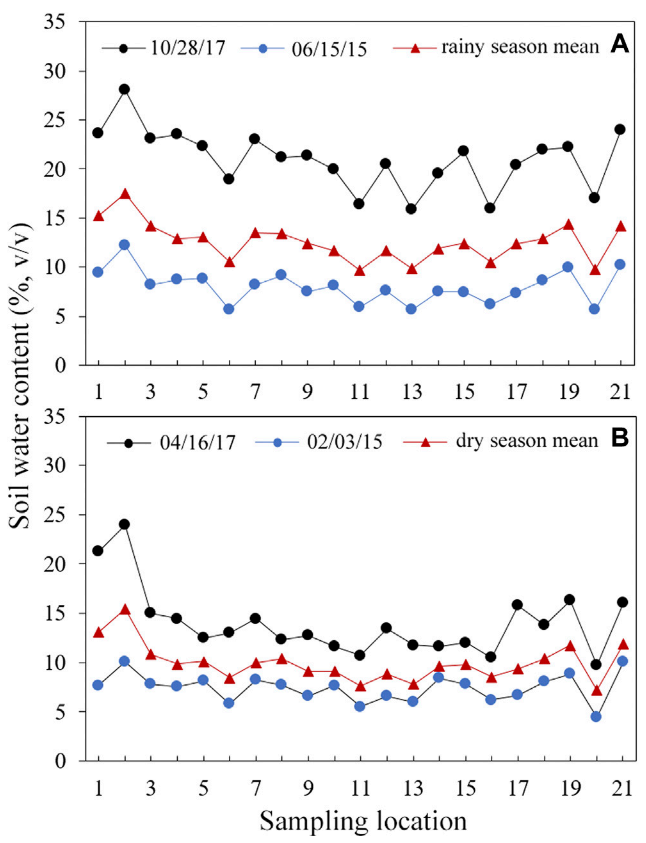

FIGURE 3 | Mean SWC Change of 21 locations in the rainy season **(A)** and dry season **(B)** on the driest and wettest dates in the depth of 100 cm.

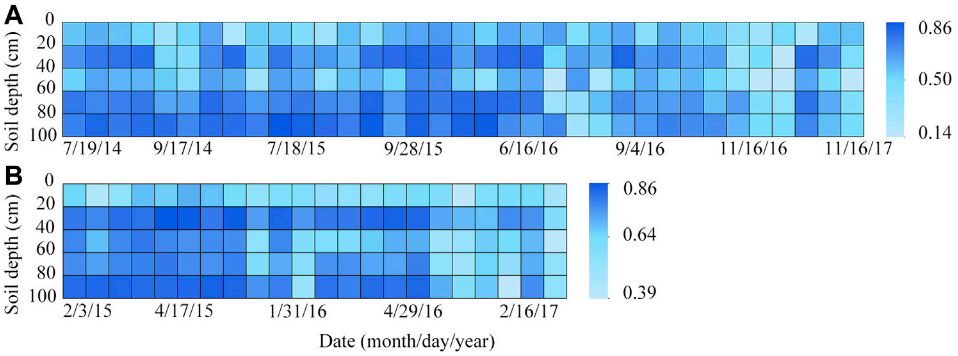

FIGURE 4 | Time series of mean Spearman rank correlation coefficients (r_s) at different depths in the **(A)** rainy season and **(B)** dry season.

and the mean SWC on the slope (Gao and Shao, 2012). The difference between the estimated and observed values was analyzed by the root mean square error (RMSE) and mean absolute error (MAE). The smaller RMSE and MAE, the smaller the difference between the SWC and the mean SWC at the representative location.

RESULTS

Statistical Characteristics of SWC

The statistical characteristics of SWC at different depths during the rainy and dry seasons are shown in **Table 2**. The mean SWC ranged between 9.69–14.49% in the rainy season and 6.60–11.63% in the dry season. The mean SWC at 0–20 cm in the two periods was the lowest, while the mean SWC at 40–60 cm was the highest, indicating that more water can be stored at 40–60 cm soil depth. Also, the SWC at each depth in the rainy season was higher than that at the corresponding depth in the dry season. SWC in five soil depths ranged between 0.30–28.97% and 0.27–27.02% in the rainy and dry seasons, respectively. The coefficient of variation (CV), standard deviation (SD), standard error (SE) for the rainy and dry seasons generally decreased with increasing soil depth. The CV in the rainy season and dry season ranged between 33–51% and 26–50% respectively, both of which belong to moderate variability (Nielsen and Bouma, 1985).

Temporal Stability of Spatial Distribution of SWC

The variation characteristics of mean SWC measured on the entire observation period during the rainy and dry seasons, and the driest and the wettest date at a depth of 0–100 cm in 21 locations are shown in **Figure 3**. The driest and wettest dates for the mean SWC at 0–100 cm depth during the rainy season occurred on Jun. 15, 2015 and Oct. 28, 2017 respectively (**Figure 3A**). In contrast, the driest and wettest dates for mean SWC at 0–100 cm depth during the dry season occurred on Feb. 3, 2015 and Apr. 16, 2017, respectively (**Figure 3B**). There was a significant difference between the wettest and driest dates of mean SWC in the rainy and dry seasons ($p = 0.000$). However, the spatial distribution of SWC on the entire observation period, the driest and wettest dates were strongly correlated ($p < 0.01$), and the spatial distribution pattern of SWC was almost unchanged.

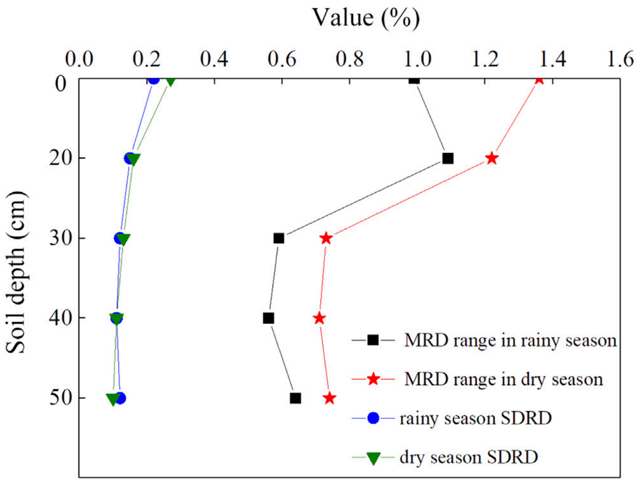

FIGURE 5 | Variation of mean MRD range and mean SDRD of different soil layers change with depth in the rainy season and dry season.

The Spearman's rank correlation coefficient, r_s, was used to later analyze the temporal stability of the spatial distribution of SWC. **Figure 4** shows the mean Spearman's rank correlation coefficient time series at different soil depths in two periods. During the rainy season, the rs values varied from 0.15 to 0.85 at different soil depths for each measurement date, and the lowest rs value occurred on August 24, 2017 (**Figure 4A**). The mean values of the correlation coefficients r_s from H1 to H5 were 0.65, 0.74, 0.63, 0.74, and 0.76, respectively. During the dry season, the rs value varied from 0.39 to 0.86 at different soil depths for each measurement date, and the lowest rs value was on December 1, 2016 (Figure 4B). The mean values of H1 to H5 correlation coefficients r_s in the dry season were 0.60, 0.78, 0.68, 0.70, and 0.75, respectively. The r_s values in the rainy season and the dry season were generally close to 1, indicating that there was strong temporal stability in the spatial pattern of SWC at each depth. The mean r_s at H2, H3, H4, H5 depth was

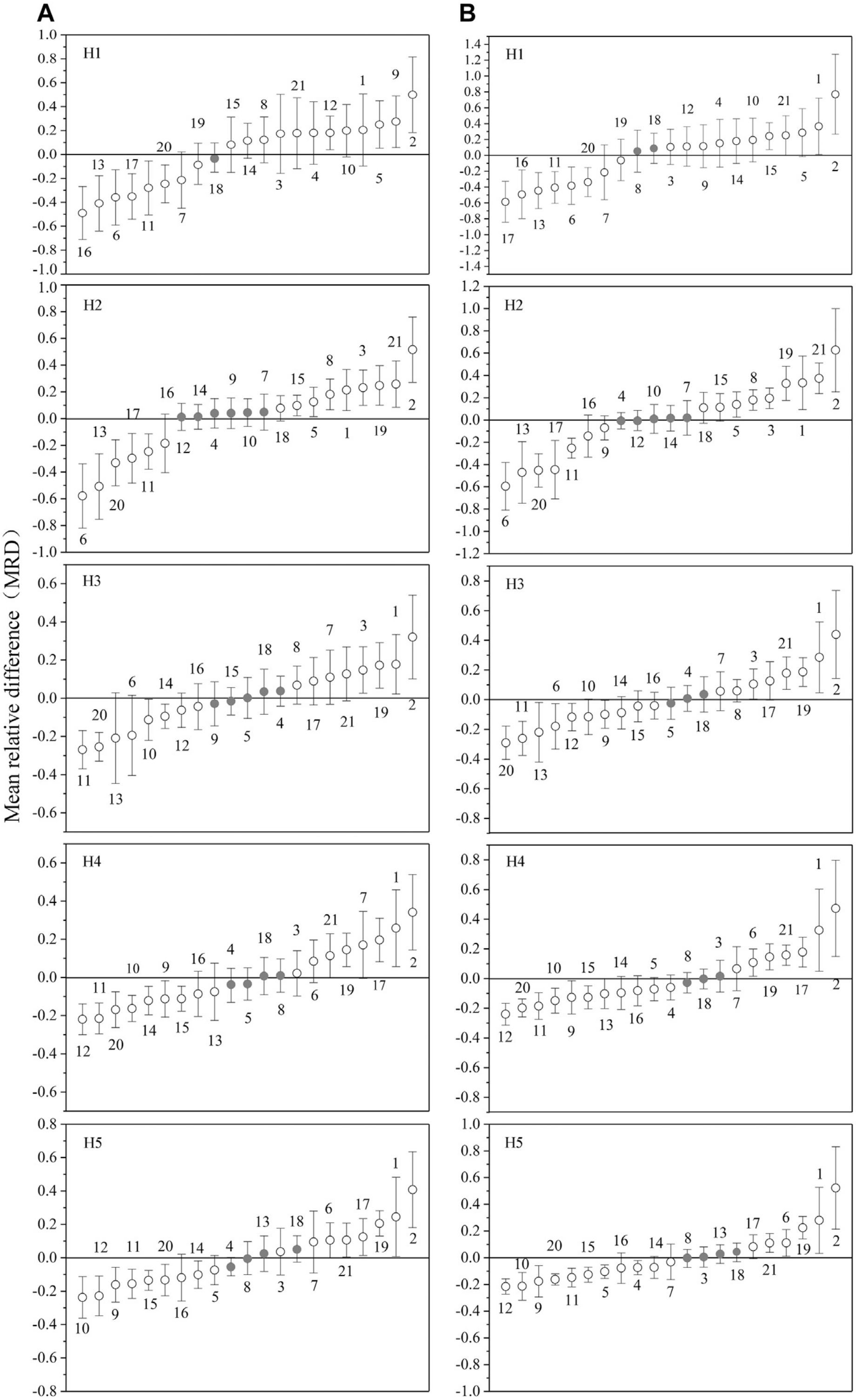

FIGURE 6 | The mean relative differences of each different soil depth in the rainy season **(A)** and dry season **(B)**. The error bar represents the standard deviation of the relative difference. The gray solid circle is the representative location of each soil layer.

higher in the dry season than in the rainy season (**Figure 5**), indicating that SWC temporal stability in the dry season was stronger compared with the rainy season at those depths. There was no significant difference between the average r_s values of different depths of soil layers in the rainy season and those of the corresponding soil layers in the dry season ($p > 0.05$). The r_s

TABLE 3 | The soil characteristics of the representative locations and the whole study area.

Location	Elevation (m)	SOC (g/kg)	STN (g/kg)	STP (g/kg)	Clay (%)	Silt (%)	Sand (%)	Root density (cm/cm^3)
1	997	13.54	4.58	3.38	0.24	68.52	31.24	0.10
2	995	14.62	4.71	3.63	0.21	70.76	29.03	0.13
3	986	15.43	7.53	3.36	0.17	67.47	32.36	0.10
4[a]	985	12.18	1.64	3.15	0.22	69.23	30.55	0.21
5[a]	989	13.33	6.10	4.19	0.17	68.49	31.34	0.22
6	989	13.85	5.07	3.65	0.12	67.58	32.30	0.29
7[a]	988	14.23	1.64	3.30	0.21	69.00	30.78	0.42
8[a]	988	13.94	4.87	3.36	0.23	69.14	30.63	0.23
9[a]	987	14.60	6.56	3.61	0.23	64.12	35.65	0.28
10[a]	984	13.38	5.44	2.60	0.21	64.99	34.80	0.29
11	985	13.28	6.71	3.94	0.17	66.06	33.77	0.23
12[a]	985	15.29	4.66	4.03	0.17	63.17	36.66	0.28
13[a]	984	11.16	5.30	3.54	0.22	67.54	32.24	0.17
14[a]	980	13.33	3.61	3.70	0.30	76.38	23.32	0.13
15	980	13.38	5.72	3.78	0.18	65.63	34.19	0.21
16	967	11.88	4.26	3.74	0.25	61.10	38.65	0.14
17	966	9.97	4.36	3.11	0.18	60.16	39.66	0.50
18[a]	967	9.47	4.30	2.98	0.20	62.47	37.33	0.27
19	965	10.90	4.50	2.99	0.21	61.36	38.43	0.26
20	964	9.76	3.57	2.30	0.23	55.91	43.85	0.24
21	964	8.91	4.40	3.41	0.33	67.91	31.76	0.26
Mean	981	12.69	4.74	3.42	0.21	66.05	33.74	0.24

[a] *Refers to the representative locations; SOC, soil organic carbon; STP, soil total phosphorus; STN, soil total nitrogen.*

values at soil depths from H2 to H5 in the rainy season and dry season were significantly higher than the r_s values at H1. The spatial patterns of SWC in the two periods were significantly correlated ($p < 0.05$), most showing an extremely significant correlation ($p < 0.01$), indicating that the spatial patterns of SWC at each depth had strong temporal stability.

Representative Locations at Different Soil Depths

Some locations which can represent or estimate the mean SWC value can be quantitatively obtained by the relative difference method. This method involves calculating the MRD and the SDRD under different soil depths, and plotting the relative difference diagram of different soil depths in two periods, as shown in **Figure 6**. The ranges between the maximum and minimum MRD values at H1, H2, H3, H4 and H5 in the rainy season and dry season were 0.99%, 1.09%, 0.59%, 0.56%, 0.64% and 1.36%, 1.22%, 0.73%, 0.71%, 0.74%, respectively. The ranges of MRD values at H3, H4, and H5 were smaller than that of the soil layers H1 and H2, indicating that the spatial variability of SWC was smaller and the temporal stability of SWC was stronger at the depth of 40–100 cm. The range of MRD values in the dry season was higher than in the rainy season. The Spearman's rank correlation coefficient of MRD in the rainy and dry seasons was close to 1, and the MRD rank in the two periods showed an extremely significant correlation ($p < 0.01$) which gradually increased with depth. Under the same soil depth, the number of representative locations was different in the rainy and dry seasons. The number of representative locations at different soil depths during the rainy and dry seasons was also not constant. These phenomena indicated that the distribution pattern of SWC on the forestland slope in different seasons had temporal stability. And the temporal stability of the spatial distribution of SWC increased with soil depth and varied with the season.

The locations with stronger SWC temporal stability should have smaller SDRD. The average SDRD values of H1, H2, H3, H4 and H5 in rainy and dry seasons were 0.22, 0.15, 0.13, 0.11, 0.12 and 0.27, 0.16, 0.13, 0.11, 0.10, respectively. The variations of mean MRD range and mean SDRD of different soil layers with depth in the rainy and dry seasons are shown in **Figure 5**. As a whole, the mean SDRD value decreased with soil depth. The mean SDRD value at H1 was the highest, indicating that the temporal stability of SWC at H1 was the lowest in both periods. Also, we found that representative locations had average elevation, TP, clay, silt, or sand compared with the corresponding study area average. The soil characteristics of the representative locations and the whole study area are compared in **Table 3**.

Estimation and Accuracy Analysis of Mean SWC on Forestland Slope by Representative Location

According to the location of temporal stability determined by MRD and SDRD, selecting a single location representing four or five layers can be used to estimate the mean SWC. Location 18 was determined to best represent the mean SWC at different depths during the two periods. In the two seasons at each soil depth, a portion of the measurement events was used to establish a linear regression line between the measured mean SWC and the estimated SWC by the representative location, while the remaining events were used to test the accuracy of

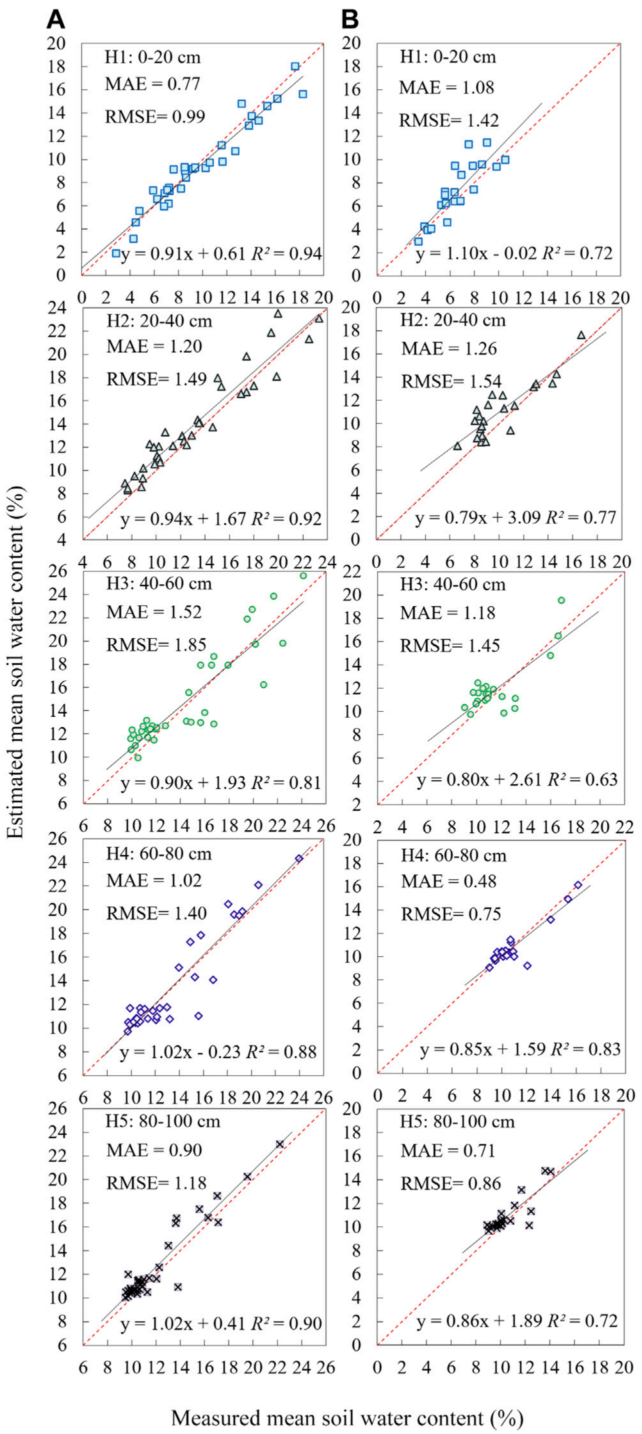

FIGURE 7 | Plot mean soil water content vs. SWC at representative locations for the 0–20, 20–40, 40–60, 60–80, and 80–100 cm soil layers (location 18 for the five soil layer) during the **(A)** rainy season and **(B)** dry season.

the estimation of the mean SWC on the slope by the representative location. **Figure 7** shows the linear regression line between the measured SWC and estimated SWC at the representative location during the two periods. The determination coefficient R^2 of the linear regression in the rainy and dry seasons ranges from 0.81 to 0.94 and 0.63 to 0.83 respectively, and all the linear regressions are significant at the level of $p < 0.01$. The accuracy of estimating the mean SWC on forestland slope by representative location points was further analyzed. For the rainy season, the RMSE value ranged from 0.62 to 1.81% and the MAE value ranged from 0.48 to 1.68%. For the dry season, the RMSE value ranged from 0.52 to 1.45% and the MAE value ranged from 0.42 to 1.08%. Cosh et al. (2008) considered that estimation is accurate when the RMSE between the estimated and measured values is less than 2%. The RMSE values in two periods at each depth were less than 2%. The lower the RMSE and MAE values in the two periods, the smaller the error between the predicted and the measured values, and the higher the confidence of estimating the average SWC. Therefore, we considered that a single representative location can be reliably used to estimate the mean SWC at different depths of the slope in the two periods, and the estimation accuracy was within the acceptable range.

Factors Affecting the Stability of SWC

The Pearson's correlation coefficients of the temporal stability parameters MRD, SDRD, and altitude, SOC, total N (TN), total P (TP), silt, sand, and clay and root density are shown in **Table 4**. From the relationship between MRD and soil properties mentioned above, MRD in rainy and dry seasons was significantly positively correlated with elevation and silt ($p < 0.05$), and negatively correlated with sand ($p < 0.05$). SDRD in the rainy and dry seasons was significantly positively correlated with elevation, SOC, and root density ($p < 0.05$). The factors affecting MRD and SDRD during the rainy season were fewer than those during the dry season. There was no significant correlation between TN, TP, clay content, and MRD and SDRD. The Pearson's correlation showed that soil particle size, root system, elevation, and SOC were the main factors affecting the spatial pattern and temporal stability of SWC in sloping forestland.

Redundancy analysis (RDA) was used to further analyze the relationship between SWC and soil properties. The SWC data matrix consisted of MRD and SDRD, and the soil properties data matrix was composed of elevation, root density, SOC, TN, and TP. The longest arrow lines of elevation, and sand and root density indicated that they had significant effects on soil properties in the RDA ordination chart of **Figure 8**. During the two periods, MRD was positively correlated with elevation and negatively correlated with root density and sand content. SDRD was positively correlated with elevation and root density, and negatively correlated with sand content.

DISCUSSION

Temporal Variability and Temporal Stability of SWC

The SWC at different depths on the slope of the forest area under study was lower than 15% due to relatively low precipitation and strong evapotranspiration in the rainy and dry seasons (Gao and Shao, 2012; Liu and Shao, 2015; Xu et al., 2017a). The SWC at

TABLE 4 | Pearson correlation between MRD, SDRD, and influencing factors in rainy and dry seasons.

	Period	Elevation (m)	SOC (g/kg)	STN (g/kg)	STP (g/kg)	Clay (%)	Silt (%)	Sand (%)	Root density (cm/cm³)
MRD	Rainy season	0.217[a]	0.091	0.036	0.010	0.121	0.254[b]	−0.255[b]	−0.178
	Dry season	0.226[a]	0.083	0.046	0.006	0.160	0.284[b]	−0.284[b]	−0.202[a]
SDRD	Rainy season	0.229[a]	0.239[a]	0.035	0.108	0.142	0.164	−0.165	0.306[b]
	Dry season	0.287[b]	0.290[b]	0.025	0.111	0.192	0.221[a]	−0.223[a]	0.392[b]

[a]*Correlation is significant at the 0.05 probability level.*

[b]*correlation is significant at the 0.01 probability level. SOC, soil organic carbon; STP, soil total phosphorus; STN, soil total nitrogen.*

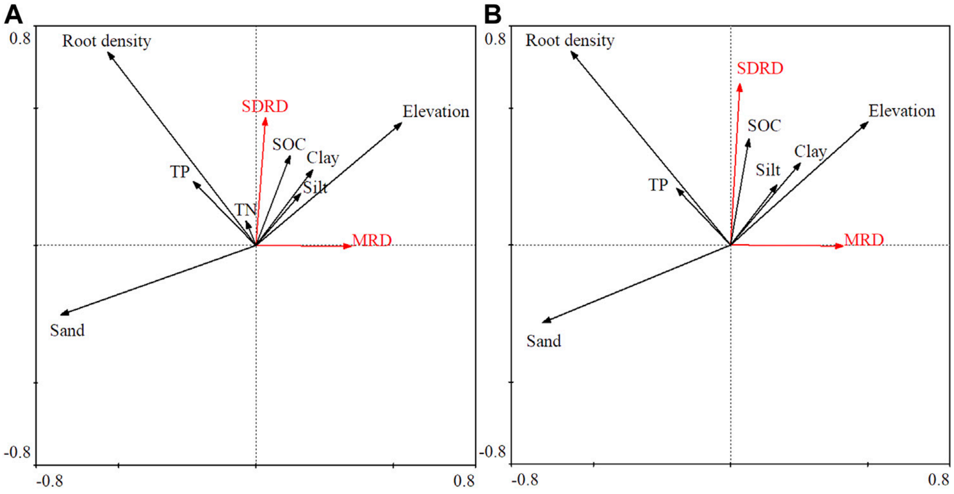

FIGURE 8 | Two dimensional ordination diagram of redundancy analysis of MRD and SDRD in **(A)** rainy season and **(B)** dry season.

40–60 cm depth was the highest, due to the lower distribution of high water consumption root organisms and relatively high precipitation replenishment at this depth (He et al., 2019). SWC in the rainy season was higher than that in the dry season, attributed to the different distributions of the root, rainfall recharge, and transpiration in different seasons. The spatial variability of deep SWC was low, consistent with other reports (Jia et al., 2013). Deep SWC was relatively weakly affected by rainfall events, evaporation, and climate ((Penna et al., 2009; Duan et al., 2017).

The spatial distribution patterns and Spearman's rank correlation coefficient of SWC in the rainy and dry seasons showed strong temporal stability in all the five soil layers, consistent with previous studies (Vachaud et al., 1985; Schneider et al., 2008; Brocca et al., 2009; Gao and Shao, 2012; Zhao et al., 2017). According to the change of mean Spearman's rank correlation coefficient, and MRD and SDRD calculated in the two periods, the temporal stability of SWC in deep soil depth were stronger than that in shallow soil depth. The main reasons for this phenomenon were that the effects of vegetation, topography, climate change and surface hydrological conditions on the temporal stability of SWC in deep layers decreased with the increase of soil depth (Hu et al., 2010b; Biswas and Cheng Si, 2011; Gao et al., 2011; Vanderlinden et al., 2012; Penna et al., 2013). At the same time, soil structure, strong heterogeneity of canopy interception, and the capacity of soil to retain water also reduced the temporal stability of shallow SWC (Korsunskaya et al., 1995; He et al., 2019).

However, the mean Spearman's rank correlation coefficient at 20–60 cm depth was higher in the dry season than in the rainy season, indicating that SWC temporal stability in the dry season was stronger than in the rainy season at this depth. This conclusion is inconsistent with the previous results in other regions. For example, Williams et al. (2009) and Penna et al. (2013) found that SWC has more temporal stability in the rainy season. The 21 sampling locations in our study area ranged between 964–997 m in elevation, and the relatively large topographic relief had a certain impact on the temporal stability of SWC in different seasons. Gao et al. (2011) found that the temporal stability of SWC at 20–60 cm depth was higher in dry seasons than in wet seasons due to the complex topography of the jujube forest on the loess plateau. Lin (2006) also reported that the temporal stability of SWC spatial patterns in complex terrain may vary between seasons.

Mean SWC at Representative Locations

The variation range of MRD values in rainy and dry seasons decreased with depth, due to the weak spatial variability of soil water in deep layers (**Table 2**). Other studies have found that the range of MRD values increases with soil depth (Gao and Shao, 2012; Jia et al., 2013; Li et al., 2015), related to the soil, terrain, vegetation characteristics, and the study area scale (Schneider et al., 2008; Brocca et al., 2009). Average SDRD values in rainy and dry seasons decreased with the soil depth, similarly to previous research results (Guber et al., 2008; Penna et al., 2013; Liu and Shao, 2014). The influence of climate, biological, and hydrological factors on deep soil were smaller than on shallow soil, resulting in the low SDRD value of deep soil. The main reason for the low SDRD value of deep soil was that the influence of climate, biological, and hydrological factors on deep soil decreased with depth (Vanderlinden et al., 2012; Gao et al., 2016), which increased the temporal stability of SWC in deep layers. As in other studies, the representative locations of temporal stability varied with the depth and the number was not constant (Hu et al., 2010a; Coppola et al., 2011; de Souza et al., 2011; Martinez et al., 2013; Liu and Shao, 2014).

We found that representative locations were those having average elevation, TP, clay, silt, sand content, or root density compared to the corresponding means on the sloped forestland. Some studies have also reported that time-stable locations present some significant characteristics, such as mean soil bulk density, leaf area index, slope, slope direction, elevation, or relatively low canopy interception loss compared to the corresponding field means (Vanderlinden et al., 2012; He et al., 2019). Many previous studies have shown that it is difficult to accurately estimate the average SWC of multiple soil depths using a single stable location (Vanderlinden et al., 2012; Li et al., 2015), and even that no single stable location can represent the mean SWC at different depths (Duan et al., 2017). This study found a single stable location could estimate the field mean SWC at different depths satisfactorily, confirming the results (Jia et al., 2013; Penna et al., 2013; He et al., 2019). More importantly, our results showed that SWC in different seasons can also be estimated by the same representative location. The R^2 in the rainy season was all larger than in the dry season, indicating that the estimation accuracy of representative locations was higher for the rainy season. Also, the low RMSE and MAE values of the two periods indicated that the estimation of mean SWC was accurate (Cosh et al., 2008).

Major Factors Influencing the Spatial and Temporal Changes of SWC

The Pearson's correlation coefficient carried out showed that the factors affecting MRD and SDRD varied with the season, and more factors affected SWC parameters in the dry season than in the rainy season. The differences in climate, temperature, vegetation, and rainfall between the dry and rainy seasons are the main reason for the different factors influencing MRD and SDRD in the two periods. The RDA ordination chart of the two periods in **Figure 8** indicates that elevation, root density, and sand content were the main factors influencing the temporal stability of SWC. The temporal stability of complex terrain is strongly affected by altitude (Cosh et al., 2008), and the distribution of root biomass leads to the dynamic of the required water height of vegetation (Zhao et al., 2010; He et al., 2019). The temporal stability of the SWC spatial pattern was related to soil, terrain, and vegetation (Gao and Shao, 2012).

The elevation, silt, and sand content had significant effects on MRD in the dry and rainy seasons. During the two periods, MRD was significantly negatively correlated with sand content ($p < 0.01$), and positively correlated with elevation and silt content. MRD in the dry season was also significantly affected by root density ($p < 0.05$), mainly because rainfall replenishment of soil water in the dry season was less than in the rainy season, leading to a significant influence of root water absorption on MRD. MRD was significantly influenced by soil particle size, in agreement with previous research (Vachaud et al., 1985; Penna et al., 2013; Chaney et al., 2015). However, the correlation between MRD and clay was not significant because soil texture was dominated by silt and sand in the study area, while clay content was less than 0.5%. Also, MRD was not significantly correlated with SOC, TP, and TN. Jia et al. (2013) also found that TP was not significantly correlated with MRD, but Zhao et al. (2010), Biswas and Cheng Si (2011) showed that MRD was significantly correlated with SOC. MRD was significantly associated with elevation, and many studies also reported that elevation had a slight or significant effect on SWC temporal stability (Hébrard et al., 2006; Zhao et al., 2010; Biswas and Cheng Si, 2011; Gao and Shao, 2012).

There have been few studies on the factors influencing SDRD in different seasons. In our study, in the two periods, SDRD was significantly positively correlated with elevation, SOC, and root density. Previous studies showed that elevation mainly affects the redistribution of SWC after rainfall (Vivoni et al., 2008), and indirectly affects evapotranspiration through solar radiation time and temperature (Xu et al., 2017a). Zhang et al. (2019) reported that soil particle size affects SOC content, so the effect of SOC content on SDRD was essentially still the effect of soil particle size on SWC temporal stability. Root water absorption has an important effect on SWC (Graefe et al., 2011). Soil particle size had a significant effect on SDRD in the dry season ($p < 0.05$), especially the content of clay and sand. A relatively high silt content and a low sand content result in a smaller SDRD, which is consistent with the result of RDA. However, SDRD was not significantly correlated with TN, TP, and clay content in two seasons.

CONCLUSION

Based on SWC data from 57 monitoring events in rainy and dry seasons, we studied the temporal stability and temporal spatial variability of SWC for several consecutive years in the Loess Plateau in China. SWC in this area showed moderate variability and presented strong temporal stability in dry and rainy seasons. The SWC temporal stability and representative location varied with the season and soil depth. The mean SWC at five depths in different seasons can be simultaneously predicted by a single representative location and allows accurate estimations. The factors influencing MRD and SDRD varied with the seasons. Moreover, elevation, root density, and sand content were the dominant factors affecting the temporal stability of SWC in two seasons.

More attention should be emphasized to the comprehensive effects of season, complex topography, and soil properties on SWC in arid and semi-arid areas. Our results provide support for the targeted management of water resources during the dry and rainy seasons and the restoration of reasonable vegetation in arid and semi-arid areas.

DATA AVAILABILITY STATEMENT

The raw data supporting the conclusions of this article will be made available by the authors, without undue reservation.

AUTHOR CONTRIBUTIONS

All authors contributed to the study conception and design. Material preparation, data collection and analysis were performed by MX, GX, YC, ZM, PL, BZ, PS, and LX. The first draft of the manuscript was written by MX and all authors commented on previous versions of the manuscript. All authors read and approved the final manuscript.

FUNDING

This research was supported by the National Key Research and Development Program (Grant No.: 2017YFC0504704), the National Natural Science Foundations of China (Grant No.: 52022081), the Innovative Talent Promotion Plan of Shaanxi Province (Grant No.: 2018TD-037), the Science and Technology Program of Yulin (Grant No.: 2019-144).

ACKNOWLEDGMENTS

We thank the reviewers for their useful comments and suggestions.

REFERENCES

Biswas, A., and Cheng Si, B. (2011). Scales and locations of time stability of soil water storage in a hummocky landscape. *J. Hydrol.* 408 (1-2), 100–112. doi:10.1016/j.jhydrol.2011.07.027

Brocca, L., Melone, F., Moramarco, T., and Morbidelli, R. (2009). Soil moisture temporal stability over experimental areas in Central Italy. *Geoderma* 148 (3-4), 364–374. doi:10.1016/j.geoderma.2008.11.004

Chaney, N. W., Roundy, J. K., Herrera-Estrada, J. E., and Wood, E. F. (2015). High-resolution modeling of the spatial heterogeneity of soil moisture: applications in network design. *Water Resour. Res.* 51 (1), 619–638. doi:10.1002/2013wr014964

Cheng, Y., Li, P., Xu, G., Wang, X., Li, Z., Cheng, S., et al. (2021). Effects of dynamic factors of erosion on soil nitrogen and phosphorus loss under freeze-thaw conditions. *Geoderma* 390, 114972. doi:10.1016/j.geoderma.2021.114972

Coppola, A., Comegna, A., Dragonetti, G., Lamaddalena, N., Kader, A. M., and Comegna, V. (2011). Average moisture saturation effects on temporal stability of soil water spatial distribution at field scale. *Soil Till. Res.* 114 (2), 155–164. doi:10.1016/j.still.2011.04.009

Cosh, M. H., Jackson, T. J., Moran, S., and Bindlish, R. (2008). Temporal persistence and stability of surface soil moisture in a semi-arid watershed. *Remote Sens. Environ.* 112 (2), 304–313. doi:10.1016/j.rse.2007.07.001

de Souza, E. R., Montenegro, A. A. d. A., Montenegro, S. M. G., and Matos, J. d. A. (2011). Temporal stability of soil moisture in irrigated carrot crops in Northeast Brazil. *Agric. Water Manag.* 99 (1), 26–32. doi:10.1016/j.agwat.2011.08.002

Douaik, A., Van Meirvenne, M., and Tóth, T. (2006). Temporal stability of spatial patterns of soil salinity determined from laboratory and field electrolytic conductivity. *Arid Land Res. Manag.* 20, 1–13. doi:10.1080/15324980500369392

Duan, L., Huang, M., and Zhang, L. (2016). Use of a state-space approach to predict soil water storage at the hillslope scale on the Loess Plateau, China. *Catena* 137, 563–571. doi:10.1016/j.catena.2015.11.003

Duan, L., Huang, M., Li, Z., Zhang, Z., and Zhang, L. (2017). Estimation of spatial mean soil water storage using temporal stability at the hillslope scale in black locust (Robinia pseudoacacia) stands. *Catena* 156, 51–61. doi:10.1016/j.catena.2017.03.023

Gao, L., Lv, Y., Wang, D., Muhammad, T., Biswas, A., and Peng, X. (2016). Soil water storage prediction at high space-time resolution along an agricultural hillslope. *Agric. Water Manag.* 165, 122–130. doi:10.1016/j.agwat.2015.11.012

Gao, L., and Shao, M. (2012). Temporal stability of shallow soil water content for three adjacent transects on a hillslope. *Agric. Water Manag.* 110, 41–54. doi:10.1016/j.agwat.2012.03.012

Gao, X., Wu, P., Zhao, X., Shi, Y., and Wang, J. (2011). Estimating spatial mean soil water contents of sloping jujube orchards using temporal stability. *Agric. Water Manag.* 102 (1), 66–73. doi:10.1016/j.agwat.2011.10.007

Gómez-Plaza, A., Alvarez-Rogel, J., Albaladejo, J., and Castillo, V. (2000). Spatial patterns and temporal stability of soil moisture across a range of scales in a semi-arid environment. *Hydrol. Process* 14 (7), 1261–1277. doi:10.1002/(SICI)1099-1085(200005)14

Gómez-Plaza, A., Martínez-Mena, M., Albaladejo, J., and Castillo, V. M. (2001). Factors regulating spatial distribution of soil water content in small semiarid catchments. *J. Hydrol.* 253 (1), 211–226. doi:10.1016/S0022-1694(01)00483-8

Graefe, S., Leuschner, C., Coners, H., and Hertel, D. (2011). Root functioning in tropical high-elevation forests: environmental vs. biological control of root water absorption. *Environ. Exp. Bot.* 71 (3), 329–336. doi:10.1016/j.envexpbot.2011.01.001

Grayson, R. B., and Western, A. W. (1998). Towards areal estimation of soil water content from point measurements: time and space stability of mean response. *J. Hydrol.* 207 (1-2), 68–82. doi:10.1016/s0022-1694(98)00096-1

Guber, A. K., Gish, T. J., Pachepsky, Y. A., van Genuchten, M. T., Daughtry, C. S. T., Nicholson, T. J., et al. (2008). Temporal stability in soil water content patterns across agricultural fields. *Catena* 73 (1), 125–133. doi:10.1016/j.catena.2007.09.010

He, Z. B., Zhao, M. M., Zhu, X., Du, J., Chen, L.-F., Lin, P. F., et al. (2019). Temporal stability of soil water storage in multiple soil layers in high-elevation forests. *J. Hydrol.* 569, 532–545. doi:10.1016/j.jhydrol.2018.12.024

Heathman, G. C., Cosh, M. H., Han, E., Jackson, T. J., McKee, L., and McAfee, S. (2012). Field scale spatiotemporal analysis of surface soil moisture for evaluating point-scale *in situ* networks. *Geoderma* 170, 195–205. doi:10.1016/j.geoderma.2011.11.004

Heathman, G. C., Larose, M., Cosh, M. H., and Bindlish, R. (2009). Surface and profile soil moisture spatio-temporal analysis during an excessive rainfall period in the Southern Great Plains, USA. *Catena* 78 (2), 159–169. doi:10.1016/j.catena.2009.04.002

Hébrard, O., Voltz, M., Andrieux, P., and Moussa, R. (2006). Spatio-temporal distribution of soil surface moisture in a heterogeneously farmed Mediterranean catchment. *J. Hydrol.* 329 (1), 110–121. doi:10.1016/j.jhydrol.2006.02.012

Hu, W., and Si, B. C. (2014). Can soil water measurements at a certain depth be used to estimate mean soil water content of a soil profile at a point or at a hillslope scale? *J. Hydrol.* 516, 67–75. doi:10.1016/j.jhydrol.2014.01.053

Hu, W., and Si, B. C. (2016). Estimating spatially distributed soil water content at small watershed scales based on decomposition of temporal anomaly and time stability analysis. *Hydrol. Earth Syst. Sci.* 20 (1), 571–587. doi:10.5194/hess-20-571-2016

Hu, W., Shao, M., Wang, Q., and Reichardt, K. (2009). Time stability of soil water storage measured by neutron probe and the effects of calibration procedures in a small watershed. *Catena* 79 (1), 72–82. doi:10.1016/j.catena.2009.05.012

Hu, W., Shao, M., Han, F., Reichardt, K., and Tan, J. (2010a). Watershed scale temporal stability of soil water content. *Geoderma* 158 (3-4), 181–198. doi:10.1016/j.geoderma.2010.04.030

Hu, W., Shao, M., and Reichardt, K. (2010b). Using a new criterion to identify sites for mean soil water storage evaluation. *Soil Sci. Soc. Am. J.* 74 (3), 762–773. doi:10.2136/sssaj2009.0235

Jacobs, J. M., Hsu, E.-C., and Choi, M. (2010). Time stability and variability of electronically scanned thinned array radiometer soil moisture during southern great plains hydrology experiments. *Hydrol. Process.* 24, 2807–2819. doi:10.1002/hyp.7703

Jacobs, J., Mohanty, B., Hsu, E.-C., and Miller, D. (2004). SMEX02: field scale variability, time stability and similarity of soil moisture. *Remote Sens. Environ.* 92, 436–446. doi:10.1016/j.rse.2004.02.017

Jia, X., Shao, M. a., Wei, X., and Wang, Y. (2013). Hillslope scale temporal stability of soil water storage in diverse soil layers. *J. Hydrol.* 498, 254–264. doi:10.1016/j.jhydrol.2013.05.042

Jian, S., Zhao, C., Fang, S., and Yu, K. (2015). Effects of different vegetation restoration on soil water storage and water balance in the Chinese Loess Plateau. *Agric. For. Meteorol.* 206, 85–96. doi:10.1016/j.agrformet.2015.03.009

Kachanoski, R. G., and De Jong, E. (1988). Scale dependence and the temporal persistence of spatial patterns of soil water storage. *Water Resour. Res.* 24 (1), 85–91. doi:10.1029/wr024i001p00085

Korsunskaya, L., Gummatov, N., and Pachepskiy, Y. A. (1995). Seasonal changes in root biomass, carbohydrate content, and structural characteristics of Gray Forest soil. *EurAsian Soil Sci.* 27 (9), 45–52.

Li, X., Shao, M., Jia, X., Wei, X., and He, L. (2015). Depth persistence of the spatial pattern of soil-water storage along a small transect in the Loess Plateau of China. *J. Hydrol.* 529, 685–695. doi:10.1016/j.jhydrol.2015.08.039

Lin, H. (2006). Temporal stability of soil moisture spatial pattern and subsurface preferential flow pathways in the shale hills catchment. *Vadose Zone J.* 5, 317–340. doi:10.2136/vzj2005.0058

Liu, B., and Shao, M. (2014). Estimation of soil water storage using temporal stability in four land uses over 10 years on the Loess Plateau, China. *J. Hydrol.* 517, 974–984. doi:10.1016/j.jhydrol.2014.06.003

Liu, B., and Shao, M. (2015). Modeling soil-water dynamics and soil-water carrying capacity for vegetation on the Loess Plateau, China. *Agric. Water Manag.* 159, 176–184. doi:10.1016/j.agwat.2015.06.019

Liu, Y., Li, P., Wang, T., Liu, Q., and Wang, W. (2020). Root respiration and belowground carbon allocation respond to drought stress in a perennial grass (Bothriochloa ischaemum). *Catena* 188, 104449. doi:10.1016/j.catena.2019.104449

Nielsen, D. R., and Bouma, J. (1985). *Soil spatial variability* Wageningen:. Pudoc, 2–30.

Martinez, G., Pachepsky, Y. A., Vereecken, H., Hardelauf, H., Herbst, M., and Vanderlinden, K. (2013). Modeling local control effects on the temporal stability of soil water content. *J. Hydrol.* 481, 106–118. doi:10.1016/j.jhydrol.2012.12.024

Mohanty, B. P., and Skaggs, T. H. (2001). Spatio-temporal evolution and time-stable characteristics of soil moisture within remote sensing footprints with varying soil, slope, and vegetation. *Adv. Water Resour.* 24 (9-10), 1051–1067. doi:10.1016/s0309-1708(01)00034-3

Pachepsky, Y. A., Guber, A. K., and Jacques, D. (2005). Temporal persistence in vertical distributions of soil moisture contents. *Soil Sci. Soc. Am. J.* 69, 347–352. doi:10.2136/sssaj2005.0347

Pan, Y.-X., and Wang, X.-P. (2009). Factors controlling the spatial variability of surface soil moisture within revegetated-stabilized desert ecosystems of the Tengger Desert, Northern China. *Hydrol. Process.* 23 (11), 1591–1601. doi:10.1002/hyp.7287

Penna, D., Borga, M., Norbiato, D., and Dalla Fontana, G. (2009). Hillslope scale soil moisture variability in a steep alpine terrain. *J. Hydrol.* 364 (3-4), 311–327. doi:10.1016/j.jhydrol.2008.11.009

Penna, D., Brocca, L., Borga, M., and Dalla Fontana, G. (2013). Soil moisture temporal stability at different depths on two alpine hillslopes during wet and dry periods. *J. Hydrol.* 477, 55–71. doi:10.1016/j.jhydrol.2012.10.052

Schneider, K., Huisman, J. A., Breuer, L., Zhao, Y., and Frede, H. G. (2008). Temporal stability of soil moisture in various semi-arid steppe ecosystems and its application in remote sensing. *J. Hydrol.* 359 (1), 16–29. doi:10.1016/j.jhydrol.2008.06.016

Shi, P., Feng, Z., Gao, H., Li, P., Zhang, X., Zhu, T., et al. (2020). Has “grain for green” threaten food security on the Loess Plateau of China? *Ecosyst. Health Sustainability* 6 (1), 1709560. doi:10.1080/20964129.2019.1709560

Vachaud, G., Passerat de Silans, A., Balabanis, P., and Vauclin, M. (1985). Temporal stability of spatially measured soil water probability density function. *Soil Sci. Soc. Am. J.* 49 (4), 822–828. doi:10.2136/sssaj1985.03615995004900040006x

Vanderlinden, K., Vereecken, H., Hardelauf, H., Herbst, M., Martinez, G., Cosh, M. H., et al. (2012). Temporal stability of soil water contents: a review of data and analyses. *Vadose Zone J.* 11 (4), 280–288. doi:10.2136/vzj2011.0178

Vivoni, E. R., Gebremichael, M., Watts, C. J., Bindlish, R., and Jackson, T. J. (2008). Comparison of ground-based and remotely-sensed surface soil moisture estimates over complex terrain during SMEX04. *Remote Sens. Environ.* 112 (2), 314–325. doi:10.1016/j.rse.2006.10.028

Wang, X., Fan, J., Xing, Y., Xu, G., Wang, H., Deng, J., et al. (2019). The effects of mulch and nitrogen fertilizer on the soil environment of crop plants. *Adv. Agron.* 153, 121–173. doi:10.1016/bs.agron.2018.08.003

Wang, B., Xu, G., Li, P., Li, Z., Zhang, Y., Cheng, Y., et al. (2020). Vegetation dynamics and their relationships with climatic factors in the Qinling Mountains of China. *Ecol. Indic.* 108, 105719. doi:10.1016/j.ecolind.2019.105719

Western, A. W., and Blöschl, G. (1999). On the spatial scaling of soil moisture. *J. Hydrol.* 217, 203–224. doi:10.1016/S0022-1694(98)00232-7

Williams, C. J., McNamara, J. P., and Chandler, D. G. (2009). Controls on the temporal and spatial variability of soil moisture in a mountainous landscape: the signature of snow and complex terrain. *Hydrol. Earth Syst. Sci.* 13 (7), 1325–1336. doi:10.5194/hess-13-1325-2009

Xiao, L., Liu, G., Li, P., Li, Q., and Xue, S. (2020). Ecoenzymatic stoichiometry and microbial nutrient limitation during secondary succession of natural grassland on the Loess Plateau, China. *Soil Till. Res.* 200, 104605. doi:10.1016/j.still.2020.104605

Xu, G., Lu, K., Li, Z., Li, P., Liu, H., Cheng, S., et al. (2015). Temporal stability and periodicity of groundwater electrical conductivity in luohuiqu irrigation district, China. *Clean Soil Air Water* 43 (7), 995–1001. doi:10.1002/clen.201400488

Xu, G., Li, Z., Li, P., Zhang, T., Chang, E., Wang, F., et al. (2017a). The spatial pattern and temporal stability of the soil water content of sloped forestland on the Loess Plateau, China. *Soil Sci. Soc. Am. J.* 81 (4), 902–914. doi:10.2136/sssaj2016.10.0331

Xu, G., Zhang, T., Li, Z., Li, P., Cheng, Y., and Cheng, S. (2017b). Temporal and spatial characteristics of soil water content in diverse soil layers on land terraces of the Loess Plateau, China. *Catena* 158, 20–29. doi:10.1016/j.catena.2017.06.015

Xu, G., Huang, M., Li, P., Li, Z., and Wang, Y. (2021). Effects of land use on spatial and temporal distribution of soil moisture within profiles. *Environ. Earth Sci.* 80 (4), 128. doi:10.1007/s12665-021-09464-2

Yaseef, N. R., Yakir, D., Rotenberg, E., Schiller, G., and Cohen, S. (2010). Ecohydrology of a semi-arid forest: partitioning among water balance components and its implications for predicted precipitation changes. *Ecohydrology* 3 (2), 143–154. doi:10.1002/eco.65

Yu, Y., Zhao, W., Martinez-Murillo, J. F., and Pereira, P. (2020). Loess Plateau: from degradation to restoration. *Sci. Total Environ.* 738, 140206. doi:10.1016/j.scitotenv.2020.140206

Zhang, Y., Li, P., Liu, X., Xiao, L., Shi, P., and Zhao, B. (2019). Effects of farmland conversion on the stoichiometry of carbon, nitrogen, and phosphorus in soil aggregates on the Loess Plateau of China. *Geoderma* 351, 188–196. doi:10.1016/j.geoderma.2019.05.037

Zhao, Y., Peth, S., Wang, X. Y., Lin, H., and Horn, R. (2010). Controls of surface soil moisture spatial patterns and their temporal stability in a semi-arid steppe. *Hydrol. Process.* 24, 2507–2519. doi:10.1002/hyp.7665

Zhao, W., Cui, Z., Zhang, J., and Jin, J. (2017). Temporal stability and variability of soil-water content in a gravel-mulched field in northwestern China. *J. Hydrol.* 552, 249–257. doi:10.1016/j.jhydrol.2017.06.031

Zhao, B., Li, Z., Li, P., Cheng, Y., and Gao, B. (2019). Effects of ecological construction on the transformation of different water types on Loess Plateau, China. *Ecol. Eng.* 144, 105642. doi:10.1016/j.ecoleng.2019.105642

Conflict of Interest: The authors declare that the research was conducted in the absence of any commercial or financial relationships that could be construed as a potential conflict of interest.

frontiers
in Earth Science

METHODS
published: 29 March 2021
doi: 10.3389/feart.2021.621780

Daily Runoff Forecasting Using Ensemble Empirical Mode Decomposition and Long Short-Term Memory

Ruifang Yuan[1], Siyu Cai[2], Weihong Liao[2]*, Xiaohui Lei[2], Yunhui Zhang[2], Zhaokai Yin[3], Gongbo Ding[4], Jia Wang[5] and Yi Xu[6]

[1]School of Water Resources and Environment, China University of Geosciences, Beijing, China, [2]State Key Laboratory of Simulation and Regulation of Water Cycle in River Basin, China Institute of Water Resources and Hydropower Research, Beijing, China, [3]China Three Gorges Corporation, Beijing, China, [4]College of Water Resource and Hydropower, Sichuan University, Chengdu, China, [5]School of Environmental Science and Technology, Tianjin University, Tianjin, China, [6]College of Civil Engineering and Architecture, Zhejiang University, Hangzhou, China

Edited by:
Ataollah Kavian,
Sari Agricultural Sciences and Natural Resources University, Iran

Reviewed by:
Pan Liu,
Wuhan University, China
Jun Niu,
China Agricultural University, China

***Correspondence:**
Weihong Liao
behellen@163.com

Specialty section:
This article was submitted to Hydrosphere,
a section of the journal
Frontiers in Earth Science

Received: *27 October 2020*
Accepted: *12 February 2021*
Published: *29 March 2021*

Citation:
Yuan R, Cai S, Liao W, Lei X, Zhang Y, Yin Z, Ding G, Wang J and Xu Y (2021) Daily Runoff Forecasting Using Ensemble Empirical Mode Decomposition and Long Short-Term Memory.
Front. Earth Sci. 9:621780.
doi: 10.3389/feart.2021.621780

Hydrological series data are non-stationary and nonlinear. However, certain data-driven forecasting methods assume that streamflow series are stable, which contradicts reality and causes the simulated value to deviate from the observed one. Ensemble empirical mode decomposition (EEMD) was employed in this study to decompose runoff series into several stationary components and a trend. The long short-term memory (LSTM) model was used to build the prediction model for each sub-series. The model input set contained the historical flow series of the simulation station, its upstream hydrological station, and the historical meteorological element series. The final input of the LSTM model was selected by the MI method. To verify the effect of EEMD, this study used the Radial Basis Function (RBF) model to predict the sub-series, which was decomposed by EEMD. In addition, to study the simulation characteristics of the EEMD-LSTM model for different months of runoff, the GM(group by month)-EEMD-LSTM was set up for comparison. The key difference between the GM-EEMD-LSTM model and the EEMD-LSTM model is that the GM model must divide the runoff sequence on a monthly basis, followed by decomposition with EEMD and prediction with the LSTM model. The prediction results of the sub-series obtained by the LSTM and RBF exhibited better statistical performance than those of the original series, especially for the EEMD-LSTM. The overall GM-EEMD-LSTM model performance in low-water months was superior to that of the EEMD-LSTM model, but the simulation effect in the flood season was slightly lower than that of the EEMD-LSTM model. The simulation results of both models are significantly improved compared to those of the LSTM model.

Keywords: ensemble empirical mode decomposition, long short-term memory, three gorges reservoir, runoff forecasting, streamflow series, hydrological model

INTRODUCTION

The Three Gorges Reservoir is located in the upper reaches of the Yangtze River. The Three Gorges Project is the largest water conservancy project in the world. It plays an important role in the governance and development of the Yangtze River and has comprehensive benefits such as flood control, hydropower generation, and increased water supply (News and Focus, 2015). Forecasting Three Gorges River inflows is critical for dispatching cascaded hydropower stations for optimal production and operation. Accurate hydrological forecasts are not beneficial for deciding the optimal dispatch time and reservoir station locations, but they are conducive to the development and adjustment of station power generation plans (Cheng et al., 2015). Two primary types of runoff prediction methods have been developed: physical analysis models and data-driven methods. Physical models are based on the hydrological dynamic process, and they are closely integrated with the spatio-temporal precipitation distribution, meteorological conditions, and underlying surface conditions (Lee et al., 2020). Zhu et al. (2019) proposed a method to improve runoff simulation by fusing multi-source precipitation products. Patil and Ramsankaran (2017) improved the flow simulation and prediction performance of the Soil and Water Assessment Tool (SWAT) by assimilating remotely sensed soil moisture observations. Due to the high data requirements of physical analysis models and the complexity of runoff generation and flow concentration processes, it is difficult to establish precise hydrological models, which restricts the application of physical models. Therefore, scholars have utilized data-driven methods to solve these problems (Abbaspour et al., 2015; Wang et al., 2018).

Data-driven methods rely on historical observation data to predict data characteristics and the relationship between model inputs and outputs. Data-driven methods have been widely used and have achieved excellent results (Kan et al., 2016). Wu et al. (2005) developed an artificial neural network (ANN) model and successfully applied it to short-term flow forecasting. Nanda et al. (2016) used a linear autoregressive moving average model to forecast floods with a forecast period of 1 d–3 days Ahmadi et al., 2019 used ANN models on a daily, monthly, and annual basis in the Kan watershed, which is located in western Tehran, Iran. Certain data-driven forecasting methods, such as the ANN, adaptive-network-based fuzzy inference system, and support vector machine methods assume that streamflow series are stable, which contradicts reality and causes the simulated value to deviate from the observed one (Adamowski et al., 2014).

In order to solve the instability problem of the runoff series and improve the simulation accuracy of model, many studies employed ensemble empirical mode decomposition (EEMD) to process the runoff series and decompose the non-stationary original series into a trend with several stable sub-series. This method has been widely used in combination with data-driven methods in recent years. Tan et al. (2018) used an EEMD-ANN model to forecast the monthly runoff at three stations in Ertan, Cuntan, and Yichang. Wang et al. (2020) used ANN and SVR to regress a monthly flow series decomposed by EEMD according to the climate index.

The EEMD is an optimized version of empirical mode decomposition (EMD) method. Huang et al. (1998) proposed the EMD method in 1998. The EMD method innovatively introduces “intrinsic mode functions” based on the local characteristics of the signal, which makes the instantaneous frequency meaningful. This makes it suitable for nonlinear and linear stationary processes. The final results of EMD decomposition are reflected in an energy-frequency-time distribution (Huang et al., 1998). Zhao et al. (2017) used the EMD method to decompose annual runoff; they effectively improved the simulation accuracy of the Chaotic Least Squares Support Vector Machine model. Based on EMD, the EEMD method improves the phenomenon of EMD modal aliasing by adding white noise. It can add white noise without any basic function, so that signals with different scales can be clearly sorted in the appropriate intrinsic mode function (IMF) (Huang and Wu, 2008). Wang et al. (2015) used the EEMD method to decompose an annual runoff sequence, and constructed an EEMD-ANN model. Their results showed that the EEMD method effectively improved the simulation performance of their ANN. Yu et al. (2018) combined the EEMD method with a radial basis function (RBF) neural network and an autoregression (AR) model to forecast annual runoff, effectively improving the simulation accuracies of the two models.

Combining EEMD and data-driven methods for data series prediction has been extensively studied in various fields, but few studies combine the EEMD and long short-term memory (LSTM) methods or use these combined methods to perform runoff predictions. Zhang et al. (2018) used the EEMD-LSTM method to predict the daily surface temperature, comparing it with the EMD-LSTM and EEMD-RNN methods and demonstrating that the EEMD-LSTM model is the most suitable tool for temperature prediction. An et al. (2020) used singular spectrum analysis (SSA) and EEMD to extract the frequency and trend features of Niangziguan spring discharge, and then they used LSTM to simulate each frequency and trend sub-sequence. The results demonstrate that the SSA-LSTM and EEMD-LSTM performances are superior to that of LSTM, and the EEMD-LSTM model achieved the optimal prediction performance. Therefore, this study utilizes LSTM to determine whether runoff data processed by EEMD can improve the prediction performance of the LSTM model for runoff data. In addition, this study utilized the mutual information method which is suitable for handling the nonlinear relationship between hydrological series to select the input variables.

The remainder of this paper is organized as follows. *Materials and Method* contains the methods used in the research and relevant information about the study area, model inputs, parameter settings, and verification strategy. *Results and Discussion* describes the calculation results and analysis of each step, and *Conclusion* contains the research conclusions.

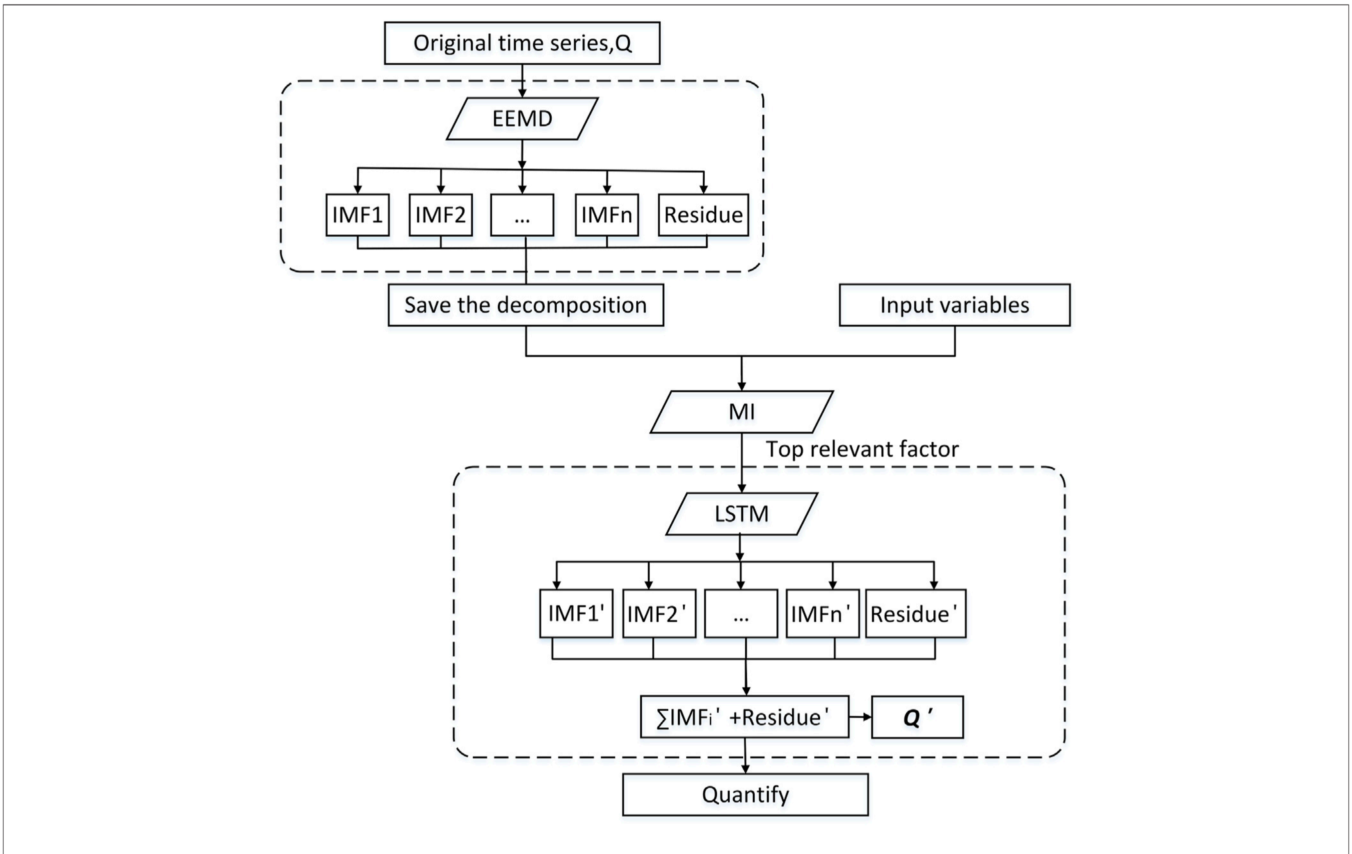

FIGURE 1 | Research flowchart.

MATERIALS AND METHODS

The main purpose of this research is to study whether the data processed by EEMD can improve the simulation performance of the LSTM model for runoff data. Therefore, the main structure of the model is decomposition-analysis-simulation, as shown in **Figure 1**.

EEMD

EEMD optimizes EMD, improving the mode mixing phenomenon of EMD by adding white noise. The EEMD method adds the appropriate amount of white noise to the original sequence and then divides the original sequence into a trend and *n* finite intrinsic mode functions (IMFs) (Huang and Wu, 2008; Wang et al., 2020). The specific EEMD steps are as follows:

- Step 1: Input the data to be decomposed as the original signal *x*(*t*) and set the EEMD parameters, including the noise standard deviation (*Nstd*), number of realizations (*NR*), and maximum number of sifting iterations allowed (*MaxIter*).
- Step 2: Add white noise (*wi*(*t*)) to the original sequence to form the following new sequence:

$$x_i(t) = x(t) + w_i(t) \tag{1}$$

- Step 3: Using the following formula, EMD divides the new sequence obtained in Step 2 into *n* finite IMFs and a trend item.

$$x_i(t) = \sum_{j=1}^{n} c_{ij}(t) + r_i(t) \tag{2}$$

- Step 4: Repeat Steps 2 and 3 until the maximum *NR* is achieved for *i*.
- Step 5: IMFs are calculated using **Eq. 3**, and the final result is obtained using **Eq. 4**.

$$c_j(t) = \sum_{i=1}^{NR} cij(t) \Big/ NR \tag{3}$$

$$x(t) = \sum_{j=1}^{n} c_j(t) + r(t) \tag{4}$$

where *cj(t)* represents the *j*th IMF, and *r(t)* is the trend item.

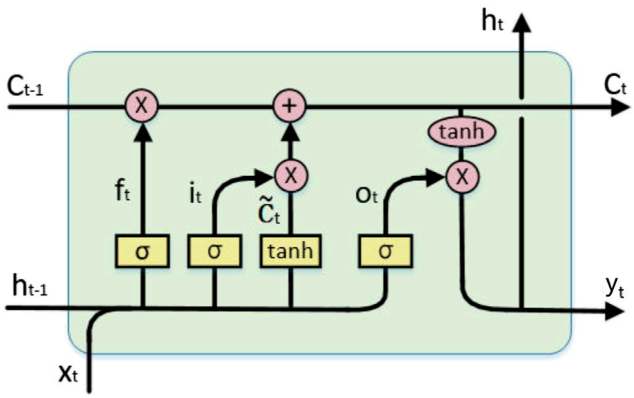

FIGURE 2 | Diagram of LSTM memory cell structure. (Yin et al., 2019)

Mutual Information

The mutual information method describes the degree of correlation between two random variables, and it can reflect both the non-linear and linear correlations. If variables x and y are related, and x is known, the uncertainty of y can be reduced according to the degree of mutual information between x and y. If variables x and y are independent of each other, the joint density is equal to the product of their edge distribution density (Sharma, 2000; Zhao and Yang, 2011; Ding et al., 2019), which can be expressed as follows:

$$P_{x,y}(x,y) = P_x(x)P_y(y) \tag{5}$$

When variables x and y have N observations and are discrete random variables, the mutual information between the variables can be expressed as follows:

$$MI = \frac{1}{N}\sum_{i=1}^{N} Ln\left[\frac{P_{x,y}(x_i,y_i)}{P_x(x_i)P_y(y_i)}\right] \tag{6}$$

When the variables x and y are continuous random variables, the mutual information equation between the variables is

$$MI = \iint \mu(x,y) Lg \frac{\mu(x,y)}{\mu_x(x)\mu_y(y)} dxdy \tag{7}$$

where $\mu(x,y)$ represents the joint distribution density of continuous random variables x and y; and $\mu_x(x)$ and $\mu_y(y)$ represent the marginal distribution densities of continuous random variables x and y, respectively.

When the random variables x and y are independent of each other, $Ln\left[\frac{P_{x,y}(x_i,y_i)}{P_x(x_i)P_y(y_i)}\right] = 0$, and $Lg\frac{\mu(x,y)}{\mu_x(x)\mu_y(y)} = 0$, then MI = 0. When x and y are not independent of each other, MI approaches positive infinity.

Long Short-Term Memory

LSTM is an improved recurrent neural network (RNN) that resolves the problem of gradient disappearance during an RNN simulation. LSTM replaces the cell unit in the RNN with a memory unit, which effectively improves the long-term memory ability of the neural network (Kratzert et al., 2018). LSTM is connected in a time sequence. At time t, the input of the memory unit includes the hidden layer state variable h_{t-1} at time t_1 and the state variable C_{t-1} of the memory unit and input information x_t at time t. Additionally, the forget gate f_t, input gate i_t, and output gate o_t are coordinately controlled. Finally, the calculation result y_t of the LSTM at time t is obtained, and it is passed into the calculation at time $t+1$ together with C_t (Yin et al., 2019). The LSTM memory unit structure is displayed in **Figure 2**.

The specific calculation process of LSTM is as follows:

- Step 1: Forget gate (ft) calculation. f_t determines the amount of information discarded, and the calculation is as follows:

$$f_t = \sigma\left(U_f x_t + W_f h_{t-1} + b_f\right) \tag{8}$$

where U_f, W_f, and b_f are adjustable parameter matrices or vectors of the forgetting gate that can be optimized during neural network training, and σ is the sigmoid activation function.

- Step 2: Input gate (i_t) calculation. i_t determines the amount of information used to update the state.

$$i_t = \sigma(U_i x_t + W_i h_{t-1} + b_i) \tag{9}$$

where U_i, W_i, and b_i are the adjustable parameter matrices or vectors of the input gate that can be optimized during the neural network training process. The calculation formula for the newly acquired information $\tilde{C}_t$ is as follows:

$$\tilde{C}_t = \tanh(U_{\tilde{C}} x_t + W_{\tilde{C}} h_{t-1} + b_{\tilde{C}}) \tag{10}$$

where $U_{\tilde{C}}$, $W_{\tilde{C}}$, and $b_{\tilde{C}}$ are the adjustable parameter matrices or vectors of $\tilde{C}_t$ that can be optimized during neural network training, and *tanh* is the hyperbolic tangent activation function.

- Step 3: Neuron state update. The neuron state update is calculated as follows:

$$C_t = f_t * C_{t-1} + i_t * \tilde{C}_t \tag{11}$$

where $*$ represents the product of the matrix elements. Because C_t interacts linearly with other LSTM units, the information can be kept unchanged for a longer period.

- Step 4: Output gate (o_t) calculation. o_t can generate the hidden layer state variable h_t at time t, and the corresponding formulas are as follows:

$$o_t = \sigma(U_o x_t + W_o h_{t-1} + b_o) \tag{12}$$

$$h_t = o_t * \tanh(C_t) \tag{13}$$

where U_o, W_o, and b_o are adjustable parameter matrices or vectors of the output gate that can be optimized during neural network training.

- Step 5: Output (y_t) calculation. The y_t calculation formula is as follows:

$$y_t = W_d h_t + b_d \tag{14}$$

where W_d and b_d are the adjustable parameter matrices or vectors of the output layer that can be optimized during neural network training.

EEMD-LSTM

The EEMD method has been demonstrated to effectively improve the prediction ability of ANN, SVR, and other methods for processing non-stationary series. To study the effect of EEMD on the LSTM model, an EEMD-LSTM model was established. EEMD is used to process the non-linear and non-stationary runoff series into several stable sub-series, and the LSTM model is used to build the prediction model for each sub-series.

The EEMD-LSTM model is based on a decomposition-analysis-prediction framework, and it includes three stages: 1) decompose the original runoff series into IMF and residue; 2) use the mutual information method to select the predictor with the largest amount of mutual information within each sub-series; and 3) use the LSTM model to predict each sub-sequence and obtain the sum to calculate the prediction result of the original series.

Radial Basis Function and EEMD-RBF

The Radial Basis Function Neural Network (RBF) is a forward type network based on the radial basis function, which can approximate any finite function with arbitrary precision (Tayyab et al., 2018; She and You, 2019). Compared with other neural networks, RBF has the advantages of fast convergence, it does not easily fall into local minima, good robustness and easy implementation, and has been widely used in the field of nonlinear time series forecasting (Meshram et al., 2020).

The EEMD-RBF model uses EEMD to decompose the original data series, and then uses the RBF model to predict the sub-series. We then superimposed the RBF prediction results for each sub-series to obtain the EEMD-RBF prediction results for the original series.

GM-EEMD-LSTM

To study the simulation characteristics of the LSTM model for various month series, the GM-EEMD-LSTM model (The GM-EEMD-LSTM model is a model in which data is grouped monthly and then decomposed and predicted) was set as the control. This study uses data from 2005 to 2017 for research, dividing the data from 2005 to 2014 into the training set and the data from 2015 to 2017 into the validation set. The GM-EEMD-LSTM model first separates the original runoff series by month and arranges the sub-series chronologically to obtain a 12-month series. Then, it sorts the input variables of each monthly series. The 12-month series are then separately processed using EEMD. Each monthly series is divided into eight or nine sub-series. The predictor with the largest mutual information within each sub-series is selected as the input of the LSTM model. The simulation results of each sub-series are superimposed to obtain the simulation results of the monthly sequence and are arranged chronologically to obtain the simulation results from 2015 to 2017.

Case Study

Study Area

The Three Gorges Reservoir is a national strategic freshwater resource and an important ecological barrier in the upper reaches of the Yangtze River (Cheng et al., 2015). The reservoir was impounded for the first time in 2003, and the water level in front of the dam was 135 m. In 2006, the impoundment water level reached 156 m. In 2008, a 175-m experimental impoundment was commenced (Tian et al., 2020). The inflow flow forecast of the Three Gorges Reservoir is vital for optimizing scheduling to make correct decisions regarding production and operation. Accurate hydrological forecasts not only provide the basis for optimal decision-making regarding reservoir dispatching times but are also critical to power station formulations and power generation plan adjustments (Cheng et al., 2015).

This study used daily inflow data from 2005 to 2017 to forecast the inflows of the Three Gorges Reservoir. The reservoir is located in the middle reaches of the Yangtze River Basin. The research area and station distribution, as shown in **Figure 3**. It controls a drainage area of 1 million km^2 and has an average annual runoff of 451 billion m^3 (Zhou et al., 2019). The monsoon characteristics of the Yangtze River Basin indicate that the region is greatly affected by extreme weather events. Over the past few decades, especially since the 1990s, the climate has warmed and the frequency of flood disasters in the Yangtze River Basin has increased. Future climate changes may further aggravate this phenomenon (Zhao et al., 2020). Extremely severe flood, ice, and snow disasters and drought events are also on the rise (Yu et al., 2020). Human activities and climate change have altered the underlying surface conditions of the Yangtze River Basin, leading to more complex runoff changes (Jiang et al., 2008).

Model Inputs and Parameter Settings

When forecasting the daily inflows of the Three Gorges Reservoir, daily flows (inflows) measured for 1–7 days for the Three Gorges Reservoir and its upstream stations in Cuntan and Wanxian were selected as the predictors. Because runoff is a comprehensive result of meteorological and hydrological processes, the arithmetic average method was used to obtain the arithmetic average of the meteorological elements of the meteorological stations upstream of the Three Gorges Reservoir, and the meteorological elements from the previous 7 days to the forecast day were used as the model forecast factors. The meteorological elements considered by the model included rainfall, relative humidity, light, daily average temperature, and wind speed; thus, there were 5 + 8 × 7 forecast factors in the forecast factor set. LSTM uses a month of previous data as the input for each simulation. Both the inflow and predictor data series of the Three Gorges Reservoir use daily data from 2004 to 2017. The data from 2004 were used as preliminary predictors, and the data from 2005 to 2017 were used for model training and testing. The 2014 data were used as the training set, and the

2015–2017 data were used as the test set. The data were obtained from the Information Center of the Ministry of Water Resources.

In the EEMD model, the white noise amplitude was set to 0.2 times the standard deviation of the sample data, *NR* was set to 100, and the maximum number of filtering iterations was set to 500. Each decomposed sub-sequence must establish a unique LSTM model; thus, $\sum_{i=1}^{12} mi + M$ models must be established, where m_i is the number of series in the *ith* month, and *M* is the number of sub-series divided by the number of natural flow series.

In the LSTM model, the number of hidden layers was 1, the number of neurons in the hidden layer *n* was proportional to the complexity of the model, the value was 2^k ($k = 1,2,3,...,10$), and the sequence value range was [2,7]. For training, the learning rate was set to 0.0005, and the maximum training generation *m* was 500 generations. The model adopts the z-score algorithm for standardization. After standardization, the mean value of the data was 0, and the standard deviation was 1. In this study, the training and test sets were standardized Tan et al. (2018) separately, and the mean and standard deviation used in the calculation and de-standardization of the model results were derived from the training set.

Verification Strategy

To quantify the performance of the LSTM model, this study used three indicators, the Nash coefficient (*NSE*), relative deviation (*BIAS*), and mean absolute percentage error (*MAPE*), to evaluate the forecast accuracy of the model. The value range of the *NSE* was [−∞, 1]. The closer the value is to 1, the higher the degree of fit between the simulated and measured values. *BIAS* was used to evaluate the accuracy of the overall water balance of the model results, and the value range was [−100%, 100%]. The optimal value is 0; a positive value indicates that the water volume is higher overall. *MAPE* was used to reflect the relative deviation between the forecast and measured values; the value range was [0,100%], and the month was close to 0. The corresponding formulas are as follows:

$$NSE = 1 - \frac{\sum_{i=1}^{N} (y_i - \hat{y}_i)^2}{\sum_{i=1}^{N} (y_i - \bar{y})^2} \tag{15}$$

$$BIAS = \frac{\sum_{i=1}^{N} (\hat{y}_i - y_i)}{\sum_{i=1}^{N} y_i} \times 100\% \tag{16}$$

$$MAPE = \frac{1}{N} \sum_{i=1}^{N} \left| \frac{\mathrm{y_i} - \hat{y}_i}{y_i} \right| \times 100\% \tag{17}$$

where *i* is the *ith* moment, *N* is the total number of time steps, represents the simulation value, *y* represents the observation value, and $y(-)$ is the mean value of the observation data.

RESULTS AND DISCUSSION

Decomposition Results Using EEMD

EEMD was used to decompose non-linear and non-stationary raw flow data into linear and stable sub-sequences. The monthly runoff sequence of the GM-EEMD-LSTM model was divided into eight or nine independent sub-sequences. In addition, the original sequences from 2005 to 2017 were broken down into 13 independent levels in the EEMD-LSTM model. The frequency of these components gradually decreased from IMF1 to IMFn, and the residual was the slowest trend of the original sequence. Due to space constraints, **Figure 4** displays the decomposition results of the May month sequence of the GM-EEMD-LSTM model.

Figure 4 displays the sub-sequences of different periods. IMF1 is short, with a higher frequency and greater fluctuation. The positions of IMF1, IMF2, and IMF3 related to larger amplitude

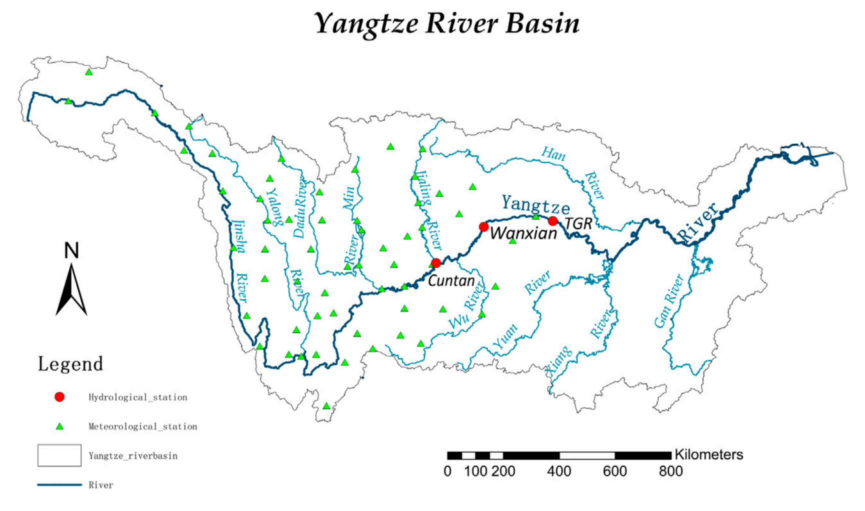

FIGURE 3 | Research area and station distribution. Tan et al. (2018)

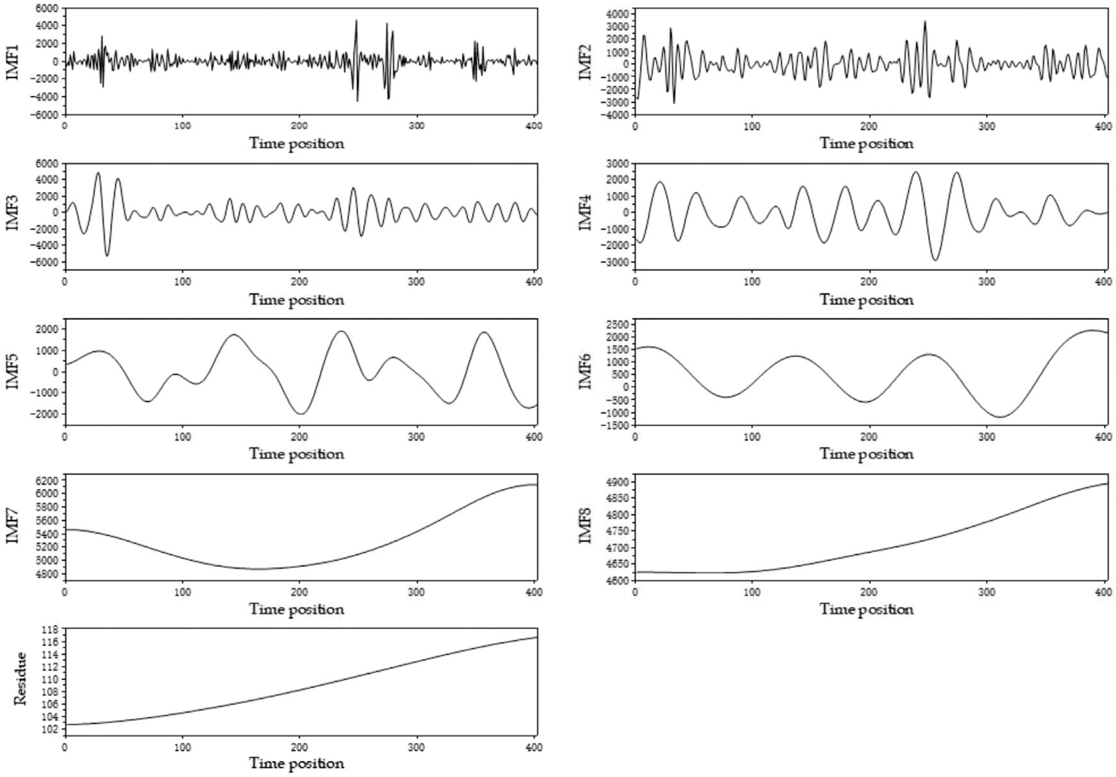

FIGURE 4 | Components decomposed by EEMD for May.

fluctuations are consistent. IMF3 contains 13 cycles in total, which is consistent with the original sequence (2005–2017). The residue was the upward change trend of the data in May, which is consistent with the slight upward trend of the May monthly series.

Correlations Between Related Factors and Original/Decomposed Components

Through a cross-correlation analysis, the correlation coefficients between the forecast factors and flow series (LSTM, EEMD-LSTM, and GM-EEMD-LSTM model target series) were assessed, and the forecast factor with the largest mutual information value was selected as the model input.

The original sequence, the target sequence of the LSTM model, and the sub-sequences decomposed by EEMD based on the original sequence are counted and displayed in **Table 1**.

Based on **Table 1**, the high-frequency sub-sequences exhibit a higher correlation with the runoff sequences of the Three Gorges Reservoir, while the lower-frequency sub-sequences are related to the runoff sequences of the Three Gorges Reservoir and Wanxian.

TABLE 1 | Top three maximum mutual information values of original and decomposed series.

IMF1		IMF2		IMF3		IMF4		IMF5		IMF6		IMF7	
Var	**MI**	**Var**	**MI**	**Var**	**MI**	**Var**	**MI**	**Var**	**MI**	**Var**	**MI**	**Var**	**MI**
TG-1	0.30	TG-1	0.51	TG-1	0.64	TG-1	0.61	TG-1	0.67	TG-4	0.61	WX-2	1.08
CT-1	0.26	TG-2	0.47	TG-2	0.58	TG-2	0.57	TG-2	0.66	TG-5	0.60	WX-3	1.08
TG-2	0.26	TG-3	0.46	CT-1	0.56	TG-3	0.55	TG-3	0.64	TG-3	0.60	WX-1	1.07

IMF8		IMF9		IMF10		IMF11		IMF12		IMF13		Original series	
Var	**MI**	**Var**	**MI**	**Var**	**MI**	**Var**	**MI**	**Var**	**MI**	**Var**	**MI**	**Var**	**MI**
TG-1	1.31	WX-7	0.51	T-7	0.89	T0	1.47	T0	1.47	WS-2	0.57	TG-1	3.04
TG-2	1.31	WX-5	0.51	T-6	0.88	T-1	1.47	T-1	1.47	WS-7	0.56	TG-2	2.36
TG-3	1.30	WX-6	0.51	T-5	0.88	T-2	1.46	T-2	1.46	WS-5	0.56	CT-1	2.19

Note: Variables (Var) are the predictors in the input variable set. CT, WX, and TG are the abbreviations for Cuntan, Wanxian, and Three Gorges Reservoir. The number in Var indicates the number of days the predictor is ahead of the forecast day.

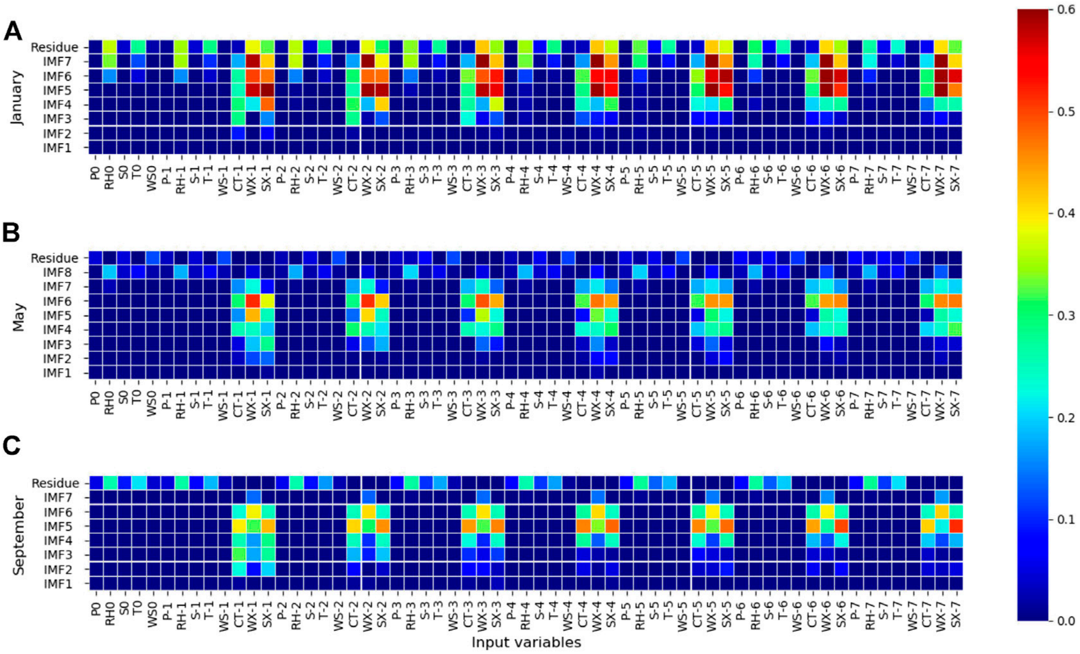

FIGURE 5 | Two-dimensional correlations between model inputs and sub-inflow series by month. Vertical axis indicates the lag time, and the horizontal axis represents the indices. The redder the color, the greater the correlation. Sub-inflow series correspond to **(A)** January **(B)** May, and **(C)** September.

Residual items and sub-items whose periods are close to trend items exhibit higher correlations with meteorological elements. The original data series exhibit the highest correlation with the runoff series of the previous day, and that of the mutual information is much higher than that of the highest mutual trust coefficient of each sub-sequence after EEMD decomposition.

This study also analyzed the mutual confidence coefficients between the sub-sequences of the GM-EEMD-LSTM model and the predictors after decomposing the monthly sequence. **Figure 5** displays certain sub-sequences of the GM-EEMD-LSTM model (1, 5, and 9). Based on **Figure 5A**, the residue in January exhibited the strongest correlation with the traffic sequence of Wanxian, reaching its peak on day 3. IMF7 exhibited the strongest correlation with the flow of Wanxian on day 4, and it exhibited a strong correlation with meteorological elements compared with other sub-series except that of residue. Both IMF6 and IMF5 were strongly correlated with the runoff series of the Three Gorges Reservoir and Wanxian County, and the peak value was the runoff of Wanxian on day 6. IMF4 and IMF3 exhibited strong correlations with the runoff sequence of Cuntan and the Three Gorges Reservoir. IMF4 exhibited the strongest correlation with the Three Gorges Reservoir on day 1, and IMF3 had the strongest correlation with Cuntan on day 1. The other two graphs in **Figure 5** display similar characteristics; sub-sequences with high frequencies are more likely to be

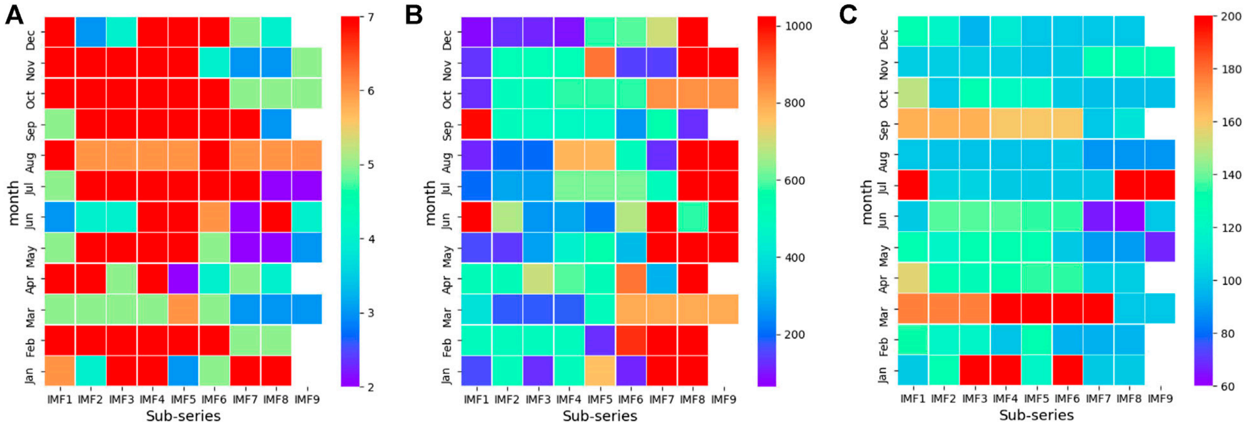

FIGURE 6 | Two-dimensional correlations between model parameters and sub-inflow series.

TABLE 2 | Model performances.

	RBF			EEMD-RBF			LSTM			EEMD-LSTM			GM-EEMD-LSTM		
	NSE	**BIAS(%)**	**MAPE (%)**	**NSE**	**BIAS(%)**	**MAPE (%)**	**NSE**	**BIAS(%)**	**MAPE (%)**	**NSE**	**BIAS(%)**	**MAPE (%)**	**NSE**	**BIAS(%)**	**MAPE (%)**
Jan	0.80	**0.44**	3.16	**0.86**	1.76	**2.84**	–0.11	–6.84	8.43	**0.61**	–**4.05**	**4.95**	0.91	–0.69	2.20
Feb	0.87	**0.07**	3.13	**0.91**	1.21	**2.74**	0.69	–**2.55**	5.01	**0.76**	–4.68	**4.93**	0.93	1.14	2.27
Mar	0.87	**0.37**	3.68	**0.96**	0.80	**2.42**	0.62	–**3.11**	5.95	**0.89**	–3.39	**3.82**	0.94	–0.18	2.58
Apr	0.82	1.04	5.08	**0.98**	**0.49**	**2.27**	0.71	–2.88	6.12	**0.96**	–**0.37**	**2.65**	0.91	1.50	4.12
May	0.63	1.64	6.90	**0.94**	**0.26**	**2.93**	0.66	2.16	8.40	**0.94**	**1.76**	**3.57**	0.92	–1.12	3.91
Jun	0.63	-1.72	11.46	**0.92**	**0.27**	**5.44**	0.62	**0.20**	12.41	**0.91**	2.87	**5.95**	0.86	–0.28	8.24
Jul	0.50	0.52	9.33	**0.91**	**0.26**	**4.54**	0.56	4.42	12.23	**0.84**	**4.36**	**6.74**	0.78	0.81	7.83
Aug	0.79	1.17	7.04	**0.96**	**0.79**	**2.91**	0.74	2.68	8.88	**0.94**	**2.61**	**4.90**	0.94	0.99	4.65
Sep	0.77	0.75	8.78	**0.97**	**0.05**	**3.29**	0.76	–0.49	9.92	**0.95**	–**0.37**	**4.38**	0.93	2.30	5.94
Oct	0.76	2.16	8.41	**0.96**	**-0.19**	**3.10**	0.81	–**0.68**	6.58	**0.95**	–1.50	**3.32**	0.89	–1.55	4.98
Nov	0.88	3.74	5.62	**0.99**	**1.39**	**2.25**	0.85	0.51	5.51	**0.98**	–**0.49**	**2.49**	0.93	0.12	4.22
Dec	0.72	1.36	3.11	**0.86**	**1.05**	**2.62**	0.58	–3.10	3.98	**0.72**	–**2.17**	**3.59**	0.92	0.23	1.89
Entirely	0.91	0.88	6.32	**0.98**	**0.48**	**3.11**	0.91	**0.28**	7.80	**0.98**	0.63	**4.27**	0.97	0.36	4.40

Note: Bold values indicate the optimal statistics between LSTM and EEMD-LSTM or RBF and EEMD-RBF. Underlined values indicate where the GM-EEMD-LSTM statistics are superior to those of EEMD-LSTM.

highly correlated with Cuntan and the Three Gorges Reservoir, while sub-sequences with low frequencies are more likely to be correlated with Wanxian and the Three Gorges Reservoir. The trend item and IMFn are highly correlated with meteorological elements, which is consistent with the sub-sequences of the EEMD-LSTM model above.

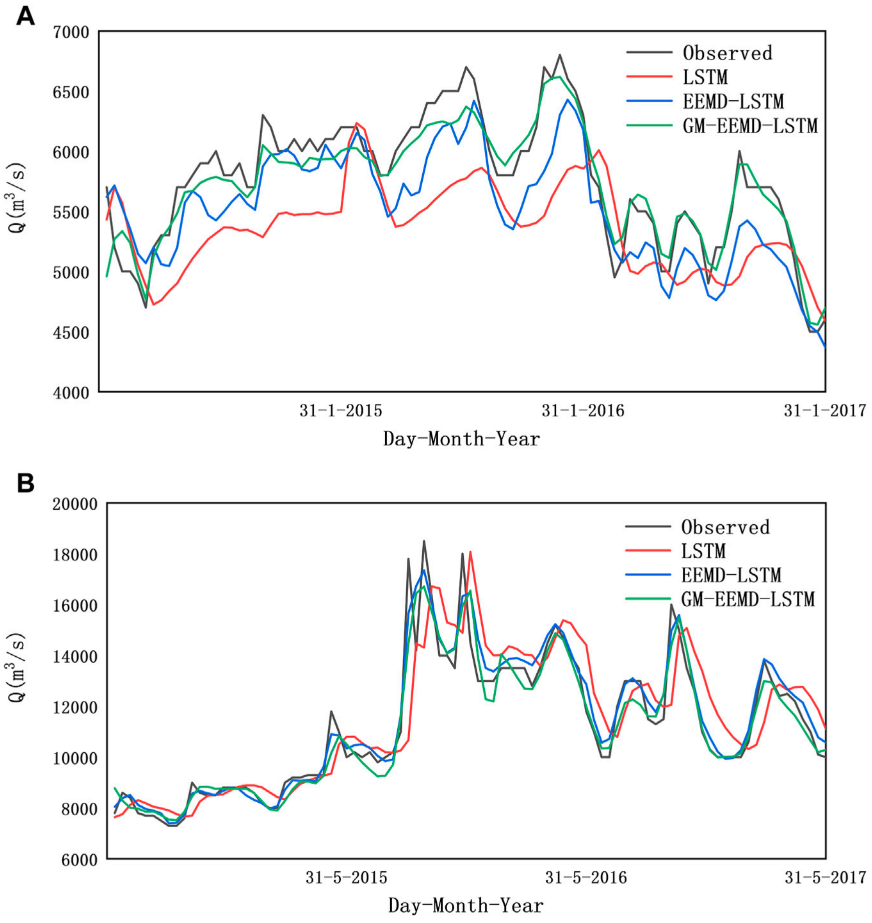

FIGURE 7 | Comparison of forecast and original inflow values for 2015–2017 for the Three Gorges Reservoir.

TABLE 3 | Forecast results for different forecasting periods.

Forecast target	LSTM			EEMD-LSTM		
	NSE	BIAS(%)	MAPE (%)	NSE	BIAS(%)	MAPE (%)
Q_t	0.91	0.28	7.80	0.98	0.63	4.27
Q_{t+1}	0.84	0.78	11.20	0.96	0.63	5.44
Q_{t+2}	0.80	1.74	13.31	0.95	0.29	5.85
Q_{t+3}	0.79	1.97	14.49	0.94	0.59	6.96

Optimal Parameters of LSTM Model for Decomposed Series

Statistical analysis was performed on the target sequence of the EEMD-LSTM model. Thirteen sub-sequences were decomposed by the EEMD of the original sequence, and statistical analysis was performed on the optimal parameters. IMF1 exhibited the highest frequency, and the optimal parameter values of the LSTM model were $seq = 7$, $n = 128$, and $m = 100$. The optimal parameter values of IMF12 and residue were $seq = 3$, $n = 1,024$, and $m = 70$.

The LSTM parameters were calculated when the prediction results of each sub-sequence of the 12-month sequence of the GM-EEMD-LSTM model were optimal, and a two-dimensional correlation diagram was obtained, as displayed in **Figure 6**. In the figure, IMF9 is the residue obtained by decomposing the sequence with the number of sub-sequences of 9, and the sequence residue with eight sub-sequences is IMF8 when IMF9 is blank.

Based on **Figure 6A**, it can be seen that the sequence values of IMF7, IMF8, and IMF9 are proportionally smaller, while the period of IMF7–MF9 is long, which is substantially different from the input variable period. This result can be obtained by inputting less information during the simulation. The analysis illustrated in **Figure 6B** demonstrates that the ratio of IMF1–IMF4 to IMF7–IMF9, where the number of hidden neurons is less than n, is great. IMF7–IMF9 is more complicated because the period is significantly larger than that of the input variable. The proposed model can simulate this period more accurately than the simple model. **Figure 6C** demonstrates that IMF7–IMF9 is smaller than the other sub-sequence training times. Because the n value of IMF7–IMF9 is higher, the model is more complicated and has a stronger fitting ability; thus, when the number of training values is large, over-fitting can be easily caused. This is consistent with the sub-sequence parameter selection rule of the EEMD-LSTM model.

Model Performance Evaluation

Effectiveness Evaluation of EEMD Method

To evaluate the effectiveness of the EEMD method across multiple directions, this study uses the LSTM, EEMD-LSTM, and GM-EEMD-LSTM models to establish a model with a forecast period of 0 day to forecast the inflows of the Three Gorges Reservoir from 2015 to 2017. The predictor with the highest cross-correlation information for the measured runoff sequence was selected as the model input to predict the runoff sequence. The prediction ability of the different models was evaluated with NSE, BIAS, and MAPE. To study the simulation characteristics of the EEMD-LSTM model for different months of runoff, after evaluating the test set with the evaluation indicators, the prediction results of the test set were also counted on a monthly basis, whose results are listed in **Table 2**.

According to the analysis (**Table 2**), the simulation effect of the decomposition sequence was superior to that of the original series. In other words, the model performance of the EEMD-LSTM and EEMD-RBF models is better than the simulation performance of the LSTM and RBF models, especially for the *NSE* and *MAPE* indicators.

The LSTM model does not exhibit any clear rules for the runoff sequences of different months. A comparison between the EEMD-LSTM and GM-EEMD-LSTM models demonstrates that the GM-EEMD-LSTM model simulates the high-flow months (April to November) well. The result is slightly lower than that of the EEMD-LSTM model, but the overall performance in the low-water months (January, February, March, and December) was significantly better than that of the EEMD-LSTM model. **Figure 7** displays the simulation results for January and May.

Based on **Figure 7**, the decomposed model can more accurately simulate the peak and valley values of the runoff sequence. The GM-EEMD-LSTM simulation result was the closest to the measured value, while the results of the EEMD-LSTM model were the best in May. The results of both models were far superior to those of the undecomposed model. Therefore, the two methods can be combined to predict traffic. The EEMD-LSTM model can be used to make predictions in high-traffic months, and the GM-EEMD-LSTM model can be used to make predictions in low-flow months.

In addition, when the LSTM model is used alone for runoff prediction research, there is a widespread delay problem that manifests as translational misalignments on the images (Kratzert et al., 2018; Xiang et al., 2020). As displayed in **Figure 7**, the predicted values of the LSTM model vary and are slower to predict than the true value. This is because the LSTM network cannot accurately detect the degree of fluctuation in a time series; thus, the result of the prediction from the previous moment may be reflected at the present moment. The decomposition model using the EEMD method effectively remedies this issue. The time series is decomposed into several sub-sequences. Compared with the original series, the fluctuation degree of the sub-sequences is more stable, and it is easier to obtain the time-series fluctuations of each LSTM unit. The prediction of the network sub-model is more accurate, solving the delay problem of the LSTM network.

Results for Different Forecast Periods

To evaluate the effect of EEMD on LSTM more comprehensively, this research established EEMD-LSTM and LSTM models for different forecast periods (0–3 day, represented as Q_t, Q_{t+1}, Q_{t+2}, and Q_{t+3}). And all forecast periods are based on falling rain. The results are displayed in **Table 3**.

Based on **Table 3**, the EEMD-LSTM exhibits a superior forecasting performance. For all forecast periods, the *BIAS* indicators of the LSTM and EEMD-LSTM models are less than 5%, indicating that the LSTM model water balance is accurate. As the forecast period increases, the *BIAS* indicator value of the LSTM model significantly increases. However, the *BIAS* index of the EEMD-LSTM model is irregular, indicating that the EEMD method can improve the accuracy of the overall water balance of the model when the forecasting period increases. Both models exhibit the greatest effect when forecasting Q_t runoff. As the forecast period increased, the forecast accuracy decreased, and the forecast accuracy of the EEMD-LSTM model decreased less than that of the LSTM model. When the forecast period was 3 day, the Nash coefficients of the LSTM and EEMD-LSTM models were 0.79 and 0.94, respectively.

CONCLUSION

This study uses approximately 14 years of historical, meteorological, and runoff data as the forecast factor set and employs EEMD, mutual information, and LSTM for data processing, forecast factor selection, and runoff forecasting, respectively. The results demonstrate that the prediction performance of the LSTM model can be improved through EEMD processing. Based on the study results, the following conclusions can be drawn.

(1) After the data was processed by EEMD, sub-sequences with different frequencies were obtained. The high-frequency sub-sequences exhibited a higher correlation with the runoff sequences of Cuntan and the Three Gorges Reservoir, while the lower-frequency sub-sequences were related to the runoff sequences of the Three Gorges Reservoir and Wanxian. The other items and sub-items with periods close to those of the trend items were highly correlated with meteorological elements. The original series exhibited the highest correlation with the data series of the day prior to the forecast, and the mutual information value was substantially higher than those of the sub-sequence and input variables. However, the decomposed series exhibited superior simulation results in the LSTM model.

(2) The parameters of the LSTM model for sub-sequences with different frequencies presented the following laws: sub-sequences with low frequencies and longer periods contained less input information during simulation, more hidden neurons, were part of a more complex model, and exhibited higher training times. Additionally, the sequence parameter value was smaller, the n value was greater, and the m value was smaller.

(3) The results demonstrate that the prediction results of the sub-series obtained by the LSTM and RBF exhibited better statistical performance than those of the original series.

(4) The EEMD-LSTM model performs well across forecasting periods. As the forecast period increases, the forecasting accuracy decreases.

The combination of EEMD and LSTM methods for hydrological series prediction is the main novelty of this study. Moreover, while considering the autocorrelation in the runoff series, this study also considered its relationship with meteorological elements. In addition, when selecting the model input, the mutual information method suitable for linear and nonlinear relationships was selected. However, the correlation between the final model input and the prediction sequence was not strong enough, which will affect the model performance. Thus, further improvements are needed in regard to the correlation.

DATA AVAILABILITY STATEMENT

The original contributions presented in the study are included in the article/Supplementary Material, further inquiries can be directed to the corresponding author.

AUTHOR CONTRIBUTIONS

RY, WL, SC, and XL contributed to the design of the study and the discussion, and they wrote a draft of the manuscript. ZY, GD, JW, and YX organized the methodology. RY and YZ wrote individual sections of the manuscript. All authors contributed to manuscript revisions and have read and approved the submitted version.

FUNDING

This work was jointly supported by the National Key R&D Program of China (2017YFB0203104) and the National Natural Science Fund (51709273).

ACKNOWLEDGMENTS

The authors are grateful to the information center at the Ministry of Water Resources of the People’s Republic of China for the provisioning of reservoir and hydrological data.

REFERENCES

Abbaspour, K. C., Rouholahnejad, E., Vaghefi, S., Srinivasan, R., Yang, H., and Kløve, B. (2015). A continental-scale hydrology and water quality model for Europe: calibration and uncertainty of a high-resolution large-scale SWAT model. *J. Hydrol.* 524, 733–752. doi:10.1016/j.jhydrol.2015.03.027

Adamowski, J., Morin, E., and Karran, D. J. (2014). Multi-step streamflow forecasting using data-driven non-linear methods in contrasting climate regimes. *J. Hydroinformatics* 16 (3), 671–689. doi:10.2166/hydro.2013.042

Ahmadi, M., Moeini, A., Ahmadi, H., Motamedvaziri, B., and Zehtabiyan, G. R. (2019). Comparison of the performance of SWAT, IHACRES and artificial neural networks models in rainfall-runoff simulation (case study: Kan watershed, Iran). *Phys. Chem. Earth, Parts A/B/C* 111, 65–77. doi:10.1016/j.pce.2019.05.002

An, L., Hao, Y., Yeh, T.-C. J., Liu, Y., Liu, W., and Zhang, B. (2020). Simulation of karst spring discharge using a combination of time-frequency analysis methods and long short-term memory neural networks. *J. Hydrol.* 589, 125320. doi:10.1016/j.jhydrol.2020.125320

Cheng, C.-t., Niu, W.-j., Feng, Z.-k., Shen, J.-j., and Chau, K.-w. (2015). Daily reservoir runoff forecasting method using artificial neural network based on quantum-behaved particle swarm optimization. *Water* 7 (12), 4232–4246. doi:10.3390/w7084232

Ding, G. B., Nong, Z. X., Wang, C., Song, P. B., and Lei, X. H. (2019). Long-term runoff forecasting model based on MI-PCA and BP neural network in shiyang River Basin. *China Rural Water and Hydropower* (10), 66–69. (in Chinese).

Huang, N. E., Shen, Z., Long, S. R., Wu, M. C., Shih, H. H., Zheng, Q., et al. (1998). The empirical mode decomposition and the Hilbert spectrum for nonlinear and non-stationary time series analysis. *Proc. R. Soc. Lond. A.* 454, 903–995. doi:10.1098/rspa.1998.019310.1098/rspa.1998.0193

Huang, N. E., and Wu, Z. (2008). A review on Hilbert-Huang transform: method and its applications to geophysical studies. *Rev. Geophys.* 46 (2). doi:10.1029/2007rg000228

Jiang, T., Kundzewicz, Z. W., and Su, B. (2008). Changes in monthly precipitation and flood hazard in the Yangtze River Basin, China. *Int. J. Climatol.* 28 (11), 1471–1481. doi:10.1002/joc.1635

Kan, G., Li, J., Zhang, X., Ding, L., He, X., Liang, K., et al. (2016). A new hybrid data-driven model for event-based rainfall-runoff simulation. *Neural Comput. Applic* 28 (9), 2519–2534. doi:10.1007/s00521-016-2200-4

Kratzert, F., Klotz, D., Brenner, C., Schulz, K., and Herrnegger, M. (2018). Rainfall-runoff modelling using long short-term memory (LSTM) networks. *Hydrol. Earth Syst. Sci.* 22 (11), 6005–6022. doi:10.5194/hess-22-6005-2018

Lee, D., Lee, G., Kim, S., and Jung, S. (2020). Future runoff analysis in the mekong River Basin under a climate change scenario using deep learning. *Water* 12 (6), 1556. doi:10.3390/w12061556

Meshram, S. G., Singh, V. P., Kisi, O., Karimi, V., and Meshram, C. (2020). Application of artificial neural networks, support vector machine and multiple model-ANN to sediment yield prediction. *Water Resour. Manage.* 34 (15), 4561–4575. doi:10.1007/s11269-020-02672-8

Nanda, T., Sahoo, B., Beria, H., and Chatterjee, C. (2016). A wavelet-based non-linear autoregressive with exogenous inputs (WNARX) dynamic neural network model for real-time flood forecasting using satellite-based rainfall products. *J. Hydrol.* 539, 57–73. doi:10.1016/j.jhydrol.2016.05.014

News and Focus (2015). The three Gorges project. *Engineering* 1 (1), 011–013. doi:10.15302/j-eng-2015022

Patil, A., and Ramsankaran, R. (2017). Improving streamflow simulations and forecasting performance of SWAT model by assimilating remotely sensed soil moisture observations. *J. Hydrol.* 555, 683–696. doi:10.1016/j.jhydrol.2017.10.058

Sharma, A. (2000). Seasonal to interannual rainfall probabilistic forecasts for improved water supply management: Part 1 - a strategy for system predictor identification. *J. Hydrol.* 239 (1-4), 232–239. doi:10.1016/s0022-1694(00)00346-2

She, L., and You, X.-y. (2019). A dynamic flow forecast model for urban drainage using the coupled artificial neural network. *Water Resour. Manage.* 33 (9), 3143–3153. doi:10.1007/s11269-019-02294-9

Tan, Q.-F., Lei, X.-H., Wang, X., Wang, H., Wen, X., Ji, Y., et al. (2018). An adaptive middle and long-term runoff forecast model using EEMD-ANN hybrid approach. *J. Hydrol.* 567, 767–780. doi:10.1016/j.jhydrol.2018.01.015

Tayyab, M., Ahmad, I., Sun, N., Zhou, J., and Dong, X. (2018). Application of integrated artificial neural networks based on decomposition methods to predict streamflow at upper indus basin, Pakistan. *Atmosphere* 9 (12), 494. doi:10.3390/atmos9120494

Tian, M., Zhou, J., Jia, B., Lou, S., and Wu, H. (2020). Impact of three Gorges reservoir water impoundment on vegetation-climate response relationship. *Remote Sensing* 12 (17), 2860. doi:10.3390/rs12172860

Wang, J., Wang, X., Lei, X. h., Wang, H., Zhang, X. h., You, J. j., et al. (2020). Teleconnection analysis of monthly streamflow using ensemble empirical mode decomposition. *J. Hydrol.* 582, 124411. doi:10.1016/j.jhydrol.2019.124411

Wang, W. C., Chau, K. W., Qiu, L., and Chen, Y. B. (2015). Improving forecasting accuracy of medium and long-term runoff using artificial neural network based on EEMD decomposition. *Environ. Res.* 139, 46–54. doi:10.1016/j.envres.2015.02.002

Wang, Z.-Y., Qiu, J., and Li, F.-F. (2018). Hybrid models combining EMD/EEMD and ARIMA for long-term streamflow forecasting. *Water* 10 (7), 853. doi:10.3390/w10070853

Wu, J. S., Han, J., Annambhotla, S., and Bryant, S. (2005). Artificial neural networks for forecasting watershed runoff and stream flows. *J. Hydrol. Eng.* 10 (3), 216–222. doi:10.1061/(asce)1084-069910.1061/(asce)1084-0699(2005)10:3(216)

Xiang, Z., Yan, J., and Demir, I. (2020). A rainfall-runoff model with LSTM-based sequence-to-sequence learning. *Water Resour. Res.* 56 (1). doi:10.1029/2019wr025326

Yin, Z.-K., Liao, W.-H., Wang, R.-J., and Lei, X.-H. (2019). Rainfall-runoff modelling and forcasting based on long short-term memory(LSTM). *South-to-North Water Transfers Water Sci. Tech.* 17 (6). doi:10.13476/j.cnki.nsbdqk.2019.0129 (in Chinese).

Yu, Y., Zhao, W., Martinez-Murillo, J. F., and Pereira, P. (2020). Loess Plateau: from degradation to restoration. *Sci. Total Environ.* 738, 140206. doi:10.1016/j.scitotenv.2020.140206

Yu, Y., Zhang, H., and Singh, V. (2018). Forward prediction of runoff data in data-scarce basins with an improved ensemble empirical mode decomposition (EEMD) model. *Water* 10 (4), 388. doi:10.3390/w10040388

Zhang, X., Zhang, Q., Zhang, G., Nie, Z., Gui, Z., Que, H. F., et al. (2018). A novel hybrid data-driven model for daily land surface temperature forecasting using long short-term memory neural network based on ensemble empirical mode decomposition. *Ijerph* 15 (5), 1032. doi:10.3390/ijerph15051032

Zhao, Steel., and Yang, D.-W. (2011). Mutual information-based input variable selection method for runoff -forecasting neural network model. *J. Hydroelectric Eng.* 30 (1), 24–30. (in Chinese).

Zhao, X., Chen, X., Xu, Y., Xi, D., Zhang, Y., and Zheng, X. (2017). An EMD-based chaotic Least Squares support vector machine hybrid model for annual runoff forecasting. *Water* 9 (3), 153. doi:10.3390/w9030153

Zhao, Y., Li, Z., Cai, S., and Wang, H. (2020). Characteristics of extreme precipitation and runoff in the Xijiang River Basin at global warming of 1.5 °C and 2 °C. *Nat. Hazards* 101 (3), 669–688. doi:10.1007/s11069-020-03889-x

Zhou, J., Jia, B., Chen, X., Qin, H., He, Z., and Liu, G. (2019). Identifying efficient operating rules for hydropower reservoirs using system dynamics approach-A case study of three Gorges reservoir, China. *Water* 11 (12), 2448. doi:10.3390/w11122448

Zhu, Q., Gao, X., Xu, Y.-P., and Tian, Y. (2019). Merging multi-source precipitation products or merging their simulated hydrological flows to improve streamflow simulation. *Hydrological Sci. J.* 64 (8), 910–920. doi:10.1080/02626667.2019.1612522

Conflict of Interest: Author ZY was employed by the company China Three Gorges Corporation.

The remaining authors declare that the research was conducted in the absence of any commercial or financial relationships that could be construed as a potential conflict of interest.

frontiers in Earth Science

BRIEF RESEARCH REPORT
published: 29 April 2021
doi: 10.3389/feart.2021.671985

Terrestrial Signature of a Recently-Tidewater Glacier and Adjacent Periglaciation, Windy Glacier (South Shetland Islands, Antarctic)

Kacper Kreczmer[1], Maciej Dąbski[2]* and Anna Zmarz[3]

[1] College of Inter-faculty Individual Studies in Mathematics and Natural Sciences, University of Warsaw, Warsaw, Poland,
[2] Faculty of Geography and Regional Studies, Department of Geomorphology, University of Warsaw, Warsaw, Poland,
[3] Faculty of Geography and Regional Studies, Department of Geoinformatics, Cartography and Remote Sensing, University of Warsaw, Warsaw, Poland

Contemporary retreat of glaciers is well visible in the West Antarctic region. The aim of this study is to identify, map and quantify terrestrial glacial and periglacial landforms developed in front of Windy Glacier (Warszawa Icefield, King George Island, South Shetlands), which recently turned from being tidewater to land-terminating, and on nearby Red Hill. The study is based on an orthophoto map and a DEM elaborated with a use of images obtained during a UAV BVLOS photogrammetric survey in 2016, Google Earth Pro images from 2006 and an orthophoto map from 1978/1979. The geomorphological map obtained includes 31 types of landforms and water bodies, grouped into: (1) glacial depositional landforms, (2) fluvial and fluvioglacial landforms, (3) littoral and lacustrine landforms, (4) solifluction landforms, (5) other mass movement landforms, (6) patterned ground, (7) debris flows, landslides and mudflows, (8) water bodies, (9) other (bedrock, boulders, glacial ice, snow patches, and not recognized surface). Most area is occupied by glacial lagoon, fluvial and fluvioglacial landforms, not recognized surfaces and littoral landforms. Between 2006 and 2016 the glacier deposited a well-developed patch of fluted moraine with small drumlins. We recognize the glacial-periglacial transition zone between 41 and 47 m GPS height above which solifluction landforms and sorted patterned ground dominate. Advantages of UAV and BVLOS missions are highlighted and problems with vectorization of landforms are discussed. Distinction between flutes and small drumlins is shown on length-to-elongation and length-to-width diagrams and critical reference to previous geomorphological mappings on King George Island is presented.

Keywords: glacial landforms, periglacial landforms, King George Island, Antarctic, unmanned aerial vehicles, glacial recession, photointerpretation

OPEN ACCESS

Edited by:
Jesús Rodrigo-Comino,
Universität Trier, Germany

Reviewed by:
Enrique Serrano,
University of Valladolid, Spain
Kátia Kellem Rosa,
Federal University of Rio Grande do Sul, Brazil

***Correspondence:**
Maciej Dąbski
mfdabski@uw.edu.pl

Specialty section:
This article was submitted to Environmental Informatics and Remote Sensing, a section of the journal Frontiers in Earth Science

Received: *24 February 2021*
Accepted: *07 April 2021*
Published: *29 April 2021*

Citation:
Kreczmer K, Dąbski M and Zmarz A (2021) Terrestrial Signature of a Recently-Tidewater Glacier and Adjacent Periglaciation, Windy Glacier (South Shetland Islands, Antarctic). Front. Earth Sci. 9:671985. doi: 10.3389/feart.2021.671985

INTRODUCTION

Contemporary retreat of glaciers (World Glacier Monitoring Service [WGMS], 2020), well visible in alpine environments and in the Arctic is also significant in the West Antarctic region, including Antarctic Peninsula and South Shetland Islands (Cook et al., 2005; Meredith and King, 2005; Turner et al., 2014). Antarctic ecosystems, frequently protected as the

Antarctic Specially Protected Areas (ASPA) are now subject to rapid transformation which influences wildlife and the source-to-sink sediment budgets (Zwoliński et al., 2016; Lee et al., 2017; Znój et al., 2017). New ice-free oasis are developed due to recent on-shore termination of formerly tidewater glaciers. The southern and eastern margins of the Warszawa Icefield (**Figure 1**) on King George Island (KGI), South Shetland Islands, are also subjected to retreat which transformed tidewater glacial fronts to land-terminating ones and liberated from glacial ice over 6 km^2 since the first general survey in 1979 (Pudełko, 2003; Pętlicki et al., 2017; Pudełko et al., 2018; Da Rosa et al., 2020).

The development of the terrestrial glacial landforms in front of the retreating glacier and periglacial phenomena in this area received considerable attention since the end of the 20th century due to the nearby location of the Henryk Arctowski Polish Antarctic Station (Arctowski) (Birkenmajer, 1980; Dutkiewicz, 1982; Kostrzewski et al., 1998, 2002; Rachlewicz, 1999). Satellite and conventional aerial imagery recently allowed for deepening our understanding of glacial dynamics and gave some information on the rate of development of glacial landforms (Pętlicki et al., 2017; Pudełko et al., 2018; Sziło and Bialik, 2018; Da Rosa et al., 2020), however, they sometimes lead to improper interpretations.

In years 2014–2016 the MONICA project (A novel approach to monitoring the impact of climate change on Antarctic ecosystems) was realized in the area of Arctowski, which utilized unmanned aerial vehicle (UAV) platforms and Beyond Visual Line of Sight (BVLOS) operations. The project resulted in three geomorphological studies so far, including: periglaciation of Demay Point (Dąbski et al., 2017), general morphology of Penguin Island (Zmarz et al., 2018) and development of forelands of Ecology, Sphinx and Baranowski glaciers (Dąbski et al., 2020). However, the foreland of near-by Windy Glacier (**Figure 1**) was omitted, due to its marginal location and relatively small size of the foreland.

The aim of this study is to fill this gap by identification, mapping and quantification of terrestrial glacial and periglacial landforms developed in front of Windy Glacier, which recently turned from being tidewater to land-terminating. The analysis of the landform assemblages allowed to infer about the glacial dynamics and the significance of contemporary periglacial processes developed in the adjacent area. Moreover, we critically address the previous geomorphological mapping of the area under study based on satellite images (Da Rosa et al., 2020).

The research was based on a high-resolution orthophoto map and a digital elevation model (DEM) created by A. Zmarz on the basis of images obtained during a photogrammetric survey performed over the west coast of Admiralty Bay in 2016. The mapping was not confirmed in the field by checking the internal structure of landforms, however, identified landforms were sufficiently visible of the aerial images to allowed for relatively detailed geomorphological interpretation.

Location, Climatic and Geological Setting of the Windy Glacier Foreland

Windy Glacier is located at the southern boundary of the Antarctic Specially Protected Area No. 128 (ASPA 128) which covers the west coast of Admiralty Bay in the vicinity of Arctowski (**Figures 1A,B**). Glacial recession in ASPA 128 since 1979 was documented by Pudełko et al. (2018), and the general

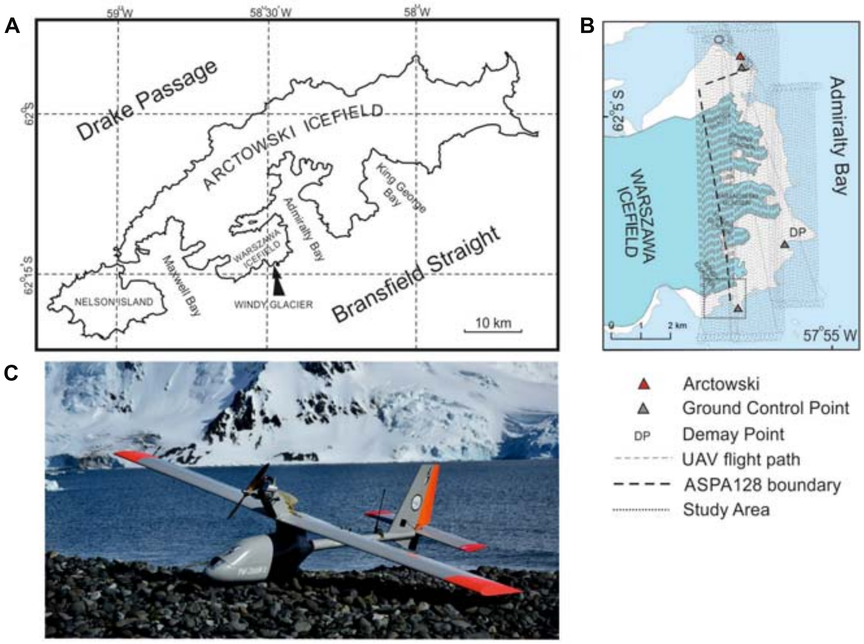

FIGURE 1 | (A) Location of Windy Glacier on King George Island (South Shetland Islands); **(B)** flight path over ASPA128 and surroundings; **(C)** PW-ZOOM unmanned aerial vehicle.

geomorphological mapping the forelands of Ecology Glacier, Sphinx Glacier and Baranowski Glacier (main glaciers of ASPA 128) was recently performed by Dąbski et al. (2020).

Bedrock of the area includes basaltic (tholeiites) and andesitic lavas interbedded with Eocene–Oligocene sediments and volcanic plugs and dikes of Pleistocene age (Birkenmajer, 1980). Quaternary sediments are represented by glacial and fluvioglacial sediments, periglacial, weathering and mass-movement sediments as well as marine sands and gravels (Birkenmajer, 1981; Rachlewicz, 1999; Kostrzewski et al., 2002).

Mean annual air temperature (MAAT) in the study area is −1.5°C, rainfall or snowfall occur throughout most of the year, and snow cover is highly variable, redistributed by strong winds (Dutkiewicz, 1982; Gonera and Rachlewicz, 1997; Robakiewicz and Rakusa-Suszczewski, 1999; Marsz and Styszyńska, 2000; Wierzbicki, 2009; López-Martínez et al., 2012; Kejna et al., 2013; Zwoliński et al., 2016). Polar maritime climate of the area is responsible for highly dynamic weather conditions which are demanding for any UAV operations and for photointerpretation of medium- to small-scale landforms or margins of glaciers which can be covered by snow drift. Climatic changes observed since the onset of instrumentalization in this area (MAAT in years 1948–2011 increased by 1.2°C), results in glacial recession, disappearance of permafrost from coastal areas and inactivation of certain large-scale periglacial landforms (Dąbski et al., 2017, 2020; Pudełko et al., 2018). However, since the beginning of the 21st c. regional cooling is observed (Oliva et al., 2016) which is responsible for slowing deglaciation rates or glacial still-stands.

Windy Glacier flows SE of the Warszawa Icefield (max elevation 450 m a.s.l.) and its equilibrium line altitude varied between 140 m a.s.l. and 290 m a.s.l. in years 1979–2018 (Pudełko et al., 2018). Ice thickness in the frontal part of the glacier does not exceed 100 m, and ice flow velocity is below 100 m year^{-1} (Osmanoğlu et al., 2013). Dąbski et al. (2020) concluded that the neighboring glaciers in ASPA 128 probably experienced discontinuous fast ice flow typical of tidewater glaciers. Recent contact of the Windy Glacier with the lagoon, allowed for more dynamic behavior of the glacier by allowing for calving. Thermal state of the glacier is unknown, and both polythermal and temperate glaciers are present on KGI (Benjumea et al., 2003; Young Kim et al., 2010). According to Da Rosa et al. (2020) during 1979–2018 Windy Glacier area loss amounted to 1.10 km^2 (31% of 3.51 km^2 in 1979). The rate of deglaciation decreased in years during the 2000–2018 due to climatic cooling and the transition of glacier margin from tidewater to land-terminating.

Tidal range of about 1.5 m (Robakiewicz and Rakusa-Suszczewski, 1999) results in a well-developed beach, coastal cliffs and a glacier lagoon in the Windy Glacier foreland. The lagoon played a significant role in shaping the glacier's dynamics before 2006, but afterward the glacier underwent a transformation from tidewater to land-terminating.

The western and southern margins of the Warszawa Icefield, including the Windy Glacier foreland, constitute a lowland ice-free area (about 16.8 km^2), covered by diverse tundra communities (Chwedorzewska and Bednarek, 2011) suitable for huge breeding colonies of marine birds and pinnipeds (Sierakowski et al., 2017), e.g., on Patelnia Point (**Figure 2**) near the Windy Glacier margin (Fudala and Bialik, 2020).

METHODS

Data Acquisition

During realization of the MONICA project a photogrammetric survey was performed over ASPA 128 on 15-17 November 2016 with a use of a PW-ZOOM fixed-wing UAV and a BVLOS operation (**Figures 1B,C**). The UAV was designed especially for polar conditions and manufactured in the Warsaw University of Technology (Goetzendorf-Grabowski and Rodzewicz, 2017; Rodzewicz et al., 2017). The starting and landing points of the PW-ZOOM were located near Arctowski. An automatic control system linked with a telemetry module in the Ground Control Station (GSC), connected to a computer running HORIZONmp software allowed for a fully autonomous flight. The flight path lines were spaced circa 70 m apart, which provided 70% forward and side overlap and flight altitude was 500 m a.s.l. The images were gathered in three flights 7 h in total, covering a distance of 720 km. All images obtained had georeferences (X, Y, Z) registered by the autopilot logger mounted on the UAV. The GPS Receiver GP-E2 was used for geolocation of the images allowing for horizontal accuracy of measurement <5 m. GPS measurements of three ground control points (GCP), marked in **Figure 1B**, were used to determine the vertical accuracy (accuracy of measurement was <2 m).

Other sources of aerial imagery used in this study included Google Earth Pro (GE) images from 2006 and an orthophoto map based on aerial photography from 1978/1979 (Pudełko, 2003). The GE images obtained were of relatively low resolution (1.7 m), but they allowed to get valid data on the glacier margin position in 2006, because the glacier margin was clearly visible against characteristic foreland features (**Figure 2**).

Data Processing

Images obtained with the use of the UAV platform were processed into an orthophoto with a resolution of 0.06 m (**Figure 2**) and a DEM of 0.25 m resolution in the WGS84 coordinate system (**Supplementary Figure 1**) showing elevation in meters GPS height (m GPS h.). The orthophoto map and DEM were created with use of the Agisoft Metashape Professional software (Version 1.3.2) and the Structure from Motion (SfM) algorithm. The orthophoto was converted to UTM system in ESRI ArcGIS 10.3 software. Google Earth satellite images (from 2006) were geo-referenced in ESRI ArcGIS to the WGS84 coordinate system, the same as one used in the orthophoto map (**Figure 2**). The root mean square error (RMSE) was 1.46 m. The orthophoto and DEM (**Supplementary Figure 1**) allowed to manually determine boundaries of landforms or patches of land surface exhibiting uniform morphological characteristics (e.g., sorted circles) by vectorization in ESRI ArcGIS 10.3 software at scales between 1:500 and 1:2000 (**Figure 3** and **Supplementary Figures 2, 3**). The length-to-elongation ratio diagram allowed for distinction between flutes and drumlins (**Figure 4**).

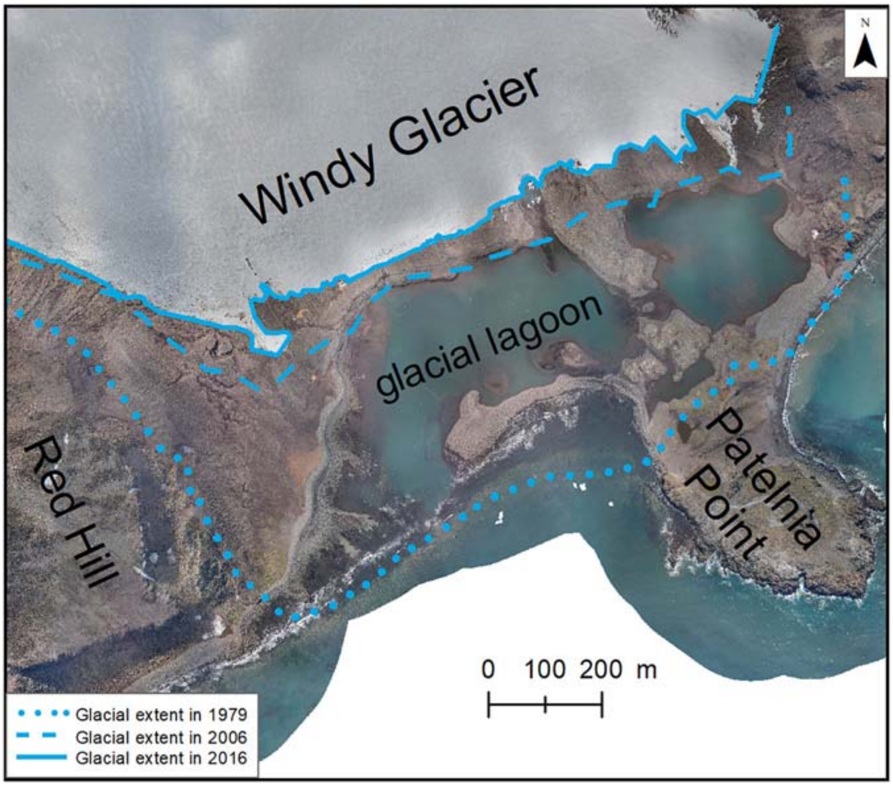

FIGURE 2 | Retreat of Windy Glacier since 1979; sources: UAV-based imagery from 2016, Google Earth (glacial extent in 2006) and orthophoto of Pudełko (2003) showing glacial extent in 1979.

RESULTS

Windy Glacier is a thin and short glacier lobe filling a shallow glacier trough which delivered the ice to the open sea until 1979 (**Figure 2**). There are no terrestrial Little Ice Age (LIA) terminal moraine ridges, because the glacier terminated in the see in the LIA maximum. The oldest end moraine complex (recessional moraine ridges) is deposited on the Patelnia Point (**Figures 2**, **3**) and should be associated with the 20th century still-stands or short advances (see Discussion). Well-developed beaches and storm ridges can be found along the coastline and a strip of a shallow coastal cliff cut in bedrock is visible along the shore of Patelnia Point.

The following glacial retreat resulted in a creation of the glacial lagoon which now is composed of two main water bodies and constitutes most of the glacial foreland – almost 23% of study area (**Figures 2**, **3**). Apart from the lagoon, the area liberated from glacier ice between 1979 and 2006 is characterized by a well-developed alluvial fan (sandur) west of the lagoon and a large relatively flat "not recognized surface" (**Figure 3**).

The interior part of the glacier foreland, deglaciated after 2006 (**Figure 2**), is dominated by the ground moraine with small recessional moraine ridges, especially in its western part (close to Red Hill foothills), as well as small drumlins and flutes – fluted moraine with a direct contact with the glacier (**Figures 3**, **4** and **Supplementary Figure 3**). The area is dotted with erratic boulders, some exceeding 1 m in diameter, and dissected by river channels up to 15 m wide and 6 m deep. Most of them were dry during the photogrammetric flight.

Among mapped fluvial and fluvioglacial landforms, we distinguished a large area of paraglacial erosion which is a surface built with glacial sediments (*sensu largo*) and heavily dissected by small gullies and rills (**Figure 3**). The area of paraglacial erosion is best developed on foothills of the glacial trough, most probably covered by glacial drift. Two narrow latero-frontal moraine ridges are developed, one along the eastern upper edge of the glacial trough (directly above the area of paraglacial erosion), and another one at foothills of taluses deposited on the eastern slopes of Red Hill. There is also a significant area (16% of the study area) of "not recognized surface" in terms of morphogenesis due to the lack of characteristic indicative morphological features (**Figure 3**).

There is no clear-cut periglacial trimline, because we do not observe the abrupt boundary between the ground shaped predominantly by freeze-thaw processes and the erosional or depositional glacial landforms. However, we can determine a glacial-periglacial transition zone between the lowest limit of periglacial landforms (the lowest reach of solifluction landforms – 47 m GPS h.) and the upper limit of glacial landforms (the uppermost reach of the lateral moraine ridge – 41 m GPS h.).

Periglacial phenomena are restricted to upper part of Red Hill (**Figures 2**, **3**), above the upper edge of the scarp located

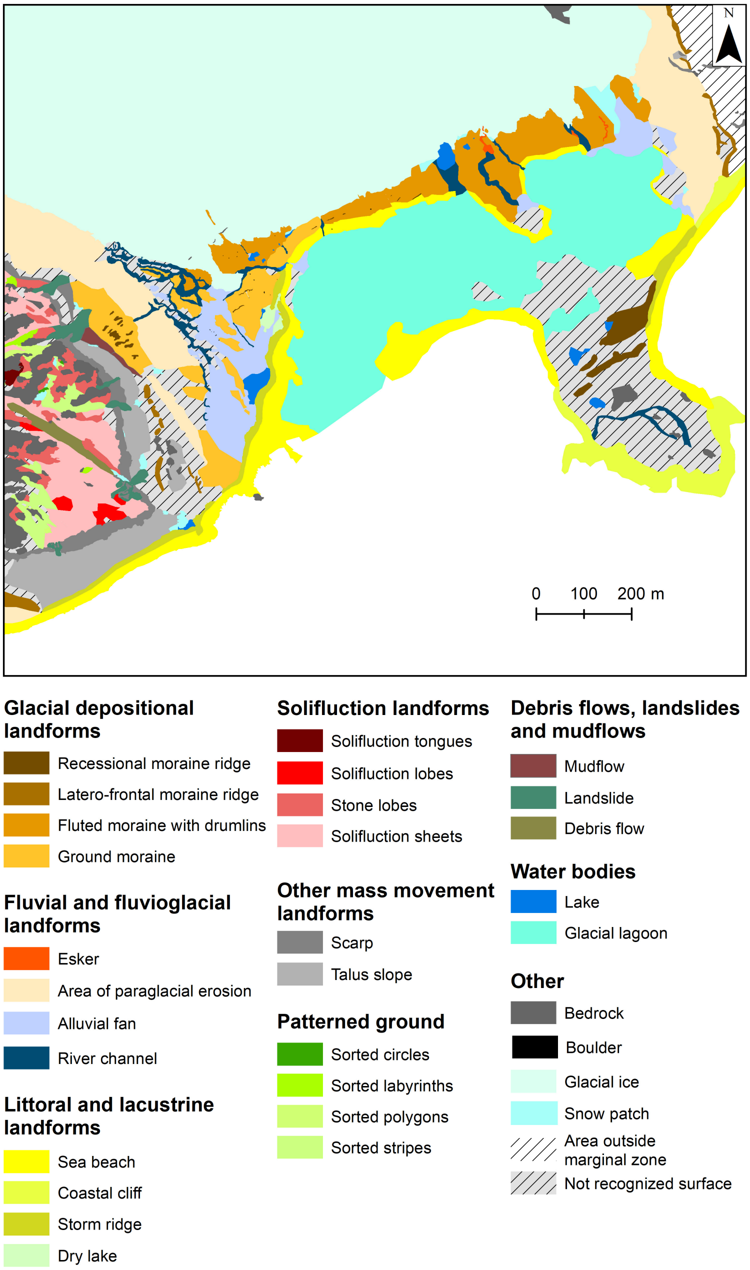

FIGURE 3 | Geomorphological map of Windy Glacier foreland and east side of Red Hill.

at 70–90 m GPS h. (**Supplementary Figure 1**). Most of this area is covered by solifluction landforms, especially solifluction sheets (3.95 ha). Among patterned ground, sorted stripes prevail (1.05 ha) and sorted circles occupy the smallest area (0.02 ha).

DISCUSSION

Methodological Considerations

Results of our large-scale geomorphological mapping of Windy Glacier foreland disagrees with the small-scale mapping of the same area performed by Da Rosa et al. (2020) based solely on satellite images. For example, stretches of beach are interpreted in the mentioned study as recessional moraine ridges, and a very well visible recessional moraine complex on Patelnia Point (**Supplementary Figure 1** and **Figure 3**) is not mapped by Da Rosa et al. (2020). Furthermore, the referenced study depicts three zones in terms of proglacial geomorphic activity: (i) zone of high activity (deglaciated in years 2000 – 2018, characterized by intensive paraglacial susceptibility), (ii) zone of moderate activity, deglaciated in years 1970s – 2000, and (iii) zone of low activity, deglaciated before 1970. We question the validity of the zonation in terms of dating and paraglacial activity. This is because contemporary intensive rilling and gullying can be seen on a slope in the western part of the foreland, immediately below the latero-frontal moraine ridge, deglaciated since 1979 (**Figures 2**, **3**). However, this area was labeled by Da Rosa et al. (2020) as the low activity zone, deglaciated before 1970s.

Similar, the periglacial investigation of López-Martínez et al. (2012) for South Shetland Islands based on relatively small-scale aerial photographs and satellite imagery did not take into account small ice-free areas on KGI such as Demay Point (**Figure 1B**) or Red Hill. This shows that the high-resolution images, e.g., obtained with the use of a UAV platform, is much more suited for detailed geomorphological studies. In many cases, the UAV BVLOS operations constitute a very good solution to reach remote locations and to provide security for the researchers.

Vectorization in GIS software can be easily performed on high-resolution orthophoto showing landforms which have easily distinguishable boundaries (e.g., sorted stripes, fluted moraine, and recessional moraine ridges), but it can be problematic when sorted polygons or solifluction sheets are delimited due to the lack of clear-cut morphological boundaries (**Supplementary Figure 2**). This is a source of a potential error in our mapping, however, this problem occurs also when field-based methods of mapping are used. Probably it neither would be overcome by machine learning, because at the end, manual identification would be necessary to validate the automatic mapping.

Certain small landforms can be relatively well visible but difficult to interpret based solely on the orthophoto map, because of snow or ice cover masking the full picture. In the western part of the Windy Glacier, inside the white surface (interpreted as glacier ice) we noticed a small and fragmented ridge running perpendicular to the glacier flow (**Figure 4A**, **Supplementary Figure 4**). If the white surface SE of the ridge was glacier ice, then the ridge could be interpreted as some erosional bedrock feature (e.g., a volcanic dike). It could be also an ablation cone, but there are no debris bands visible on the glacier surface to support such interpretation. We are inclined to interpret the outer SE fragments of the white surface as snow patches directly adjacent to the glacier margin. Therefore, the ridge is possible a small and fragmented recessional moraine ridge. We did not show this ridge, neither possible snow patches adjacent to the glacier on the geomorphological map (**Figure 3**) due to uncertainties mentioned.

Glacial Processes and Landforms

The two-part structure of the Windy Glacier foreland, composed of end-moraines and a lagoon in the distal and ground

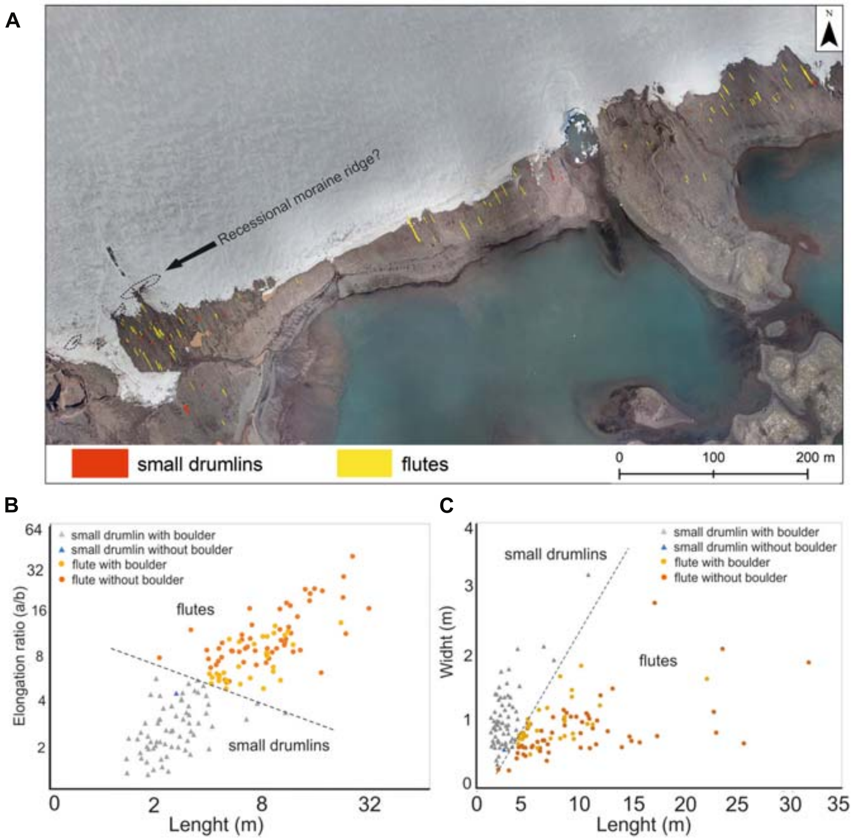

FIGURE 4 | Division between small drumlins and flutes in the Windy Glacier foreland based on their morphological characteristics; **(A)** spatial pattern of small drumlins and flutes; **(B)** length-to-elongation ratio diagram; **(C)** length-to-width diagram.

moraine, partly fluted, in the proximal part is typical of many contemporary low-relief mountain environments (Benn and Evans, 1998). The Windy Glacier foreland is somewhat similar to that of near-by Sphinx Glacier as both lack LIA terminal moraine ridges, because both terminated in the sea in the LIA maximum. The recessional moraine ridges of Windy Glacier, found beyond 1979 glacial limit, were probably formed between 1950 and 1977, because this is the time when nearby Ecology Glacier and Baranowski Glacier transgressed and formed significant push moraines (Birkenmajer, 2002; Dąbski et al., 2020).

Between 1979 and 2016 Windy Glacier front has retreated by 409 m (mean of 10 transects parallel to the glacier flow), which gives an average retreat rate of 11 m $year^{-1}$. This can be compared with 17 m $year^{-1}$ for near-by Ecology Glacier, 5–10 m $year^{-1}$ for Sphinx Glacier and 6.5–17 m $year^{-1}$ for Baranowski Glacier (Dąbski et al., 2020). The surface area loss and changes in accumulation area ratios of the glaciers is presented by Da Rosa et al. (2020). They concluded that the outlet glaciers of Warszawa Icelfield slowed down their recession in the 21st century due to regional cooling, which has been shown by Oliva et al. (2016). The small fragmented ridge (partly covered with snow or ice) adjacent and parallel to the Windy Glacier margin can be interpreted as a recessional moraine ridge resulting from a still-stand, possibly linked to this cooling. Another cause of the decrease in recession rate is the transition from tidewater to land-terminating character of the glaciers snouts, which recently became a case of Windy Glacier.

Subglacially streamlined landforms mapped as small drumlins (**Figure 4A**) could be also recognized as tapering flutes after Benn and Evans (1996), because of their small length, usually less than 5 m. However, their elongation ratio is less than seven (in most cases less than four) which is typical for drumlins according to Rose (1987). Two semi-separate swarms visible on the length-to-elongation ratio diagram allowed us to draw a line boundary between the small drumlins and flutes (**Figures 4B,C**). Except for one case, all small drumlins start with a relatively large boulder. The flutings are parallel-sided with or without boulders visible on stoss sides of the flutings (**Supplementary Figure 3**). However, lack of a visible boulder can results from a till cap deposited on top of it which prevents a boulder from exposure (Benn and Evans, 1996).

The tapering shape of small drumlins together with parallel-sided character of flutes can result from differences in till rheology, where the latter forms are created in places of weaker, more dilatant deformation till (Benn and Evans, 1996). Both forms are developed side by side on the Windy Glacier ground moraine patch, therefore it can be inferred that the basal till shear strength is significantly diversified. Two eskers developed in the eastern part of the fluted moraine (**Figure 3**) can indicate that the deformation till is relatively thin and channelized conduit flow is developed at the ice-bed interface (Clark and Walder, 1994). The subglacial channels are probably R-channels (Röthlisberger, 1972) due to low ice pressure (thin glacier) and shallow bedrock. Therefore, glacially eroded bedrock fragments can undergo uneven comminution producing diversified shear strength of the basal till.

Periglacial and Paraglacial Processes and Landforms

López-Martínez et al. (2012) published an extensive spatial analysis of periglacial landforms in South Shetland Islands based on fieldwork, standard aerial photography and satellite imagery. However, they disregarded the eastern and southern margins of Warszawa Icefield on KGI (including Red Hill). López-Martínez et al. (2012) concluded that the wet periglacial environment of the archipelago allows for active freeze-thaw processes on slopes and elevated platforms, especially between 30 and 100 m a.s.l. which accords with our findings. Former studies of periglacial landforms in ASPA 128 indicated dominance of solifluction landforms, taluses and some presence of sorted patterned ground as well as frost wedges (Birkenmajer, 1980; Dutkiewicz, 1982; Kostrzewski et al., 2002; Dąbski et al., 2017). However, large-scale sorted circles are inactive or semi-active (Dutkiewicz, 1982; Dąbski et al., 2017), which testifies for the climatic amelioration since their development.

The study of Dąbski et al. (2017) performed on near-by Demay Point (**Figure 1B**) revealed sorted patterned ground already at 25.5 m GPS h., but mean elevation for this type of periglacial landforms was determined at 95.0 m GPS h. Solifluction landforms were detected on Demay Point already at 22.1 m GPS h. but mean elevation for solifluction was 85.9 m GPS h. The values of mean altitudes on the mentioned landforms are similar to those obtained in this study (95.25 m GPS h. for sorted patterned ground and 90.25 m GPS h. for solifluction landforms). The main difference between Damay Point and Red Hill is that the scarp on the latter one (**Supplementary Figure 1**) constitutes a threshold for the lowermost occurrence of the periglacial landforms, while the southern slope of Demay Point descends gently to about 20 m GPS h. allowing for significantly lower elevation of the freeze-thaw driven landforms. In both places solifluction sheets predominate among periglacial landforms (Dąbski et al., 2017). Some sorted patterned ground (e.g., large-scale sorted circles) are not developed on Red Hill at all, however, most of the sorted patterned ground looks active or semi-active as only some coarse dominates are covered by lichens or shallow tundra vegetation, while on Demay Point they look rather inactive or semi-active.

Recent liberation from glacier ice triggers quick readjustment of the landsystem to subaerial conditions which results in paraglacial processes (Ballantyne, 2002), responsible for delivery of sediments for glacial landforms to the lagoon or marine environments (Zwoliński, 2007). Da Rosa et al. (2020) emphasize the role of intense paraglacial processes acting close to the Warszawa Icelfield margin. Our results fully support this finding as evidence of intense gullying and rilling (area of paraglacial erosion) is visible on 9.5 ha in the forelands of Windy Glacier – almost half of the large glacial lagoon area.

CONCLUSION

The UAV BVLOS photogrammetric survey over Windy Glacier foreland and Red Hill allowed for elaboration of a high-resolution orthophoto and DEM on which we mapped 31 types of landforms, water bodies and other surfaces (e.g., glacier ice, snow patches, not recognized surface). The glacier margin was directly exposed to marine environment until 1979. Most area liberated from glacier ice afterward is occupied by a glacial lagoon with which the glacier lost contact and became completely land-terminated in 2006 which stopped glacial calving – the most efficient process of ablation, slowing the rate of deglaciation.

Largest terrestrial surface is occupied by fluvial (with a significant share of paraglacial rills and gullies), fluvioglacial and littoral landforms. Between 2006 and 2016 the glacier deposited a well-developed patch of fluted moraine with small drumlins. Distinction between flutes and small drumlins is based on length-to-elongation diagram, more elongated landforms being treated as flutes.

The upper part of Red Hill, above the scarp is subject of intensive periglaciation with well-developed solifluction landforms and sorted patterned ground. The frost-sorted structures look active (due to the lack of vegetation) but there are no large-scale sorted circles as on a near-by Demay Point. Between 41 m and 47 m GPS h. we set a zone of transition between the glacial and periglacial domains.

The PW-ZOOM fixed-wing UAV BVLOS operation, followed by image processing, including the use of SfM algorithm and photointerpretation, proved to be helpful in gathering valuable geomorphological information in a location distant from the polar station where field study is difficult.

DATA AVAILABILITY STATEMENT

The original contributions presented in the study are included in the article/**Supplementary Material**, further inquiries can be directed to the corresponding author/s.

AUTHOR CONTRIBUTIONS

KK: geomorphological mapping, calculations of landforms area, and glacial recession rate, and comments to the manuscript. MD: writing of the manuscript. AZ: coordination and programming of UAV flights over Windy Glacier and preparation of source data (orthophoto) and comments to the manuscript. All authors contributed to the article and approved the submitted version.

FUNDING

Funding was provided by: (1) Project No 197810, A novel approach to monitoring the impact of climate change on Antarctic ecosystems – MONICA, funded from Norway Grants in the Polish-Norwegian Research Programme operated by the National Centre for Research and Development; (2) Project H2020-MSCA-RISE-2016: innoVation in geOspatiaL and 3D daTA (VOLTA), Reference GA No. 734687. H2020 VOLTA activities are supported by the Polish Ministry of Science and Higher Education in the frame of H2020 co-financed projects No. 3934/H2020/2018/2 and 379067/PnH/2017. Open-access financed by the University of Warsaw within "Excellence Initiative – Research University" Programme.

ACKNOWLEDGMENTS

The article is based on a B.Sc. diploma of KK prepared with a use of data obtained in two projects (MONICA and VOLTA) and with the support of Henryk Arctowski, Polish Antarctic Station.

SUPPLEMENTARY MATERIAL

The Supplementary Material for this article can be found online at: https://www.frontiersin.org/articles/10.3389/feart.2021.671985/full#supplementary-material

REFERENCES

Ballantyne, C. K. (2002). Paraglacial geomorphology. *Quat. Sci. Rev.* 21, 1935–2017. doi: 10.1016/S0277-3791(02)00005-7

Benjumea, B., Macheret, Y., Navarro, F., and Teixidó, T. (2003). Estimation of water content in a temperate glacier from radar and seismic sounding data. *Ann. Glaciol.* 37, 317–324. doi: 10.3189/172756403781815924

Benn, D. I., and Evans, D. J. A. (1996). The interpretation and classification of sublacially-deformed materials. *Quat. Sci. Rev.* 15, 23–52. doi: 10.1016/0277-3791(95)00082-8

Benn, D., and Evans, D. J. A. (1998). *Glaciers and Glaciations*. London: Arnold.

Birkenmajer, K. (1980). Geology of admiralty bay, king george Island (South Shetland Islands) -an outline. *Pol. Polar Res.* 1, 29–54.

Birkenmajer, K. (1981). Raised marine features and glacial history in the vicinity of H. Arctowski station, King George Island (South Shetland Islands, West Antarctica). *Bull. Acad. Pol. Sci. Ser. Sci. Terre* 29, 109–117.

Birkenmajer, K. (2002). Retreat of ecology glacier, admirality bay, king george Island (South Shetland Islands, West Antarctica), 1956–2001. *Bull. Pol. Acad. Sci. Earth Sci.* 50, 16–29.

Chwedorzewska, K. J., and Bednarek, P. T. (2011). Genetic and epigenetic studies on populations of Deschampsia antarctica Desv. from contrasting environments at King George Island (Antarctic). *Pol. Polar Res.* 32, 15–26.

Clark, P. U., and Walder, J. S. (1994). Subglacial drainage, eskers, and deforming beds beneath the Laurentide and Euroasian ice sheets. *Bull. Geol. Soc. Am.* 106, 304–314. doi: 10.1130/0016-76061994106<0304:SDEADB<2.3.CO;2

Cook, A. J., Fox, A. J., Vaughan, D. G., and Ferrigno, J. G. (2005). Retreating glacier fronts on the Antarctic Peninsula over the past half-century. *Science* 308, 541–544. doi: 10.1126/science.1104235

Da Rosa, K. K., Perondi, C., Veettil, B. K., Auger, J. D., and Simões, J. C. (2020). Contrasting responces of land-terminating glaciers to recent climate variations in King George Island, Antarctica. *Antarct. Sci.* 32, 398–407. doi: 10.1017/S0954102020000279

Dąbski, M., Zmarz, A., Pabjanek, P., Korczak-Abshire, M., Karsznia, I., and Chwedorzewska, K. (2017). UAV-Based detection and spatial analyses of periglacial landforms on Demay Point (King George Island, South Shetland Islands, Antarctica). *Geomorphology* 290, 29–38. doi: 10.1016/j.geomorph.2017.03.033

Dąbski, M., Zmarz, A., Rodzewicz, M., Korczak-Abshire, M., Karsznia, I., Lach, K. M., et al. (2020). Mapping glacier forelands based on UAV BVLOS operation in Antarctica. *Remote Sens.* 12:630. doi: 10.3390/rs12040630

Dutkiewicz, L. (1982). Preliminary results of investigations on some periglacial phenomena on King George Island, South Shetlands. *Biul. Peryglac.* 29, 13–23.

Fudala, K., and Bialik, R. J. (2020). Breeding colony dynamics of southern elephant seals at patelnia point, King George Island, Antarctica. *Remote Sens.* 12:2964. doi: 10.3390/rs12182964

Goetzendorf-Grabowski, T., and Rodzewicz, M. (2017). Design of UAV for photogrammetric mission in Antarctic area. challenges in European aerospace. *Proc. Inst. Mech. Eng. G J. Aerosp. Eng.* 231, 1660–1675. doi: 10.1177/0954410016656881

Gonera, P., and Rachlewicz, G. (1997). Snow cover at Arctowski Station, King George Island, in winter 1991. *Pol. Polar Res.* 18, 3–14.

Kejna, M., Araźny, A., and Sobota, I. (2013). Climatic change on King George Island in the years 1948–2011. *Pol. Polar Res.* 34, 213–235.

Kostrzewski, A., Rachlewicz, G., and Zwolinski, Z. (1998). "Geomorphological map of the western coast of Admiralty Bay, King George Island," in *Relief, Quaternary Paleogeography and Changes of the Polar Environment*, ed. J. Repelewska-Pękalowa (Lublin: Maria Curie-Skłodowska University Press), 71–77.

Kostrzewski, A., Rachlewicz, G., and Zwolinski, Z. (2002). The relief of theWestern coast of Admiralty Bay, King George Island, South Shetlands. *Quaest. Geogr.* 22, 43–58.

Lee, J. R., Raymond, B., Bracegirdle, T. J., Chadès, I., Fuller, R. A., Shaw, J. D., et al. (2017). Climate change drives expansion of Antarctic ice-free habitat. *Nature* 547, 49–54. doi: 10.1038/nature22996

López-Martínez, J., Serrano, E., Schmid, T., Mink, S., and Linés, C. (2012). Periglacial processes and landforms in the South Shetland Islands (northern Antarctic Peninsula region). *Geomorphology* 15, 62–79. doi: 10.1016/j.geomorph.2011.12.018

Marsz, A. A., and Styszyńska, A. (2000). "Główne cechy klimatu rejonu Polskiej Stacji Antarktycznej im. H. Arctowskiego (Antarktyka Zachodnia, Szetlandy Południowe, Wyspa Króla Jerzego)," in *The maine Features of the Climate in the Region of the Polish Antarctic Station H. Arctowski (West Antarctica, South Shetland Islands, King George Island) – in Polish*, eds A. A. Marsz and A. Styszyńska (Gdynia: Wyższa Szkoła Morska).

Meredith, M. P., and King, J. C. (2005). Rapid climate change in the ocean to the west of the Antarctic Peninsula during the second half of the 20th century. *Geophys. Res. Lett.* 32:19604. doi: 10.1029/2005GL024042

Oliva, M., Navarro, F., Hrbácek, F., Hernández, A., Nývlt, D., Pereira, P., et al. (2016). Recent regional climate cooling on the Antarctic Peninsula and associated impacts on the cryosphere. *Sci. Total. Environ.* 580, 210–223. doi: 10.1016/j.scitotenv.2016.12.030

Osmanoğlu, B., Braun, B., Hock, R., and Navarro, F. J. (2013). Surface velocity and ice discharge of the ice cap on King George Island, Antarctica. *Ann. Glaciol.* 54, 111–119. doi: 10.3189/2013AoG63A517

Pętlicki, M., Sziło, J., MacDonell, S., Vivero, S., and Bialik, R. J. (2017). Recent deceleration of the ice elevation change of ecology Glacier (King George Island, Antarctica). *Remote Sens.* 9:520. doi: 10.3390/rs9060520

Pudełko, R. (2003). Topographic map of the SSSI No. 8, King George Island, West Antarctica. *Pol. Polar Res.* 24, 53–60.

Pudełko, R., Angiel, P. J., Potocki, M., Jędrejek, A. J., and Kozak, M. (2018). Fluctuation of Glacial retreat rates in the Eastern Part of Warszawa Icefield, King George Island, Antarctica, 1979–2018. *Remote Sens.* 10:892. doi: 10.3390/rs10060892

Rachlewicz, G. (1999). Glacial relief and deposits of the western coast of Admiralty Bay, King George Island, South Shetland Islands. *Pol. Polar Res.* 20, 89–130.

Robakiewicz, M., and Rakusa-Suszczewski, S. (1999). Application of 3D circulation model to Admiralty Bay, King George Island, Antarctica. *Pol. Polar Res.* 20, 43–58.

Rodzewicz, M., Głowacki, D., and Hajduk, J. (2017). Some dynamic aspects of photogrammetry missions performed by "PW-ZOOM" – the UAV of Warsaw University of Technology. *Arch. Mech. Eng.* 64, 37–55. doi: 10.1515/meceng-2017-0003

Rose, J. (1987). "Drumlins as part of a glacier bedform continuum," in *Drumlin Symposium*, eds J. Menzies and J. Rose (Rotterdam: Balkena), 103–116.

Röthlisberger, H. (1972). Water pressure in intra- and subglacial channels. *J. Glac.* 11, 177–203.

Sierakowski, K., Korczak-Abshire, M., and Jadwiszczak, P. (2017). Changes in bird communities of Admiralty Bay, King George Island (West Antarctica): insights from monitoring data (1977–1996). *Pol. Polar Res.* 38, 229–260. doi: 10.1515/popore-2017-0010

Sziło, J., and Bialik, R. J. (2018). Recession and ice surface elevation changes of baranowski glacier and its impact on proglacial relief (King George Island,West Antarctica). *Geosciences* 8:355. doi: 10.3390/geosciences8100355

Turner, J., Barrand, N. E., Bracegirdle, T. J., Convey, P., Hodgson, D. A., Jarvis, M., et al. (2014). Antarctic climate change and the environment: an update. *Polar Rec.* 50, 237–259. doi: 10.1017/S0032247413000296

Wierzbicki, G. (2009). Wiatry huraganowe w 2008 roku w Zatoce Admiralicji, Wyspa Króla Jerzego, Antarktyda Zachodnia (Storm winds in 2008 in Admiralty Bay, King George Island, West Antarctica–in Polish). *Przeg. Nauk. Inż. Kształt. Środ.* 18, 47–55.

World Glacier Monitoring Service [WGMS] (2020). *World GlacierMonitoring Service*. Available online at: http://wgms.ch. (Accessed January 7, 2021).

Young Kim, K., Lee, J., Ho Hong, M., Kuk Hong, J., Keun Jin, Y., and Shon, H. (2010). Seismic and radar investigations of Fourcade Glacier on King George Island, Antarctica. *Polar Res.* 29, 298–310. doi: 10.3402/polar.v29i3.6082

Zmarz, A., Rodzewicz, M., Dąbski, M., Karsznia, I., Korczak-Abshire, M., and Chwedorzewska, K. J. (2018). Application of UAV BVLOS remote sensing data for multi-faceted analysis of Antarctic ecosystem. *Remote Sens. Environ.* 217, 375–388. doi: 10.1016/j.rse.2018.08.031

Znój, A., Chwedorzewska, K. J., Androsiuk, P., Cuba-Diaz, M., Giełwanowska, I., Koc, J., et al. (2017). Rapid environmental changes in the Western Antarctic Peninsula region due to climate change and human activity. *Appl. Ecol. Environ. Res.* 15, 525–539. doi: 10.15666/aeer/1504_525539

Zwoliński, Z. (2007). *Mobilnośœ Materii Mineralnej na Obszarach Paraglacjalnych, Wyspa Króla Jerzego, Antarktyka Zachodnia (The Mobility of Mineral Matter in Paraglacial Area, King George Island, Western Antarctica—in Polish). Seria Geograficzna 74*. Poznań: Adam Mickiewicz University Press.

Zwoliński, Z., Kejna, M., Rachlewicz, G., Sobota, I., and Szpikowski, J. (2016). "Solute and sedimentary fluxes on King George Island," in *Source-to-Sink Fluxes in Undisturbed Cold Environments*, eds A. A. Beylich, J. C. Dixon, and Z. Zwoliński (Cambridge: Cambridge University Press), 213–237.

Conflict of Interest: The authors declare that the research was conducted in the absence of any commercial or financial relationships that could be construed as a potential conflict of interest.

frontiers in Earth Science

ORIGINAL RESEARCH
published: 10 May 2021
doi: 10.3389/feart.2021.664201

Research on the Dispatching Rules of Inter-Basin Water Transfer Projects Based on the Two-Dimensional Scheduling Diagram

Siyu Cai[1], *Long Sun*[2], *Qingtao Liu*[2]*, *Yi Ji*[3] *and Hao Wang*[4]

[1] Department of Hydraulic Engineering, Tsinghua University, Beijing, China, [2] Information Center (Hydrology Monitor and Forecast Center), Ministry of Water Resources, Beijing, China, [3] School of Water Conservancy and Civil Engineering, Northeast Agricultural University, Harbin, China, [4] China Institute of Water Resources and Hydropower Research, Beijing, China

Inter-basin water transfer projects play an important role in allocating water resources that vary both in temporal and spatial scale while supporting regional development. In the practical operation of inter-basin water transfer projects, high water level and less inflow runoff would result in water supply destruction, while low water level and more inflow runoff would cause abandoned water. How to play the compensation roles of hydrological characteristics and storage capacities of multi-reservoirs to maximize the utilization efficiency of water resources, the key is to select the basis for the decision-making of starting water transfer process. In this paper, we selected the "Datong-Huangshui" water transfer project as the research subject, analyzed the composition of the inter-basin water transfer system, and constructed a dispatching rule extraction model including water transfer rules, water diversion rules, and water supply rules. Then the NSGA-II was used to solve the multi-objective optimization model to obtain the Pareto frontier solution set of the dispatching rules. Finally, the optimal operation scheme was determined and discussed according to the scheduling scheme decision model. The model itself was based on the gray target model and prospect theory. We found that: (1) The optimal target frontier obtained by the two-dimensional scheduling diagram and the hedging rules for water supply was closer to the theoretical optimal frontier of the multi-objective problem. This result indicated that the two-dimensional scheduling diagram and the hedging rules for water supply could better guide the water diversion operation of inter-basin water transfer projects. (2) Based on the multi-objective optimal operation schemes set, the OPT scheme obtained by the scheduling scheme decision model using gray target model and prospect theory could generate 359 million Kwh. At the same time, it could guarantee 90% of municipal and industrial water supply and 85% of agricultural water supply.

Keywords: inter-basin water transfer, two-dimensional scheduling diagram, hedging rules for water supply, NSGA- II, scheme optimization

Edited by:
Yang Yu,
Beijing Forestry University, China

Reviewed by:
Haibo Ma,
China Three Gorges University, China
Jun Niu,
China Agricultural University, China
Peng Shi,
Xi'an University of Technology, China

***Correspondence:**
Qingtao Liu
liuqtmwr@163.com

Specialty section:
This article was submitted to Hydrosphere, a section of the journal Frontiers in Earth Science

Received: *04 February 2021*
Accepted: *07 April 2021*
Published: *10 May 2021*

Citation:
Cai S, Sun L, Liu Q, Ji Y and Wang H (2021) Research on the Dispatching Rules of Inter-Basin Water Transfer Projects Based on the Two-Dimensional Scheduling Diagram. Front. Earth Sci. 9:664201. doi: 10.3389/feart.2021.664201

INTRODUCTION

Inter-basin water transfer projects are critical to minimize the conflicts between competing water resource demands and supplies (Bonacci and Andric, 2010; Sadegh et al., 2010; Yu et al., 2020). The inter-basin water transfer rules, particularly the scheduling process, are subject to numerous studies because it is challenging to balance between local water demand, the environmental consequences and the economy and effectiveness of water diversion to avoid water loss (Li et al., 2015). The process requires a formulation of optimal scheduling decisions and reasonable arrangements for diversion time, as well as the amount of water diversion and supply (Jafarzadegan et al., 2014).

The joint dispatching rules for multi-reservoirs of the inter-basin water transfer project usually focus on two aspects: the determination of water transfer rules and the determination of water supply rules. Water transfer rules included consideration from upper-level decision makers regarding: (1) when and how much water should be transferred from the source reservoir (group) to the receiving reservoir (group), (2) water allocation in the receiving area. Water supply rules included consideration from the lower-level decision makers about how the reservoir (group) can provide water users with timely and appropriate amounts of water when the water transfer behavior is initiated. So far, the most commonly used dispatching rules for joint operation of multi-reservoirs are scheduling diagrams and functions. Chang et al. (Chang and Chang, 2009) added a joint water supply dispatching line to a reservoir scheduling diagram, and determined which reservoir should supply water to the public water supply area according to the positional relationship between the storage capacity of the reservoir and the joint dispatching line. Guo et al. (2011) used aggregate reservoir scheduling diagrams and two-dimensional reservoir scheduling diagrams to determine the total water supply volume of multi-reservoirs, and then calculated the adjustment of each reservoir according to the water allocation rules. Zhou (Zhou et al., 2012) used the implicit stochastic optimization method to determine the optimal operation process of the multi-reservoirs, and then determined the scheduling function for each scheduling period within a year through the regression analysis, and finally used the simulation method to verify and modify the determined scheduling function.

Simulation, optimization, simulation and optimization are the common methods for rule extractions. Simulation methods are divided into general simulation systems and specific basin simulation systems according to their versatility (Yeh, 1985; Wurbs, 1993; Rani and Moreira, 2010). Optimization methods are mainly divided into mathematical programming methods and artificial intelligence optimization methods (Hall et al., 1969; Heidari et al., 1971; Lund and Ferreira, 1996; Hsu and Cheng, 2002; Tung et al., 2003; Reis et al., 2006). Currently, the most widely used method is the simulation and optimization method, which uses the parameters of dispatching rules as the decision variables to directly optimize the dispatching rules. Neelakantan and Pundarikathan (Neelakantan and Pundarikanthan, 2000) embedded the feed-back neural network method into the nonlinear programming model, and established a relatively special simulation and optimization model. Chang et al. (2003, 2010), Tung et al. (2003); Suiadee and Tingsanchali (2007), Hormwichian et al. (2009) used different forms of genetic algorithms to determine the joint operation rules of reservoir groups based on the simulation and optimization method. Sulis (2009) established a simulation optimization model for multi-reservoirs based on GRID optimization method. Kangrang et al. (2009) used a combination method of heuristic algorithm and simulation model to determine the scheduling diagram of Ubolratana Reservoir in Thailand.

In the past, the starting standards for transferring water were based on the current storage volume of the reservoir. However, it did not consider the inflow runoff of the source and receiving reservoir during the water transfer period. As a result, "high water level and less inflow runoff" would result in water supply destruction while "low water level and more inflow runoff" would cause abandoned water. In this paper, we tried to solve the above problem using the dispatching rules extracted from the two-dimensional scheduling diagram. Accordingly, the objective of this paper is: (1) to analyze the composition of the inter-basin water transfer system, and to construct a dispatching rule extraction model including water transfer rules, water diversion rules, and water supply rules; (2) to use the Pareto frontier solution set of the dispatching rules obtained from the NSGA-II (Liu et al., 2020) to solve the multi-objective optimization model; and (3) to determine the optimal operation scheme according to the scheduling scheme decision model based on gray target model (Luo et al., 2001) and prospect theory (Tversky and Kahneman, 1992). The results should provide a basis for decision-making process in the "Datong-Huangshui" area.

STUDY AREA

The Huangshui Basin, that drains from the Huangshui River (latitude N 36°02′∼37°28′, longitude E 100°42′∼103°01′) and the Datong River (latitude N 36°30′∼38°25′, longitude E 98°30′∼103°15′), is a first-level tributary of the upper reaches of the Yellow River. As shown in **Figure 1**, the Huangshui River flows from northwest to southeast, originating in Haiyan County, Qinghai Province, flowing eastward to Minhe County, and entering the Yellow River in Yongjing County, Gansu Province. Of the 374 km long and the 17,733 km^2 area of the Huangshui River, 336 km and 16,120 km^2 are located in Qinghai Province. This paper examined the "Datong-Huangshui" water transfer project as an example to study the optimal joint operation of inter-basin multi-reservoirs. The hydraulic connection of the inter-basin water transfer project is shown in **Figure 2**. In this project, the Shitouxia Reservoir (STX for short), as a water source reservoir, has no hydraulic connection with the receiving reservoir (Heiquan Reservoir, HQ for short), but they are connected to each other through the main water transfer canal. The two reservoirs have different dispatching targets in the inter-basin water transfer system. The STX Reservoir transfers water and generates power, and the electric dispatching is subject to water dispatching. The HQ Reservoir supplies water by using

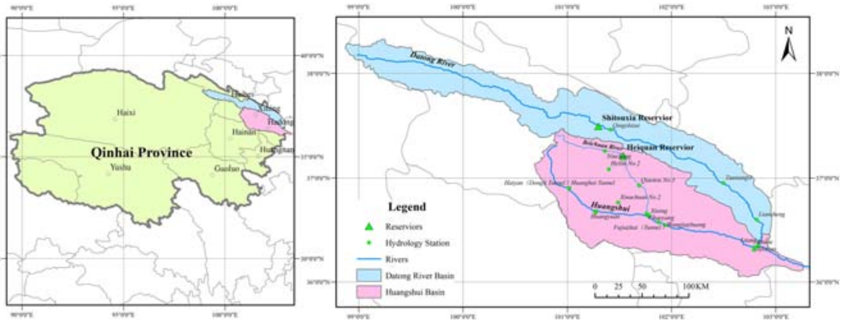

FIGURE 1 | The location of research area.

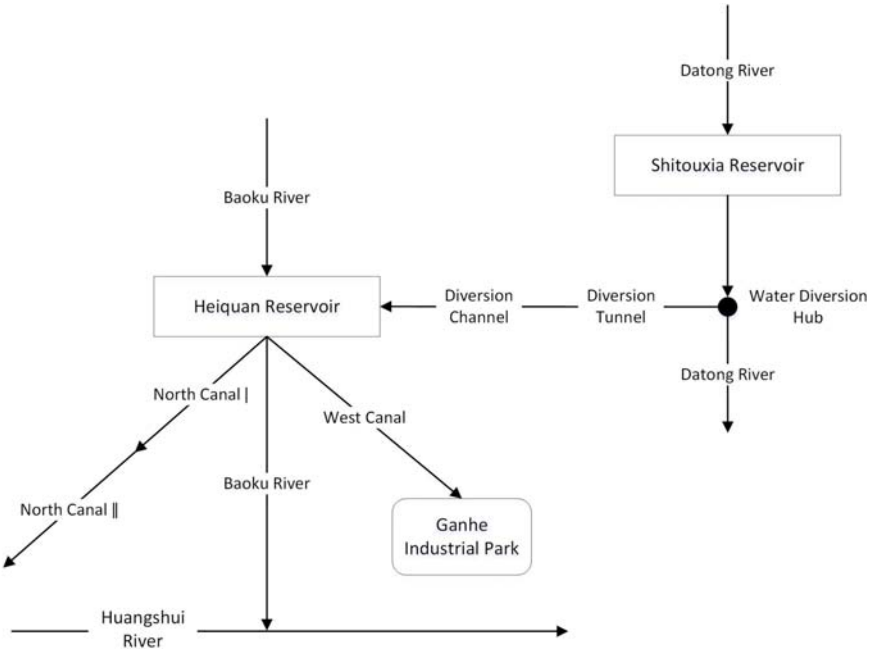

FIGURE 2 | The hydraulic connection of the “Datong-Huangshui” water transfer project.

natural reservoir inflow and transferring water through its own function of regulation and storage.

METHODS

Compared with the normal water supply system of multi-reservoirs, the dispatching rules of the inter-basin water transfer system should consider reasonable water supply, water transfer and diversion. Therefore, the dispatching rules generally include: water transfer rule, water diversion rule and water supply rule, which jointly guide the operation of reservoirs and optimize the benefits of water transfer system. Water transfer rule and water diversion rule are used to guide the operation of the source and the receiving reservoir, respectively. The optimization of the two rules is to realize the optimal benefit of water transfer projects on the basis of weighing water using efficiency of the source reservoir and water diversion target of the receiving reservoir. Water supply rule is to maximize the water use benefit of the receiving reservoir under consideration of water diversion. Consequently, the joint dispatching rule model proposed in this paper mainly involved three modules: power generation module, water transfer and diversion module, water supply module. For each module, its dispatching rules were constructed based on power generation scheduling diagram, two-dimensional water diversion scheduling diagram and hedging rules for water supply, respectively.

Water Diversion Operation Model Based on the Two-Dimensional Water Diversion Scheduling Diagram

Water Diversion Dispatching Rule

The two-dimensional water diversion scheduling diagram selected the state variables at the beginning of the scheduling

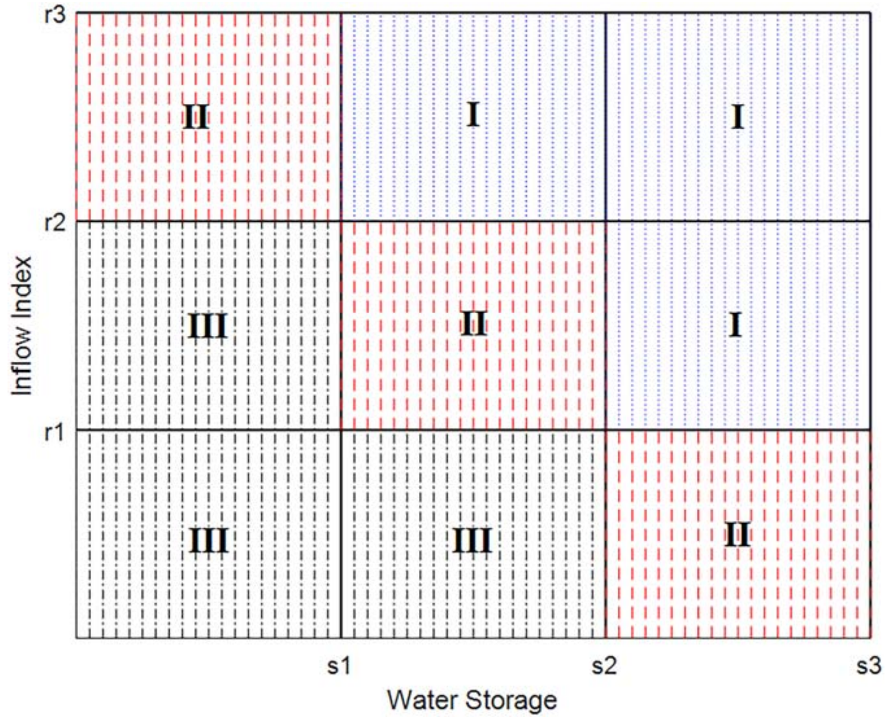

FIGURE 3 | The two-dimensional water diversion scheduling diagram.

period and the state variables during the scheduling period as the coordinate axes, respectively. The water storage capacity of the receiving reservoir was used as the state variable at the beginning of the scheduling period, and the inflow index calculated based on the reservoir inflow and the water supply target were taken as the state variables during the scheduling period. Because monthly water demand varied greatly with the increase in the proportion of agricultural water in the study area, there were different satisfaction degrees of water demand under the same inflow runoff. Therefore, this paper chose to use the ratio of the reservoir inflow and the difference between water demand and the minimum diversion amount as the inflow index. From the perspective of mapping, the water diversion dispatching rule was a multivariate function of the scheduling period and the two state variables. The mapping relationship between the function and the independent variable was expressed as the water diversion dispatching rule based on two-dimensional reservoir scheduling diagram.

In order to explain the specific water diversion rules shown in the two-dimensional water diversion scheduling diagram, we projected the section perpendicular to the time axis of the scheduling diagram in a certain scheduling period to the coordinate plane determined by two state variables. This method resulted in a plane figure of the two-dimensional water diversion scheduling diagram during a scheduling period (**Figure 3**). Water diversion rules of the inter-basin water transfer project are determined by the two state variables: water storage and inflow index. The decisions of water diversion can be divided into three situations: minimum water diversion, restricted water diversion and full water diversion. The combination of the two state variables constituted three types of water diversion modes under nine situations in the two-dimensional scheduling diagram. The specific rules are shown in **Table 1**.

Objective of Water Diversion

Water diversion aims to meet the water demand of the water receiving area. Therefore, the minimum difference between the annual actual diversion amount and the target diversion amount can be used as the objective of the water transfer and diversion module.

$$\min_{x} f_1 = \sum_{i=1}^{m} \left| D - \sum_{j=1}^{n} B_{i,j} \right| \tag{1}$$

Where, D and $B_{i,j}$ represent the target diversion amount and the actual water diversion amount, respectively. The target water diversion amount is determined according to the inflow runoff and water demand of the receiving reservoir. i and j represent the serial number of year and month, respectively. m and n

TABLE 1 | Dispatching areas and rules of the water diversion scheduling diagram.

Area No.	Dispatching area	Dispatching rule (Mode)
I	Minimum water diversion area	Mode 1: $Q = 10\text{m}^3/\text{s}$
II	Restricted water diversion area	Mode 2: $Q = 20\text{m}^3/\text{s}$
III	Full water diversion area	Mode 3: $Q = 35\text{m}^3/\text{s}$

Q means the amount of water diversion.

represent the amount of years and months during the calculated period, respectively.

Water Supply Operation Model Based on Hedging Rules for Water Supply

Water Supply Dispatching Rule

There are three types of water use units for HQ Reservoir. However, when hedging rules (Ji et al., 2016) for water supply are applied, only the optimal total water supply amount during the dispatching period can be obtained. Therefore, the total water supply calculated by the hedging rules need to be allocated to each water use unit. For the three water use units of HQ Reservoir, the priority of water use from high to low is for municipal, industrial and agricultural use. Assuming that the water supply volume of the three water use units during the period *t* were $R_1(t)$, $R_2(t)$ and $R_3(t)$, respectively, we established water supply rules for orderly allocation based on the elastic coefficients of different water use units. The specific rules are as follows:

The amount of water supply for municipal water:

$$R_1(t) = \begin{cases} D_1(t), & R^*(t) \geq D_1(t) \\ R^*(t), & R^*(t) < D_1(t) \end{cases} \tag{2}$$

The amount of water supply for industrial water:

$$R_2(t) = \begin{cases} D_2(t), & R^*(t) - R_1(t) \geq D_2(t) + \alpha_3 D_3(t) \\ \alpha_2 D_2(t), & R^*(t) - R_1(t) < D_2(t) + \alpha_3 D_3(t) \end{cases} \tag{3}$$

The amount of water supply for agricultural water:

$$R_3(t) = \begin{cases} D_3(t), & R^*(t) - R_1(t) - R_2(t) \geq D_3(t) \\ R^*(t) - R_1(t) - R_2(t), & else \end{cases} \tag{4}$$

Where, $R^*(t)$ represents available water supply, which is calculated according to initial water storage and water diversion amount. $D_1(t)$, $D_2(t)$ and $D_3(t)$ represent municipal water demand, industrial water demand and agricultural water demand, respectively. α represents restricting coefficient for water supply.

Objective of Water Supply

The purpose of water supply scheduling is to minimize the loss of water during the reservoir operation. In addition to the linear function relationship within the elasticity of demand, the amount of water losses and water shortage generally show a convex function relationship. In other words, the minimum cumulative water shortage amount does not necessarily guarantee the minimum economic water loss. Therefore, this paper chose water shortage index as the objective of water supply. The calculation formula of the water shortage index is as follows:

$$SI_{i,t} = \left(\frac{D_{i,t} - R_{i,t}}{D_{i,t}} \right)^m \tag{5}$$

Where, $SI_{i,t}$ represents the water shortage index of water use unit *i* during time period *t*. $D_{i,t}$ represents water demand amount of water use unit *i* during time period *t*. $R_{i,t}$ represents water supply amount of water use unit *i* during time period *t*. *m* is the benefit index, and the value is generally 2.

Constrained Conditions

(1) Constraint of water balance:

$$V_{t+1} = V_t + I_t - S_t - q_t - l_t \tag{6}$$

Where, V_{t+1}, V_t are the reservoir storage volume at time *t* and *t+1*, respectively; I_t is the inflow runoff at time *t*; S_t is the water amount for power generation at time *t*; q_t is the abandoned water at time *t*; l_t is the water loss at time *t*, including evaporation and leakage.

(2) Constraint of reservoir storage capacity:

$$V_d \leq V_t \leq V_c \tag{7}$$

Where, V_d, V_c are the dead storage capacity and normal storage capacity of the reservoir, respectively.

(3) Constraint of output during the period:

$$N_{\min} \leq N_t \leq N_{\max} \tag{8}$$

Where, $N_{\min}$, $N_{\max}$ are the minimum output and the installed output of the reservoir, respectively.

(4) Constraint of discharged water:

$$q_{\min} \leq q_t \leq q_{\max} \tag{9}$$

Where, $q_{\min}$ is the minimum discharged water, in this paper it refers to the ecological water demand in the downstream. $q_{\max}$ is the maximum discharged water that will not cause damage to the downstream.

(5) Constraint of power generation guarantee rate:

$$p_{pg} \geq p_{pg,d} \tag{10}$$

Where, p_{pg} is the power generation guarantee rate, $p_{pg,d}$ is the designed value for the power generation guarantee rate.

(6) Constraint of water transfer guarantee rate:

$$p_{tg} \geq p_{tg,d} \tag{11}$$

Where, p_{tg} is the water transfer guarantee rate; $p_{tg,d}$ is the designed value for the water transfer guarantee rate.

Implementation of the Joint Operation Models

A FORTRAN program was coded to implement the joint operation model and NSGA-II algorithm. The joint operation model includes water transfer rules, water diversion rules, and water supply rules. Among which, the water diversion rules and water supply rules were designed based on the two-dimensional scheduling diagram and the hedging rules for water supply, respectively. In addition, the population size, the maximum number of iterations, the crossover probability and the mutation probability of NSGA-II were set to 100, 1000, 0.75 and 0.01, respectively. Then 200 groups of Pareto optimal solutions were obtained after calculation. The implementation processes are shown in **Figure 4**.

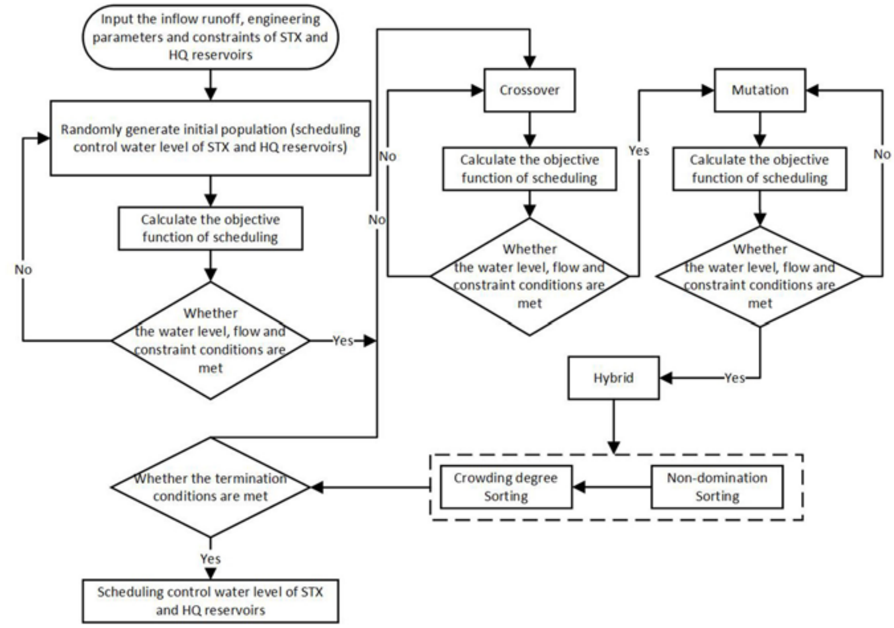

FIGURE 4 | The implementation processes.

RESULTS

Solution and Result Analysis of the Joint Operation Model

In order to analyze the rationale and effectiveness of the dispatching rules designed in this paper, a set of comparison schemes (CS1 and CS2) were set (**Table 2**). The NSGA-II algorithm was used for optimization, and the optimized operation results of the two sets of comparison schemes were compared. The Pareto frontier solution set obtained by CS 1 is shown in **Figure 5**.

The main purpose of the joint operation of inter-basin water transfer projects is to solve the contradiction between the operation targets of the source and the receiving reservoir. There are three targets for the joint operation model constructed in this paper: power generation, water diversion, and water supply. Power generation is only for the source reservoir that has power generation target. Water diversion and water supply are for the receiving reservoir. Therefore, the amount of power generation and water supply, and the amount of power generation and water diversion can be compared in pairs. This paper projected the three-dimensional distribution map of the Pareto solution set to obtain the spatial distribution maps of the two sets of non-inferior scheduling schemes for the average annual power generation and the average annual water shortage index, and the average annual power generation and the average annual water diversion difference, respectively (**Figure 6**).

Our results showed that: (1) the numerical trends of the average annual water shortage index and the average annual water diversion difference were the same despite changes in the average annual power generation (**Figure 6**). As the average annual power generation increased, the average annual water shortage index and the average annual water diversion difference of the two schemes both increased, and vice versa. Since the average annual power generation is a profit-based indicator; it is better when the value is larger. In contrast, the average annual water shortage index and the water diversion difference are both cost-based indicators; they are better when the values are smaller. Based on these similar changing trends, there was a restriction and competition relationship between power generation target, water supply target, and water diversion target. In other words, there was a contradiction between the source and the receiving reservoir in the scheduling process. The water supply and diversion targets of the receiving reservoir need to be improved at the expense of the power generation benefit of the source reservoir. (2) The non-inferior frontiers of CS1 based on the two-dimensional water diversion scheduling diagram were below the non-inferior frontiers obtained from CS2. Under the same power generation conditions, water shortage index and water diversion difference of CS1 were smaller than the target values of CS2. This result indicated that the optimal target frontier obtained from CS1 was closer to the theoretical optimal frontier

TABLE 2 | Dispatching rules set for comparison schemes.

Scheme No.	Power generation rules	Water diversion rules	Water supply rules
Scheme 1 (CS1)	power generation scheduling diagram	Two-dimensional water diversion scheduling diagram	Hedging rules for water supply
Scheme 2 (CS2)	power generation scheduling diagram	Normal water diversion scheduling diagram	Hedging rules for water supply

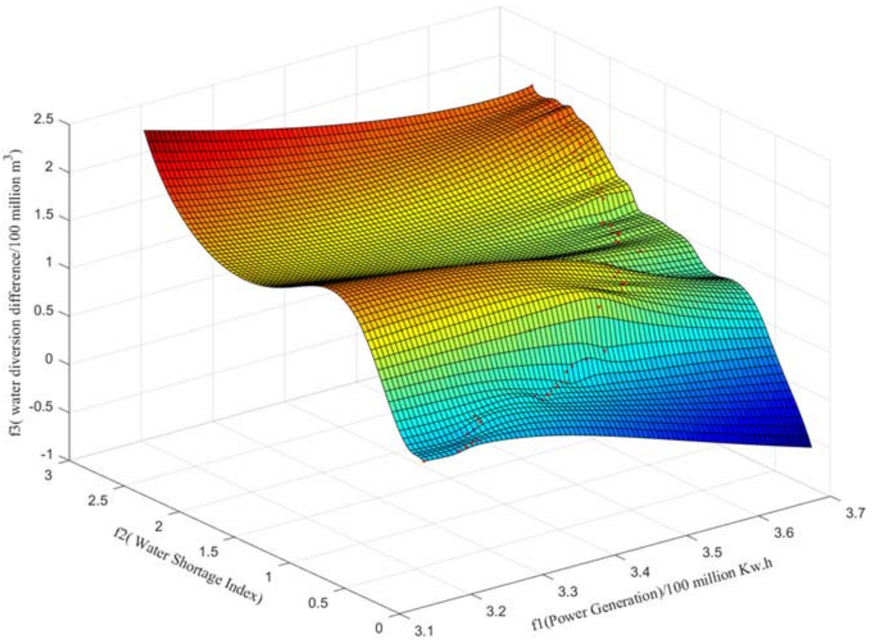

FIGURE 5 | Three-dimensional distribution diagram of Pareto solution set.

of the multi-objective problems. The inter-basin dispatching rules constructed based on the two-dimensional water diversion scheduling diagram can better guide the operation of inter-basin water diversion projects and provide more accurate scheduling information for decision-makers. (3) As the average annual power generation increased, the water shortage index and water diversion difference of CS1 rose rapidly (**Figure 6A**). When the power generation reached about 370 million Kwh, the water shortage index and water diversion difference of the two schemes were similar. With the increase of power generation, the method of water discharge from STX Reservoir became more unfavorable for the diversion of the main water transfer canal and the water supply of HQ Reservoir. When the power generation target reached the maximum value, the water shortage index and water diversion difference of CS1 and CS2 were the same.

Scheduling Scheme Decision Model Based on Gray Target Model and Prospect Theory

Based on the complexity and uncertainty of reservoir operation, four evaluation indicators for joint operation were selected to construct an evaluation index system for the inter-basin scheduling schemes, namely, power generation difference (*f1*), water shortage index (*f2*), water diversion target difference (*f3*), and abandoned water (*f4*). The joint operation optimization model was used to calculate the eigenvalues of the four evaluation indicators in the comparison schemes (Pareto non-inferior solution set). The gray target model was then used to calculate the positive and negative value functions in the scenario theory. By establishing an optimization model based on weights and using Lingo to solve the model, the optimal weight vector of *f1*~*f4* can be obtained as:

$$q^* = (0.418, 0.312, 0.230, 0.050) \tag{12}$$

Based on the analysis of the optimal weight vector, we found that: 1) The evaluation index with the largest weight ratio was the power generation difference (*f1*), and the weight ratio of abandoned water (*f4*) was the smallest. However, the sum of the weights of the water shortage index (*f2*) and the water diversion target difference (*f3*) exceeded 50% of the total weight, which was greater than the weight ratio of *f1*. It can be concluded that the water transfer and water supply targets had the greatest impact on scheduling scheme decisions, which was consistent with the principle that the power regulation subject to water regulation of "Datong-Huangshui" water transfer project.

By substituting the optimal weight vector q^* into the comprehensive prospect value function of the alternative schemes, the optimal comprehensive prospect value of the schemes was obtained. Then by comparing the comprehensive prospect value of each scheme, the alternative schemes were ranked. The results showed that the alternative scheme numbered 62 (namely, the OPT Scheme in **Figure 7**) ranked first and was called the optimal (OPT for short) scheduling scheme.

DISCUSSION

Rationale Analysis of Power Generation

The power generation dispatching rule of the OPT scheme was compared with the two typical feasible solutions (CS1 and CS2) in the Pareto solution set. **Figures 8**, **9** showed that the

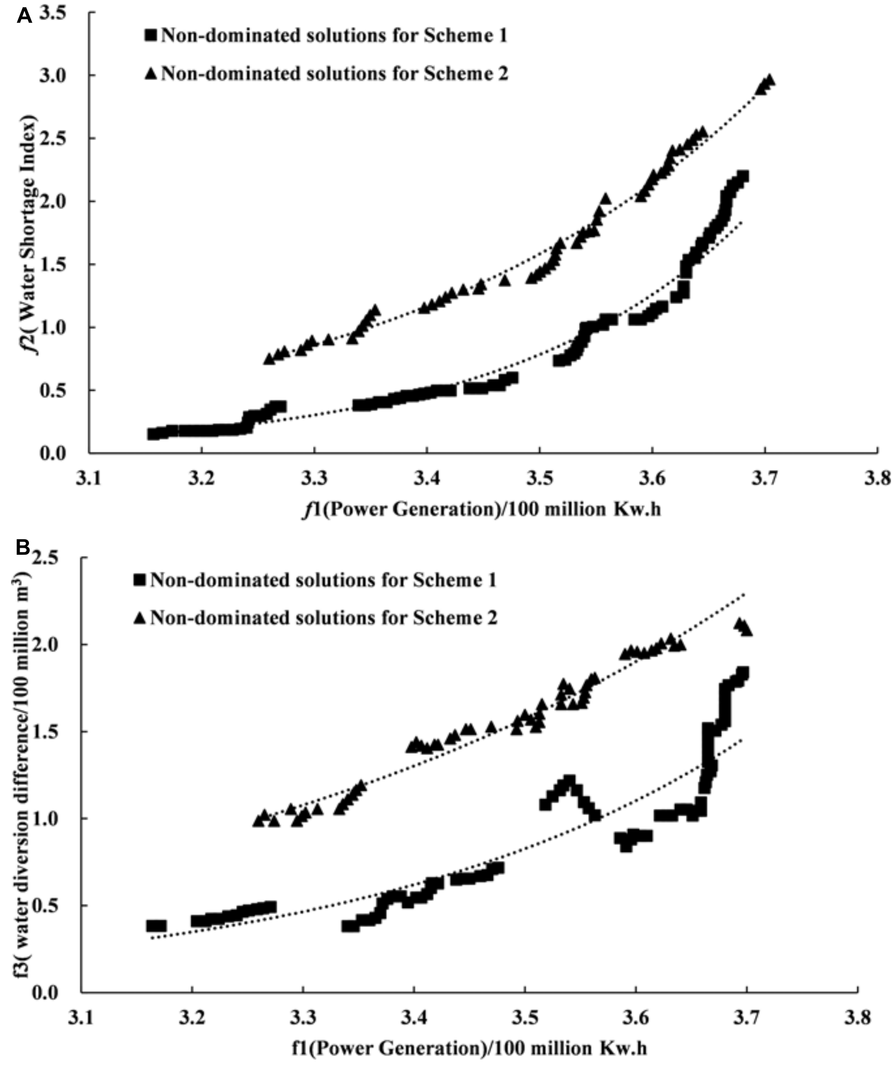

FIGURE 6 | The frontier projection of Pareto solution set. **(A)** Pareto frontier projection of power generation target and water supply target. **(B)** Pareto frontier projection of power generation target and water diversion target.

guaranteed output area of CS2 and its power generation were the largest. On the contrary, the guaranteed output area of CS1 and its power generation were the smallest. These results implied that the size of the guaranteed output area was directly related to power generation. Among the three comparison schemes, the OPT scheme had the most even distribution of guaranteed output areas.

By comparing the CS1 scheme and the OPT scheme, we found that the dispatching rules of CS1were to increase the amount of discharged water to meet the water transfer requirements. The restricted output area from January to May was small. Especially between March and May, the increased output line was greatly reduced to meet the requirements of water transfer (**Figure 8**). We found that except for April, the amount of discharged water of CS1 was higher than that of the OPT scheme from January to May, resulting in the lowest value of the storage capacity in March (**Figure 10**). From June to September, due to the increase in reservoir runoff during the flood season and the decrease in water transfer pressure, the restricted output area of CS1 increased. Consequently, there was an increase in the storage capacity, but a decrease in water discharge volume. Due to the large amount of water discharged from January to March, the potential energy during this period was low, making the output of CS1 far less than the OPT scheme.

Based on the comparison between CS2 scheme and OPT scheme, we found that from January to June, the guaranteed output line of CS2 was smaller than the OPT scheme in the increased output area, but greater than the OPT scheme in the restricted output area (**Figure 9**). As a result, the amount of discharged water of CS2 scheme during this period was continuously smaller than that of the OPT scheme (**Figure 11**), which was very unfavorable for the diversion of main canal in the downstream.

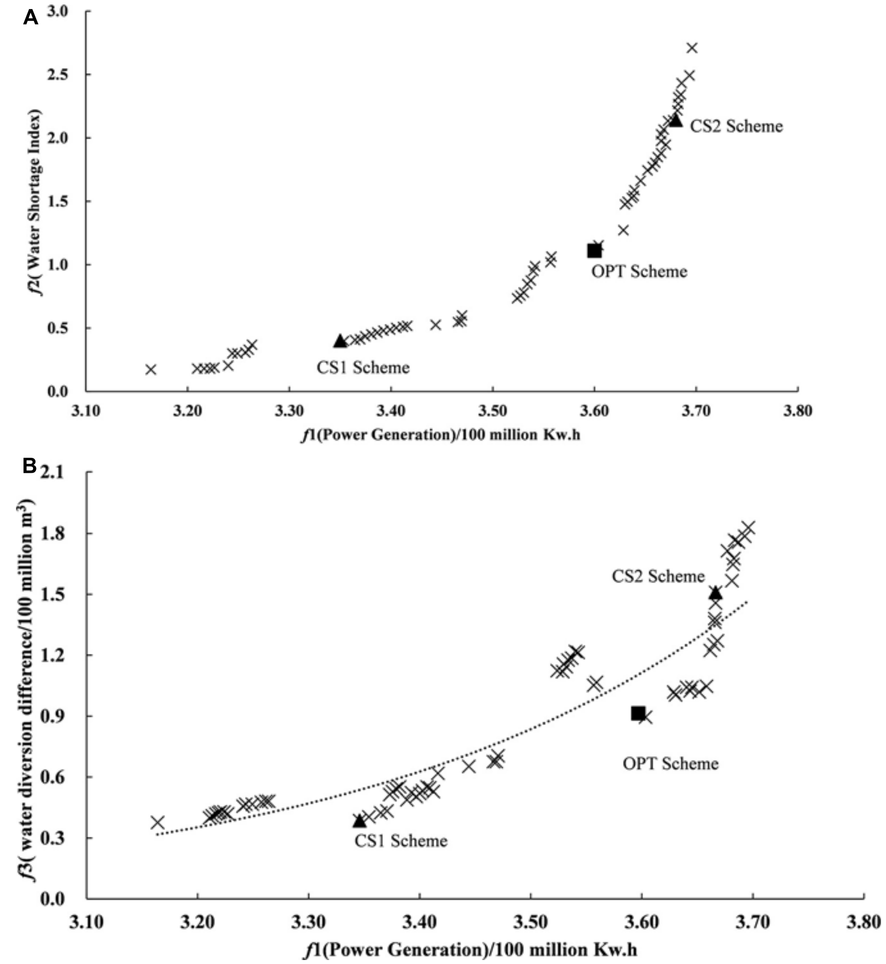

FIGURE 7 | Location of the optimal schemes in the Pareto scheme set. Triangle represents the comparison schemes (CS1 and CS2) and square represents the optimal scheme (OPT). **(A)** Pareto frontier projection of power generation target and water supply target. **(B)** Pareto frontier projection of power generation target and water diversion target.

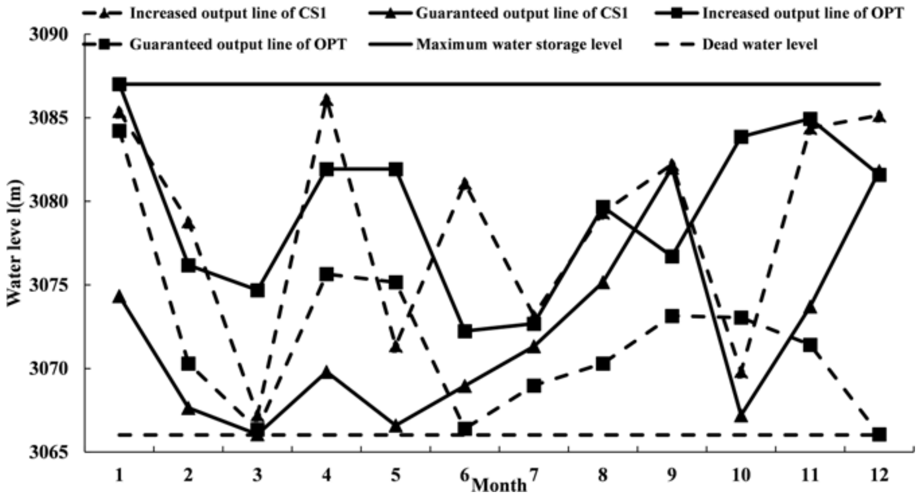

FIGURE 8 | Comparison of power generation rules between OPT and CS1.

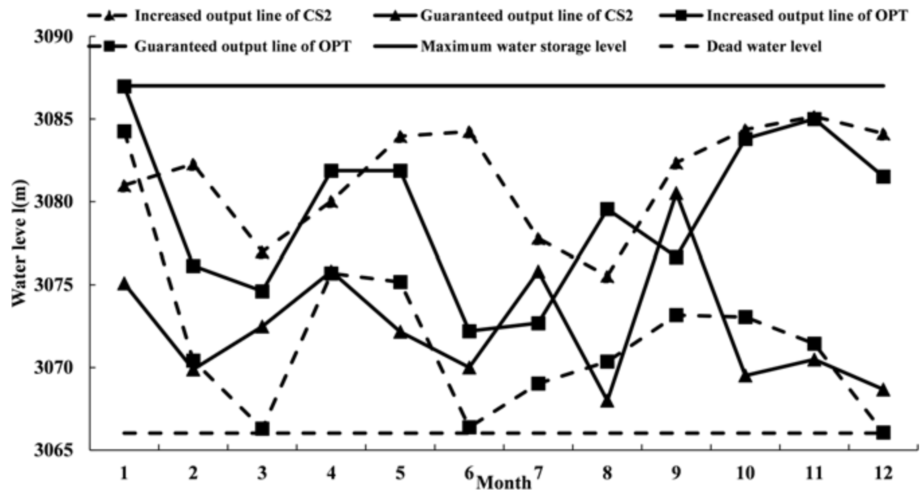

FIGURE 9 | Comparison of power generation rules between OPT and CS2.

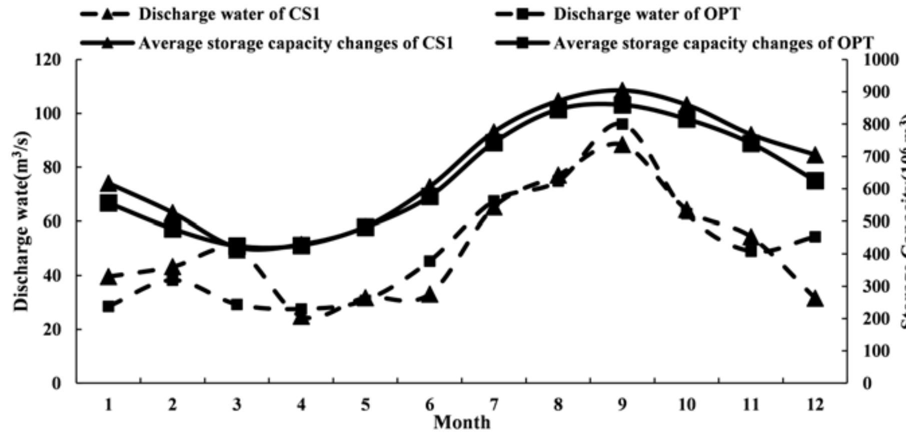

FIGURE 10 | Comparison of power generation scheduling results between OPT and CS1.

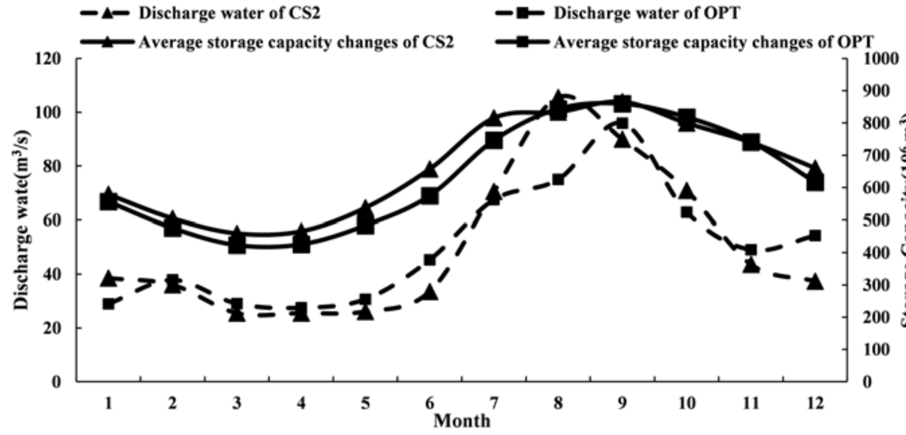

FIGURE 11 | Comparison of power generation scheduling results between OPT and CS2.

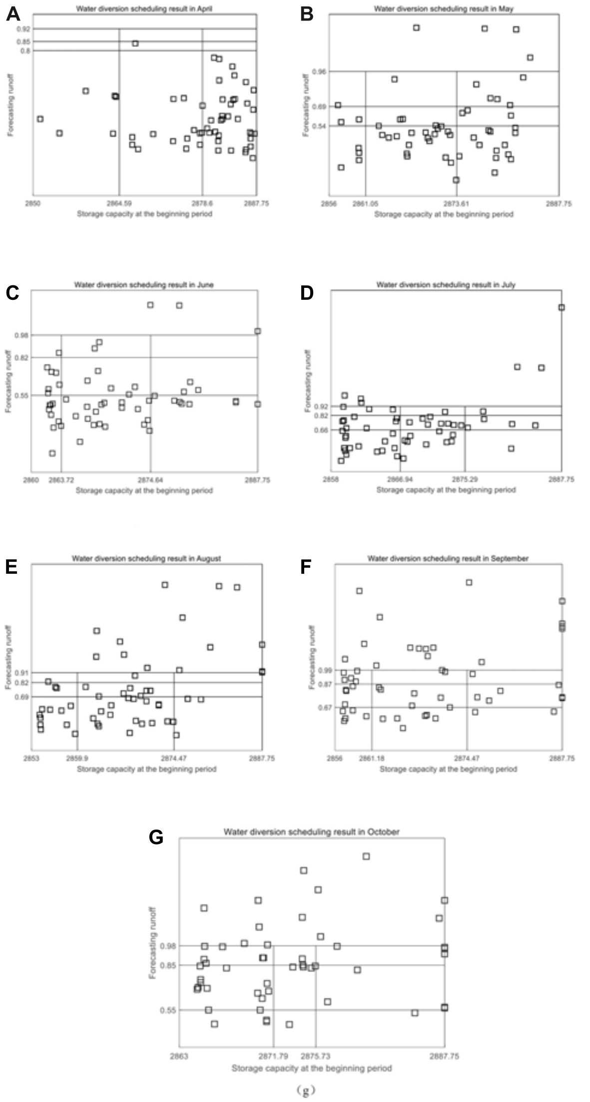

FIGURE 12 | Water diversion scheduling results between April and October. Each square point represents the scheduling status at the beginning of the scheduling period, so that the corresponding mode can be selected. **(A–G)** Water diversion scheduling results in April, May, June, July, August, September, and October, which have been displayed in the upper part of each sub-figure.

Rationale Analysis of Water Diversion

Scheduling schemes could be generated through optimizing dispatching rules to simulate long-time series (1956–2010) of water transfers. Since the inflow runoff was small during the dry season, from November to March of the following year, it had little impact on the decision-making of water supply operation of HQ Reservoir after the increase in water supply targets. As a result, the use of the two-dimensional scheduling diagram to guide the water diversion operation of the reservoir was not required during these months. Instead, we adopted the normal water diversion scheduling diagram method. According to the OPT scheme to simulate water diversion, we counted the number of diversion modes used in different periods (**Figure 12**), and introduced the probability distribution of water diversion state to illustrate how improved rules could increase diversion efficiency (**Table 3**). The probability of water diversion state is defined as the ratio of the number of diversion modes to the total number of years.

By combining the results of different water diversion scheduling modes with the changes of the monthly average storage volume of HQ Reservoir (**Figure 13**), we found that:

(1) From January to March, mode 1 showed that each month, the number of time periods for water diversion was less than 30%. Mode 2 showed an increasing trend while mode 3 had a decreasing trend. Because the storage capacity of the reservoir was large while the water demand was small at the beginning of January, the amount of water diversion was reduced to avoid abandoned water. Since the amount of water diversion was less than water supply, the storage capacity continued to decrease during this period. To avoid future reduction in water supply, the proportion of mode 2 gradually increased.

(2) During the flood season from April to September, the inflow runoff gradually increased, but the demand also increased. Because the inflow of the HQ Reservoir was much smaller than water demand, it could not meet the water supply target. Therefore, except for September at the end of the flood season, the proportion of water diversion in other months using mode 3 was within 30%. Especially in the middle of the flood season (June to August), due to the continuous increase in water supply, the storage capacity was continuously reduced. In order to meet the water supply target, the probability of water diversion of mode 1 should be maintained at more than 50% during this period.

(3) Due to the decrease of water demand from October to December, the probability of water diversion of mode 1 was lower than that of the flood season. However, the sum of the water diversion probability of mode 1 and model 2 was still relatively large to meet the demand at the end of the dry season (January to March). Especially in December, in order to supplement water loss caused by winter irrigation, the sum of the water diversion probability of mode 1 and mode 2 reached 91.01%.

Rationale Analysis of Water Supply

The water supply rules used the hedging rules for water supply constructed in Chapter "Water Supply Operation Model Based on Hedging Rules for Water Supply.". The target storage level and water supply weight coefficient were used as decision-making variables to determine the hedging rules for water supply of HQ Reservoir. **Figure 14** shows that the target storage level in the hedging rules for water supply had the following two characteristics:

(1) The water demand of Heiquan Reservoir was relatively large, accounted for 45.6%∼80.0% of the active storage capacity in each month. The total annual water transfer was much larger than the reservoir storage capacity. Therefore, the water storage benefit of HQ Reservoir was small and

TABLE 3 | Results of different water diversion modes.

Month	Mode 1		Mode 2		Mode 3	
	Occurrence	Probability	Occurrence	Probability	Occurrence	Probability
1	7	12.73%	15	27.27%	33	60.00%
2	8	14.55%	17	30.91%	30	54.55%
3	10	18.18%	20	36.36%	25	45.45%
4	12	21.82%	39	70.91%	4	7.27%
5	22	40.00%	20	36.36%	13	23.64%
6	28	50.91%	16	29.09%	11	20.00%
7	27	49.09%	12	21.82%	16	29.09%
8	24	43.64%	14	25.45%	17	30.91%
9	15	27.27%	10	18.18%	30	54.55%
10	12	21.82%	10	18.18%	33	60.00%
11	18	32.73%	22	40.00%	15	27.27%
12	25	45.45%	20	36.36%	10	18.18%
Sum/Avg	208	31.52%	215	32.58%	237	35.91%

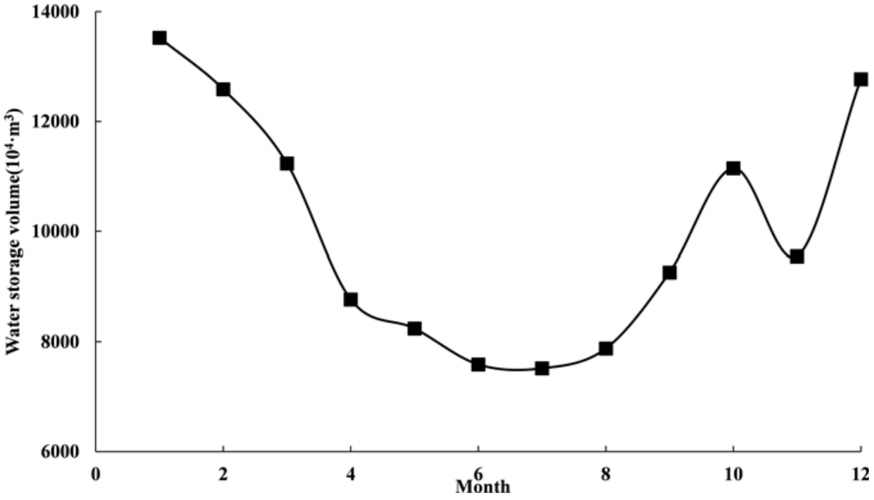

FIGURE 13 | Monthly average storage volume of HQ Reservoir.

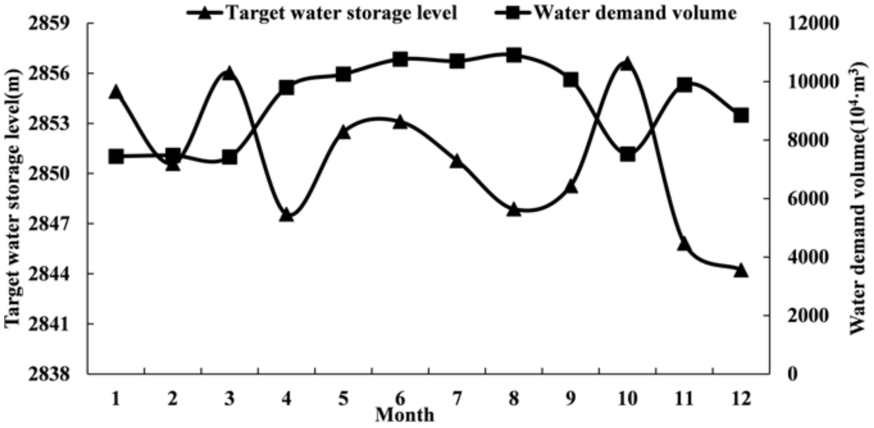

FIGURE 14 | The target storage level and water demand of HQ Reservoir.

TABLE 4 | The process of water supply for different schemes units: 10^4 m^3.

Month	OPT Scheme			CS1 Scheme			CS2 Scheme		
	Municipal water supply	Industrial water supply	Agricultural water supply	Municipal water supply	Industrial water supply	Agricultural water supply	Municipal water supply	Industrial water supply	Agricultural water supply
1	1974.0	3625.0	443.9	1968.7	3559.1	436.9	1974.0	3615.5	442.6
2	1965.8	3546.5	434.5	1948.2	3559.1	436.9	1966.5	3464.8	420.7
3	1928.8	3506.0	421.4	1924.0	3541.2	428.8	1908.3	3233.6	374.7
4	1974.0	3531.8	3146.1	1974.0	3611.8	3430.6	1974.0	3344.0	2605.0
5	1988.0	3568.0	3788.0	1988.0	3625.0	4075.6	1988.0	3573.6	3896.7
6	2014.0	3611.8	4552.2	2014.0	3602.8	4584.5	2014.0	3553.3	4339.7
7	2041.0	3623.2	4568.8	2041.0	3619.7	4517.2	2041.0	3625.0	4546.7
8	2068.0	3607.9	4721.2	2068.0	3625.0	4873.0	2068.0	3582.7	4603.4
9	2055.0	3506.2	3342.3	2055.0	3625.0	3770.0	2055.0	3525.7	3407.5
10	2028.0	3625.0	445.0	2028.0	3625.0	445.0	2028.0	3625.0	445.0
11	2014.0	3625.0	3574.0	2014.0	3625.0	3574.0	2014.0	3625.0	3574.0
12	1988.0	2986.0	1321.7	1988.0	3124.0	1485.1	1988.0	2993.8	1357.9
Sum	24038.6	42362.5	30758.9	24010.9	42742.8	32057.7	24018.8	41762.0	30013.8
Water supply guarantee rate	99.5%	91.1%	85.4%	99.5%	97.9%	95.6%	99.2%	85.4%	75.0%
Annual average water shortage	26.4	1137.5	2440.1	54.1	757.2	1141.3	46.2	1738.0	3185.2

it had a relatively low storage level target in the joint dispatching rules. This can trigger the stop condition of hedging rules for water supply as early as possible, and narrow the restricted water supply area, which is beneficial for water supply.

(2) The trend of the target water storage level was opposite to that of the water demand volume. During the months when water demand was large, the target storage level was low, and vice versa. The requirements for water supply and water storage in different months can be satisfied when the restricted water supply area was narrowed through reducing the target water storage level as much as possible during the water supply process.

According to the dispatching rules of the selected OPT scheme and the two comparison schemes (CS1 and CS2), the simulated water supply results showed that for both OPT and CS1 scheme, water supply guarantee rates were: 1) more than 90% for municipal and industrial water and 2) more than 85% for agriculture. In contrast, the agricultural water supply guarantee rate of CS2 was only 75% (**Table 4**). In the OPT scheme, the annual available water supplies for industry and agriculture accounted for 97.4% and 92.7% of the annual water demand, respectively, while in the CS1 scheme, they were 98.2% and 96.6%, respectively. The difference between the two schemes were only 0.8% and 3.9%.

CONCLUSION

In the previous study, only the current storage volume of the receiving reservoir was used as the basis for decision-making of starting water transfer process. Due to the lack of inflow runoff information, the receiving reservoir is prone to water supply destruction at high water levels and abandoned water at low water levels. Through extracting dispatching rules based on the two-dimensional scheduling diagram, this paper used the current storage state and inflow runoff of the receiving reservoir as the basis for decision-making during the scheduling period, which effectively solved the problems existing in the starting rules of regular water transfer. Aimed at the multi-objective joint optimization scheduling problem of "Datong-Huangshui" water transfer project, we concluded that:

(1) The non-inferior frontiers of the two scheduling targets obtained by the OPT scheme were below the non-inferior frontiers obtained from the CS1 and CS2 schemes. The optimal target frontier obtained by the optimized scheme was closer to the theoretical optimal frontier of the multi-objective problem. Therefore, the two-dimensional scheduling diagram can better guide the water diversion operation of inter-basin water transfer projects.

(2) Based on the multi-objective optimal operation schemes set, the OPT scheme obtained by the scheduling scheme decision model using gray target model and prospect theory could generate power by as much as 359 million Kwh. It was also able to guarantee 90% of municipal and industrial water supply, as well as 85% of agricultural water supply. This model could better meet the real scheduling requirements.

DATA AVAILABILITY STATEMENT

The original contributions presented in the study are included in the article/supplementary material, further inquiries can be directed to the corresponding author/s.

AUTHOR CONTRIBUTIONS

SC and LS did the conceptualization. SC and QL did the methodology. SC Wrote-original draft preparation. SC and YJ

Wrote-review and edited. HW Guided. All authors read and approved the final manuscript.

FUNDING

This work was funded by the National Key Research and Development Program of China (2018YFE0196000) and the National Key Research and Development Program of China (2018YFC0407701).

ACKNOWLEDGMENTS

We are very grateful to the editors and reviewers for their critical comments and thoughtful suggestions.

REFERENCES

Bonacci, O., and Andric, I. (2010). Impact of an inter-basin water transfer and reservoir operation on a karst open streamflow hydrological regime an example from the Dinaric karst (Croatia). *Water Resourc. Manag.* 24, 3852–3863. doi: 10.1002/hyp.7817

Chang, F. J., Lai, J. S., and Kao, L. S. (2003). Optimization of operation rule curves and flushing schedule in a reservoir. *Hydrol. Process.* 17, 1623–1640. doi: 10.1002/hyp.1204

Chang, L. C., and Chang, F. J. (2009). Multi-objective evolutionary algorithm for operating parallel reservoir system. *J. Hydrol.* 377, 12–20. doi: 10.1016/j.jhydrol.2009.07.061

Chang, L. C., Chang, F. J., Wang, K. W., and Dai, S. Y. (2010). Constrained genetic algorithms for optimizing multi-use reservoir operation. *J. Hydrol.* 390, 66–74. doi: 10.1016/j.jhydrol.2010.06.031

Guo, X., Hu, T., Huang, B., and Han, Y. (2011). Joint operation rules for multi-reservoir water supply system based on the model of simulation and optimization. *J. Hydraulic Eng.* 42, 705–712.

Hall, W. A., Tauxe, G. W., and Yeh, W. W.-G. (1969). An alternative procedure for the optimization of operations for planning with multiple river, multiple purpose systems. *Water Resourc. Res.* 5, 1367–1372. doi: 10.1029/wr005i006p01367

Heidari, M., Chow, V. T., Kokotovic, P. V., and Meredith, D. D. (1971). Discrete differential dynamic programming approach to water resources system optimization. *Water Resourc. Res.* 7, 273–283. doi: 10.1029/wr007i002p00273

Hormwichian, R., Kangrang, A., and Lamom, A. (2009). A conditional genetic algorithm model for searching optimal reservoir rule curves. *J. Appl. Sci.* 9, 3575–3580. doi: 10.3923/jas.2009.3575.3580

Hsu, N. S., and Cheng, K. W. (2002). Network flow optimization model for basin-scale water supply planning. *J. Water Resourc. Plan. Manag.* 128, 102–112. doi: 10.1061/(asce)0733-9496(2002)128:2(102)

Jafarzadegan, K., Abedelmdoust, A., and Kerachian, R. (2014). A stochastic model for optimal operation of inter-basin water allocation systems: a case study. *Stochast. Environ. Res. Risk Assess.* 28, 1343–1358. doi: 10.1007/s00477-013-0841-8

Ji, Y., Lei, X., Cai, S., and Wang, X. (2016). Hedging rules for water supply reservoir based on the model of simulation and optimization. *Water* 8:249. doi: 10.3390/w8060249

Kangrang, A., Compliew, S., and Chaiyapoom, W. (2009). Heuristic Algorithm with simulation model for searching optimal reservoir rule curves. *Am. J. Appl. Sci.* 6, 263–267. doi: 10.3844/ajassp.2009.263.267

Li, Y., Zhang, C., Chu, J., Cai, X., and Zhou, H. (2015). Reservoir operation with combined natural inflow and controlled inflow through interbasin transfer: biliu Reservoir. *J. Water Resourc. Plan. Manag.* 142:5015009.

Liu, D., Huang, Q., Yang, Y., Liu, D., and Wei, X. (2020). Bi-objective algorithm based on NSGA-II framework to optimize reservoirs operation. *J. Hydrol.* 585:124830. doi: 10.1016/j.jhydrol.2020.124830

Lund, J., and Ferreira, I. (1996). Operating rule optimization for missouri river reservoir system. *J. Water Resourc. Plan. Manag.* 122, 287–295. doi: 10.1061/(asce)0733-9496(1996)122:4(287)

Luo, Y., Deng, J., Zhen, J., and Fan, H. (2001). Grey target method on the pipe corrosion analysis. *J. Chin. Soc. Corros. Protect.* 53, 56–60.

Neelakantan, T. R., and Pundarikanthan, N. V. (2000). Neural network based simulation-optimization model for reservoir operation. *J. Water Resourc. Plan. Manag.* 126, 57–64. doi: 10.1061/(asce)0733-9496(2000)126:2(57)

Rani, D., and Moreira, M. M. (2010). Simulation optimization modeling: a survey and potential application in reservoir systems operation. *Water Resourc. Manag.* 24, 1107–1138. doi: 10.1007/s11269-009-9488-0

Reis, L. F. R., Bessler, F. T., Walters, G. A., and Savic, D. (2006). Water supply reservoir operation by combined genetic algorithm – linear programming (GA-LP) approach. *Water Resourc. Manag.* 20, 227–255. doi: 10.1007/s11269-006-8049-z

Sadegh, M., Mahjouri, N., and Kerachian, R. (2010). Optimal inter-basin water allocation using crisp and fuzzy shapley games. *Water Resourc. Manag.* 24, 2291–2310. doi: 10.1007/s11269-009-9552-9

Suiadee, W., and Tingsanchali, T. (2007). A combined simulation genetic algorithm optimization model for optimal rule curves of a reservoir a case study of the Nam Oon Irrigation Project, Thailand. *Hydrol. Process.* 21, 3211–3225. doi: 10.1002/hyp.6528

Sulis, A. (2009). GRID computing approach for multi reservoir operating rules with uncertainty. *Environ. Model. Softw.* 24, 859–864. doi: 10.1016/j.envsoft.2008.11.003

Tung, C. P., Hsu, S. Y., Liu, C. M., and Li, J. S. (2003). Application of the genetic algorithm for optimizing operation rules of the Liyutan Reservoir in Taiwan. *J. Am. Water Resourc. Assoc.* 39, 649–657. doi: 10.1111/j.1752-1688.2003.tb03682.x

Tversky, A., and Kahneman, D. (1992). Advances in prospect theory: cumulative representation of uncertainty. *J. Risk Uncertain.* 5, 297–323. doi: 10.1007/bf00122574

Wurbs, R. A. (1993). Reservoir-system simulation and optimization models. *J. Water Resourc. Plan. Manag.* 119, 455–472. doi: 10.1061/(asce)0733-9496(1993)119:4(455)

Yeh, W. W.-G. (1985). Reservoir management and operations models: a state-of-the-art review. *Water Resoure. Res.* 21, 1797–1818. doi: 10.1029/wr021i012p01797

Yu, Y., Zhao, W., Martinez-Murillo, J., and Pereira, P. (2020). Loess Plateau: from degradation to restoration. *Sci. Total Environ.* 738:140206. doi: 10.1016/j.scitotenv.2020.140206

Zhou, Y., Mei, Y., Yang, L., Xu, Y., and Duan, K. (2012). Derivation of optimal operation rules for cascade reservoirs of Dadu river. *J. Hydroelectr. Eng.* 31, 78–82.

Conflict of Interest: The authors declare that the research was conducted in the absence of any commercial or financial relationships that could be construed as a potential conflict of interest.

frontiers
in Earth Science

ORIGINAL RESEARCH
published: 20 May 2021
doi: 10.3389/feart.2021.615692

Lake Inflow Simulation Using the Coupled Water Balance Method and Xin'anjiang Model in an Ungauged Stream of Chaohu Lake Basin, China

Zijun Li[1,2], Xiaohui Lei[1], Weihong Liao[1]*, Qingchun Yang[3], Siyu Cai[1], Xiaoying Wang[4], Chao Wang[1] and Jia Wang[5]

[1] China Institute of Water Resources and Hydropower Research, Beijing, China, [2] College of Resources and Environmental Sciences, Hebei Normal University, Shijiazhuang, China, [3] Key Laboratory of Groundwater Resources and Environment, Ministry of Education, Jilin University, Changchun, China, [4] College of Water Resources Science and Engineering, Taiyuan University of Technology, Taiyuan, China, [5] State Key Laboratory of Hydraulics and Mountain River Engineering, Sichuan University, Chengdu, China

OPEN ACCESS

Edited by:
Ataollah Kavian,
Sari Agricultural Sciences and Natural Resources University, Iran

Reviewed by:
Jing Zhang,
Capital Normal University, China
Chiyuan Miao,
Beijing Normal University, China
Dejun Zhu,
Tsinghua University, China

***Correspondence:**
Weihong Liao
behellen@163.com

Specialty section:
This article was submitted to Hydrosphere, a section of the journal Frontiers in Earth Science

Received: 09 October 2020
Accepted: 25 March 2021
Published: 20 May 2021

Citation:
Li Z, Lei X, Liao W, Yang Q, Cai S, Wang X, Wang C and Wang J (2021) Lake Inflow Simulation Using the Coupled Water Balance Method and Xin'anjiang Model in an Ungauged Stream of Chaohu Lake Basin, China. Front. Earth Sci. 9:615692. doi: 10.3389/feart.2021.615692

Water resources are crucial for maintaining daily life and a healthy ecological environment. In order to gain a harmonious development among water resources and economic development in Lake Watershed, it is urgent to quantify the lake inflow. However, the calculation of inflow simulations is severely limited by the lack of information regarding river runoff. This paper attempts calculated inflow in an ungauged stream through use of the coupling water balance method and the Xin'anjiang model, applying it to calculate the inflow in the Chaohu Lake Basin, China. Results show that the coupled model has been proved to be robust in determining inflow in an ungauged stream. The error of daily inflow calculated by the water balance method is between 1.4 and −19.5%, which is within the standard error range (±20%). The calibration and verification results of the coupled model suggest that the simulation results are best in the high inflow year (2016), followed by the normal inflow year (2007) and the low inflow year (1978). The Nash-Sutcliffe efficiencies for high inflow year, normal inflow year, and low inflow year are 0.82, 0.72, and 0.63, respectively, all of which have reached a satisfactory level. Further, the annual lake inflow simulation in the normal inflow year is 19.4 × 10^8 m^3, while the annual average land surface runoff of the study area is 18.9 × 10^8 m^3, and the relative error is −2.6% by the two ways. These results of the coupled model offer a new way to calculate the inflow in lake/reservoir basins.

Keywords: ungauged stream, bivariate model, coupled water balance and Xin'anjiang model, lake inflows simulate, Chaohu Lake Basin

INTRODUCTION

Water resources are of significance to maintain daily life because they not only provide directly available water resources for households, industry, and agriculture but also play a key role in maintaining healthy ecosystems (Li et al., 2017; Yang et al., 2020; Yu et al., 2020). Therefore, the available quantity should be calculated accurately as possible. In general, however, inflow observation data cannot be obtained directly in many lake/reservoir basins (Mohebzadeh and Fallah, 2019), especially in the areas where hydrological measurement stations have been poorly developed.

In the inflow studies of lake/reservoir basins, abundant observation data of water level and the relationship of water level and capacity of lake/reservoir make it possible to use the water balance method to calculate the lake/reservoir inflow (Deng et al., 2015; Gal et al., 2016). In this method, however, the estimated reliable inflow is a great challenge because the detailed daily water consumption data, including agricultural water, industrial water, domestic water, infiltration, etc., is difficult to obtain accurately. The results of daily lake/reservoir inflows calculated by the water balance method may be unreasonable and even negative values. In this context, the coupling of the water balance method and the hydrological model is needed to study the lake/reservoir inflows, in which flood events observations (estimated by the water balance method and called true inflows) were used to calibrate the hydrological model.

The hydrologic model used in this study is the Xin’anjiang model, which has emerged as a particularly promising method of dealing with complex hydrological phenomena due to the simple model structure (Bai et al., 2017), the clear physical meaning of the parameters (Lü et al., 2013), the well-defined model calibration procedure (Bai et al., 2017), and model development ability (Lin et al., 2014) following its first reported application to hydrological modeling problems by Zhao (1984). Meanwhile, the Xin’anjiang model has been widely applied in humid and semi-humid regions in China (Lü et al., 2013; Lin et al., 2014). In the model, although some insensitive parameters can be preset or estimated based on implementation experience, the sensitive parameters must be calibrated based on continuous historical streamflow data. In this study, the single objective particle swarm optimization (SOPSO) method, which is a population-based optimization technique proposed by Eberhart and Kennedy (1995), was added to the Xin’anjiang model to find the optimal parameters of the coupled model.

However, the SOPSO method becomes invalid because the observed daily inflow data, calculated by the flood events using the water balance method, is discontinuous. Thus, an improved SOPSO (I-SOPSO) method was used to calibrate hydrological model parameters, in which the daily precipitation data input by the Xin’anjiang model is sequentially read, but the inflows of the selected flood events (calculated by water balance method) are only read as the observed inflow data. Meanwhile, the maximum weighted average Nash-Sutcliffe efficiency (WANSE) of selected flood events is used as the objective function to minimize the error in estimating the goodness-of-fit between observed and simulated values. The advantage of the method is that it not only considers the impact of the previous precipitation and reduces the influence of anthropogenic activities, especially irrigation activities, but also can simulate the long-series daily lake/reservoir inflow, which is an important factor to consider in water resources decision-making (Yun et al., 2018).

Existing reservoir inflow simulation models and water balance methods in the area lacking hydrological measurement stations become limited due to the lack of a series of daily time scale reservoir inflow data. Thus, this paper attempt to solve this problem by coupling the water balance method with the Xin’anjiang model and applying the result to the Chaohu Lake Basin where hydrological stations have been poorly developed. The objective entails the following tasks: (1) determining typical hydrological years; (2) calculating the lake inflows of selected flood events; (3) finding the optimal parameters of coupled model; and (4) simulating the lake inflows of long-series. The results of the hydrological characteristics of the typical years of Chaohu Lake Basin will be of great significance for further studying the migration and diffusion of suspended matter in lakes, improving the ecological environment of lakes, and water resource planning and management.

STUDY AREA AND DATA

Chaohu Lake, the fifth largest freshwater lake in China, is located in the central region of Anhui Province between the Yangtze and Huaihe. Also, Chaohu Lake Watershed is in the route of the Yangtze River Huaihe River water transfer project in China (Cao et al., 2018). Chaohu Lake Watershed can be divided into two large sub-basins, i.e., Upper Chaohu Lake Watershed and Lower Chaohu Lake Watershed. Upper Chaohu Lake Watershed is the study area of this paper, which is between latitudes 30°59′–32°9′ N and longitudes 116°23′–117°59′ E with a drainage area of 9153 km^2 (**Figure 1**).

The climate is northern subtropical and warm temperate humid monsoon climate, which is characterized by a mild climate, significant monsoon rainfall, a well-defined rainy season, good heat conditions, and a long frost-free season. The average annual precipitation (AP) is about 1095 mm. The spatial distribution of precipitation in the basin is uneven, decreasing from south to north. Meanwhile, precipitation is unevenly distributed during the year, and more than 60% of the annual total precipitation occurs in the period from June to September. The average annual temperature and evaporation are about 16.5°C and 880 mm, respectively.

Data from a total of 11 meteorological stations covering the approximate period of 1958∼2017 were collected, and these were retrieved from the Anhui Provincial Bureau of Hydrology. Meanwhile, basin areal precipitation and evaporation were calculated by the Thiessen polygons method. The annual highest water level (AHWL) data were collected from Zhongmiao hydrological gauging station, which is situated at the center of Chaohu Lake.

METHODOLOGY

To understand the characteristic of daily lake inflows in typical hydrological years, this research is divided into four subsections that describe the main components, including the following: (1) determination of typical hydrological years based on the bivariate frequency analysis of AP and AHWL; (2) calculation of the Chaohu Lake inflows of selected flood events depends on water balance method; (3) determination of the optimal

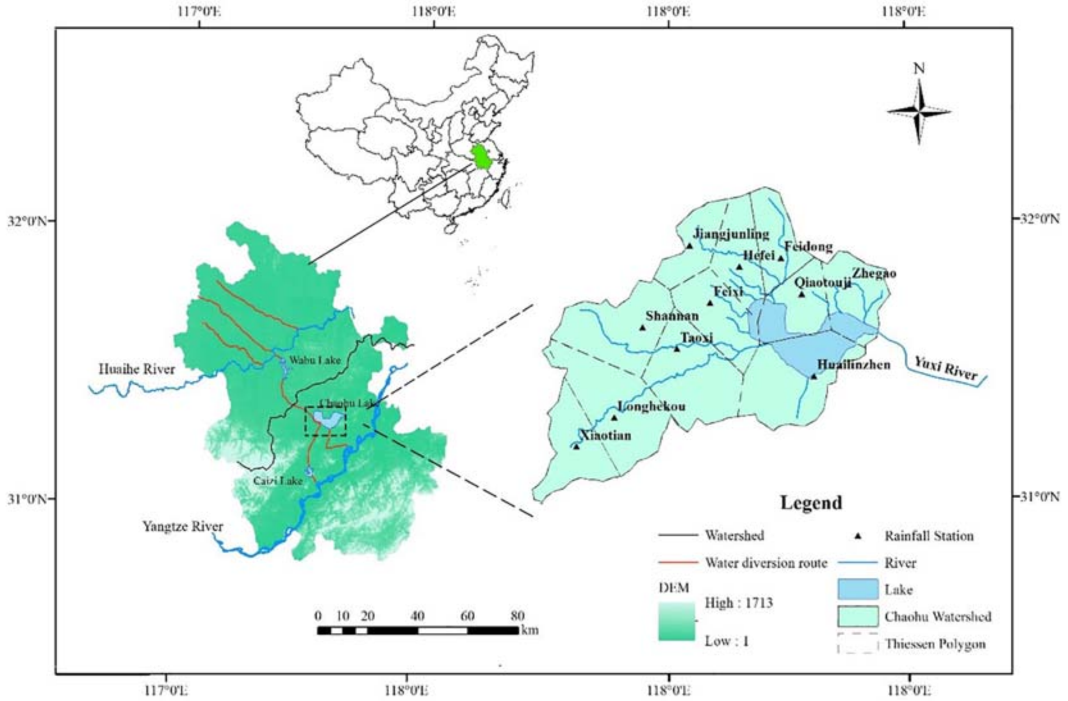

FIGURE 1 | Location map for study and gauge stations.

parameters of the coupled model predictions by I-SOPSO method; and (4) generation of long-series inflow simulate results on the basis of model optimal parameters. The details of the evaluation procedures of the above methods are discussed in the following subsections.

Hydrologic Frequency Analysis

In the actual hydrological design, several typical years are selected from the hydrological data for analysis and calculation, and the results can generally meet the requirements of planning and design. Hydrological frequency analysis is usually a more powerful tool for selecting typical years. Generally, application of the bivariate probability analysis allows researchers to investigate hydrological events with a more comprehensive view by considering the simultaneous effect of the influencing factors on the phenomenon of interest (Yue et al., 1999; Vandenberghe et al., 2011; Sraj et al., 2015). Therefore, a two-dimensional joint theoretical cumulative distribution function of AP and AHWL was constructed, and the specific process can refer to the following steps.

Step 1 Marginal Cumulative Distribution Function of AP and AHWL

Pearson-III distribution function (P-III), which can be described with three parameters, mean value ($\bar{x}$), variation coefficient (c_v), and skew coefficient (c_s) of the observation data, was considered as marginal distribution functions (MDF) of AP and AHWL. The calculation formula of the cumulative probability includes α, β, and a_0, which are the parameters of shape, scale, and location (Lei et al., 2018). The probability density function and the cumulative frequency equation (cumulative frequency greater than or equal to x_p) are shown in formulas 2 and 3:

$$\alpha = \frac{4}{C_s^2} \qquad \beta = \frac{2}{\bar{x} C_v C_s} \qquad a_0 = \bar{x}\left(1 - \frac{2C_v}{C_s}\right) \tag{1}$$

$$f(x) = \frac{\beta^\alpha}{\Gamma(\alpha)} (x - a_0)^{\alpha - 1} e^{-\beta(x - a_0)} \tag{2}$$

$$P = P(x \geq x_p) = \frac{\beta^\alpha}{\Gamma(\alpha)} \int_{x_p}^{\infty} (x - a_0)^{\alpha - 1} e^{-\beta(x - a_0)} \tag{3}$$

Step 2 Investigation of Correlation Between Variables

In the copula approach, the dependence between the pairs of considered variables should be analyzed. Kendall's correction coefficient, which is widely used because Kendall's tau (τ) is more insensitive to ties in data, was selected and calculated by the Eq. 1:

$$\tau = (C_n^2)^{-1} \sum_{i?j} sign[x_i - x_j)(y_i - y_j)] \tag{4}$$

where n is the number of variable data pairs (x_i, y_i). In addition, *sign*(.) is a symbolic function, which is defined as follows:

$$sign = \begin{cases} 1 & (x_i - x_j)(y_i - y_j) > 0 \\ -1 & (x_i - x_j)(y_i - y_j) < 0 \\ 0 & (x_i - x_j)(y_i - y_j) = 0 \end{cases} \tag{5}$$

where x_i and y_i are observed data corresponding to random variables X and Y in the *ith* year.

Step 3 Construction of Copula Function

Generally, the copula function can be classified into three types, i.e., copulas with a quadratic form, copulas with a cubic form, and Archimedean copulas. Among them, the Archimedean copulas, the one-parameter bivariate copulas, are found to be more desirable for hydrologic analysis (Genestm and Mackaym, 1986). Meanwhile, Clayton, Frank, and Gumbel–Hougaard's copula functions were adopted because the proper copulas directly depend on the value of Kendall's tau (τ) (Ahmadi et al., 2018):

(A) Clayton Copula

$$C_\theta\left[x, y\right] = [x^{-\theta} + y^{-\theta} - 1]^{-1/\theta} \qquad \theta = \frac{\tau}{1-\tau} \qquad \theta \in (0, \infty) \tag{6}$$

(B) Gumbel–Hougaard Copula

$$C_\theta\left[x, y\right] = \exp\left\{-\left[-(\ln x)^{\theta} + (-\ln y)^{\theta}]^{1/\theta}\right]\right\} \theta = \frac{1}{1-\tau} \theta \in [-1, \infty) \tag{7}$$

(C) Frank Copula

$$C_\theta\left[x, y\right] = -\frac{1}{\theta}\left[1 + \frac{\left[\exp(-\theta x) - 1\right]\left[\exp(-\theta y) - 1\right]}{\exp(-\theta) - 1}\right]$$

$$\tau = (\frac{3\theta - 2}{\theta}) - \frac{2}{3}(1 - \frac{1}{\theta})^2 \ln(1 - \theta) \qquad \theta \in R \tag{8}$$

where parameter θ describes the relationship between the two random variables X and Y.

Step 4 Selection of the Best-Fit of Copula

The limitation of the copula approach is that there are no specific ways to check whether the dependency structure of a data set is appropriately modeled by the chosen copula (Dodangeh et al., 2019). In this part, three commonly used methods, including the graphic analysis, Kolmogorov–Smirnov, and Akaike Information Criterion (*AIC*), were applied to select the best suitable copula function for Chaohu Lake Watershed.

(A) Graphic analysis

The graphic analysis method is a method that uses a graph to intuitively represent the effect of a theoretical probability distribution on the measured value. In this graphic, bivariate joint empirical cumulative frequency (BJECF) is often calculated to compare with the copula theoretical curves (Sraj et al., 2015). The BJECF can be estimated using the approach of Yue et al. (1999):

$$F_o(x_i, y_i) = P(X \leq x_i, Y \leq y_j) = \frac{\sum_{m=1}^{i}\sum_{l=1}^{j} n_{ml} - 0.44}{n + 0.12} \tag{9}$$

(B) Kolmogorov–Smirnov

$$D_n = \max_{1 \leq i \leq n}\left[\left|\frac{m(i) - 1}{n} - F_c(x_i, y_i)\right|, \left|F_c(x_i, y_i) - \frac{m(i)}{n}\right|\right] \tag{10}$$

(C) Akaike Information Criterion (*AIC*)

$$AIC = n\ln(MSE) + 2m$$

$$MSE = \frac{1}{n}\sum_{i=1}^{n}[P_c(i) - P_o(i)]^2 \tag{11}$$

where, n is the number of variable data pairs (x_i, y_i); n_{ml} is the number of joint observation sample satisfying two conditions at the same time:$x_m \leq x_i$and$y_l \leq y_j$, which have the same meanings as *m(i)* in this paper. $F_c(x_i, y_i)$ and $F_o(x_i, y_i)$ are the cumulative joint theoretical probability and experience frequency distribution function, respectively; $P_o(i)$ is the *ith* year observed value obtained from cumulative joint empirical frequency function; $P_c(i)$ is the calculated value of the *ith* year of by the bivariate copula function; and *m* is the number of model parameters. Moreover, the smaller the values of D_n and *AIC* are, the better the simulation results are.

Water Balance Method

For a given lake basin, the water balance equation is as follows:

$$P + R_a + R_g = E + R'_a + R'_g + u + \Delta S \tag{12}$$

where P is the precipitation on the lake during the period; R_a, R'_a are the surface runoff into and out of the lake during the period; R_g, R'_g are the underground runoff into and out of the lake during the period; E is the effective evaporation during the period; μ represents the consumption of industrial and agricultural; and ΔS indicates the change of water storage within a period of time. The above units are all in m^3.

Hydrologic Model

The input data of the Xin'anjiang model includes precipitation (*P*) and pan evaporation (*EM*), while the output of the module the is discharge of the outlet (Q_m). There are 15 parameters (outside the box in **Figure 2**) involved in the model for flow routing, which could be grouped as **Supplementary Table 1**. In principle, these parameters are spatially uniform, meaning that they represent integrated effects of catchment properties. More details about the calculation of the Xin'anjiang model can be found in Zhao (1992).

Model Calibration

In a hydrologic model, some model parameters cannot be directly obtained from the basin characteristics using existing measured streamflow data in the field. It is common that a set of accurate model parameters are determined by fitting the observation data and simulation values that are calculated by adjusting the model parameters, which is called the calibration of the model. In order to find the optimal parameters of the model, the SOPSO method, which is a population-based optimization technique proposed in 1995 (Eberhart and Kennedy, 1995), was added to the Xin'anjiang model to simulate the Lake inflows. However, the SOPSO method may not be able to directly calibrate the model given the limitations of the actual inflow data (intermittent flood events) calculated by water balance. Therefore, the I-SOPSO method is applied to the Xin'anjiang model, and three things need to be done during the running of the model: (1) reading the input daily precipitation and evaporation data in sequence; (2) the daily inflow data of selected flood events are used to calibrate the parameters of the model; and (3) using the optimized parameters to calculate the long series of daily lake inflows.

More details on the calculation process of the SOPSO can be found in the literature (Kamali et al., 2013). The maximum *WANSE* of selected flood events is used as the objective function

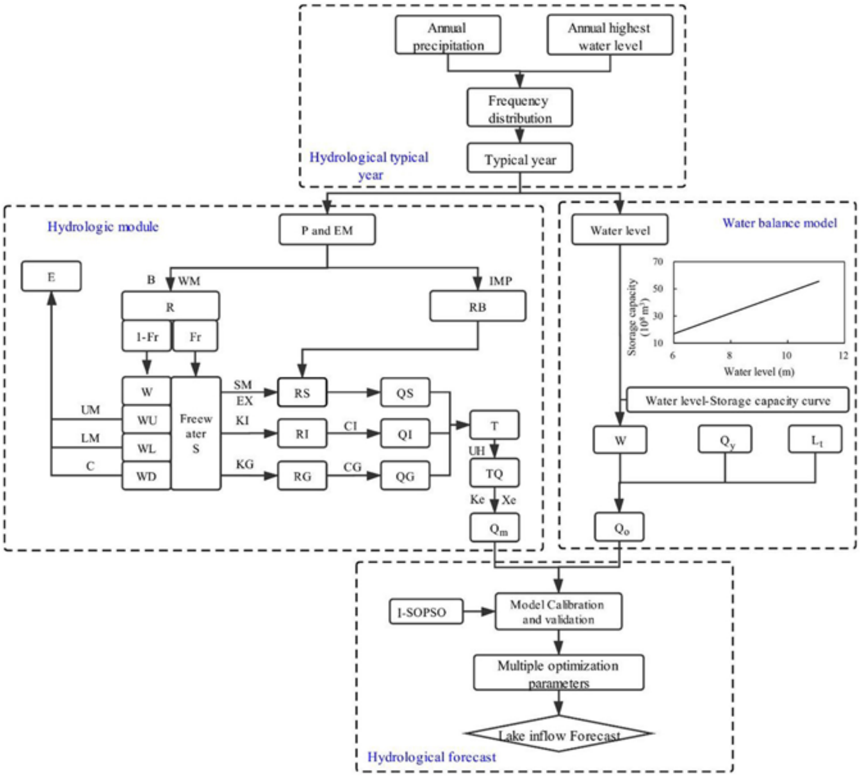

FIGURE 2 | Technique path map of the research. Fr: contribution area; RB: runoff of impervious area; S: free water; QS: total surface runoff; QI: total interflow; QG: total groundwater runoff; Other parameter meanings can be seen in **Supplementary Table 1**.

to minimize the error in estimating the goodness-of-fit between observed and simulated values shown in Eq. (13) below:

$$WANSE = \frac{1}{N}\left(\sum_{i=1}^{N} \omega_i \times (1 - \frac{\sum_{t=1}^{T}(Q_{oi}^t - Q_{mi}^t)^2}{\sum_{t=1}^{T}(Q_{oi}^t - \bar{Q}_{oi})^2})\right) \tag{13}$$

where N is the total number of calibration flood events; ω_i shows the degree of important given to *ith* flood event; $\bar{Q}_{oi}$ is the mean of observed inflows of *ith* flood event; Q_{mi}^t and Q_{oi}^t are the modeled and observed inflows of *ith* flood at time t; and T is the final time step. The *WANSE* value is selected because it is more sensitive to peak flows, and approximate values close to 1 indicate better performances.

Model Performance Assessment

The flood peak, volume, and hydrograph shape are three basic elements describing a flood event (Yue et al., 1999). In this study, the following commonly used five statistical indicators, including the water balance index (*WBI*) (Deng et al., 2015), Nash-Sutcliffe efficiency (*NSE*), percent error in peak flow (F_{peak}), flood volume estimation error (F_{vol}), and determination coefficient (R^2), were adopted to further evaluate the performance of the coupled model, which can provide a quantitative and aggregate estimate of model reliability as follows:

$$WBI(\%) = \frac{\Delta V - (W_I - W_O)}{\Delta V} \times 100 \tag{14}$$

$$NSE = 1 - \frac{\sum_{t=1}^{T}(Q_o^t - Q_m^t)^2}{\sqrt{\sum_{t=1}^{T}(Q_o^t - \bar{Q}_o)^2}} \tag{15}$$

$$F_{peak}(\%) = \frac{Q_o^{peak} - Q_m^{peak}}{Q_o^{peak}} \times 100 \tag{16}$$

$$F_{vol}(\%) = \frac{Vol_o - Vol_m}{Vol_o} \times 100 \tag{17}$$

$$R^2 = \frac{\sum_{t=1}^{T}(Q_m^t - \bar{Q}_m)(Q_o^t - \bar{Q}_o)}{\sqrt{\sum_{t=1}^{T}(Q_m^t - \bar{Q}_m)^2(Q_o^t - \bar{Q}_o)^2}} \tag{18}$$

W_I and W_O are the total volumes of lake inflow and release calculated by water balance method (10^8 m^3) in which the time step to be considered is 1 day; ΔV is lake storage change, which represents the difference between the initial and final lake storages during a flood event; Q_o^{peak} and Q_m^{peak} designate as peak flows of observed and simulated hydrographs (m^3/s); Q_o^t, Q_m^t, $\bar{Q}_m$, and $\bar{Q}_o$ are the observed and simulated lake inflow at time t, mean of observed and simulated lake inflows (m^3/s), respectively; and Vol_o and Vol_m are the observed and the simulated total volume during a flood event (10^8 m^3). The standard error range of the WBI index refers to the allowable error of flood volume (runoff depth) of reservoir hydrological simulate.

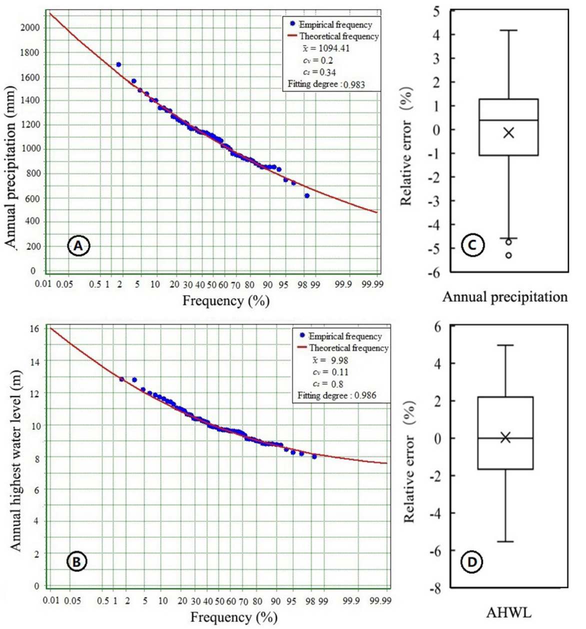

FIGURE 3 | Probability of univariate empirical scatter plots and fitted theoretical probability curve (**A**: Annual precipitation; **B**: Annual maximum water level) and the relative error between empirical frequency and theoretical frequency (**C**: Annual precipitation; **D**: Annual maximum water level).

RESULTS AND DISCUSSION

Selection of Typical Hydrological Year

Marginal Cumulative Probability Distribution Analysis

Before performing frequency analysis, the data homogeneity of AP and the annual maximum water level series have been tested.

Probability analysis of annual precipitation

As we all know, natural runoff is the basis of hydrological analysis. However, natural streamflow observations are not always available in many parts of the world, especially in Lake Basins that have multiple tributaries, see the impact of anthropogenic activities, and do not have observation data. Therefore, in actual research, many scholars use precipitation data that is less affected by anthropogenic activities to carry out the hydrological frequency analysis and obtain very good results (Vandenberghe et al., 2011; Dodangeh et al., 2019).

In this paper, the results of AP frequency analysis indicate that the fitted distribution curve performs well (fitting degree = 0.983) due to good agreement between observed AP data and theoretical probability (**Figure 3A**). The 60-year AP series has an average ($\bar{x}$) of 1094.67 mm, a deviation coefficient (c_v) of 0.19, and a skewness (c_s) of 0.34. Meanwhile, box-whisker plots of absolute error of AP frequency show that the maximum and minimum relative errors are 4.18 and −5.3% (**Figure 3C**), which occurred in 1961 and 1974, respectively.

Probability analysis of annual highest water level

The amount of lake inflow will directly reflect the water level change of the lake. At the same time, considering the availability of data and the hydrological situation of the whole study area, the AHWL of the lake is also a useful index for frequency analysis. In this study, the AHWL data of the Zhongmiao station is used for frequency analysis (**Figure 3B**). **Figure 3B** shows the fitting curve followed the observed dataset reasonably well. The probability distributions of calibrated parameter values can be estimated roughly by **Figure 3B**, which are 10.06 m ($\bar{x}$), 0.11 (c_v), and 0.8 (c_s), respectively. The distribution of relative error ranges from −5.53 to 4.97% (**Figure 3D**), with an average value of 0.04%. Consequently, the P-III fitting curve is reasonable as the marginal cumulative probability distribution function.

In **Supplemental Information** (Part A), details can be found on the comparison probability analysis of AP and AHWL.

Bivariate AP-AHWL Probability Analysis

There is a causal relationship between the change of lake level and precipitation. Meanwhile, from a statistical perspective, the correlation coefficient between the AP and the AHWL is 0.82 (**Figure 4A**), which belongs to highly correlated. The correlation coefficient between the AP (11 rainfall stations) and AHWL is between 0.66 and 0.82, **Figure 4B** respectively. Therefore, the two variables (AP and AHWL) are considered at the same time to selected the typical years in the study.

The theoretical joint probability distribution of the 60-year historical hydrological series results of the three copula functions are presented in **Figure 5**. Based on the graphic analysis method (**Figures 5A,B**), the Gumbel–Hougaard function best represents the bivariate distribution of the AP and AHWL during almost the entire year, followed by the Clayton function, with the Frank function being the worst. Meanwhile, the order of *AIC* values from small (good) to large (bad) is −433.8 (Gumbel–Hougaard method), −405.2 (Clayton method), and −299 (Frank method), which is in agreement with the finding of the graphic analysis method, as, the smaller the value is, the better the fitting degree is. What is more, in the Kolmogorov–Smirnov test, the *p*-values of the three copula functions are greater than 0.05, indicating that there is no significant difference from the empirical frequency, while the D_n values of Clayton method (0.08), Gumbel–Hougaard method (0.1), and Frank method (0.15) indicate that Clayton Copula function has the best fit. Thus, considering the fit of the whole series, the Gumbel–Hougaard copula function was chosen to select the typical hydrological years, which are 1978, 2007, and 2016 (**Table 1**).

Results of Water Balance Method

The lake/reservoir inflow observation records are important for hydrological research and practice projects, such as flood simulations, hydraulic engineering design, water resource planning and management, etc. (Zhou et al., 2019). Because detailed and accurate daily data are difficult to obtain (Deng et al., 2015), a water balance analysis was only applied to calculate the daily inflow of flood events.

Before taking the inflow calculated by water balance as the measured runoff, it is necessary to verify whether the measured daily inflow (land runoff) calculated by the water balance method is reasonable. In this part, the change in the lake storage of a flood can be obtained in two ways: (1) changes

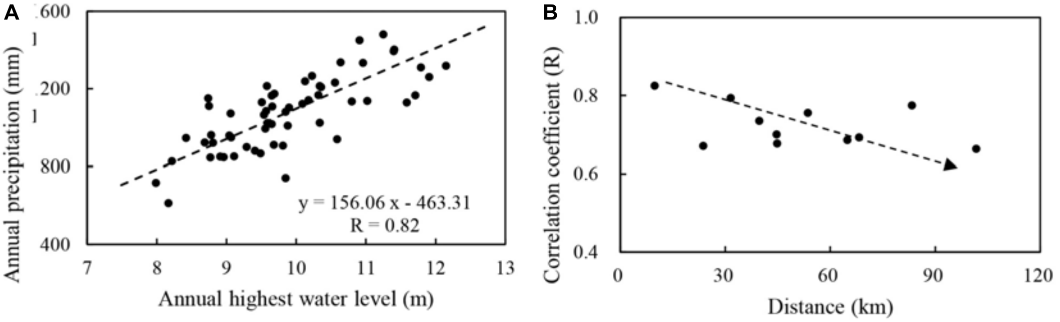

FIGURE 4 | Variable relationship analysis **(A)** AP versus AHWL and **(B)** the correlation coefficient between AHWL and AP of 11 rainfall stations versus vertical distance from Zhongmiao hydrological station.

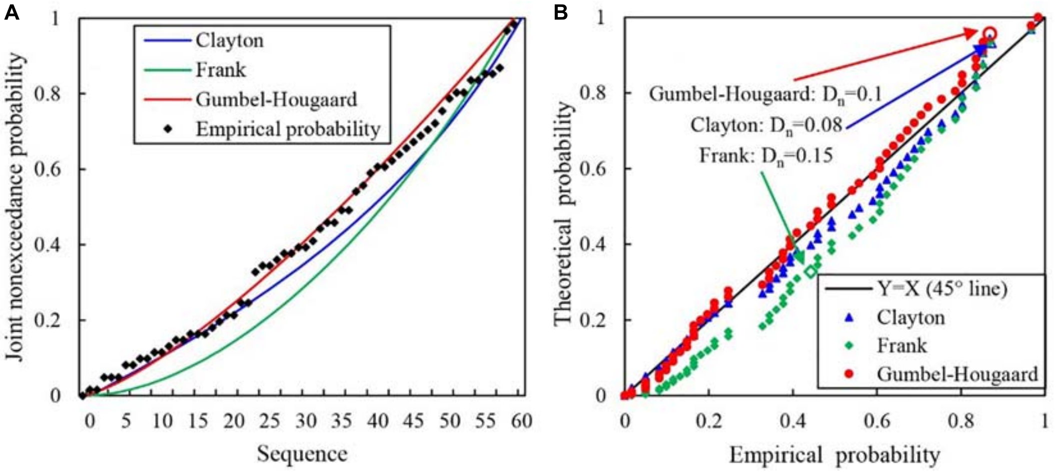

FIGURE 5 | Comparison of joint cumulative probability distributions obtained using three copula methods with empirical probability.

TABLE 1 | Characteristic statistics of typical years.

Typical year	Variables		Bivariate probability
	AP (mm)	AHWL (m)	*F* (%)
1978 (Low flow year)	612	8.17	98.4
2007 (Normal flow year)	1081	9.85	49.5
2016 (High flow year)	1530	12.76	3.3

in storage capacity corresponding to the beginning and final time of each flood event named ΔV; and (2) changes in the total runoff obtained by daily observed inflow which calculated by water balance method, namely, W_I-W_O. The *WBI* index is used to evaluate the water balance method performance for the study area during flood events. It can be seen from **Table 2** that the order of the overall calculation errors (from small to large) for the three typical years is as follows: 2007, 2016, and 1978. The *WBI* values of 12 flood events are between 1.4 and −19.5%, which is within the standard error range (±20%). The values of *WBI* of the selected flood events are positive/negative, indicating that using the water balance method would overestimate/underestimate the lake flows, which may be caused by missing data for actual scheduling rules of Chaohu sluice and Zhaohe sluice, the imprecise relationship between water level and lake storage that is obtained by linear fitting of measured discrete points. Although there are many factors that affect the accuracy of the calculation, the calculated results show that the method can be applied to calculate the daily lake inflows during the flood period.

Calibration and Validation of the Coupled Model

High Flow Year

The I-SOPSO algorithm is linked to the coupled model in a Fortran environment, and the I-SOPSO maximizes the calibration objective function, which is the sum of weighted *NSE* calculated by comparing observed (calculated by water balance method) and simulated hydrograph. Four flood events were selected at daily time steps in 2016–the April 6, July 1, and October 27 flood events are the calibration period and the June 2 flood event the validation period–considering the short time interval between the June 2 and July 1 flood events. The *NSE*,

TABLE 2 | Performance of water balance during flood events.

Typical year	Flood events	Δ *V* (10^8)	W_I-W_O (10^8)	WBI (%)
2016	20160406	1.17	1.24	−5.9
	20160602	2.23	2.5	−12.3
	20160701	23.4	24	0
	20161027	5.1	5.5	−8.7
2007	20070415	1.17	1.16	0.8
	20070710	5.42	5.42	−0.1
	20070828	2.74	2.87	−5
	20070920	1.37	1.43	1.4
1978	19780509	0.44	0.52	−18.4
	19780530	0.81	0.8	1.2
	19780625	1.89	1.88	0.5
	19781111	0.34	0.47	−19.5

TABLE 3 | Simulation performances of hydrograph of selected flood events in high inflow year by the coupled water balance method and Xin'anjiang model.

Flood events	Calibration periods			Validation period
	20160406	20160701	20161027	20160602
NSE	0.74	0.89	0.9	0.76
F_{peak} (%)	−6.8	3.2	15.6	13.6
F_{vol} (%)	−12	17.3	0.59	12.2
R^2	0.8	0.93	0.91	0.73

F_{peak}, F_{vol}, and R^2 were calculated to evaluate the performance of the coupled model, as shown in **Table 3** and **Figure 6**.

For the graphic evaluation of the model, the daily inflow of the four flood events observed were well followed by the simulated runoff from the coupled model. In **Table 3**, the values of *NSE* are 0.74, 0.89, and 0.9 during the calibration periods, and, for the validation period, the value of *NSE* is 0.76, indicating that the coupled water balance and the Xin'anjiang model can reasonably predict the general shapes of the hydrographs (**Figure 6**). In terms of R^2, which is the linear correlation between and simulated results and observed data, the R^2 values of four flood events are more than 0.73, with a mean of 0.85, which is an acceptable statistic that confirms the capability of the model simulate the catchment response (Mahmood and Jia, 2019). The total runoff volume errors (F_{vol}) and the peak inflow estimation errors (F_{peak}) are within 20% of the four flood events on a daily scale, which meet the level standard required for flood simulation (MWR, 2008). Considering the results of four evaluating indicators, the coupled model can obtain desirable results in a study area, which provides technical support, especially in the practical application process to solve the lack of data or incomplete data lake or reservoir basin.

The values of F_{peak} are −6.8, 13.6, 3.2, and 15.6%, with relatively large errors, which may be induced by the error from water level observation. For example, when the water level in Chaohu Lake is 8.0 m (normal storage level) and its observation error is 0.1 m, the induced error of reservoir storage volume and estimated daily inflow are about 0.77×10^8 m^3 and 885.4 m^3/s, respectively. The calculation of the objective function of the model may be another uncertainty source (Tian et al., 2014). In the calculation of the model, the July 1, 2016, flood event was considered with a larger weight (three times that of other flood events), taking into account the greater hazards based on the flood peak and flood volume. The advantage of using different weights can avoid fall into a situation of overfitting in a certain flood but neglecting the important flood events.

For F_{vol}, the value of the July 1, 2016, flood event (17.3%) is slightly larger than the other flood events, which is seriously under-estimated the total volume of lake inflow. There are many reasons for the deviation of model calculation results.

Precipitation is a key component to drive the hydrologic model. The heterogeneous spatial and temporal distributions in basins, inadequate precipitation stations, and location of the rainfall center may normally influence the quality of simulate accuracy (Xu et al., 2013; Zeng et al., 2018; Zhong et al., 2018). During the study period, the July 1, 2016, flood event is characterized by a long-term rainstorm and the uneven spatial distribution of precipitation. In order to

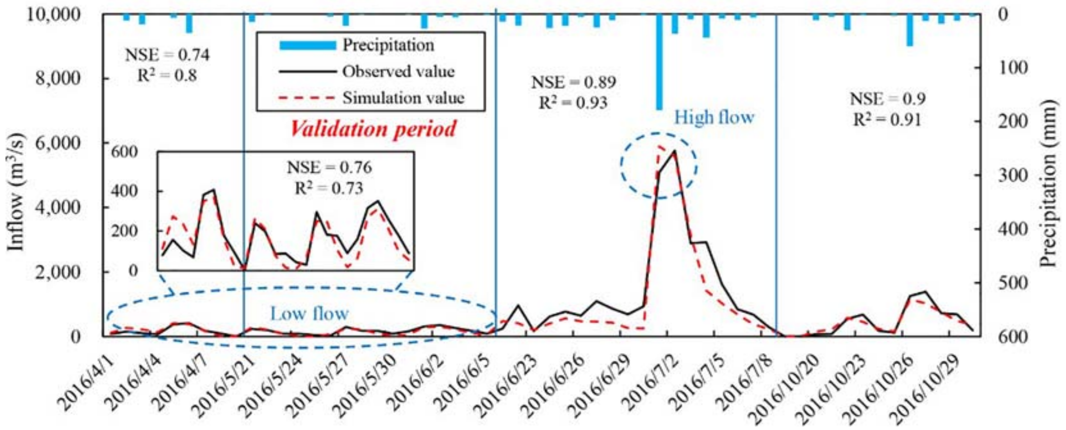

FIGURE 6 | Results for the four flood events of Lake inflows.

understand the spatial distribution of precipitation in the third (July 1, 2016) flood event in detail, 33 rainfall stations in the Yearbook were collected to make the spatial distribution map. It can be seen that the highest values of P are related to the south part of the Chaohu Lake (278.3, 410.8, 516.2, and 646.9 mm), while the northern part shows the lowest level of P for the total maximum precipitation in 1-day, 3-day, 5-day or total precipitation volume (51.8, 76.3, 91, and 187.1 mm, respectively) during the July 1, 2016, flood event (**Figure 7**). The total area precipitation based on the Thiessen polygons method in the model is 424 mm during the July 1, 2016 flood event, which lacks the flexibility to investigate possible spatial evolution of model parameters. Heterogeneous spatial precipitation, as a fundamental process of hydrological cycle, is the first major source of uncertainty in the results of the present study.

Meanwhile, the storage of small reservoirs and the regulation of sluices and dams are not considered in the model structure, which will cause deviations in the calculation results of the inflow process and flood inflow, e.g., Longhekou reservoir, located in Hangbu River, which is the biggest reservoir with a drainage area of 1120 km^2, and the inflow to the reservoir is mainly the result of localized rainfall. According to the yearbook, the maximum daily flow of Longhekou Reservoir Station was 805 m^3/s, according to the data, there is no discharge, and there should be no discharge based on the control operation rules. However, the actual release of reservoirs release is unclear in this study. In addition, the model's structure is probably another reason because the Xin'anjiang model was built for the regions either low or high surface runoff with the assumption that surface runoff is not generated until the soil moisture content reaches field capacity, but in some cases, like in the mountainous areas and cities, the flood could happen when the intensity of rainfall is large without filling up the soil storage. Therefore, limited and understanding of nature and simplifications in representing the hydrological processes, Xin'anjiang model structures must be in error to some extent, although the structure and parameters of the model can reflect the main laws and characteristics of rainfall and runoff process in humid areas and can obtain better precision.

Besides, most parameters of the model cannot be measured via direct observations in the field but through practice to estimate parameter values with historical observation data using an improved automated search algorithm (I-SOPSO). In this process, the system identification method is used to optimize the debugging, so the variables and parameters in existing hydrology models determined may not be the optimal results (Wu et al., 2017; Mahmood and Jia, 2019). These different sources of uncertainty act to compound the rainfall-runoff simulating and can have a significant impact on the accuracy of simulation results. However, if we assumed that the abovementioned uncertainties can affect the result of the present study by 15∼20% (Coe and Foley, 2001), the results of the present study are still quite satisfactory and can be a good source for understanding the lake inflow process.

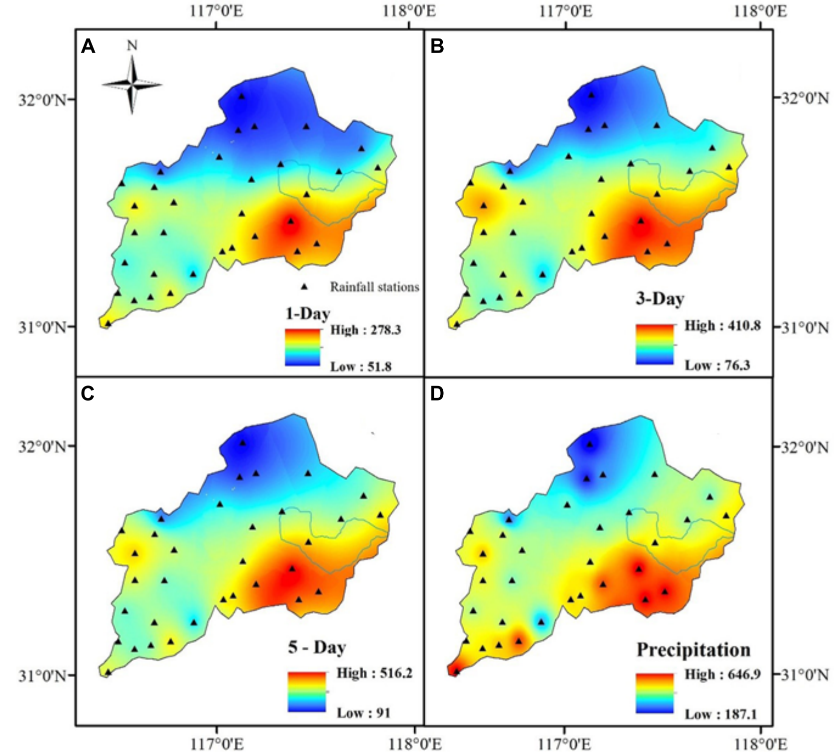

FIGURE 7 | Spatial distributions of total maximum precipitation in 1-day **(A)**, 3-day **(B)**, 5-day **(C)**, or total precipitation volumes **(D)** in the July 1, 2016 flood event (Units: mm).

TABLE 4 | Summary of performance of selected flood events in 2007 and 1978 year.

Typical year	Flood events	*NSE*	F_{peak} (%)	F_{vol} (%)	R^2
2007	20070415	0.53	−1.67	9.48	0.86
	20070710	0.75	7.03	**24.70***	0.89
	20070828	0.74	**22.15***	14.97	0.88
	20070920	0.84	0.38	**26.40***	0.97
1978	19780509	0.54	**−42.8***	**22.2***	0.81
	19780530	0.47	11.6	13.8	0.6
	19780625	0.71	**27***	11.9	0.76
	19781111	0.78	**−39.8***	**−36.9***	0.9

*Bold values and * marks indicate that the value do not meet the standard of simulation accuracy.*

Low Flow Year and Normal Flow Year

The performance of selected flood events in the normal flow year and the low flow year is summarized in **Table 4**. It can be seen from this table that there are three and five calculated index values exceeding the critical values for the normal flow year and the low flow year. Considering the comprehensive level of the four indicators, the simulation results of in the normal flow year (2007) are better than in the low flow year (1978) and worse than in the high flow year (2016), indicating that there is a more complex relationship between rainfall and runoff due to the intervention of more anthropogenic activities and climate change. As one of the primary farming areas of China, the landscape of the Chaohu Lake Basin consists mainly of farmland, woodland area, and water body accounting for 61.8, 16, and 10.3%, respectively. Meanwhile, surface water bodies (rivers and lake) in the study area are important water resources for local agriculture activities.

For better understanding and water resources planning and management, it is suggested to take into account and reduce sources of uncertainty when making hydrological simulate. In the present study, quantifying and reducing uncertainty in hydrological modeling from multiple sources, i.e., parameter uncertainty, input uncertainty, and model structural uncertainty, are not included in this study considering that the current calculation results meet the requirements. Further research can be carried out to improve the accuracy of the model through more accurate input data sets and uncertainty analysis.

Long-Series of Lake Inflow Simulation

According to the optimal parameters of the calibrated coupled model, the daily runoff hydrograph is simulated (**Figure 8**). According to the previous investigation project, the entire Chaohu Lake Basin with an area of 13486 km^2 (including the surface area of Chaohu Lake) has an average runoff of 34.9×10^8 m^3. Meanwhile, the surface runoff of Chaohu Lake is 6.3×10^8 m^3, which is calculated by multiplying the lake area with the annual mean net precipitation. Therefore, the average land surface runoff of the study area, which is calculated by weighting the land surface catchment area (weight = 0.66), is 18.9×10^8 m^3. The result of the annual inflow (land runoff) of the study area was calculated by the coupled model to be 19.4×10^8 m^3 in the normal flow year, and the corresponding bivariate probability is 49.5%. The relative error is −2.6%, indicating that the coupled water balance and Xin'anjiang model are available in the study area, which can better simulate the daily inflow process of the lake without the measured runoff data. The calculated land inflows of the high flow and the low flow years are 44.4×10^8 m^3/a and 13.7×10^8 m^3/a, respectively.

CONCLUSION

In this paper, the copula functions are adopted to establish the bivariate probabilistic model for simulating the AP and AHWL between 1956 and 2017. The coupled water balance method and Xin'anjiang model is then used to explore lake inflows of Upper Chaohu Lake Watershed to gather more information.

The goodness-of-fit test indicates that the Gumbel–Hougaard function is the best-fit for AP-AHWL with Pearson-III margin distributions, which is thereby applied to select the typical hydrological year, including high flow (2016), low flow (1978), and normal flow years (2007). Furthermore, the *WBI* values of the flood events are within 20%. Overall, the order of the *WBI* values (from small to large) for the three typical years is

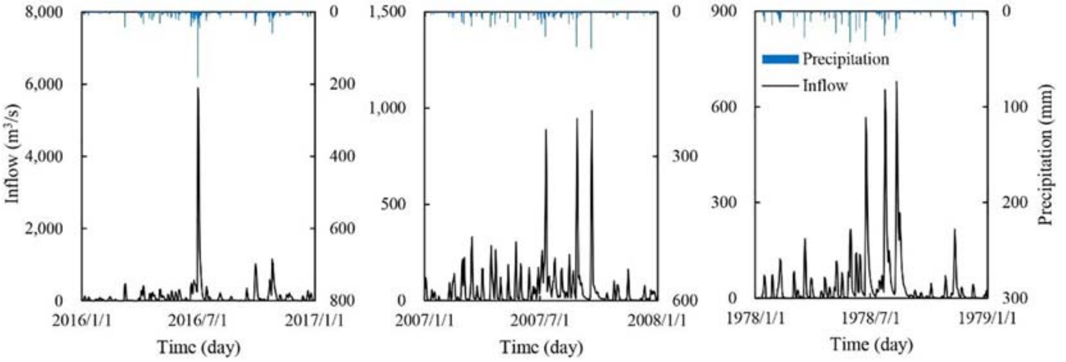

FIGURE 8 | Daily lake inflow hydrograph of the typical years.

2007, 2016, and 1978. The calibration and verification results of the coupled water balance method and the Xin'anjiang model show that the simulated results are better in the high flow year than in the normal flow and low inflow year. Some calculated index values exceed the critical values for normal inflow year and low inflow year, which is most probably caused by the parameter uncertainty, input uncertainty, and model structural uncertainty. Finally, the result of comparison the annual lake inflow simulation in normal inflow year (19.4×10^8 m^3) and the results of the average land surface runoff of the study area (18.9×10^8 m^3) indicates that the coupled Xin'anjiang model and water balance method are effective ways to calculate the daily lake inflow. The land inflows in high flow year and low flow year are 44.4×10^8 m^3 and 13.7×10^8 m^3, respectively. In conclusion, the results of this paper are helpful to understand the daily lake inflows process in Upper Chaohu Lake Basin. They can be used as a basis for determining the appropriate operation and management of water resource systems.

DATA AVAILABILITY STATEMENT

All data, models, or code generated or used during the study are available from the corresponding author by request (behellen@163.com).

AUTHOR CONTRIBUTIONS

XL provided the technical guidance. WL provided the manuscript ideas and financial support. QY mainly revised the language issues of the manuscript. SC provided basic data. XW gave amendments to the details of the manuscript. JW and CW were in the process of calculation some constructive suggestions were given. ZL organized the overall calculation, writing and drawing of the manuscript. All authors contributed to the article and approved the submitted version.

FUNDING

This manuscript was jointly supported by Young Elite Scientists Sponsorship Program by CAST (2019QNRC001), the National Key R&D Program of China (2017YFC0406004), the National Natural Science Fund (51709273), and the Key R&D Program of Power Construction Corporation of China (DJ-ZDZX-2016-02).

SUPPLEMENTARY MATERIAL

The Supplementary Material for this article can be found online at: https://www.frontiersin.org/articles/10.3389/feart.2021.615692/full#supplementary-material

REFERENCES

Ahmadi, F., Radmaneh, F., Sharifi, M. R., and Mirabbasi, R. (2018). Bivariate frequency analysis of low flow using copula functions (case study: Dez River Basin, Iran). *Environ. Earth Sci.* 77:643. doi: 10.1007/s12665-018-7819-2

Bai, P., Liu, X., Liang, K., Liu, X., and Liu, C. (2017). A comparison of simple and complex versions of the Xinanjiang hydrological model in predicting runoff in ungauged basins. *Hydrol. Res.* 48, 1282–1295. doi: 10.2166/nh.2016.094

Cao, Z., Li, S., Zhao, Y., Wang, T., Bergquist, R., Huang, Y., et al. (2018). Spatio-temporal pattern of schistosomiasis in Anhui Province, East China: potential effect of the Yangtze River - Huaihe River Water Transfer Project. *Parasitol. Int.* 67, 538–546. doi: 10.1016/j.parint.2018.05.007

Coe, M. T., and Foley, J. A. (2001). Human and natural impacts on the water resources of the Lake Chad basin. *J. Geophys. Res. Atmospheres* 106, 3349–3356. doi: 10.1029/2000JD900587

Deng, C., Liu, P., Liu, Y., Wu, Z., and Wang, D. (2015). Integrated hydrologic and reservoir routing model for real-time water level forecasts. *J. Hydrol. Eng.* 9:05014032. doi: 10.1061/(asce)he.1943-5584.0001138

Dodangeh, E., Shahedi, K., Solaimani, K., Shiau, J., and Abraham, J. (2019). Data-based bivariate uncertainty assessment of extreme rainfall-runoff using copulas: comparison between annual maximum series (AMS) and peaks over threshold (POT). *Environ. Monit. Assess.* 191:67. doi: 10.1007/s10661-019-7202-0

Eberhart, R., and Kennedy, J. (1995). "A new optimizer using particle swarm theory," in *Proceedings of the 6th International Symposium on Micro Machine and Human Science MHS'95*, Nagoya, 39–43.

Gal, L., Grippa, M., Hiernaux, P., Peugeot, C., Mougin, E., and Kergoat, L. (2016). Changes in lakes water volume and runoff over ungauged Sahelian watersheds. *J. Hydrol.* 540, 1176–1188. doi: 10.1016/j.jhydrol.2016.07.035

Genestm, C., and Mackaym, J. (1986). The joy of copulas: bivariate distributions with uniform marginals. *Am. Stat.* 40, 280–283. doi: 10.2307/2684602

Kamali, B., Mousavi, S. J., and Abbaspour, K. C. (2013). Automatic calibration of HEC-HMS using single-objective and multi-objective PSO algorithms. *Hydrol. Process.* 27, 4028–4042. doi: 10.1002/hyp.9510

Lei, G., Yin, J., Wang, W., and Wang, H. (2018). The analysis and improvement of the fuzzy weighted optimum curve-fitting method of pearson – type III distribution. *Water Resour. Manag.* 32, 4511–4526. doi: 10.1007/s11269-018-2055-9

Li, Y., Cui, Q., Li, C., Wang, X., Cai, Y., Cui, G., et al. (2017). An improved multi-objective optimization model for supporting reservoir operation of China's South-to-North Water Diversion Project. *Sci. Total Environ.* 575, 970–981. doi: 10.1016/j.scitotenv.2016.09.165

Lin, K., Lv, F., Chen, L., Singh, V. P., Zhang, Q., and Chen, X. (2014). Xinanjiang model combined with Curve Number to simulate the effect of land use change on environmental flow. *J. Hydrol.* 519, 3142–3152. doi: 10.1016/j.jhydrol.2014.10.049

Lü, H., Hou, T., Horton, R., Zhu, Y., Chen, X., Jia, Y., et al. (2013). The streamflow estimation using the Xinanjiang rainfall runoff model and dual state-parameter estimation method. *J. Hydrol.* 480, 102–114. doi: 10.1016/j.jhydrol.2012.12.011

Mahmood, R., and Jia, S. (2019). Assessment of hydro-climatic trends and causes of dramatically declining stream flow to Lake Chad, Africa, using a hydrological approach. *Sci. Total Environ.* 675, 122–140. doi: 10.1016/j.scitotenv.2019.04.219

Mohebzadeh, H., and Fallah, M. (2019). Quantitative analysis of water balance components in Lake Urmia, Iran using remote sensing technology. *Rem. Sens. Appl. Soc. Environ.* 13, 389–400. doi: 10.1016/j.rsase.2018.12.009

MWR (2008). *Standard for Hydrological Information and Hydrological Forecasting (GB/T 22482–2008)*. Beijing: Ministry of Water Resources of the People's Republic of China.

Sraj, M., Bezak, N., and Brilly, M. (2015). Bivariate flood frequency analysis using the copula function: a case study of the Litija station on the Sava River. *Hydrol. Process.* 29, 225–238. doi: 10.1002/hyp.10145

Tian, Y., Booij, M. J., and Xu, Y. (2014). Uncertainty in high and low flows due to model structure and parameter errors. *Stoch. Environ. Res. Risk Assess.* 28, 319–332. doi: 10.1007/s00477-013-0751-9

Vandenberghe, S., Verhoest, N. E. C., Onof, C., and De Baets, B. (2011). A comparative copula-based bivariate frequency analysis of observed and simulated storm events: a case study on Bartlett-Lewis modeled rainfall. *Water Resour. Res.* 47:W07529. doi: 10.1029/2009WR008388

Wu, Q., Liu, S., Cai, Y., Li, X., and Jiang, Y. (2017). Improvement of hydrological model calibration by selecting multiple parameter ranges. *Hydrol. Earth Syst. Sci.* 21, 393–407. doi: 10.5194/hess-21-393-2017

Xu, H., Xu, C., Chen, H., Zhang, Z., and Li, L. (2013). Assessing the influence of rain gauge density and distribution on hydrological model performance in a humid region of China. *J. Hydrol.* 505, 1–12. doi: 10.1016/j.jhydrol.2013.09.004

Yang, J., Yu, Z., Yi, P., Frape, S. K., Gong, M., and Zhang, Y. (2020). Evaluation of surface water and groundwater interactions in the upstream of Kui river and Yunlong lake, Xuzhou, China. *J. Hydrol.* 583:124549. doi: 10.1016/j.jhydrol.2020.124549

Yu, Y., Zhao, W., Martinez-Murillo, J. F., and Pereira, P. (2020). Loess Plateau: from degradation to restoration. *Sci. Total Environ.* 738:140206. doi: 10.1016/j.scitotenv.2020.140206

Yue, S., Ouarda, T. B. M. J., Bobée, B., Legendre, P., and Bruneau, P. (1999). The Gumbel mixed model for flood frequency analysis. *J. Hydrol.* 226, 88–100. doi: 10.1016/S0022-1694(99)00168-7

Yun, B., Sun, Z., Zeng, B., Long, J., Li, C., and Zhang, J. (2018). Reservoir inflow forecast using a clustered random deep fusion approach in the three gorges reservoir, China. *J. Hydrol. Eng.* 10:04018041. doi: 10.1061/(asce)he.1943-5584.0001694

Zeng, Q., Chen, H., Xu, C., Jie, M., Chen, J., Guo, S., et al. (2018). The effect of rain gauge density and distribution on runoff simulation using a lumped hydrological modelling approach. *J. Hydrol.* 563, 106–122. doi: 10.1016/j.jhydrol.2018.05.058

Zhao, R. (1984). *Watershed Hydrological Simulation—Xin'an River Three-Source Model and Northern Shanxi model*. Beijing: Water Power Press.

Zhao, R. (1992). Xinanjiang model applied in China. *J. Hydrol.* 135, 371–381. doi: 10.1016/0022-1694(92)90096-e

Zhong, W., Li, R., Liu, Y. Q., and Xu, J. (2018). Effect of different areal precipitation estimation methods on the accuracy of a reservoir runoff inflow forecast model. *IOP Conf. Ser. Earth Environ. Sci.* 208:12043. doi: 10.1088/1755-1315/208/1/012043

Zhou, W., Yang, Z., Liu, P., Bai, F., and Zheng, C. (2019). Estimation of reservoir inflow with significant lateral inflow by using the adjoint equation method. *J. Hydrol.* 574, 360–372. doi: 10.1016/j.jhydrol.2019.04.047

Conflict of Interest: The authors declare that the research was conducted in the absence of any commercial or financial relationships that could be construed as a potential conflict of interest.

frontiers in Earth Science

ORIGINAL RESEARCH
published: 14 July 2021
doi: 10.3389/feart.2021.704901

Soil Freeze-Thaw and Water Transport Characteristics Under Different Vegetation Types in Seasonal Freeze-Thaw Areas of the Loess Plateau

Lanfeng Bo[1,2], Zhanbin Li[1,2]*, Peng Li[3], Guoche Xu[3], Lie Xiao[3] and Bo Ma[1,2]

[1]State Key Laboratory of Soil Erosion and Dryland Farming on the Loess Plateau, Institute of Soil and Water Conservation, CAS and MWR, Yangling, China, [2]University of Chinese Academy of Sciences, Beijing, China, [3]State Key Laboratory of Eco-hydraulics in Northwest Arid Region of China, Xi'an University of Technology, Xi'an, China

In the arid and semi-arid regions of the Loess Plateau, seasonal freezing and thawing influence soil water movement, and water movement directly influences vegetation growth. However, currently, research with regard to freezing and thawing processes under various vegetation types and the mechanism of soil water movement is lacking. Therefore, the present study explored soil water migration characteristics of two typical vegetation types [arbor land (AL) and shrub land (SL)] on the Loess Plateau during seasonal freezing and thawing processes using bare land (BL) as a control. We used field measured data for hourly soil temperature (ST) and soil water content (SWC) at a depth of 100 cm below the soil surface from November 2017 to March 2018. Freezing and thawing process was divided into three stages based on ST change (initial freezing period, stable freezing period, and thawing period). Compared with previous studies in this area, ST is lower than expected, and SWC migration characteristics are also different. The results revealed that: 1) the maximum freezing depth of AL and SL was 60 cm, which was 30 cm less than that of BL. The freezing date of each soil layer in BL was the earliest and average ST value was the lowest. BL had the highest degree of freezing. The freezing of all soil layers in AL occurred at a later date than that of SL. ST and the minimum soil freezing temperatures were higher than those of SL, and the capacity of AL to resist freezing was higher; 2) the SWCs in AL and BL at depths of 0–10 cm and 10–30 cm decreased, whereas SWCs of AL and BL at a depth of 60 cm increased by 152 and 146%, respectively. The SWCs of SL at soil depths of 0–10 cm, 10–30 cm, and 30–60 cm increased by 46.3, 78.4 and 205%, respectively. The amount and distribution of soil moisture in SL were optimum when compared to those of AL and BL. The results of the present study could provide a scientific basis for vegetation restoration in arid and semi-arid areas of the Loess Plateau.

Keywords: soil temperature, soil water content, soil hydrothermal transport, natural freeze-thaw cycle, soil heat transfer

Edited by:
Yang Yu,
Beijing Forestry University, China

Reviewed by:
Ali Keshavarzi,
University of Tehran, Iran
Kaibo Wang,
Chinese Academy of Sciences, China

***Correspondence:**
Zhanbin Li
zbli@ms.iswc.ac.cn

Specialty section:
This article was submitted to Hydrosphere, a section of the journal Frontiers in Earth Science

Received: *12 May 2021*
Accepted: *24 June 2021*
Published: *14 July 2021*

Citation:
Bo L, Li Z, Li P, Xu G, Xiao L and Ma B (2021) Soil Freeze-Thaw and Water Transport Characteristics Under Different Vegetation Types in Seasonal Freeze-Thaw Areas of the Loess Plateau.
Front. Earth Sci. 9:704901.
doi: 10.3389/feart.2021.704901

Abbreviations: AL, arbor land; SL, shrub land; BL, bare land; ST, soil temperature; SWC, soil water content; CV, coefficient of variance; R^2, the determination coefficient.

INTRODUCTION

Soil moisture is a key variable in the hydrological cycle that links precipitation, runoff, and groundwater (Sun et al., 2015; Wang et al., 2018b), and a key ecological factor that determines ecosystem functions and vegetation restoration (Pan et al., 2015; Wang et al., 2019c). Seasonal freezing and thawing influence the movement and distribution of soil moisture (Hu et al., 2013; Fu et al., 2018). Numerous studies have revealed that soil temperature (ST) is a primary driving force, which influences soil water movement during soil freeze-thaw cycles (Li et al., 2012; Wang et al., 2018a; Wang et al., 2019b). Variations in soil water potential caused by freezing of soil drive soil moisture from unfrozen areas to the freezing front (Li et al., 2013; Zhang et al., 2014; Yang and Wang., 2019), resulting in variations in soil moisture distribution (Wu et al., 2017; Lai et al., 2018; Lu et al., 2019). However, soil moisture distribution has had a direct impact on vegetation growth activities in recent years (Xiao et al., 2019; Frost et al., 2020), especially in the arid and semi-arid areas of the Loess Plateau, where long-term rainfall is insufficient and irrigation cannot be practiced (Yang et al., 2012; Cheng and Liu, 2014; Xiao et al., 2020). Therefore, studying soil freezing and thawing processes will enhance our understanding of soil moisture migration dynamics, and could have a guiding significance for the hydrological management of the study area.

Over the last few years, several local and international researchers have investigated the transport mechanisms of soil moisture in different regions and environments during freezing and thawing periods (Mohammed et al., 2013; Chen et al., 2016; Sun et al., 2011). The study areas were mainly distributed in Russia, Canada, the United States, and China, accounting for 50% of the global land area (Kruk et al., 2012; Wang et al., 2019a). A study by Nagare et al. (2011) revealed that freezing time and ground temperature conditions were influenced by soil water content (SWC) and soil texture. Soils with high SWCs are more likely to freeze under similar temperature conditions. During the freezing and thawing process of slope land, heat transfer efficiency between soil and air is higher than that of dam land; however, the amount of soil moisture migration and increase in dam land are greater than those of slope land (Wang et al., 2019a). Forests exhibit higher STs under freezing and thawing conditions, and their buffering capacity to variations in ST is greater than that of grasslands (Hu et al., 2013). In China, most of the current research regarding the effects of freezing and thawing is concentrated in the northeast mountainous areas, Inner Mongolia, and Qinghai-Tibetan Plateau where the freezing degree is severe (Liu et al., 2017; Guo et al., 2018; Zhang et al., 2019a). The freezing and thawing characteristics of the areas in terms of soil freezing days, number of freezing and thawing cycles, freezing temperature, and freezing depth are quite distinct from the seasonal freezing and thawing characteristics in areas of the Loess Plateau. Similarly, several researchers currently use the 24-h average ST (daily average ST) as a statistical unit, and a daily average ST below 0°C as a basis for determining the occurrence of soil freezing (Guo et al., 2011; Guo et al., 2020). However, the statistical method is not suitable for determining seasonal freezing and thawing in areas of the Loess Plateau. The statistical method does not take into account the freezing and thawing events with daily average temperatures greater than 0°C because the day and night temperature variations in the Loess Plateau area are extremely high in autumn and spring. In addition, soil freezing and thawing processes determined by the method, including freezing dates, freezing days, thawing dates, and thawing days, may be delayed or shortened.

Soil erosion is a major environmental challenge threatening the sustainable development of seasonal freeze-thaw areas on the Loess Plateau (Zhang et al., 2019b). Over the last few years, numerous soil and water conservation measures have been implemented in the Loess Plateau area, including terracing, construction of silt dams, farming management, and vegetation restoration (Li et al., 2013; Yu et al., 2020). Among the measures, vegetation restoration has been considered one of the most effective soil and water conservation measures (Guo et al., 2018). However, soil moisture is a key ecological factor that restricts vegetation restoration and sustainable development of agriculture and forestry in the area (Huang et al., 2012; Liu et al., 2012). Presently, numerous studies have been carried out with regard to the influence of vegetation restoration and returning farmland to forests on soil moisture characteristics in the Loess Plateau area. The studies have focused on the impact and response of rainy seasons, various vegetation growth periods or varying growth cycles on SWC (Zhou et al., 2015). Research regarding ST, moisture, and vegetation in winter has received relatively little attention due to the lack of rainfall in winter, low soil moisture transpiration, and limited vegetation growth in the Loess Plateau area. Soil water and heat transfer characteristics of different vegetation types under seasonal freezing and thawing conditions remain indeterminate. According to previous studies, we guess that different vegetation types have a certain buffering effect on freezing and thawing, and at the same time, they will also have different effects on the movement of soil moisture. Therefore, the present study investigated ST, SWC, and air temperature (AT) in two vegetation types and bare land (BL) to comprehensively elucidate the impacts of soil water and heat conditions under various vegetation types on the hydrological processes in frozen soil. The objectives of the present study were: 1) to investigate the freezing and thawing characteristics of BL and two vegetation types, 2) to monitor and assess the water redistribution process caused by freezing and thawing in BL and frozen soil in two vegetation types, and 3) to compare variations in soil moisture migration between two vegetation types during freezing and thawing periods.

MATERIALS AND METHODS

Overview of the Study Area

The study area is located in the Xindiangou Science and Technology Demonstration Park (E110°16′–E110°20′, N37°28′–N37°31′), a soil and water conservation scientific experimental research demonstration base in Suide County, Yulin City, Shaanxi Province, China. The research base is

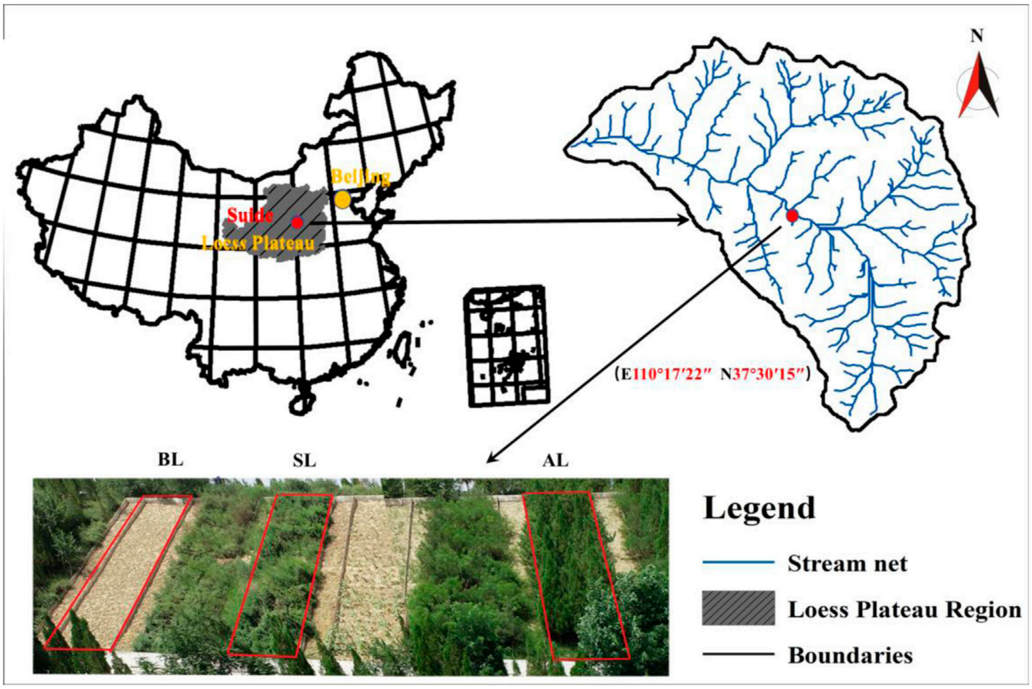

FIGURE 1 | Location map of the study area.

located in the Xindiangou Basin on the left bank of the middle reaches of the Wuding River, a tributary of the Yellow River, with an area of 1.44 km^2 and an altitude of 840–1,040 m (**Figure 1**). The climate of the area is continental temperate and semi-arid monsoon climate. The annual average temperature of the area is 9.7°C, with minimum and maximum temperatures of −27 and 39°C, respectively, and no well-defined freeze-thaw cycles. The average annual precipitation in the basin is 475.1 mm, and summer precipitation accounts for 64.4% of the total annual precipitation. The predominant soil type in the area is silty sandy loam and the vegetation type is temperate forest grassland. Artificial vegetation primarily includes poplar, white elm, dry willow, Chinese arborvitae, and Chinese pine. The shrub vegetation is dominated by yellow rose, korshinsk peashrub, sea buckthorn, and wild jujube.

Monitoring Experiment Layout

Artificial vegetation was selected as the research object. The selected tree species was *Platycladus orientalis* (family Cupressaceae) and the shrub species was *Caragana korshinskii* (family Fabaceae), which are the most commonly used species for vegetation restoration and construction in the Loess Plateau area, and *P. orientalis* is the dominant tree species in the watershed. To reduce the influence of external conditions such as topography and climate on the results of the present study, three runoff communities with similar slope length and slope direction (namely ***C.*** *korshinskii* shrub community, *P. orientalis* community, and BL community) were selected for positioning monitoring (**Figure 1**). We monitored and assessed the effects of seasonal freeze-thaw processes under various vegetation types.

ST and soil moisture (0–100 cm depth) were selected for monitoring due to the following reasons: 1) the root systems of most plants are distributed within the top 90 cm of the soil profile (Wang et al., 2018b); 2) the maximum freezing depth of soil within the monitoring area is 90 cm.

The AT monitoring data were obtained from the weather station (RX3000, United States), and ST and SWC were monitored using ET-100 intelligent soil moisture and temperature monitor (Symorui Environmental Technology Co., Ltd., XiAn, China). Thirty probes were placed in the middle of the three runoff plots (shrubs, trees, and BL). The probes were placed at soil depths of 10, 20, 30, 40, 50, 60, 70, 80, 90, and 100 cm. The soil begins to freeze when ST is below 0°C (273.15 K) and begins to melt when ST is above 0°C. The monitoring period was from November 11, 2017 to March 25, 2018 because seasonal freezing and thawing occur between the end of November and the end of March, and there was no rainfall during the monitoring period. ST and SWC at various soil depths were recorded every 60 min.

Statistical Analyses

The classification of soil freezing and thawing processes was based on hourly STs. Soil was considered frozen when the minimum ST was lower than 0°C. Similarly, soil was considered melted when the maximum ST was higher than 0°C. Freeze-thaw cycle refers to a phenomenon in which ST is above and below 0°C simultaneously in a day. Soil was considered to have entered a stable freezing period (a characteristic of the period is that the soil no longer undergoes freezing and thawing

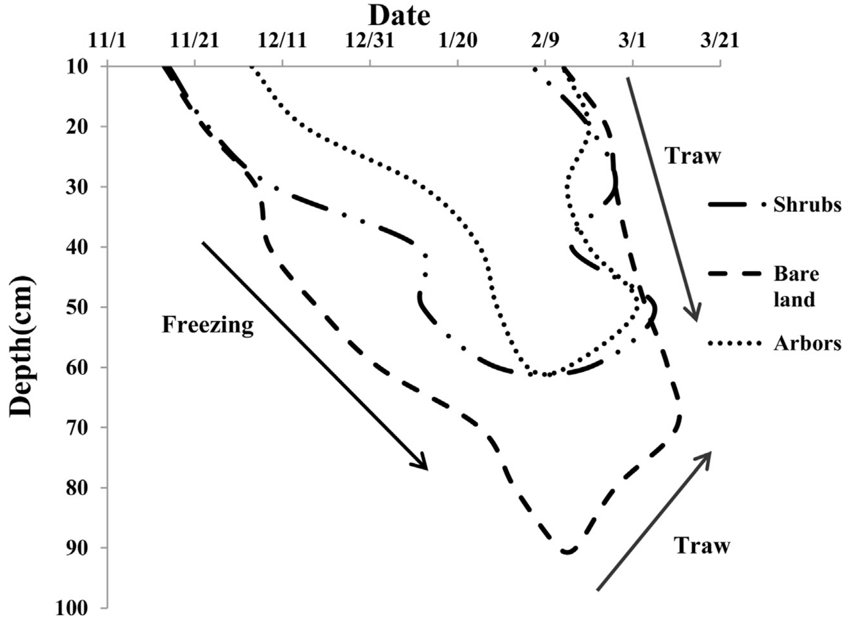

FIGURE 2 | Dynamic diagram of freezing and thawing depth.

cycles) when ST was constantly lower than 0°C. The improved statistical method could effectively reduce errors and enhance statistical accuracy.

Based on the measured ST data, soil freezing and thawing processes during the entire monitoring period was divided into three periods: initial freezing, complete freezing, and thawing periods. Initial freezing period refers to the unstable freezing period in which the soil melts during the day and freezes at night. Complete freezing period refers to the period when ST is constantly lower than 0°C in a stable freezing state for 24 h a day. Thawing period refers to the period when ST begins to be greater than 0°C to a state when ST is completely greater than 0°C.

The freezing rate is defined as the total number of days from the start of soil freezing to the time soil completely freezes at a certain depth; that is, the actual number of days in the initial period of freezing (Wang et al., 2019b).

$$v_{ifreeze} = \frac{1}{d_{iinnitial}} \quad (1)$$

where $V_{i\mathrm{freeze}}$ is the freezing rate of soil at a depth of *i (day)*, $d_{i\mathrm{initial}}$ is the total number of days in the initial freezing period at a depth of *i*.

Melting rate is defined as the number of days from the time soil at a certain depth begins to melt to the time frozen soil completely melts; that is, the actual number of days during the melting period.

$$\mathrm{v}_{\mathrm{ithaw}} = \frac{1}{d_{imelting}} \quad (2)$$

where $v_{i\mathrm{thaw}}$ is the melting rate of soil at depth *i (day)*, $d_{i\mathrm{melting}}$ is the total number of days during the melting period at a depth of *i*.

SPSS Statistics 16.0 (SPSS Inc, Chicago, IL, United States) was used to analyze the relationships among AT, ST, SWC, and soil depths in two vegetation types and BL. Levene's test was used to evaluate dynamic variations between ST and SWC during the monitoring period by measuring the coefficient of variation (CV) of soil profile. Regression analyses and plotting of graphs were performed using Origin 8.5 (OriginLab Corporation, Northampton, MA, United States).

RESULTS

Freezing Process of Soil Profile

The freezing date of arbor land [AL] soil from the surface layer to the deep layer occurred later than that of the corresponding soil layers in shrub land [SL] and [BL] (**Figures 2,3**; **Table 1**). The surface soil layers (0–10 cm) of BL, SL, and AL began to freeze on November 14, November 15, and December 4, 2017, respectively. The freezing dates of SL and AL delayed by one and 21 days, respectively when compared with that of BL (**Figure 2**; **Table 1**). The freezing rates of the three types of land were not significantly different at soil depths below 30 cm and the soil was completely frozen in only 1–2 days. The overall freezing rate of soil in SL was the lowest, followed by BL, while the freezing rate of soil in AL was the highest within the 10–30 cm soil layer. The maximum number of days of soil freezing was observed in the 20–30 cm soil layer, and followed the order of 85 days for BL > 77 days for SL > 63 days for AL. The minimum freezing STs were observed in the 0–10 cm soil layer and were as follows: −13.5°C in SL, −13.45°C in BL, and −8.3°C in AL. During the entire freeze-thaw process, ST in AL at a similar soil depth was the highest, and the soil freezing date was delayed (**Table 2**). The freezing depth of soil in BL was

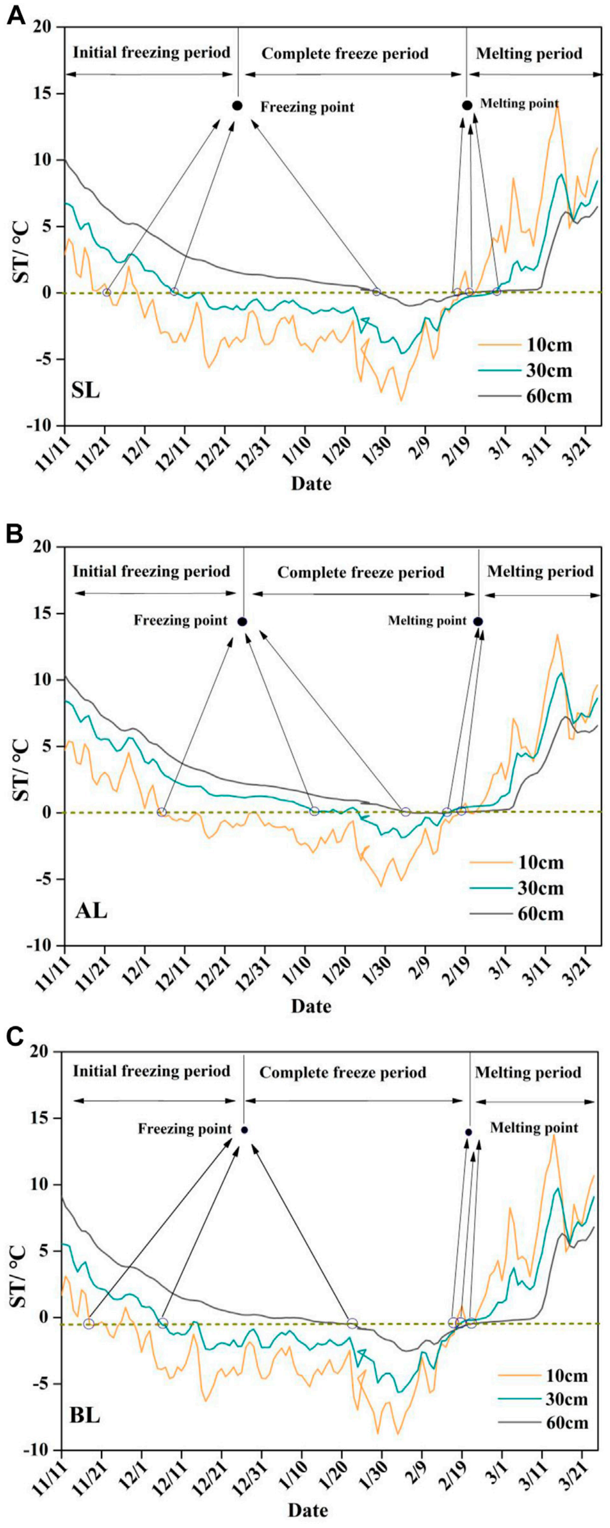

FIGURE 3 | ST dynamics of different land types **(A,B,C)**.

90 cm and that in AL and SL was 60 cm. The freezing depth of soil in BL was 30 cm greater than that of AL and SL (**Figure 2**).

CV was used to describe the degree of ST change. The CV value of ST in AL at the same soil depth was the lowest. Temperature variations in AL soil layers were similar. CV value decreased with increase in depth of the soil layers, and the fluctuating trend gradually plateaued (**Table 2**; **Figure 3**). The enclosed area formed by the intersection of the ST curve and the 0°C line was used as an evaluation criterion for the degree of soil freezing. The degree of soil freezing in BL was the highest, followed by SL, and the lowest degree of freezing was observed in AL (**Figure 3**).

Melting Process of Soil Profile

The soil freezing front moved downwards from the surface layer, in turn, resulting in a unidirectional soil freezing phenomenon. However, thawing of soil was two-way; that is, the top and deepest soil layers began to thaw first and they thawed in turn to the middle soil layers (**Figure 2**; **Table 1**). The thawing rate was similar to the freezing rate, and the thawing time of soil layers below 30 cm was 1–2 days. SL exhibited the lowest melting rate in soil layers with a surface depth of 10–20 cm, followed by BL, and AL, which exhibited the highest melting rate.

The maximum number of freeze-thaw days and the maximum number of freeze-thaw cycles were observed at a depth of 10 cm below the soil surface. The total number of freeze-thaw days observed in SL, BL, and AL were 105, 105, and 84 days, respectively, while the total number of freeze–thaw cycles observed in SL, BL, and AL were 51, 32, and 24 cycles, respectively.

Soil Water Redistribution During Freezing and Thawing

Statistical analyses were performed using SWC data for two vegetation types and BL throughout the monitoring period. The analyses results revealed that the average SWCs of the initial freeze-thaw period, the complete freezing period, and the thawing period in AL were significantly higher than those observed in SL and BL. The CV values of ST in AL were the lowest at various freeze-thaw stages and soil depths (**Table 2**; **Figure 4**). To comprehensively understand the variations in soil moisture migration at different stages during the monitoring period, SWCs at depths of 0–10 cm, 10–30 cm, and 30–60 cm were divided into initial water content (pre-freezing period), freezing period water content (freezing period), melting period water content (melting period), and final water content (average SWC seven days after the melting period). We observed that soil moisture content varied considerably at various soil depths and stages of the freezing period (**Figure 5**).

SWC in SL at soil depths of 0–10 cm, 10–30 cm, and 30–60 cm decreased by 46.5, 43.4, and 25.6%, respectively. SWC in AL at soil depths of 0–10 cm, 10–30 cm, and 30–60 cm decreased by 39, 49, and 5.3% respectively, and SWC in BL decreased by 56.7, 48.6, and 28.8%, respectively. Overall, BL exhibited the highest

TABLE 1 | Freeze-thaw characteristics of different land types.

	Depth (cm)	Initial freezing period	Number of days	Complete freezing period	Number of days	Thawing period	Number of days	The lowest temperature (°C)	The total number of days	FTC (cycles)
Shrubs	10	17/11/15–17/12/14	30	17/12/14–18/2/5	54	18/2/6–18/2/26	21	−13.05	106	51
	20	17/11/24–17/12/5	12	17/12/5–18/2/15	16	18/2/19–18/2/26	8	−9.813	95	20
	30	17/12/9–17/12/10	2	17/12/10–18/2/24	77	18/2/25–18/2/26	2	−6.125	80	4
	40	18/1/11–18/1/12	2	18/1/13–18/2/14	31	18/2/15–18/2/16	2	−3.06	25	4
	50	18/1/12–18/1/13	2	18/1/13–18/3/5	52	18/3/6–18/3/7	2	−2.5	55	4
	60	18/1/29–18/1/30	2	18/1/30–18/2/18	20	18/2/19–18/2/20	2	−1.063	23	4
Arbors	10	17/12/4–17/1215	12	17/12/16–18/2/12	59	18/2/13–18/2/25	13	−−8.3	84	24
	20	17/12/16–17/12/17	2	17/12/18–18/2/18	63	18/2/19–18/2/23	5	−5.75	70	4
	30	18/1/12–18/1/23	12	18/1/24–18/2/13	21	18/2/14–18/2/15	2	−2.63	33	10
	40	18/1/25–18/1/25	1	18/1/26–18/2/18	24	18/2/19–18/2/20	2	−1.625	25	2
	50	18/1/29–18/1/29	1	18/1/29–18/3/1	32	18/3/2–18/3/2	2	−0.625	34	2
	60	18/2/5–18/2/5	1	18/2/6–18/2/13	8	18/2/14–18/2/15	2	−0.063	9	2
Bare land	10	17/11/14–17/12/1	18	17/12/1–18/2/13	75	18/2/13–18/2/26	14	−13.375	105	32
	20	17/11/23–17/12/1	9	17/12/1–18/2/23	85	18/2/23–18/2/26	4	−10.56	95	13
	30	17/12/5–17/12/6	2	17/12/6–18/2/25	82	18/2/25–18/2/25	13	−7.33	83	3
	40	17/12/8–17/12/10	3	17/12/10–18//2/28	81	18/2/28–18/3/2	1	−5.188	85	6
	50	17/12/19–17/12/20	2	17/12/20–18/3/4	75	18/3/4–18/3/4	1	−3.56	76	3
	60	18/1/2–18/1/2	1	18/1/2–18/3/9	67	18/3/9–18/3/9	1	−2.637	67	2
	70	18/1/25–18/1/26	2	18/1/26–18/3/11	45	18/3/11–18/3/11	1	−1.57	46	3
	80	18/2/2–18/2/3	2	18/2/3–18/2/25	23	18/2/25–18/2/26	2	−0.19	25	4
	90	18/2/12–18/2/12	1	18/2/12–18/2/16	5	18/2/16–18/2/16	1	−0.063	5	2

decrease rates in SWC in each soil layer, followed by SL and AL, which exhibited the lowest decrease (**Figure 6**; **Table 2**). In addition, SWC from complete freezing to the end of thawing periods in SL exhibited the highest increase, followed by BL, and AL, which had the lowest SWC (**Figure 6**; **Table 2**).

The difference between the initial water content and the final water content was regarded as the amount of soil water migration at each soil depth during the freezing period. The SWCs in SL at a depth of 0–10 cm increased from 0.082 to 0.12 $\mathrm{cm^3\,cm^{-3}}$ (an increase of 46.3%), increased from 0.125 to 0.223 $\mathrm{cm^3\,cm^{-3}}$ (an increase of 78.4%) at a depth of 10–30 cm, and increased from 0.092 to 0.348 $\mathrm{cm^3\,cm^{-3}}$ (an increase of 205%) at a depth of 30–60 cm. The SWCs in AL in the 0–10 cm soil layer increased from 0.123 to 0.126 $\mathrm{cm^3\,cm^{-3}}$ (an increase of 2.4%), decreased from 0.136 to 0.119 $\mathrm{cm^3\,cm^{-3}}$ (a decrease of 12.5%) at a depth of 10–30 cm, and increased from 0.142 to 0.358 $\mathrm{cm^3\,cm^{-3}}$ (an increase of 152%) at a depth of 30–60 cm. The SWCs in BL in the 0–10 cm soil layer decreased from 0.118 to 0.074 $\mathrm{cm^3\,cm^{-3}}$ (a decrease of 37%), decreased from 0.117 to 0.095 $\mathrm{cm^3\,cm^{-3}}$ (a decrease of 19%) at a depth of 10–30 cm, and increased from 0.132 to 0.325 $\mathrm{cm^3\,cm^{-3}}$ (an increase of 146%) at a depth of 30–60 cm. The maximum SWCs in AL and BL were observed at a depth of 30–60 cm, while SWC in SL increased at depths of 0–10 cm, 10–30 cm, and 30–60 cm (**Figure 6**).

Regression analyses results of ST and soil moisture in SL, AL, and BL revealed that the relationship between ST and soil moisture was linear. Based on soil depths of 0–10 cm, 10–30 cm, and 30–60 cm, SL R^2 values were 0.65, 0.68, and 0.60, respectively; AL R^2 values were 0.40, 0.44, and 0.45, respectively, and BL R^2 values were 0.66, 0.70, and 0.69, respectively (**Table 3**). BL exhibited the highest R^2 values at each soil depth, followed by SL and AL, which exhibited the lowest R^2 values.

The parameter "a" in the linear relationship equation, $Y = aX + b$ was defined as the transfer efficiency between ST and SWC. Based on the equation, parameter "a" of BL was the highest and the value of "a" in AL was the lowest (**Table 3**).

TABLE 2 | Changes in ST and SWC at each stage of the monitoring period.

Land type	Stage	Depth	ST (K)	CV	SWC	CV
Shrub land (SL)	Initial freezing period	10	272.29	0.0095	0.082	0.412
		30	273.04	0.008	0.125	0.055
		60	273.02	0.0004	0.092	0.089
	Complete freezing period	10	269.19	0.0097	0.044	0.145
		30	271.66	0.0043	0.071	0.2113
		60	272.6	0.001	0.068	0.075
	Thawing period	10	272.17	0.014	0.073	0.408
		30	273.13	0.0004	0.098	0.126
		60	275.07	0.0002	0.074	0.0136
Arbor land (AL)	Initial freezing period	10	272.88	0.0025	0.123	0.189
		30	273.23	0.001	0.136	0.087
		60	273.17	0.001	0.142	0.01
	Complete freezing period	10	271.06	0.0064	0.075	0.208
		30	272.16	0.002	0.068	0.056
		60	273.14	0.0001	0.134	0.011
	Thawing period	10	273.3073	0.0042	0.127	0.29
		30	273.173	0.0002	0.074	0.012
		60	273.1526	0.0001	0.135	0.009
Bare land (BL)	Initial freezing period	10	272.834	0.006	0.118	0.289
		30	272.83	0.0016	0.1165	0.166
		60	273.13	0.0001	0.132	0.012
	Complete freezing period	10	268.81	0.0095	0.051	0.147
		30	271.06	0.0052	0.0598	0.1495
		60	272.36	0.0028	0.0937	0.263
	Thawing period	10	272.923	0.0094	0.099	0.349
		30	273.1422	0.0002	0.083	0.042
		60	273.115	0.0002	0.176	0.025

DISCUSSION

The Influence of Vegetation on Soil Freezing and Thawing Processes

Seasonal soil freezing and thawing is not only influenced by climate, topography, soil texture and hydrology but also ground vegetation. Significant differences were observed in soil freezing and thawing processes and hydrothermal characteristics with regard to initial freezing time, freezing depth, ST and soil moisture content, and soil moisture migration due to the influence of vegetation types.

The freezing depth of BL soil was 30% greater those of SL and AL, while BL had the lowest ST. The degree of soil freezing in BL was significantly higher than those of AL and SL, which suggested that vegetation exerted a positive effect on soil resistance to freezing and thawing in winter. The ST of AL was greater than that of BL, and the freezing and thawing days were 22 days less than that of SL; the freezing time was delayed by 20 days when compared to BL and the maximum number of freeze-thaw cycles was 27-fold less than that of BL. In addition, the CV value of ST in AL was lower than that of SL during the entire monitoring period. Therefore, the degree of soil freezing in AL was significantly lower than that of SL, which suggested that AL exhibited superior freezing resistance capacity to SL, and the observation is consistent with the findings of Dulamsuren and Hauck. (2010). During seasonal freezing and thawing processes, AL soil maintains a higher temperature under similar conditions. The observation could be explained by the low shrub canopy, which considerably intercepts radiation from the Sun on the ground, in turn, decreasing ST. In addition, arbor forests can promote the growth of bryophytes, reduce wind speeds, and accumulate thick humus layers (Giraldo et al., 2009), which can enhance the maintenance of high STs in AL during winter. Numerous studies have revealed that the influence of vegetation on the thermal state of frozen soils is manifested in several ways. First, through shading in which the vegetation canopy reflects and absorbs most of the downward solar radiation, in turn, reducing its impact on the soil surface (Shur and Jorgenson, 2007; Chasmer et al., 2011). Second, the canopy structure and its physiological functions alter the meteorological conditions of the vegetation, which, in turn, influences heat and moisture exchange between the atmosphere and the soil. Finally, the vegetation canopy can also influence ST by intercepting snow and reducing wind speeds (Chang et al., 2014). Therefore, freezing and thawing processes can vary due to different vegetation types when other factors remain constant. Similarly, SWC was also a factor that should be taken into consideration. Studies have revealed that SWC has a significant impact on freezing and thawing processes (Cheng et al., 2018). The SWC in AL was significantly higher than that in SL and BL. The higher the SWC, the greater the specific heat capacity of the soil. When temperature increases or decreases, the amount of heat that is required to be absorbed and released is greater than that of soil with low water content (Wang et al., 2012), which also explains why the CV value of ST in AL during the entire monitoring period was relatively low.

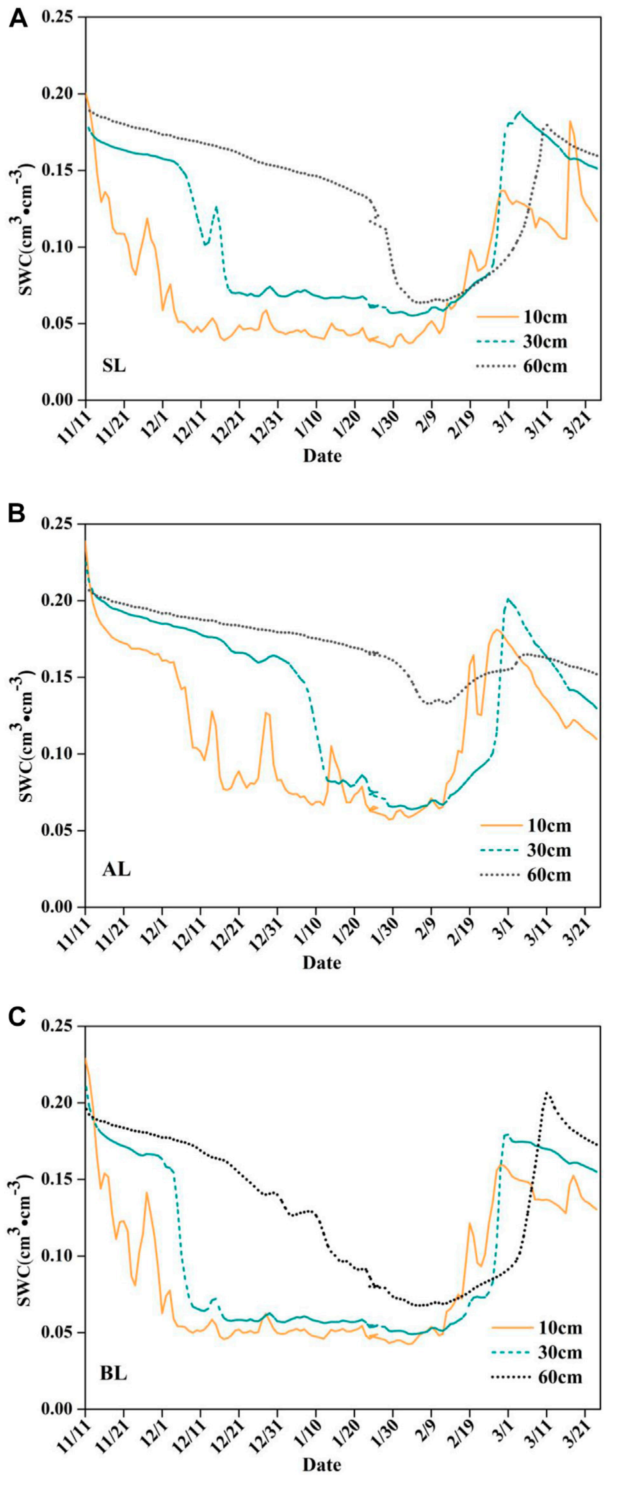

FIGURE 4 | SWC dynamics of different land types **(A,B,C)**.

Although the degree of soil freezing in BL was greater than that in SL, the numbers of freeze-thaw cycles in SL and BL soils were 51 and 32 cycles, respectively. The number of freeze-thaw cycles observed in SL was significantly greater than that in BL, which could be attributed to the variations in snow cover thickness. Several researchers have investigated the influence of snow cover on ST variations and established that snow as an insulator exerts a certain thermal insulation effect on the surface soils (Fu et al., 2018; Wang et al., 2020). The increase in snow cover thickness can reduce the freezing degree of the top soil (Hu et al., 2013). The shrub canopy partially intercepted snow; therefore, the thick bottom layer of snow on the SL surface was less than that on BL surface. The minimum frozen ST in the 0–10 cm soil layer of SL was lower than that in the 0–10 cm soil layer of BL (**Table 1**). The results indirectly demonstrate that increasing the depth of snow cover can reduce the freezing degree of surface soil.

Influence of Freezing and Thawing Processes on Water Movement

Variations in soil water potential caused by soil freezing drive soil moisture from unfrozen areas to the freezing front (Li et al., 2012). ST is a key driving factor in the movement of soil water, causing water to move upwards from deep soil layers (Chen et al., 2013). We conducted regression analyses to determine the relationship between ST and soil moisture in SL, AL, and BL, and established that the relationship between ST and soil moisture was linear. R^2 values at various soil depths varied in different soil types, and the values were influenced by the degree of soil freezing at corresponding depths. The degree of soil freezing at each depth in BL was the highest, with the highest R^2 value, followed by SL. The degree of soil freezing in each soil layer in AL was the lowest and the R^2 value was the lowest. Conversely, poor frost resistance or lack of vegetation cover results in an increase in the CV value of ST, which, in turn, increases the driving force of soil water transport and explains why the variations in ST and soil moisture in AL during the entire freezing period were the lowest.

We defined the equation parameter "a" in the linear relationship equation of ST and SWC ($Y = aX + b$) as the transfer efficiency between moisture and temperature. The value of the equation parameter "a" within the same soil layer in AL was the lowest, while "a" value within the same soil layer in BL was the highest (**Table 3**), which could be attributed to the variations in thermal conductivity of water at different phases. As a solid, thermal conductivity of ice is greater than that of liquid water. Therefore, the more the water freezes in frozen soil, the greater the thermal conductivity "a". The finding confirmed that the degree of soil freezing in AL was the lowest during the entire monitoring period, and the amount of soil water transport was the least. The difference between the final and the initial soil moisture contents can be used to estimate the amount of soil water transport. **Figure 5** illustrates the SWC variations in different soil layers in the two vegetation types and BL at various stages of the monitoring period. The amount of soil water transport in the 0–10 cm, 10–30 cm, and 30–60 cm soil layers in AL increased by 2.4%, decreased by 12.5%, and increased by 152%, respectively. The amount of soil water transport in the 0–10 cm, 10–30 cm, and 30–60 cm soil layers in BL decreased by 37%, decreased by 19%, and increased by 146%, respectively, while in SL, the amount of soil water transport increased by 46.3,

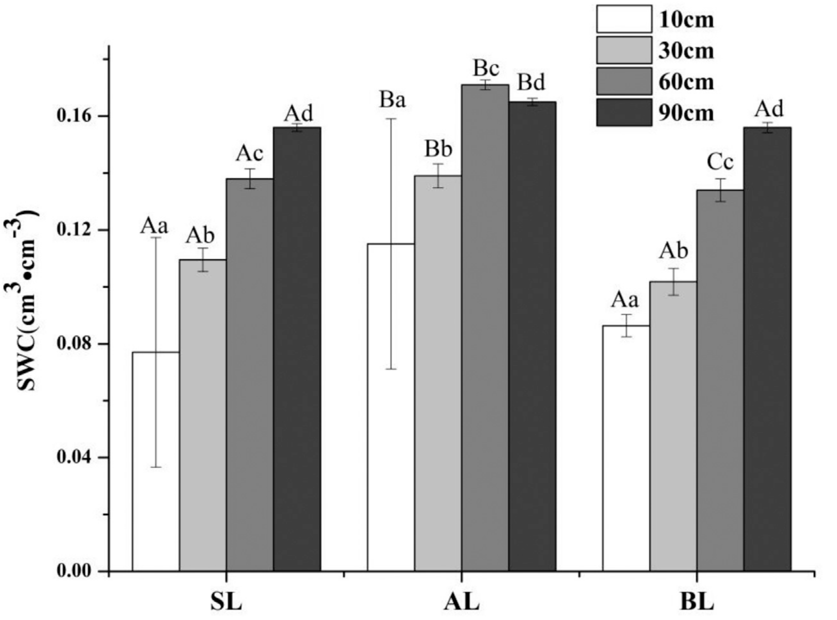

FIGURE 5 | Average soil water content of different vegetation types and depths during the monitoring period.

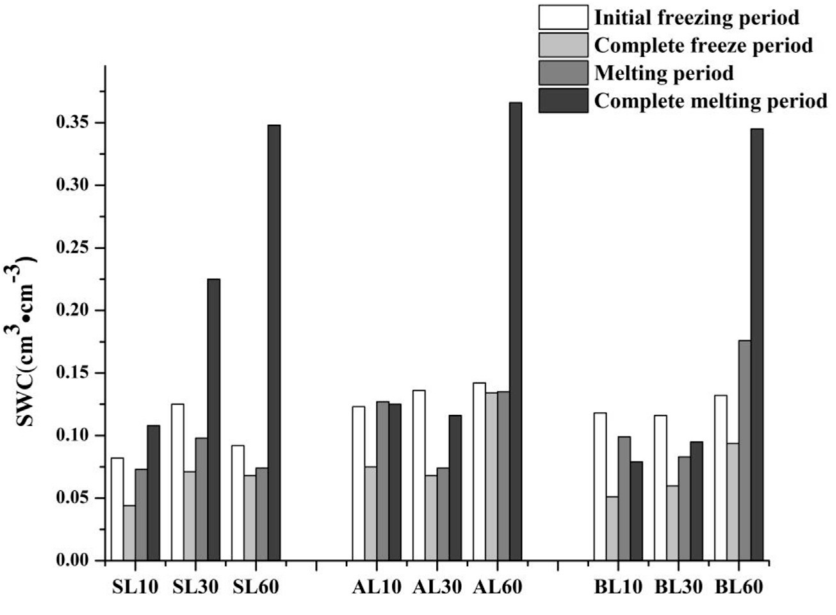

FIGURE 6 | SWC changes in different freezing stage.

78.4, and 205%, respectively. Generally, the maximum SWCs in AL and BL were observed at a depth of 60 cm, while SWC in SL increased in the 0–10 cm, 10–30 cm, and 30–60 cm soil layers. The observations could be explained by the following factors. First, the moisture in the soil profile to migrate to the 50–70 cm, since the soil layer of AL and BL thawed at a relatively later date. Second, the capacity of SL to resist freezing was relatively poor and the degree of freezing was more severe than that of AL. The CV value of SL ST was relatively higher, which makes SL to exhibit a greater driving force. Although the degree of soil freezing in BL was more severe, SL had a high number of root channels within the 30–60 cm soil layer when compared with BL, which had no vegetation. Studies have revealed that root systems can form water transport channels between various soil layers, and the rate of water movement through such channels is much faster than the flow velocity of liquid or gaseous phases of soil water (Wang et al., 2020). Therefore, SL exhibits optimum conditions for soil moisture migration.

TABLE 3 | Linear regression of soil moisture and temperature.

Depth (cm)/Land type	Shrub land (SL)		Arbor land (AL)		Bare land (BL)	
	Linear regression equation of SWC and ST	R^2	Linear regression equation of SWC and ST	R^2	Linear regression equation of SWC and ST	R^2
10	Y = 0.0069X + 0.0797	0.65	Y = 0.0072X + 0.108	0.40	Y = 0.0075X + 0.094	0.66
30	Y = 0.0125X + 0.1011	0.68	Y = 0.0104X + 0.113	0.44	Y = 0.0132X + 0.0999	0.70
60	Y = 0.0115X + 0.1121	0.60	Y = 0.0047X + 0.157	0.45	Y = 0.0135X + 0.01164	0.69

CONCLUSION

During freezing and thawing, BL soil froze to a depth of 90 cm, which was 30% greater than those of AL and SL. The maximum number of freeze-thaw cycles was observed at a depth of 10 cm in AL, SL, and BL, and the order of the number of freeze-thaw cycles was as follows: SL 51 cycles > BL 32 cycles > AL 24 cycles. The number of freeze-thaw days observed in AL was 84, which was 26% less than those of SL and BL. Average ST was greater in AL than in SL and BL. Overall, AL exhibited superior “insulation” and “buffering” effects. SWC in AL and BL was mainly concentrated near the 60 cm depth, and increased by 152 and 146%, respectively. SWC in SL increased by 46.3, 78.4, and 205% at depths of 0–10 cm, 10–30 cm, and 30–60 cm, respectively. Therefore, SL exhibited superior water transport characteristics. The results of the present study could provide a scientific basis for vegetation restoration in arid and semi-arid areas of the Loess Plateau.

DATA AVAILABILITY STATEMENT

The raw data supporting the conclusions of this article will be made available by the authors, without undue reservation.

AUTHOR CONTRIBUTIONS

LB and LX conceived the main idea of this manuscript. ZL, GX, BM, and PL designed and performed the experiment. LB wrote the manuscript and all authors contributed to improving the manuscript.

FUNDING

This research was supported by the Science and Technology Program of Yulin (Grant No. 2019-144), the Technology Project Funded by Clean Energy and Ecological Water Conservancy Engineering Research Center (QNZX-2019-03),The Science and Technology Project of Department of Transport of Shaanxi Province (Grant No. 2015-11K).

ACKNOWLEDGMENTS

We thank the reviewers for their useful comments and suggestions.

REFERENCES

Chang, J., Wang, G.-x., Gao, Y.-h., and Wang, Y.-b. (2014). The Influence of Seasonal Snow on Soil thermal and Water Dynamics under Different Vegetation Covers in a Permafrost Region. *J. Mt. Sci.* 11 (3), 727–745. doi:10.1007/s11629-013-2893-0

Chasmer, L., Quinton, W., Hopkinson, C., Petrone, R., and Whittington, P. (2011). Vegetation Canopy and Radiation Controls on Permafrost Plateau Evolution within the Discontinuous Permafrost Zone, Northwest Territories, Canada. *Permafrost Periglac. Process.* 22 (3), 780. doi:10.1002/ppp.724

Chen, D., Szostak, P., Wei, Z., and Xiao, R. (2016). Reduction of Orthophosphates Loss in Agricultural Soil by Nano Calcium Sulfate. *Sci. Total Environ.* 539, 381–387. doi:10.1016/j.scitotenv.2015.09.028

Chen, S., Ouyang, W., Hao, F., and Zhao, X. (2013). Combined Impacts of Freeze-Thaw Processes on Paddy Land and Dry Land in Northeast China. *Sci. Total Environ.* 456-457, 24–33. doi:10.1016/j.scitotenv.2013.03.059

Cheng, L.-p., and Liu, W.-z. (2014). Long Term Effects of Farming System on Soil Water Content and Dry Soil Layer in Deep Loess Profile of Loess Tableland in China. *J. Integr. Agric.* 13 (006), 1382–1392. doi:10.1016/S2095-3119(13)60292-0

Cheng, Y., Li, P., Xu, G., Li, Z., Wang, T., Cheng, S., et al. (2018). The Effect of Soil Water Content and Erodibility on Losses of Available Nitrogen and Phosphorus in Simulated Freeze-Thaw Conditions. *Catena* 166, 21–33. doi:10.1016/j.catena.2018.03.015

Dulamsuren, C., and Hauck, M. (2008). Spatial and Seasonal Variation of Climate on Steppe Slopes of the Northern Mongolian Mountain Taiga. *Grassland ence* 54 (4), 217–230. doi:10.1111/j.1744-697X.2008.00128.x

Frost, G. V., Loehman, R. A., Saperstein, L. B., Macander, M. J., Nelson, P. R., Paradis, D. P., et al. (2020). Multi-decadal Patterns of Vegetation Succession after Tundra Fire on the Yukon-Kuskokwim Delta, Alaska. *Environ. Res. Lett.* 15 (2), 025003. doi:10.1088/1748-9326/ab5f49

Fu, Q., Hou, R., Li, T., Jiang, R., Yan, P., Ma, Z., et al. (2018). Effects of Soil Water and Heat Relationship under Various Snow Cover during Freezing-Thawing Periods in Songnen Plain, China. *Sci. Rep.* 8 (1), 1325. doi:10.1038/s41598-018-19467-y

Giraldo, M. A., Madden, M., and Bosch, D. (2009). Land Use/land Cover and Soil Type Covariation in a Heterogeneous Landscape for Soil Moisture Studies Using point Data. *GIScience & Remote Sensing* 46 (1), 77–100. doi:10.2747/1548-1603.46.1.77

Guo, C. X., Zhang, W. J., Jiang, L. K., Wu, Y. P., Jiang, Y. L., and Zhou, Y. (2020). Thermal Stability Evaluation Method Based on Pile’s Bearing Capacity in a Permafrost Region. *IOP Conf. Ser. Earth Environ. Sci.* 570 (2), 022001. doi:10.1088/1755-1315/570/2/022001

Guo, D., Yang, M., and Wang, H. (2011). Sensible and Latent Heat Flux Response to Diurnal Variation in Soil Surface Temperature and Moisture under Different Freeze/thaw Soil Conditions in the Seasonal Frozen Soil Region of the central Tibetan Plateau. *Environ. Earth Sci.* 63 (1), 97–107. doi:10.1007/s12665-010-0672-6

Guo, W., Liu, H., Anenkhonov, O. A., Shangguan, H., Sandanov, D. V., Korolyuk, A. Y., et al. (2018). Vegetation Can Strongly Regulate Permafrost Degradation at its Southern Edge through Changing Surface Freeze-Thaw Processes. *Agric. For. Meteorology* 252, 10–17. doi:10.1016/j.agrformet.2018.01.010

Hu, G., Liu, H., Anenkhonov, O. A., Korolyuk, A. Y., Sandanov, D. V., and Guo, D. (2013). Forest Buffers Soil Temperature and Postpones Soil Thaw as Indicated by a Three-Year Large-Scale Soil Temperature Monitoring in the forest-steppe Ecotone in Inner Asia. *Glob. Planet. Change* 104, 1–6. doi:10.1016/j.gloplacha.2013.02.002

Huang, Y., Chen, L., Fu, B., Huang, Z., Gong, J., and Lu, X. (2012). Effect of Land Use and Topography on Spatial Variability of Soil Moisture in a Gully Catchment of the Loess Plateau, China. *Ecohydrol.* 5, 826–833. doi:10.1002/eco.273

Kruk, J., Steelman, C., and Endres, A. L. (2012). Dispersion Inversion of GPR Data Recorded across Freezing and Thawing Induced Waveguides. *Oceania* 82 (1), 125–126. doi:10.1016/j.jappmathmech.2010.03.004

Lai, J., Wang, X., Qiu, J., Zhang, G., Chen, J., Xie, Y., et al. (2018). A State-Of-The-Art Review of Sustainable Energy Based Freeze Proof Technology for Cold-Region Tunnels in China. *Renew. Sust. Energ. Rev.* 82 (3), 3554–3569. doi:10.1016/j.rser.2017.10.104

Li, R., Shi, H., Flerchinger, G. N., Zou, C., and Li, Z. (2013). Modeling the Effect of Antecedent Soil Water Storage on Water and Heat Status in Seasonally Freezing and Thawing Agricultural Soils. *Geoderma* 206, 70–74. doi:10.1016/j.geoderma.2013.04.021

Li, X., Jin, R., Pan, X., Zhang, T., and Guo, J. (2012). Changes in the Near-Surface Soil Freeze-Thaw Cycle on the Qinghai-Tibetan Plateau. *Int. J. Appl. Earth Observation Geoinformation* 17 (1), 33–42. doi:10.1016/j.jag.2011.12.002

Liu, T., Xu, X., and Yang, J. (2017). Experimental Study on the Effect of Freezing-Thawing Cycles on Wind Erosion of Black Soil in Northeast China. *Cold Regions Sci. Tech.* 136, 1–8. doi:10.1016/j.coldregions.2017.01.002

Liu, Y., Fu, B., Lü, Y., Wang, Z., and Gao, G. (2012). Hydrological Responses and Soil Erosion Potential of Abandoned Cropland in the Loess Plateau, China. *Geomorphology* 138 (1), 404–414. doi:10.1016/j.geomorph.2011.10.009

Lu, J., Wang, T. H., Cheng, W. C., Yang, T., and Luo, Y. (2019). Permeability Anisotropy of Loess under the Influence of Dry Density and Freeze-Thaw Cycles. *Int. J. Geomechanics* 19 (9), 04019103. doi:10.1061/(ASCE)GM.1943-5622.0001485

Mohammed, G. A., Hayashi, M., Farrow, C. R., and Takano, Y. (2013). Improved Characterization of Frozen Soil Processes in the Versatile Soil Moisture Budget Model. *Can. J. Soil Sci.* 93 (4), 511–531. doi:10.4141/CJSS2012-005

Nagare, R. M., Schincariol, R. A., Quinton, W. L., and Hayashi, M. (2011). Effects of Freezing on Soil Temperature, Freezing Front Propagation and Moisture Redistribution in Peat: Laboratory Investigations. *Hydrol. Earth Syst. Sci.* 16 (8), 501–515. doi:10.5194/hess-16-501-2012

Pan, Y.-X., Wang, X.-P., Zhang, Y.-F., and Hu, R. (2015). Spatio-temporal Variability of Root Zone Soil Moisture in Artificially Revegetated and Natural Ecosystems at an Arid Desert Area, NW China. *Ecol. Eng.* 79, 100–112. doi:10.1016/j.ecoleng.2015.04.019

Shur, Y. L., and Jorgenson, M. T. (2007). Patterns of Permafrost Formation and Degradation in Relation to Climate and Ecosystems. *Permafrost Periglac. Process.* 18 (1), 7–19. doi:10.1002/ppp.582

Sun, F., Lü, Y., Wang, J., Hu, J., and Fu, B. (2015). Soil Moisture Dynamics of Typical Ecosystems in Response to Precipitation: a Monitoring-Based Analysis of Hydrological Service in the Qilian Mountains. *Catena* 129, 63–75. doi:10.1016/j.catena.2015.03.001

Sun, S. M., Dai, C. L., Liao, H. C., and Xiao, D. F. (2011). A Conceptual Model of Soil Moisture Movement in Seasonal Frozen Unsaturated Zone. *Amm* 90-93, 2612–2618. doi:10.4028/www.scientific.net/10.4028/www.scientific.net/amm.90-93.2612

Wang, G. X., Liu, G. S., Li, C. J., and Yang, Y. (2012). The Variability of Soil thermal and Hydrological Dynamics with Vegetation Cover in a Permafrost Region. *Agric. For. Meteorology* 162-163, 44–57. doi:10.1016/j.agrformet.2012.04.006

Wang, J., Zhao, W., Zhang, X., Liu, Y., Wang, S., and Liu, Y. (2019a). Effects of Reforestation on Plant Species Diversity on the Loess Plateau of China: a Case Study in Danangou Catchment. *Sci. Total Environ.* 651, 979–989. doi:10.1016/j.scitotenv.2018.09.266

Wang, Q., Yang, Q., Guo, H., Xiao, X., Jin, H., Li, L., et al. (2018a). Hydrothermal Variations in Soils Resulting from the Freezing and Thawing Processes in the Active Layer of an alpine Grassland in the Qilian Mountains, Northeastern Tibetan Plateau. *Theor. Appl. Climatol* 136, 929–941. doi:10.1007/s00704-018-2529-y

Wang, R., Dong, Z.-b., and Zhou, Z.-c. (2019c). Changes in the Depths of Seasonal Freezing and Thawing and Their Effects on Vegetation in the Three-River Headwater Region of the Tibetan Plateau. *J. Mt. Sci.* 16 (12), 2810–2827. doi:10.1007/s11629-019-5450-7

Wang, T., Li, P., Li, Z., Hou, J., Xiao, L., Ren, Z., et al. (2019b). The Effects of Freeze-Thaw Process on Soil Water Migration in Dam and Slope farmland on the Loess Plateau, China. *Sci. Total Environ.* 666, 721–730. doi:10.1016/j.scitotenv.2019.02.284

Wang, X., Wang, C., Wang, X., and Huo, Z. (2020). Response of Soil Compaction to the Seasonal Freezing-Thawing Process and the Key Controlling Factors. *Catena* 184, 104247. doi:10.1016/j.catena.2019.104247

Wang, Y., Yang, J., Chen, Y., Wang, A., and De Maeyer, P. (2018b). The Spatiotemporal Response of Soil Moisture to Precipitation and Temperature Changes in an Arid Region, China. *Remote Sensing* 10 (3), 468. doi:10.3390/rs10030468

Wu, D., Zhou, X., and Jiang, X. (2017). Water and Salt Migration with Phase Change in saline Soil during Freezing and Thawing Processes. *Groundwater* 56 (5), 742–752. doi:10.1111/gwat.12605

Xiao, L., Yao, K., Li, P., Liu, Y., and Zhang, Y. (2020). Effects of Freeze-Thaw Cycles and Initial Soil Moisture Content on Soil Aggregate Stability in Natural Grassland and Chinese pine forest on the Loess Plateau of China. *J. Soils Sediments* 20 (3), 1222–1230. doi:10.1007/s11368-019-02526-w

Xiao, L., Zhang, Y., Li, P., Xu, G., Shi, P., and Zhang, Y. (2019). Effects of Freeze-Thaw Cycles on Aggregate-Associated Organic Carbon and Glomalin-Related Soil Protein in Natural-Succession Grassland and Chinese pine forest on the Loess Plateau. *Geoderma* 334, 1–8. doi:10.1016/j.geoderma.2018.07.043

Yang, K., and Wang, C. (2019). Seasonal Persistence of Soil Moisture Anomalies Related to Freeze-Thaw over the Tibetan Plateau and Prediction Signal of Summer Precipitation in Eastern China. *Clim. Dyn.* 53, 2411–2424. doi:10.1007/s00382-019-04867-1

Yang, L., Wei, W., Chen, L., and Mo, B. (2012). Response of Deep Soil Moisture to Land Use and Afforestation in the Semi-arid Loess Plateau, China. *J. Hydrol.* 475, 111–122. doi:10.1016/j.jhydrol.2012.09.041

Yu, Y., Zhao, W., Martinez-Murillo, J. F., and Pereira, P. (2020). Loess Plateau: from Degradation to Restoration. *Sci. Total Environ.* 738 (2020), 140206. doi:10.1016/j.scitotenv.2020.140206

Zhang, L., Ma, W., Yang, C., and Yuan, C. (2014). Investigation of the Pore Water Pressures of Coarse-Grained sandy Soil during Open-System Step-Freezing and Thawing Tests. *Eng. Geology.* 181, 233–248. doi:10.1016/j.enggeo.2014.07.020

Zhang, M., Wang, J., and Lai, Y. (2019a). Hydro-thermal Boundary Conditions at Different Underlying Surfaces in a Permafrost Region of the Qinghai-Tibet Plateau. *Sci. Total Environ.* 670, 1190–1203. doi:10.1016/j.scitotenv.2019.03.090

Zhang, Y., Li, P., Liu, X., Xiao, L., Shi, P., and Zhao, B. (2019b). Effects of farmland Conversion on the Stoichiometry of Carbon, Nitrogen, and Phosphorus in Soil Aggregates on the Loess Plateau of China. *Geoderma* 351, 188–196. doi:10.1016/j.geoderma.2019.05.037

Zhou, J., Fu, B., Gao, G., Lü, N., Lü, Y., and Wang, S. (2015). Temporal Stability of Surface Soil Moisture of Different Vegetation Types in the Loess Plateau of China. *Catena* 128, 1–15. doi:10.1016/j.catena.2015.01.015

Conflict of Interest: The authors declare that the research was conducted in the absence of any commercial or financial relationships that could be construed as a potential conflict of interest.

frontiers in Earth Science

ORIGINAL RESEARCH
published: 14 July 2021
doi: 10.3389/feart.2021.694773

Experimental Study of Runoff and Sediment Yield Affected by Ridge Direction and Width of Sloping Farmland

***Shanshan Liu*[1]*, Tianling Qin*[1]**, Xizhi Lv*[2]**, Xuan Shi*[3]*, Biqiong Dong*[1]*, Jianwei Wang*[1] *and Chun Liu*[4]**

[1]State Key Laboratory of Simulation and Regulation of Water Cycle in River Basin, China Institute of Water Resources and Hydropower Research, Beijing, China, [2]Key Laboratory of the Loess Plateau Soil Erosion and Water Loss Process and Control of Ministry of Water Resources, Yellow River Institute of Hydraulic Research, Zhengzhou, China, [3]College of Engineering, San Jose State University, San Jose, CA, United States, [4]School of Conservancy and Hydroelectric Power, Hebei University of Engineering, Handan, China

Edited by:
Ataollah Kavian,
Sari Agricultural Sciences and Natural Resources University, Iran

Reviewed by:
Jun Niu,
China Agricultural University, China
Mahboobeh Kiani-harchegani,
Yazd University, Iran
Iman Saleh,
Agricultural Research, Education and Extension Organization (AREEO), Iran

***Correspondence:**
Tianling Qin
tianling406@126.com
Xizhi Lv
nihulvxizhi@163.com

Specialty section:
This article was submitted to Hydrosphere, a section of the journal Frontiers in Earth Science

Received: *13 April 2021*
Accepted: *16 June 2021*
Published: *14 July 2021*

Citation:
Liu S, Qin T, Lv X, Shi X, Dong B, Wang J and Liu C (2021) Experimental Study of Runoff and Sediment Yield Affected by Ridge Direction and Width of Sloping Farmland. Front. Earth Sci. 9:694773. doi: 10.3389/feart.2021.694773

Water and soil losses from sloping farmlands potentially contribute to water eutrophication and land degradation. However, few studies explored the combined effects of ridge direction and ridge width on surface runoff and soil losses of sloping farmlands. Twenty-seven experimental plots (8 m long and 4 m wide) with nine treatments (three ridge direction: cross ridge, longitudinal ridge, and oblique ridge; and three ridge width: 40, 60, and 80 cm) were adopted under natural rainfall conditions for two years in the Luanhe River Basin of China. Results indicated that ridge direction had significant effects on runoff and sediment yield ($p < 0.05$). The ridge width had no significant effect on runoff and sediment yield. No significant interaction effect was found between ridge direction and width on runoff and sediment yield of the sloping farmland based on statistical analyses. Compared with cross-ridge (CR) tillage and oblique-ridge (OR) tillage, longitudinal-ridge (LR) tillage significantly decreased runoff by 78.9% and 64.9% and soil losses by 88.2 and 83.5%, respectively ($p < 0.05$). The effects of ridge directions on runoff and sediment yield were related to rainfall grade. When the rainfall grade reached rainstorm, the runoff yield under CR, LR, and SR had significant differences ($p < 0.05$). The runoff under LR and OR treatment was 5.16 and 3.3 times, respectively, of that under CR. When the rainfall level was heavy rain or rainstorm, the sediment yield under LR was significantly greater than that under CR. The sediment yield was 13.45 times of that under CR. Cross-ridge tillage with a ridge width of 40 cm is an optimally effective measure of soil and water conservation on sloping farmland in arid and semiarid regions of China.

Keywords: runoff, sediment, sloping farmland, ridge direction, ridge width

INTRODUCTION

As a valuable land resource, sloping farmland occupies an important position in hilly agricultural areas. Nonetheless, soil erosion on sloping farmland caused by unreasonable farming methods is frequently reported as a threat to water quality and land degradation (Pimentel, 2006; Zuazo and Pleguezuelo, 2008; Zhao et al., 2015; Fang et al., 2017; Yu et al., 2020). Ridge tillage can affect roughness of soil surface: change flow velocity, water infiltration time, the infiltration process, and the runoff process. Thereby, the surface runoff and sediment yield are influenced by ridge tillage. The key parameters of ridge tillage are ridge direction and ridge geometry indices (ridge height and ride width). The influence of ridge direction on surface runoff and sediment yield has been studied a lot. However, the combined influence of ridge direction and ridge width on surface runoff and sediment yield has not been deeply studied.

Ground surface characteristics are a key factor influencing the magnitude of runoff and soil erosion on sloping farmland (Wei et al., 2014; Zhou et al., 2016). Ridge tillage is an agricultural practice which is widely used globally due to low cost and input. Ridge direction and ridge geometry indices (ridge height and ridge width) are important parameters which influence the reduction effect of water and sediment (Wischmeier and Smith, 1978; Renard et al., 1997; USDA-ARS, 2008). The studies of the influence of the ridge direction on runoff and sediment were almost focused on the comparison among cross-ridge tillage, longitudinal-ridge tillage, and conservation tillage. Cross-ridge tillage that plants crops on the contour has many advantages in reducing runoff and sediment yield (Hu et al., 2013). 49 % of runoff and 97% of sediment were lessened by cross-ridge tillage under heavy rainfall compared with the control group based on field experiment in southern China (Dai et al., 2018). Grum et al. (2017) showed that runoff in tied cross-ridge tillage was significantly reduced by 65% compared with normal agricultural practices in northern Ethiopia. Xia et al. (2015) also pointed out that cross-ridge tillage could reduce runoff and sediment yield by 30.1 and 27.6%, respectively, in the Three Gorges area of China. In eastern Scotland, modified sediment fence pinned to a contour fence near the base of a potato field was found to be effective to retain sediment (Vinten et al., 2013). Contour ridge decreased erosion by slowing down runoff flow velocity (Guo et al., 2019). Crop leaves can intercept rainfall, roots can consolidate the cross-ridge, and cross-ridge can retain rainfall by establishing contour lines on sloping cropland (Yang et al., 2013; Liu et al., 2018). In addition, cross-ridge tillage in South Korea, England, and Italy was superior to traditional farming and longitudinal-ridge tillage in reducing runoff and sediment (Chisci and Boschi, 1988; Stevens et al., 2009; Arnhold et al., 2013). At present, few studies investigated the effect of ridge width on runoff and sediment yield in sloping farmland. The indoor control experiments showed that the ridge width had a significant effect on runoff and sediment yield in cross-ridge tillage (Liu et al., 2014a). There is a lack of research on the combined effects of ridge direction and ridge width on runoff and sediment yield in field experiments.

According to the second national land survey, there are approximately 30% of the agricultural croplands with a slope above 6°, which need soil management measures to prevent soil erosion. Previous studies evaluating tillage impact on runoff and sediment yield were mostly focused on south China (Guo et al., 2019). Few studies have paid attention on the semiarid and semi-humid areas of North China. In this study, the Luanhe River Basin was selected as the research area. Three ridge directions and ridge widths were set up for field experiments to analyze the effects of ridge direction and width on runoff and sediment yield. The purposes of this study are as follows: 1) analyzing the influence of ridge direction and ridge width on runoff and sediment yield and 2) analyzing the relationship among precipitation, runoff, and sediment yield under different ridge layouts and rain grades, so as to provide technical support for water and soil conservation of sloping farmland in arid and semiarid areas of China.

MATERIALS AND METHODS

Study Area

The Luanhe River Basin is a first-degree tributary of the Haihe River Basin. The basin is located within 115°34′E–119°50′E and 39°02′N–42°43′N, which also lies in the northeastern part of North China (**Figure 1**). This area typically has a temperate semi-humid and semiarid continental monsoon climate, which is rainy and hot in summer and cold and dry in winter (Wang et al., 2015). The mean annual air temperature is 7.8 °C. The annual average precipitation is 538.5 mm. As the main land use form in the Luanhe River Basin, the area of dry land is 26.27% of the total area of the basin. Sloping farmland with a slope between 3 and 15° accounted for 89% of dry land. Spring maize and potato are important crops in slope farmland of the Luanhe River Basin (Hebei Province. 2018). Water and soil erosion of sloping farmland that happens during June–September is an urgent problem, which causes nonpoint source pollution and soil quality decline.

Experimental Design

Based on spatial processing of DEM data and field investigation, the slope of the sloping farmland in the Luanhe River Basin is between 5° and 15°. The types of ridge tillage are mainly longitudinal-ridge tillage (LR) and cross-ridge tillage (CR). The ridge height is between 8 and 15 cm, and the ridge width is usually 60 cm. Based on the above, our study selected a typical sloping farmland with a slope of 10° to carry out *in situ* observation experiments. Three ridge directions (CR, LR, and oblique-ridge (OR) tillage) and three ridge widths (40, 60, and 80 cm) were analyzed in this study. Three × three treatments were set up with three replications. Twenty-seven field plots separated by aluminum composite plates were set up. We found that the soil depth of sloping farmland in the Luanhe River Basin is about 100 cm (Liu et al., 2021). The aluminum plastic plate was buried vertically 100 cm beneath the ground and 20 cm above the soil surface of each side of the plots to avoid water exchange. The size of each experimental plot was 32 m^2 (8 m × 4 m) according to the local field size. To collect the surface runoff and sediments under rainfall events, a tray was constructed at the bottom of each plot. Two tanks were set up in the trend for each plot. A water level gauge was installed in two 80-L tanks used to measure the volume of runoff for each rainfall event of each plot.

Before ridge pillaging, the plots were prepared to ensure that the slope of each plot is consistent. After that, ridges were arranged from bottom of the plots according to the designed ridge layout. Spring maize (*Zea mays* L) was evenly planted on the

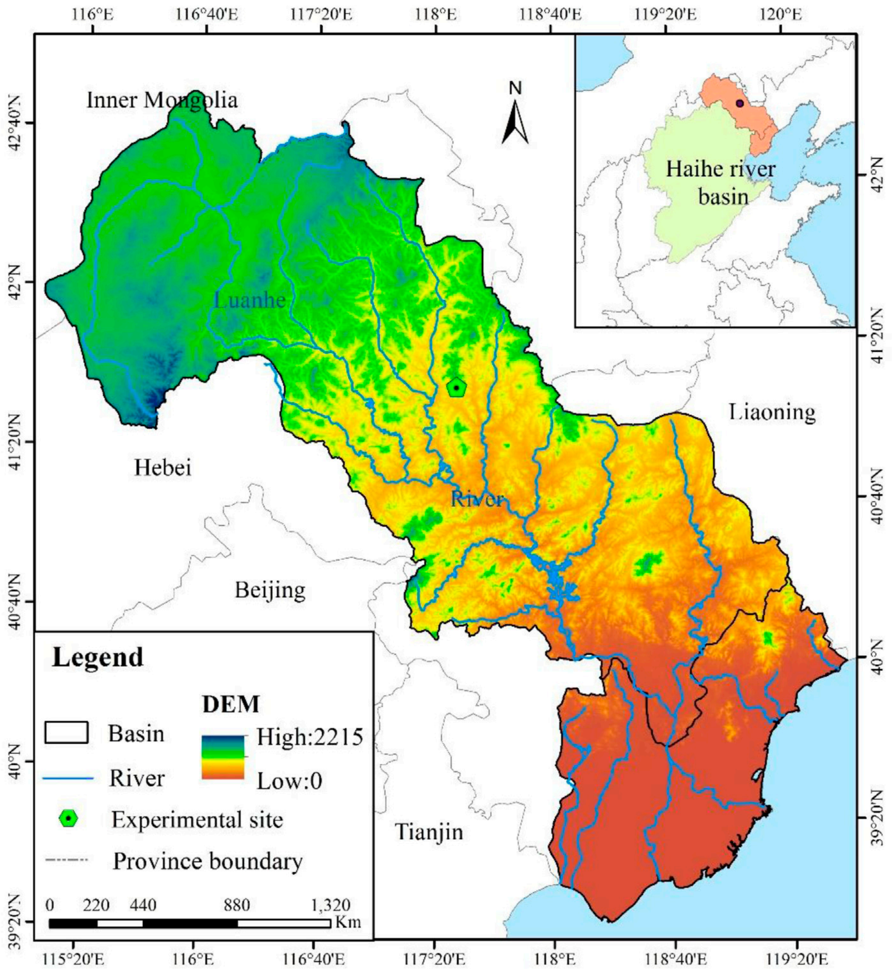

FIGURE 1 | Study area and the location of the experiment site.

ridge at 25 cm intervals. According to the ridge width, the maize planting density was 10 plants/m^2 (40 cm ridge width), 6.7 plants/m^2 (60 cm ridge width), and 5 plants/m^2 (80 cm ridge width). The design details for different experimental plots are presented in **Figure 2**. All the tests were conducted in the growing season of spring maize. The experiment was conducted from April to October in 2019 and 2020.

Rainfall, Runoff, and Sediment Yield Measurement

An SM-1 rain gauge with a diameter of 20 cm was used to observe precipitation, which was installed at the four corners and the center of the experimental site. Precipitation was continuously recorded every hour, and the average value of five gauges was taken as the precipitation of this period until the end of rainfall. The water level of the tank was multiplied by the bottom area to obtain the runoff volume of the rainfall events. The supernatant was removed, and the residual water and sediments were dried in the oven at 105 °C for 48 h to obtain the sediment amount in each experimental plot (Guo et al., 2019).

Runoff depth, runoff sediment concentration, and sediment yield were used to reflect the influence of ridge tillage practice on runoff and sediment yield. The calculation methods of runoff depth, runoff sediment concentration, and sediment yield were as follows. Runoff depth = runoff volume/plot area, with a unit of mm. Runoff sediment concentration = sediment yield/runoff volume with a unit of g/L. Sediment yield = sediment amount/plot area with a unit of kg/hm^2.

Data Analysis

Data were analyzed in IBM SPSS Statistics 18.0 and OriginPro 2019. Analysis of variance (one-way ANOVA) was used to test the significance of difference between treatment means for ridge direction and ridge width by SPSS 18.0 software (SPSS Inc., Chicago, United States) (Li and Wang, 2016). When the F value in the ANOVA analysis was statistically significant, a least significant difference test (p = 0.05) was used for the separation of means. The effects of ridge direction and ridge width on the runoff sediment concentration, yield of runoff, sediment for all experimental treatments, and interactions between these variables were tested by a multivariate analysis. Tukey's test was used to identify the significant differences among

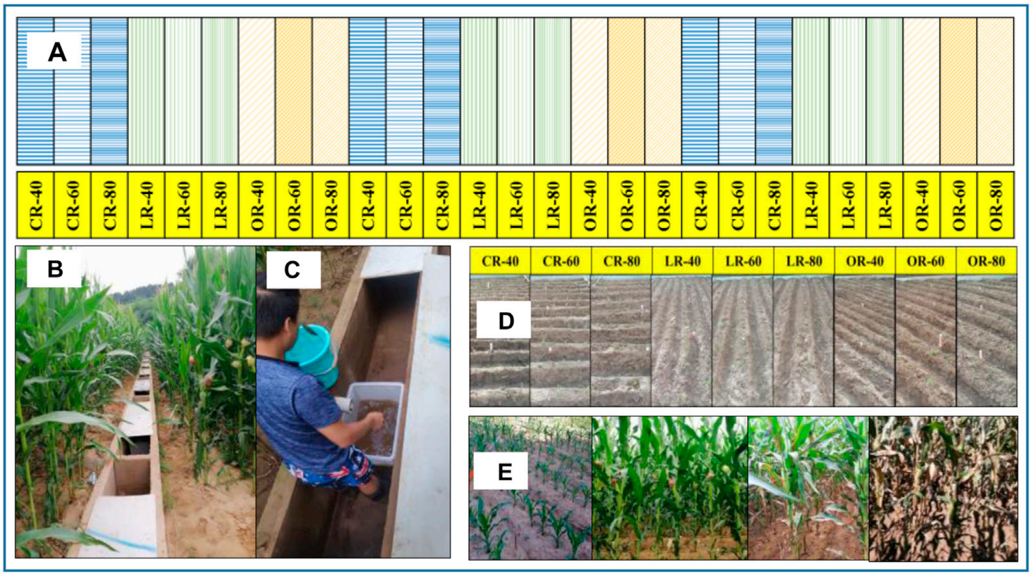

FIGURE 2 | The experimental plots and corresponding devices. **(A)** Experimental plots for measurement of runoff and sediment yield in different ridge tillage systems, **(B)** runoff and sediment collecting tray, **(C)** runoff and sediment collect tank, **(D)** ridge direction and ridge width, and **(E)** growth process of spring maize.

TABLE 1 | Rainfall characteristic for erosive events during the experiment.

Rainfall date (year/month/day)	Rainfall depth (mm)	Duration(h)	Mean intensity (mm/h)	Rainfall pattern
2019/7/6	22.9	24	0.95	Moderate
2019/7/7	18	4	4.50	Large
2019/7/17	22.5	3	7.50	Large
2019/7/29	18.3	11	1.66	Large
2019/7/31	11	3	3.67	Moderate
2019/8/20	17.5	6	2.92	Large
2019/9/1	19	3	6.33	Large
2020/5/30	25	0.67	37.50	Large
2020/6/10	20	0.50	40.00	Heavy
2020/7/5	41	0.43	94.62	Heavy
2020/8/12	87	12.92	6.74	Heavy
2020/8/18	33	1.25	26.40	Heavy
2020/8/24	47	1.50	31.33	Heavy
2020/9/12	16	1.42	11.29	Moderate
2020/9/15	61	9.43	6.47	Heavy
2020/9/28	27	2.00	13.50	Large

the treatments at a significance level of $p < 0.05$. Linear regression analyses were used to evaluate the relationships among rainfall depth, runoff depth, and sediment yield (Dai et al., 2018).

RESULTS

Rainfall Events

Ninety-six rainfalls were observed during 2019 and 2020. The total rainfall amount was 591 mm. There was no surface runoff in the rainfall of less than 10 mm. There were 16 recorded rainfall events that produced surface runoff. In accordance with the classification standard of precipitation (GBT 28592-2012, 2012), six heavy rainfall events, seven large rainfall events, and three moderate rainfall events were recorded (**Table 1**). The rainfall depth under heavy rainfalls was 347.8 mm, which was 59% of the total rainfalls. The rainfall depth of large and moderate rainfall events contributed to 41% of the total rainfalls.

Runoff Depth, Sediment Concentration, and Sediment Yield Under Different Treatments

The runoff depth was significantly affected by ridge direction ($p < 0.05$) (**Figure 3**). The average runoff depth in the CR

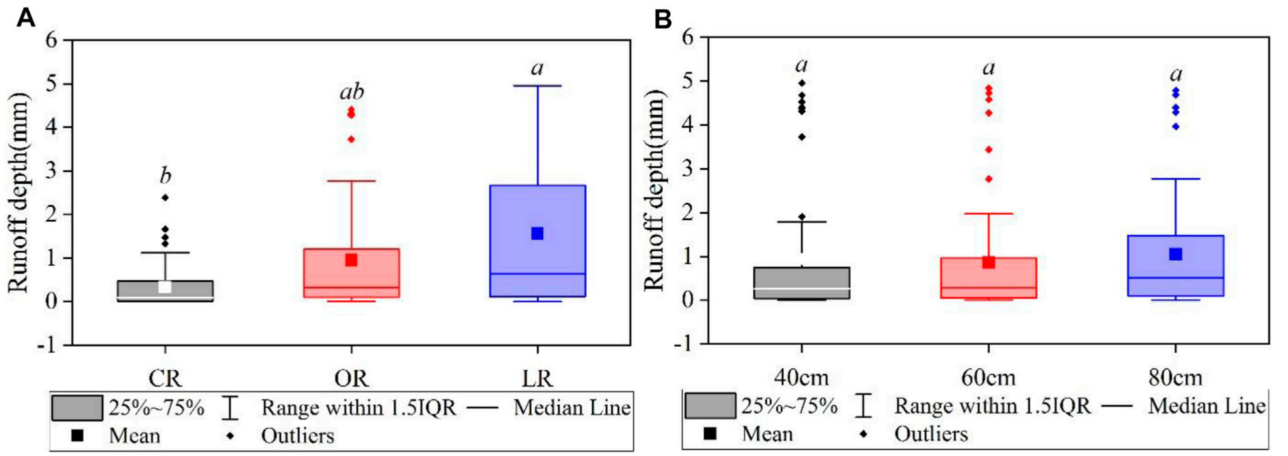

FIGURE 3 | Runoff depth under different ridge directions **(A)** and ridge widths **(B)**, and boxes labeled with different letters indicate significant differences at $p < 0.05$. CR, OR, and LR represent cross-ridge tillage, oblique-ridge tillage, and longitudinal-ridge tillage, respectively. 40, 60, and 80 cm represent 40 cm ridge width, 60 cm ridge width, and 80 cm ridge width, respectively.

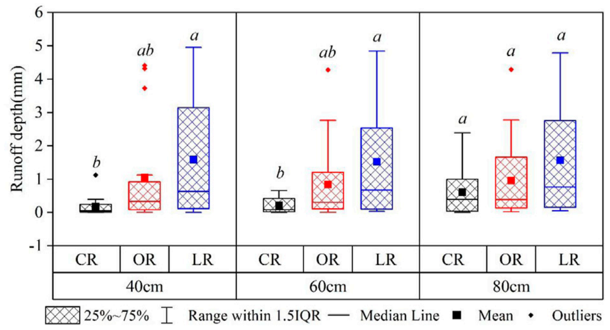

FIGURE 4 | Runoff depth under CR, LR, and OR and three ridge widths, and boxes labeled with different letters within groups indicate significant differences at $p < 0.05$. CR, OR, and LR represent cross-ridge tillage, oblique-ridge tillage, and longitudinal-ridge tillage. 40, 60, and 80 cm represent 40 cm ridge width, 60 cm ridge width, and 80 cm ridge width, respectively.

treatment was lower than that of LR and OR by 78.7 and 65.5%, respectively. The difference of the runoff depth between CR and LR treatment was significant according to the one-way ANOVA test ($p < 0.05$). Ridge width had no significant effect on the runoff depth (**Figure 3**). The average runoff depth in the 60 cm ridge width treatment was lower than that of 40 and 80 cm by 9.1 and 17.5%, respectively. When the ridge width was 40 cm, the runoff depth in the CR treatment was lower than that of LR and OR by 89 and 84%, respectively. When the ridge width was 60 cm, the runoff depth in the CR treatment was lower than that of LR and OR by 86 and 74.8%, respectively. The differences of runoff depth between CR and LR treatment were significant under 40 and 60 cm ridge width, respectively (**Figure 4**). Significant difference was not found among CR, LR, and OR under the 80 cm ridge width. The runoff depth of CR was lower than that of LR and OR by 61.2 and 36.4%, respectively. There was no between-subjects effect of ridge direction and ridge width on the runoff depth.

Ridge direction also had significant effects on sediment concentration in runoff ($p < 0.05$) (**Figure 5**). The average volume-weighted sediment concentration was the lowest under CR treatment, with a value of 8.2 g/L. The average volume-weighted sediment concentration under LR treatment was significantly higher than that of CR, with a value of 15.7 g/L. The average volume-weighted sediment concentration under OR treatment was 12.6 g/L. The average volume-weighted sediment concentration of LR under 60 cm ridge width increased significantly by 3.6 times than that of CR under 60 cm ridge width. The average volume-weighted sediment concentration of OR under 60 cm ridge width was higher than that of CR by 2.7 times under 60 cm ridge width. No significant differences were found in average volume-weighted sediment concentration among CR, LR, and OR under 40 cm or 80 cm ridge width. However, the average volume-weighted sediment concentration in runoff of LR and OR was still 1.05–1.75 times of the CR treatment (**Figure 6**). Ridge width had no significant effects on sediment concentration in runoff (**Figure 4**). 40 cm ridge width had the lowest sediment concentration, with a value of 10.8 g/L.

Ridge direction had significant effects on sediment yield ($p < 0.05$) (**Figure 7**). Compared with CR treatment, sediment yield increased by 11.3 and 5.4 times than that under LR and OR treatment, respectively. The difference of sediment yield was significant between CR and LR treatments ($p < 0.05$). When the ridge width was 60 cm, sediment yield was greatly affected by ridge direction. The sediment yield under LR and OR treatments was higher than that of CR by 35 and 13.8 times, respectively. No significant difference was found in sediment yield among CR, LR, and OR under 40 and 60 cm ridge width (**Figure 8**). The sediment yield of LR and OR was 5.7–12 times that of CR treatment. The sediment yield under 40 cm ridge width was the smallest, followed by 80 cm, and that under 60 cm ridge width was the largest. There was no significant difference in sediment yield under different ridge widths (**Figure 7**).

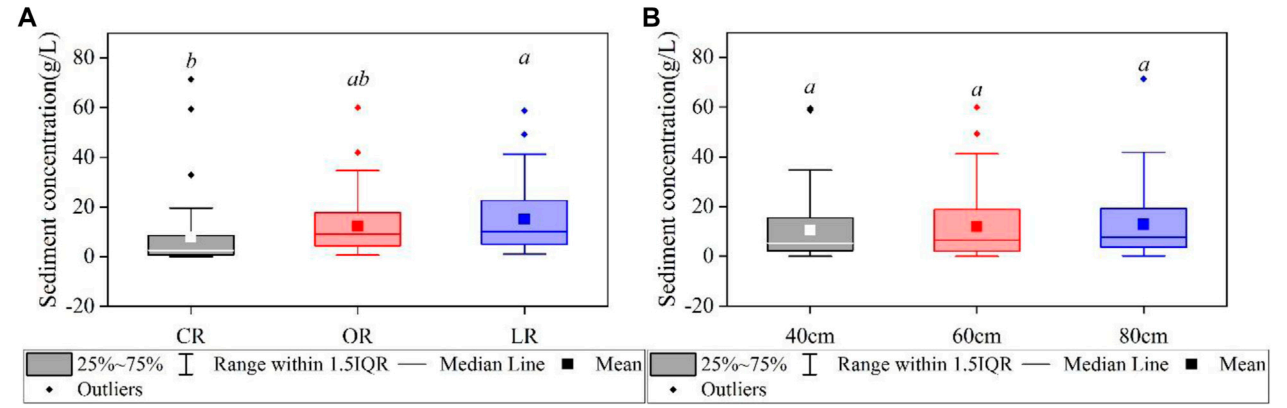

FIGURE 5 | Runoff sediment concentration under different ridge directions **(A)** and ridge widths **(B)**, and boxes labeled with different letters indicate significant differences at $p < 0.05$. CR, OR, and LR represent cross-ridge tillage, oblique-ridge tillage, and longitudinal-ridge tillage, respectively. 40, 60, and 80 cm represent 40 cm ridge width, 60 cm ridge width, and 80 cm ridge width, respectively.

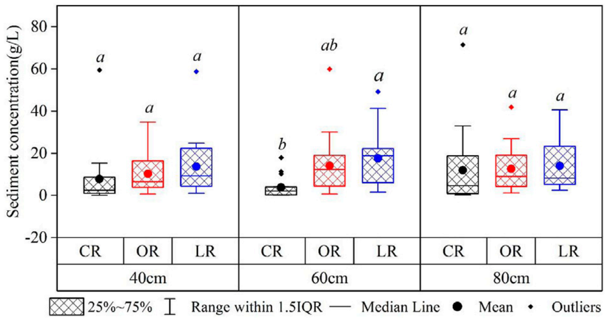

FIGURE 6 | Runoff sediment concentration under CR, LR, and OR and three ridge widths, boxes labeled with different letters within groups indicate significant differences at $p < 0.05$. CR, OR, and LR represent cross-ridge tillage, oblique-ridge tillage, and longitudinal-ridge tillage, respectively. 40, 60, and 80 cm represent 40 cm ridge width, 60 cm ridge width, and 80 cm ridge width, respectively.

Rainfall–Runoff–Sediment Relationship Under Different Ridge Directions

Significant correlation among rainfall, runoff depth, and sediment yield under the three ridge directions was found (**Figure 9**). The correlation coefficient between rainfall and runoff depth under cross-ridge tillage was the smallest and that between rainfall and runoff depth under longitudinal-ridge tillage was the largest. In the same rainfall event, the runoff depth and sediment yield under cross-ridge tillage was the smallest, that under longitudinal-ridge tillage was the largest, and that under oblique-ridge tillage was in the middle.

The Influence of Rainfall Pattern on Runoff Depth and Sediment Yield

Under different rainfall patterns, the influences of ridge direction on the runoff depth and sediment were different (**Figures 10–12**). When the rainfall pattern was moderate and large, the differences of the runoff depth and sediment yield among CR, LR, and OR were not significant. When the rainfall pattern was heavy, the runoff depth had significant differences among CR, LR, and OR. The runoff depth under LR and OR was 5.16 and 3.3 times of that under CR treatment, respectively, (**Figure 10**). The sediment yield of CR was significantly lower than that of LR when the rainfall pattern was heavy. The sediment yield under LR was 13.45 times of that under CR treatment (**Figure 12**).

Heavy rainfalls had the largest contribution to the runoff depth for all plots (**Figure 13**). In the CR tillage plots, the runoff depth under heavy rainfalls accounted for 58.72–70.72% of the total runoff depth during the experiment. In the OR tillage plots, heavy rainfalls contributed to 73.9–82.29% of the total runoff depth. The proportions of heavy rainfalls in the runoff depth were 73.42–74.83% under LR tillage. The sediment yields at OR and LR tillage plots were highest under heavy rainfalls, which accounted for 74.38–83.64% and 62.15–71.87% of the total sediment yield during the two years, respectively. Large rainfalls contributed to 48.46% of the sediment yield of the total sediment yield under CR tillage of 40 ridge width. The proportions of heavy rainfalls (46.64%) and large rainfalls (43.76%) in sediment yield were similar under CR tillage of 60 ridge width. The contributions of moderate rainfalls in the runoff depth and sediment yield were all below 10% for all plots.

DISCUSSION

The Influence of Ridge Direction and Ridge Width on the Runoff Depth and Sediment Yield

Ridge direction affected the runoff depth significantly in sloping farmland. Compared with longitudinal-ridge tillage commonly used by the locals, cross-ridge tillage exhibited a runoff depth reduction of 78.9%. Compared with oblique-ridge tillage, cross-ridge tillage decreased the runoff depth by 64.9%. Field experiments showed that the runoff depth of cross-ridge tillage was significantly less than that of longitudinal-ridge tillage at four experiment sites in south hilly regions of China (Guo et al., 2019). The performances of cross-ridge

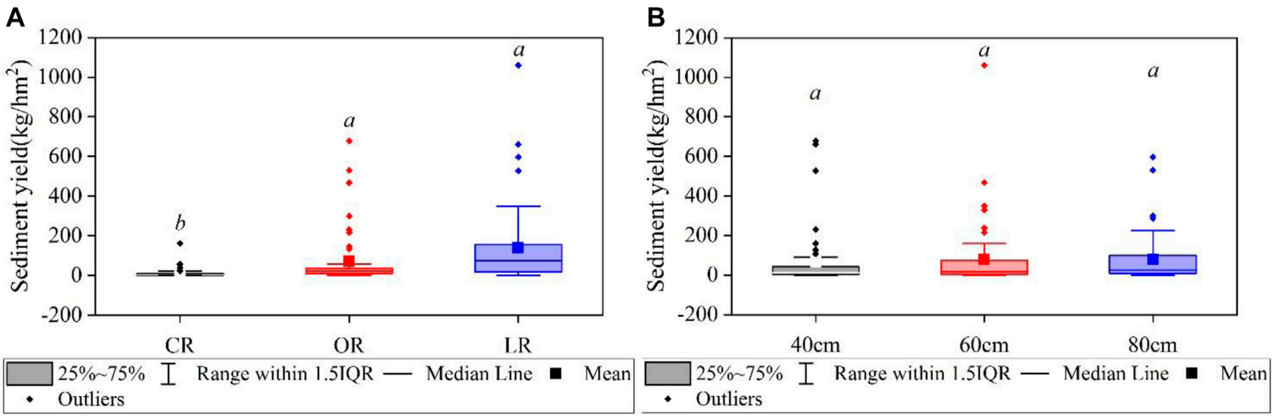

FIGURE 7 | Sediment yield under different ridge directions **(A)** and ridge widths **(B)**, and boxes labeled with different letters indicate significant differences at $p < 0.05$. CR, OR, and LR represent cross-ridge tillage, oblique-ridge tillage, and longitudinal-ridge tillage, respectively. 40, 60, and 80 cm represent 40 cm ridge width, 60 cm ridge width, and 80 cm ridge width, respectively.

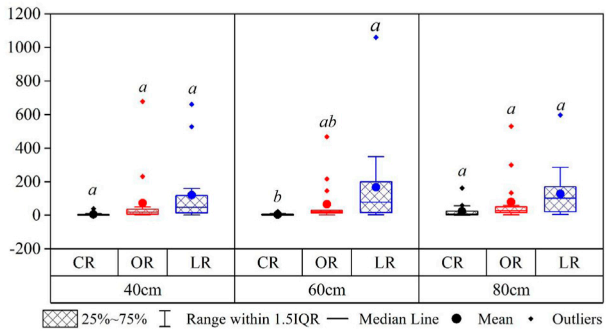

FIGURE 8 | Sediment yield under CR, LR, and OR and three ridge widths, and boxes labeled with different letters within groups indicate significant differences at $p < 0.05$. CR, OR, and LR represent cross-ridge tillage, oblique-ridge tillage, and longitudinal-ridge tillage, respectively. 40, 60, and 80 cm represent 40 cm ridge width, 60 cm ridge width, and 80 cm ridge width, respectively.

tillage in reducing the runoff depth during heavy rainfalls in this study were similar with those of Guo's result. Guo et al. (2019) pointed out that the ridges along contour lines form barriers to reduce the slope runoff depth from sloping farmland. Practices indicated that cross-ridge tillage could reduce the runoff depth and increase infiltration on sloping land compared with longitudinal-ridge tillage in north of China (Liu et al., 2010). By intercepting the runoff and decreasing the flow velocity, the water infiltration was increased, and then the surface runoff was reduced under cross-ridge tillage (Quinton and Catt, 2004; Yang et al., 2013). Crop roots also could consolidate the ridge to retain more water in the sloping farmland with the growth of crops (Liu et al., 2018).

Ridge direction also had a significant effect on sediment concentration and sediment yield ($p < 0.05$). The sediment yield of LR and OR was 12.3 and 6.4 times of that under CR tillage, respectively. Xu et al. (2018) reported that tillage systems with different direction ridges had different erosion processes. Under LR tillage, soil particles were gradually stripped from the top to the base of the ridge, and under the effect of runoff, small trench erosion was formed on the ridge (Liu et al., 2014a; Li et al., 2016; Liu et al., 2016; Shen et al., 2016). Under CR tillage, the "depression storage" in the furrows gradually increased (USDA-ARS, 2008; USDA-ARS, 2013; Liu et al., 2015). When the water volume crossed the ridge, runoff formed at the lowest point of the ridges, and destroyed the ridges and led to soil loss. If the ridge of CR tillage collapsed, a large amount of sediment was produced.

In this study, the observed rainfall and sediment yield data did not show the phenomenon of cross-ridge collapse. Therefore, the sediment yield of CR was much smaller than that of LR and OR. As the ridge of OR tillage was downward in the slope direction, the erosion effect of runoff flow on the ridges was similar to that of LR tillage. The sediment yield of OR tillage was in the range of CR—LR tillage. A heavy rainfall of 95 mm was observed on June 24, 2020. The rainfall flooded the road to the experiment site. No data about runoff and sediment were observed. During the process of clearing the sediment, it was found that the sediment of LR and OR is more than that of CR tillage although there was a certain damage for CR tillage plots. The results were consistent with the finding of Guo et al. (2019), Bu et al. (2008).

Few previous *in situ* experimental studies focused on the effects of ridge width on the runoff depth and sediment yield. As shown in this study, the ridge width has no significant effect on the runoff and sediment yield. Based on laboratory studies, Xu et al. (2018) found that when the rainfall depth was larger than 50 m/h, the microtopography and specification design of ridges are the key factors for cross-ridge tillage to reduce runoff and sediment loss. Under this circumstances, the geometric shape of the ridge plays a key role in rainfall and runoff generation. On June 24, 2020, the experiment site observed rainfall that could not measure the runoff and sediment, causing partial damage to the field ridges. The penetrating erosion ditches in the 40 cm width ridges were found, and no large erosion ditches were found in the 80 cm width ridges under CR tillage. Based on artificially simulated rainfall experiments, Liu et al. (2014b) demonstrated that there was a negative effect of ridge width on runoff and sediment yield under cross-ridge tillage. Different with Liu's finding, 60 cm ridge width had

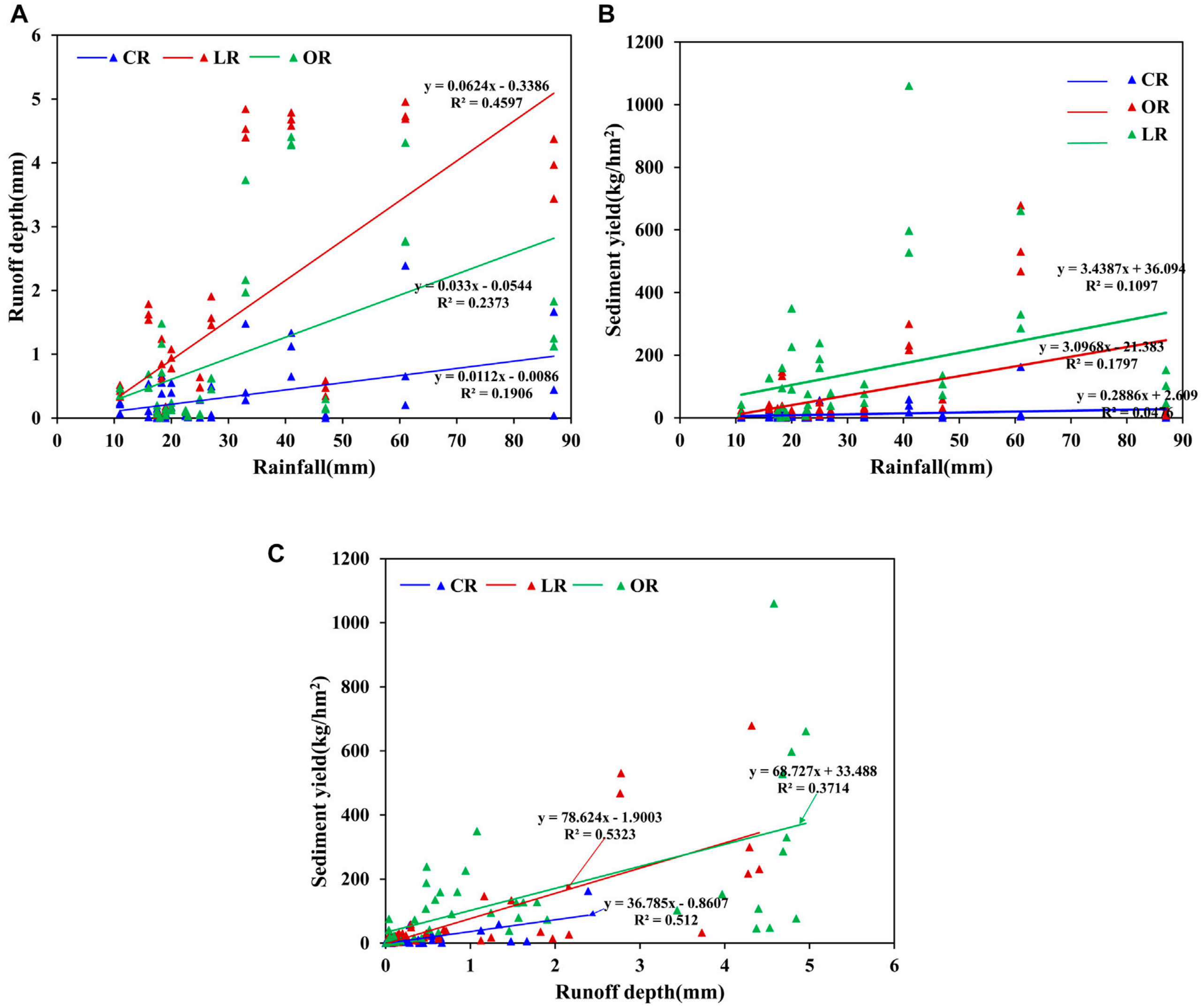

FIGURE 9 | Linear regressions of rainfall, the runoff depth, and sediment yield under CR (cross-ridge tillage), OR (oblique-ridge tillage), and LR (longitudinal-ridge tillage). **(A)** Rainfall and the runoff depth, **(B)** rainfall and sediment yield, and **(C)** the runoff depth and sediment yield.

the least sediment yield under CR tillage in our study. The difference of the results is due to less influence of indoor control experiment and more influence of *in situ* experiment. Considering that the *in situ* experiment is closer to the actual production active, the ridge width can be determined from the perspective of nutrient loss and crop yield (Wang et al., 2018; Liu et al., 2020). In this study, the runoff depth under CR tillage increased with the increase of ridge width. With the increase of the ridge width, the space between ridges, which is beneficial for storing water, decreased (Xu et al., 2018). The amount of stored water between ridges and the erosion prevention of the ridge reach a balance under 60 cm width ridge tillage.

Relationship Among Rainfall, Runoff Depth, and Sediment Yield

Many researchers have studied the relationships among rainfall, runoff depth, and sediment yield (Kothyari et al., 2004; Mathys et al., 2005; Wang et al., 2010; Liu et al., 2012; Dai et al., 2018). The relationships among them were mostly described by linear, exponential, and power functions. The results based on a field experiment by Liu et al. (2012) showed that there was a positive power function correlation between rainfall and the runoff depth. Field experiments conducted by Wang et al. (2010) found that the relationship between the runoff depth and sediment yield could be described by the exponential function. Linear correlation was found between the runoff depth and sediment loss by Kothyari's study (Kothyari et al., 2004). In this study, correlation analysis showed a significant correlated relationship among rainfall, runoff depth, and sediment yield ($p < 0.05$). **Figure 5** showed that rainfall was significantly positively correlated with the runoff depth and sediment yield. The runoff depth was significantly positively linearly correlated with sediment yield. The trend line showed that the runoff depth and sediment yield under the same rainfall increased when the ridge direction changed from CR to OR to LR.

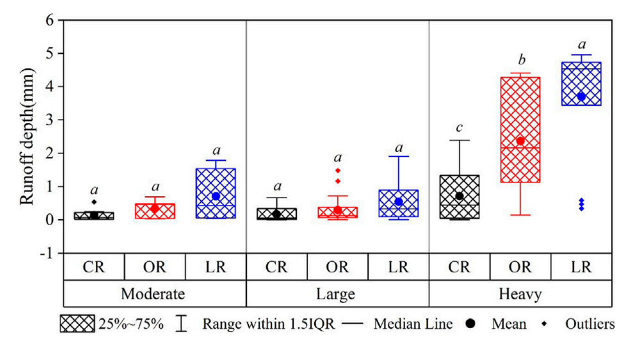

FIGURE 10 | Runoff depth of CR, OR, and LR under different rainfall patterns, and boxes labeled with different letters within groups indicate significant differences at $p < 0.05$. CR, OR, and LR represent cross-ridge tillage, oblique-ridge tillage, and longitudinal-ridge tillage, respectively. Moderate, large, and heavy represent moderate, large, and heavy rainfall patterns, respectively.

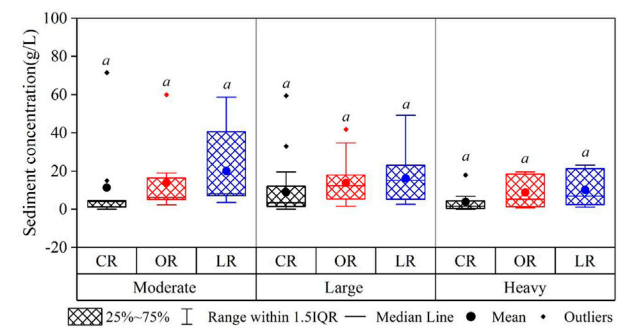

FIGURE 11 | Sediment concentration of CR, OR, and LR under different rainfall patterns, and boxes labeled with different letters within groups indicate significant differences at $p < 0.05$. CR, OR, and LR represent cross-ridge tillage, oblique-ridge tillage, and longitudinal-ridge tillage, respectively. Moderate, large, and heavy represent moderate, large, and heavy rainfall patterns, respectively.

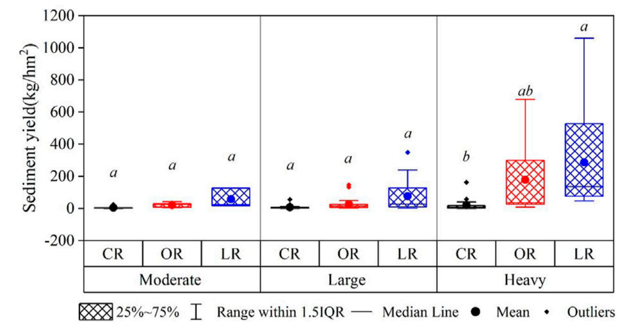

FIGURE 12 | Sediment yield of CR, OR, and LR under different rainfall patterns, and boxes labeled with different letters within groups indicate significant differences at $p < 0.05$. CR, OR, and LR represent cross-ridge tillage, oblique-ridge tillage, and longitudinal-ridge tillage. Moderate, large, and heavy represent moderate, large, and heavy rainfall patterns, respectively.

The Influence of Rainfall Grade on the Runoff Depth and Sediment Yield

Rainfall is a main driving force for the runoff depth and sediment yield in rain-fed agriculture (de Lima and Singh, 2002; Wei et al., 2009; Sasal et al., 2010). Rainfall patterns had significant effects on the runoff depth and sediment yield (Zhang et al., 2016; Yang et al., 2018). The runoff depth and sediment yield of CR tillage were consistently less than those of OR and LR tillage under the same rainfall grade. The performance in reducing runoff and sediment yield of cross-ridge tillage was the best during heavy rainfall. As mentioned in 5.1, cross-ridge tillage formed barriers and decreased surface runoff from the plot. Moreover, Liu et al. (2010) also reported that cross-ridge tillage retain runoff compared with LR tillage. The cross-ridge could also effectively increase soil water infiltration and reduce runoff volume by intercepting the runoff and reducing the flow velocity (Quinton and Catt, 2004; Yang et al., 2013).

Comparing OR and LR tillage, the reduction effect of CR tillage on runoff and sediment yield was not significant under moderate and large rainfall. When the rainfall was heavy, the runoff depth and sediment yield under CR tillage were significantly less than those of OR and LR tillage. Most runoff depth and sediment yield for all plots except for CR at 40 cm ridge width occurred under heavy rainfall. The runoff proportion under heavy rainfalls varied from 58.73 to 82.29% for all plots. Except that large rainfall contributed 48.36% to sediment under CR at 40 ridge width, the contribution of heavy rainfall varied from 46.64 to 83.64% for other plots. The results were consistent with the previous study that heavy rainfall had the most effect on soil erosion (Sharma et al., 1993; van Dijk et al., 2002; Gao et al., 2005; Kinnell, 2005; Ran et al., 2012; Mohamadi and Kavian, 2015). The study of Wei et al. (2010) also pointed out that extreme rainfall causes severe soil erosion, for example, the rainfalls that happened on 15th July and 15th September caused 56% of the total soil loss. For the Luanhe River Basin, July and August are the months with the most frequent heavy rainfalls in the Luan River Basin. The government and farmers should pay more attention to this period when soil erosion is easy to occur.

The results of CR at 40 ridge width were different from those of other plots and previous studies, considering that the sediment yield of CR tillage was significantly lower than that of LR tillage under heavy rainfall. The reason may be that most of the heavy rain occurred during the jointing and heading stages of spring maize. At this time, spring maize roots were abundant, and there were a lot of aerial roots (Thidar et al., 2020), which could fix the soil of the ridge and reduce soil loss from the ridge.

At present, many studies are conducted on the runoff depth and sediment yield on sloping farmland in southern China (Dai et al., 2018; Guo et al., 2019). However, in the arid and semiarid areas of northern China, although the average annual rainfall is smaller than that in south China, the rainfall is concentrated from June to September, which can easily cause soil erosion on the sloping farmland. In this study, cross-ridge tillage was demonstrated to be an effective tillage method in reducing

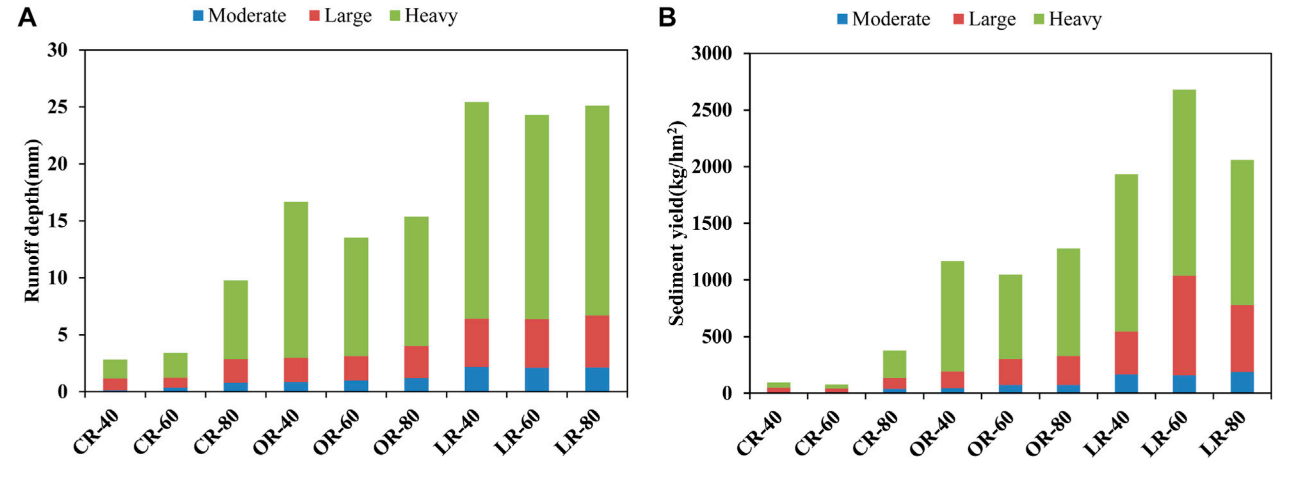

FIGURE 13 | Runoff depth **(A)** and sediment yield **(B)** of different treatments under different rainfall patterns, and CR-40, CR-60, and CR-80 represent cross-ridge tillage with 40, 60, and 80 cm ridge width, respectively. OR-40, OR-60, and OR-80 represent oblique-ridge tillage with 40, 60, and 80 cm ridge widths, respectively. LR-40, LR-60, and LR-80 represent longitudinal-ridge tillage with 40, 60, and 80 cm ridge widths, respectively. Moderate, large, and heavy represent moderate, large, and heavy rainfall patterns, respectively.

surface runoff and soil loss of sloping farmland in the northern regions of China.

CONCLUSION

Based on two-year *in situ* experiments, the effect of ridge direction and ridge width on the runoff depth and sediment yield was analyzed in sloping farmland of the Luan River Basin. The results showed the following:

1) Ridge direction had significant impacts on the runoff depth and sediment yield of sloping farmland ($p < 0.05$). The runoff depth and sediment under cross-ridge tillage (CR) were the least. Ridge width had no significant effect on the runoff depth and sediment yield. The runoff depth and sediment yield of 80 cm ridge width were the largest under CR and OR tillage. The runoff depth of 40 cm ridge width and the sediment yield of 60 cm ridge were the largest under LR tillage. There were no between-subjects effects of ridge direction and ridge width on the runoff depth and sediment yield.
2) When the rainfall pattern was heavy, ridge direction had a significant impact on the runoff depth and sediment yield ($p < 0.05$). The runoff depth of cross-ridge tillage was significantly less than that of longitudinal-ridge tillage and oblique-ridge tillage. When the rainfall pattern was moderate and large, ridge tillage had no significant effect on the runoff depth and sediment yield.

From the perspective of water conservation and soil conservation, cross-ridge tillage with 40 cm ridge width is the best tillage method for slope farming in the Luan River Basin. In order to study the effects of ridge direction and ridge width on the runoff depth and sediment yield at the watershed scale, a watershed-scale refined hydrological model should be built on the basis of this study.

DATA AVAILABILITY STATEMENT

The original contributions presented in the study are included in the article/supplementary material; further inquiries can be directed to the corresponding authors.

AUTHOR CONTRIBUTIONS

SL, TQ, and XL conceived the main idea of this manuscript. BD, JW, and CL designed and carried out the experiment. SL wrote the manuscript, and XS and BD put forward suggestions on language modification of the manuscript.

FUNDING

This research was supported by the National Key Research and Development Project (No. 2017YFA0605004), the National Science Fund for Distinguished Young Scholars (No. 51725905), and the National Key Research and Development Project (No. 2016YFA0601503).

ACKNOWLEDGMENTS

We thank the farmers who helped us during the experiment, and we thank the editors and reviewers for their suggestions and comments.

REFERENCES

Bu, C.-F., Cai, Q.-G., Ng, S.-L., Chau, K.-C., and Ding, S.-W. (2008). Effects of Hedgerows on Sediment Erosion in Three Gorges Dam Area, China. *Int. J. Sediment Res.* 23, 119–129. doi:10.1016/S1001-6279(08)60011-6

Chisci, G., and Boschi, V. (1988). Runoff and Erosion Control with hill Farming in the Sub-coastal Apennines Climate. *Soil Tillage Res.* 12, 105–120. doi:10.1016/0167-1987(88)90035-9

Dai, C., Liu, Y., Wang, T., Li, Z., and Zhou, Y. (2018). Exploring Optimal Measures to Reduce Soil Erosion and Nutrient Losses in Southern China. *Agric. Water Manag.* 210, 41–48. doi:10.1016/j.agwat.2018.07.032

de Lima, J. L. M. P., and Singh, V. P. (2002). The Influence of the Pattern of Moving Rainstorms on Overland Flow. *Adv. Water Resour.* 25, 817–828. doi:10.1016/S0309-1708(02)00067-2

Fang, N. F., Wang, L., and Shi, Z. H. (2017). Runoff and Soil Erosion of Field Plots in a Subtropical Mountainous Region of China. *J. Hydrol.* 552, 387–395. doi:10.1016/j.jhydrol.2017.06.048

Gao, C., Zhu, J., Zhu, J., Hosen, Y., Zhou, J., Wang, D., et al. (2005). Effects of Extreme Rainfall on the export of Nutrients from Agricultural Land. *Acta Geographica Sinica* 60, 991–997. doi:10.11821/xb200506012(In Chinese with English abstract)

GBT 28592-2012 (2012). *Grade of Precipitation*. Beijing: China meteorological administration.

Grum, B., Woldearegay, K., Hessel, R., Baartman, J. E. M., Abdulkadir, M., Yazew, E., et al. (2017). Assessing the Effect of Water Harvesting Techniques on Event-Based Hydrological Responses and Sediment Yield at a Catchment Scale in Northern Ethiopia Using the Limburg Soil Erosion Model (LISEM). *CATENA* 159, 20–34. doi:10.1016/j.catena.2017.07.018

Guo, S., Zhai, L., Liu, J., Liu, H., Chen, A., Wang, H., et al. (2019). Cross-ridge Tillage Decreases Nitrogen and Phosphorus Losses from Sloping Farmlands in Southern Hilly Regions of China. *Soil Tillage Res.* 191, 48–56. doi:10.1016/j.still.2019.03.015

Hebei Province (2018). *Hebei Rural Statistical Yearbook*. Beijing, China: Economic Science Press.

Hu, Z.-F., Gao, M., Xie, D.-T., and Wang, Z.-F. (2013). Phosphorus Loss from Dry Sloping Lands of Three Gorges Reservoir Area, China. *Pedosphere* 23, 385–394. doi:10.1016/S1002-0160(13)60030-2

Kinnell, P. I. A. (2005). Raindrop-impact-induced Erosion Processes and Prediction: a Review. *Hydrol. Process.* 19, 2815–2844. doi:10.1002/hyp.5788

Kothyari, B. P., Verma, P. K., Joshi, B. K., and Kothyari, U. C. (2004). Rainfall-runoff-soil and Nutrient Loss Relationships for Plot Size Areas of Bhetagad Watershed in Central Himalaya, India. *J. Hydrol.* 293, 137–150. doi:10.1016/j.jhydrol.2004.01.011

Li, F. H., and Wang, A. P. (2016). Interaction Effects of Polyacrylamide Application and Slope Gradient on Potassium and Nitrogen Losses under Simulated Rainfall. *Catena* 136, 162–174. doi:10.1016/j.catena.2015.05.008

Li, G., Zheng, F., Lu, J., Xu, X., Hu, W., and Han, Y. (2016). Inflow Rate Impact on Hillslope Erosion Processes and Flow Hydrodynamics. *Soil Sci. Soc. America J.* 80 (3), 711–719. doi:10.2136/sssaj2016.02.0025

Liu, H., Yao, L., Lin, C., Wang, X., Xu, W., and Wang, H. (2018). 18-year Grass Hedge Effect on Soil Water Loss and Soil Productivity on Sloping Cropland. *Soil Tillage Res.* 177, 12–18. doi:10.1016/j.still.2017.11.007

Liu, L., Liu, Q. J., and Yu, X. X. (2016). The Influences of Row Grade, ridge Height and Field Slope on the Seepage Hydraulics of Row Sideslopes in Contour ridge Systems. *Catena* 147, 686–694. doi:10.1016/j.catena.2016.08.025

Liu, Q. J., An, J., Wang, L. Z., Wu, Y. Z., and Zhang, H. Y. (2015). Influence of ridge Height, Row Grade, and Field Slope on Soil Erosion in Contour Ridging Systems under Seepage Conditions. *Soil Tillage Res.* 147, 50–59. doi:10.1016/j.still.2014.11.008

Liu, Q. J., Zhang, H. Y., An, J., and Wu, Y. Z. (2014a). Soil Erosion Processes on Row Sideslopes within Contour Ridging Systems. *Catena* 115, 11–18. doi:10.1016/j.catena.2013.11.013

Liu, Q. J., Shi, Z. H., Yu, X. X., and Zhang, H. Y. (2014b). Influence of Microtopography, ridge Geometry and Rainfall Intensity on Soil Erosion Induced by Contouring Failure. *Soil Tillage Res.* 136, 1–8. doi:10.1016/j.still.2013.09.006

Liu, S., Qin, T., Dong, B., Shi, X., Lv, Z., and Zhang, G. (2021). The Influence of Climate, Soil Properties and Vegetation on Soil Nitrogen in Sloping Farmland. *Sustainability* 13, 1480. doi:10.3390/su13031480

Liu, X. B., Zhang, X. Y., Wang, Y. X., Sui, Y. Y., Zhang, S. L., Herbert, S. J., et al. (2010). Soil Degradation: a Problem Threatening the Sustainable Development of Agriculture in Northeast China. *Plant Soil Environ.* 56 (2), 87–97. doi:10.17221/155/2009-pse

Liu, X., Wang, Y., Yan, X., Hou, H., Liu, P., Cai, T., et al. (2020). Appropriate ridge-furrow Ratio Can Enhance Crop Production and Resource Use Efficiency by Improving Soil Moisture and thermal Condition in a Semi-arid Region. *Agric. Water Manag.* 240, 106289. doi:10.1016/j.agwat.2020.106289

Liu, Y., Tao, Y., Wan, K. Y., Zhang, G. S., Liu, D. B., Xiong, G. Y., et al. (2012). Runoff and Nutrient Losses in Citrus Orchards on Sloping Land Subjected to Different Surface Mulching Practices in the Danjiangkou Reservoir Area of China. *Agric. Water Manag.* 110, 34–40. doi:10.1016/j.agwat.2012.03.011

Mathys, N., Klotz, S., Esteves, M., Descroix, L., and Lapetite, J. M. (2005). Runoff and Erosion in the Black Marls of the French Alps: Observations and Measurements at the Plot Scale. *Catena* 63 (2-3), 261–281. doi:10.1016/j.catena.2005.06.010

Mohamadi, M. A., and Kavian, A. (2015). Effects of Rainfall Patterns on Runoff and Soil Erosion in Field Plots. *Int. Soil Water Conservation Res.* 3, 273–281. doi:10.1016/j.iswcr.2015.10.001

Pimentel, D. (2006). Soil Erosion: a Food and Environmental Threat. *Environ. Dev. Sustain.* 8, 119–137. doi:10.1007/s10668-005-1262-8

Quinton, J. N., Quinton, J. N., and Catt, J. A. (2004). The Effects of Minimal Tillage and Contour Cultivation on Surface Runoff, Soil Loss and Crop Yield in the Long-Term Woburn Erosion Reference Experiment on sandy Soil at Woburn, England. *soil use manage* 20, 343–349. doi:10.1111/j.1475-2743.2004.tb00379.x10.1079/sum2004267

Ran, Q., Su, D., Li, P., and He, Z. (2012). Experimental Study of the Impact of Rainfall Characteristics on Runoff Generation and Soil Erosion. *J. Hydrol.* 424-425, 99–111. doi:10.1016/j.jhydrol.2011.12.035

Renard, K. G., Foster, G. R., Weesies, G. A., McCool, D. K., and Yoder, D. C. (1997). *Predicting Soil Erosion by Water. A Guide to Conservation Planning with the Revised Universal Soil Loss Equation (RUSLE)*. in *Agriculture Handbook 703*. Washington, D.C: USDA. doi:10.1007/springerreference_77104

Sasal, M. C., Castiglioni, M. G., and Wilson, M. G. (2010). Effect of Crop Sequences on Soil Properties and Runoff on Natural-Rainfall Erosion Plots under No Tillage. *Soil Tillage Res.* 108, 24–29. doi:10.1016/j.still.2010.03.010

Sebastian Arnhold, S., Marianne Ruidisch, M., Svenja Bartsch, S., Christopher L. Shope, C. L., and Bernd Huwe, B. (2013). Simulation of Runoff Patterns and Soil Erosion on Mountainous farmland with and without Plastic-Covered ridge-furrow Cultivation in South Korea. *Trans. ASABE* 56 (2), 667–679. doi:10.13031/2013.42671

Sharma, P. P., Gupta, S. C., and Foster, G. R. (1993). Predicting Soil Detachment by Raindrops. *Soil Sci. Soc. America J.* 57, 674–680. doi:10.2136/sssaj1993.03615995005700030007x

Shen, H., Zheng, F., Wen, L., Han, Y., and Hu, W. (2016). Impacts of Rainfall Intensity and Slope Gradient on Rill Erosion Processes at Loessial Hillslope. *Soil Tillage Res.* 155, 429–436. doi:10.1016/j.still.2015.09.011

Stevens, C. J., Quinton, J. N., Bailey, A. P., Deasy, C., Silgram, M., and Jackson, D. R. (2009). The Effects of Minimal Tillage, Contour Cultivation and In-Field Vegetative Barriers on Soil Erosion and Phosphorus Loss. *Soil Tillage Res.* 106, 145–151. doi:10.1016/j.still.2009.04.009

Thidar, M., Gong, D., Mei, X., Gao, L., Li, H., Hao, W., et al. (2020). Mulching Improved Soil Water, Root Distribution and Yield of maize in the Loess Plateau of Northwest China. *Agric. Water Manag.* 241, 106340. doi:10.1016/j.agwat.2020.106340

Usda-ARS (2008). Draft Science Documentation, Revised Universal Soil Loss Equation Version 2 Avaliable at: http./www.ars.usda.gov/sp2UserFiles/Place/64080510/RUSLE/RUSLE2_Science_Doc.pdf.(accessed 09 01, 15).

Usda-ARS (2013). Science documentation, Revised Universal Soil Loss Equation Version 2 Avaliable at: https://www.ars.usda.gov/ARSUserFiles/60600505/RUSLE/RUSLE2_Science_Doc.pdf.

van Dijk, A. I. J. M., Bruijnzeel, L. A., and Rosewell, C. J. (2002). Rainfall Intensity-Kinetic Energy Relationships: a Critical Literature Appraisal. *J. Hydrol.* 261, 1–23. doi:10.1016/S0022-1694(02)00020-3

Vinten, A. J., Loades, K., Addy, S., Richards, S., Stutter, M., Cook, Y., et al. (2014). Reprint of: Assessment of the Use of Sediment Fences for Control of Erosion and Sediment Phosphorus Loss after Potato Harvesting on Sloping Land. *Sci. Total Environ.* 468-469, 1234–1244. doi:10.1016/j.scitotenv.2013.10.050

Wang, K.-y., Li, Q.-f., Yang, Y., Zeng, M., Li, P.-c., and Zhang, J.-x. (2015). Analysis of Spatio-Temporal Evolution of Droughts in Luanhe River Basin Using Different Drought Indices. *Water Sci. Eng.* 8 (4), 282–290. doi:10.1016/j.wse.2015.11.004

Wang, L., Tang, L., Wang, X., and Chen, F. (2010). Effects of Alley Crop Planting on Soil and Nutrient Losses in the Citrus Orchards of the Three Gorges Region. *Soil Tillage Res.* 110 (2), 243–250. doi:10.1016/j.still.2010.08.012

Wang, Q., Li, F., Zhang, D., Liu, Q., Li, G., Liu, X., et al. (2018). Sediment Control and Fodder Yield Increase in Alfalfa (Medicago Sativa L) Production with tied-ridge-furrow Rainwater Harvesting on Sloping Land. *Field Crops Res.* 225, 55–63. doi:10.1016/j.fcr.2018.05.017

Wei, W., Chen, L., Fu, B., Lü, Y., and Gong, J. (2009). Responses of Water Erosion to Rainfall Extremes and Vegetation Types in a Loess Semiarid Hilly Area, NW China. *Hydrol. Process.* 23, 1780–1791. doi:10.1002/hyp.7294

Wei, W., Chen, L., Fu, B., Lü, Y., and Gong, J. (2010). Responses of Water Erosion to Rainfall Extremes and Vegetation Types in a Loess Semiarid Hilly Area, NW China. *Hydrol. Process.* 23, 1780–1791. doi:10.1002/hyp.7294

Wei, W., Chen, L., Zhang, H., Yang, L., Yu, Y., and Chen, J. (2014). Effects of Crop Rotation and Rainfall on Water Erosion on a Gentle Slope in the Hilly Loess Area, China. *Catena* 123, 205–214. doi:10.1016/j.catena.2014.08.002

Wischmeier, W. H., and Smith, D. D. (1978). *Predicting Rainfall Erosion Losses A Guide to Conservation Planning. Agriculture Handbook*, 537. Washington, D.C: USDA. doi:10.1016/s0341-8162(00)00089-8

Xia, L.-Z., Liu, G.-H., Wu, Y.-H., Ma, L., and Li, Y.-D. (2015). Protection Methods to Reduce Nitrogen and Phosphorus Losses from Sloping Citrus Land in the Three Gorges Area of China. *Pedosphere* 25, 478–488. doi:10.1016/S1002-0160(15)30015-1

Xu, X., Zheng, F., Wilson, G. V., He, C., Lu, J., and Bian, F. (2018). Comparison of Runoff and Soil Loss in Different Tillage Systems in the Mollisol Region of Northeast China. *Soil Tillage Res.* 177, 1–11. doi:10.1016/j.still.2017.10.005

Yang, J., Zheng, H., Chen, X., and Shen, L. (2013). Effects of Tillage Practices on Nutrient Loss and Soybean Growth in Red-Soil Slope farmland. *Int. Soil Water Conserv. Res.* 1, 49–55. doi:10.1016/S2095-6339(15)30030-7

Yang, S., Han, R., Xing, L., Liu, H., Wu, H., and Yang, Z. (2018). Effect of Slope farmland Soil and Water and Soil Nitrogen and Phosphorus Loss Based on Different Crop and Straw Applications and ridge Patterns in the basin of the Main Stream of the Songhua River. *Acta Ecologica Sinica* 38, 42–47. doi:10.1016/j.chnaes.2018.01.007

Yu, Y., Zhao, W., Martinez-Murillo, J. F., and Pereira, P. (2020). Loess Plateau: from Degradation to Restoration. *Sci. Total Environ.* 738, 140206. doi:10.1016/j.scitotenv.2020.140206

Zhang, Q., Liu, D., Cheng, S., and Huang, X. (2016). Combined Effects of Runoff and Soil Erodibility on Available Nitrogen Losses from Sloping farmland Affected by Agricultural Practices. *Agric. Water Manag.* 176, 1–8. doi:10.1016/j.agwat.2016.05.018

Zhao, P., Tang, X., Tang, J., and Zhu, B. (2015). The Nitrogen Loss flushing Mechanism in Sloping Farmlands of Shallow Entisol in Southwestern China: a Study of the Water Source Effect. *Arab. J. Geosci.* 8 (12), 10325–10337. doi:10.1007/s12517-015-1983-4

Zhou, P., Zhuang, W. H., Wen, A. B., and Shi, Z. L. (2016). Fractal Features of Soil Particle Redistribution along Sloping Landscapes with Hedge Berms in the Three Gorges Reservoir Region of China. *Soil Use Manage* 32, 594–602. doi:10.1111/sum.12307

Zuazo, V. H. D., and Pleguezuelo, C. R. R. (2009). Soil-Erosion and Runoff Prevention by Plant Covers: A Review. *A. Review. Agron. Sustain. Dev.* 28, 785–811. doi:10.1007/978-90-481-2666-8_48

Conflict of Interest: The authors declare that the research was conducted in the absence of any commercial or financial relationships that could be construed as a potential conflict of interest.

frontiers
in Earth Science

ORIGINAL RESEARCH
published: 28 March 2022
doi: 10.3389/feart.2022.686441

Water Uptake by *Artemisia ordosica* Roots at Different Topographic Positions in an Alpine Desert Dune on the Northeastern Qinghai–Tibet Plateau

Haijiao Wang[1,2], Lihui Tian[1,3]*, Hongwei Zhang[3], Yang Yu[2] and Huawu Wu[4]

[1]State Key Laboratory of Plateau Ecology and Agriculture, Qinghai University, Xining, China, [2]School of Soil and Water Conservation, Beijing Forestry University, Beijing, China, [3]State Key Laboratory of Earth Surface Processes and Resource Ecology, Beijing Normal University, Beijing, China, [4]Key Laboratory of Watershed Geographic Sciences, Nanjing Institute of Geography and Limnology, Chinese Academy of Sciences, Nanjing, China

Different strategies of water uptake by roots in a semi-arid desert are one way that plants adapt to the water-limited environment. In this study, stable isotopes of $\delta^{18}O$ were used to analyze the variability in water sources of the native species *Artemisia ordosica* during the growing season in an alpine semi-arid desert on the Qinghai–Tibet Plateau, China. *A. ordosica* depended primarily on water from upper soil layers in the early growing season, except for those windward, which obtained water from three soil layers and groundwater from 0.19 to 0.28. In the summer, *A. ordosica* switched sources, and those individuals at the top of the dune used 0.85 of water from middle soil layers, whereas those on windward (0.27–0.33) and leeward slopes (0.31–0.37) absorbed water from three soil layers. Shallow soil water was the main water source at all sites at the end of the growing season. The water uptake pattern of *A. ordosica* was consistent with the root distribution in positions with different dune geomorphology. The results suggest that the micro-landforms of sand dunes affect vegetation growth not only through aeolian activities and soil properties but also through plant water use.

Keywords: water uptake, root distribution, native species, different topography of dune, alpine semi-arid desert, stable oxygen isotopes

Edited by:
María Fernandez,
Universidad de León, Spain

Reviewed by:
Hongkai Gao,
East China Normal University, China
Gang Fu,
Institute of Geographic Sciences and Natural Resources Research (CAS), China

****Correspondence:***
Lihui Tian
lhtian@qhu.edu.cn

Specialty section:
This article was submitted to Hydrosphere,
a section of the journal
Frontiers in Earth Science

Received: *26 March 2021*
Accepted: *07 February 2022*
Published: *28 March 2022*

Citation:
Wang H, Tian L, Zhang H, Yu Y and Wu H (2022) Water Uptake by Artemisia ordosica Roots at Different Topographic Positions in an Alpine Desert Dune on the Northeastern Qinghai–Tibet Plateau.
Front. Earth Sci. 10:686441.
doi: 10.3389/feart.2022.686441

INTRODUCTION

The ability of plants to obtain water is a key factor that determines whether plants can adapt to the environment. Water availability varies according to geomorphic position, and therefore, the water utilization strategy of plants is adaptively adjusted, resulting in separate niches of plants based on geomorphology (Li et al., 2004). In arid and semi-arid areas, plants may change their source of water as the season changes, and some plants may use deep soil water or groundwater during drought. Plant roots are highly plastic and adaptable in order to maintain water absorption. To access the necessary soil water volume, plants can modify their root zones by lateral or vertical growth (Fan et al., 2017). In most ecosystems, water availability limits rooting depth rather than other resources (Yu et al., 2016). Plant roots were revealed as key drivers for water flow processes and different components of the water balance (Yu et al., 2016). In addition, root morphology and distribution also determine the areas from which plants absorb water (Xu and Li, 2009; Xu et al., 2011). When water is available in shallow soils, plants mainly rely on shallow roots to obtain near-surface water and rely less on deep soil water (Dai et al., 2014). However, soil moisture availability is very heterogeneous in arid and semi-arid areas. In these areas, plants no longer rely only on shallow soil water but use deep roots to respond to changes in soil moisture (Ehleringer et al., 1991). Topography is a good indicator of vegetation cover, rooting depth, root zone evaporation and transpiration deficits, soil properties, and even geology (Gao et al., 2018). Thus, the sources of water used by plants are clearly affected by topography (Song et al., 2014).

Stable isotopes are a powerful tool to identify water sources and determine water use patterns of woody species in arid and semi-arid regions (Zhang et al., 2017; Wu et al., 2019a), especially in soils with a high portion of sand (Beyer et al., 2020). Plant water sources can be determined by comparing the stable hydrogen and oxygen isotopes of all potential water sources with those extracted from xylem water (Ehleringer and Dawson, 1992; Song et al., 2014). Plants in semi-arid and arid ecosystems not only absorb most of their water from shallow soil layers under wet conditions but also obtain additional water from deep water pools (such as groundwater) under dry conditions (Dawson and Pate, 1996; McCole and Stern, 2007; Song et al., 2016; Wang-Erlandsson et al., 2016; Zhou et al., 2017). Shifts in the water sources used among different soil layers, depending on water availability, are an important strategy by which deciduous plants cope with drought in water-limited ecosystems (Hasselquist et al., 2010). The ability to extract water from different soil layers is closely related to root morphology and architecture (Xu and Li, 2006). Different species within the same habitat also exhibit considerable differentiation in the water sources used in order to minimize competition for water. Such differentiation is likely a potential mechanism that allows species to coexist, explaining the high diversity and high resilience of plant communities to drought in arid and semi-arid regions (Wu et al., 2014; Yang et al., 2015). In the Mu Us Desert, *Artemisia ordosica* (Ao) uses shallow groundwater with roots that reach a depth of 200 cm, but fine roots are mainly distributed in the upper 40 cm (Zhang et al., 2012). Deciduous species in seasonally arid ecosystems use different strategies to respond to drought stress. Species that can shift water sources can maximize their soil water use and avoid interspecific competition with other plants in the community, which may be an important survival mechanism in water-limited ecosystems (Ehleringer and Dawson, 1992).

Oxygen isotopes of water molecules are useful tools to reconstruct hydro-climatic variations, analyze hydrological processes and pathways, and better understand current metabolic pathways in plants (Szymczak et al., 2020). Stem water reflects the isotope value of the source water, because no oxygen isotopic fractionation of source water occurs during water uptake by roots (Dawson and Ehleringer, 1991), except in certain plants in extreme environments. Hence, the isotope value in stem water corresponds to that in the source water. However, the isotope signature of source water itself may change depending on soil properties, precipitation amount, season, and influence of groundwater or evaporative enrichment of soil water (Ehleringer and Dawson, 1992). Therefore, stem water $\delta^{18}O$ can directly reflect source water $\delta^{18}O$ in alpine semi-arid and arid zones (Jia et al., 2012; Wu et al., 2016a; Wu et al., 2016b; Wu et al., 2018).

Desertification is an extreme manifestation of degradation issue in the northern Tibet–Qinghai Plateau (Sun et al., 2019; Zong and Fu, 2021). Qinghai Lake is in the northeast of the Qinghai–Tibet Plateau in a semi-arid ecologically fragile alpine district and a global climate change-sensitive area, which also be threatened by desertification around the lakeside. Previous studies in this area focused primarily on wind protection mechanisms and ecological functions of sand-fixing plants (Tian et al., 2019; Wu et al., 2019c; Tian et al., 2020). The water sources of revegetation species have received less attention (Wu et al., 2016b), especially those of native species under different conditions of water availability in different micro-landforms.

The aim of this study was to evaluate the water use of a native species on an alpine semi-arid dune, and three questions were addressed: 1) what are the seasonal water sources used by a native plant? 2) What are the key controls on differences in water use of plants at different topographical positions on a sand dune? 3) What are the effects of root distribution and environmental conditions on the water use patterns of a native species? The hypotheses were the following: 1) plants at different topographical positions on a dune would use different water use strategies at different times in the growing season, and 2) plants would tend to use deep soil water or groundwater in water-limited conditions. The results of this study will help guide plantings in alpine deserts to ensure ecological adaptation and structural optimization.

MATERIALS AND METHODS

Study Site

The study was conducted in the Ketu Wind Prevention and Sand Fixation Experimental Range (WPSER; 36°40′N, 100°45′E; 3,224 m a.s.l.) in the southeast corner of Haiyan Bay of Qinghai Lake, China (for details, see Tian et al., 2019). The Ketu Sandy Land covers approximately 753 km^2 and is the largest area on the eastern shore of Qinghai Lake. The field is primarily composed of barchans and transversal sand ridges that average 6–10 m in height and stretch from north to south. The WPSER is in an alpine climatic zone with relatively wet summers and cold winters. Daily meteorological data were provided by a weather station approximately 20 km from the study site from 1981 to 2019. The mean annual temperature was 0.93°C, and the annual average precipitation was 438.6 mm, approximately 80% of which occurred between May and September. Precipitation and temperature in the WPSER have increased since 2004, especially in 2010 (Cui and Li, 2015).

Ao is a typical species in fixed sand dunes. It was introduced as an afforestation species in the 1980s, but the current plants are naturally regenerated. Three plots of 10 × 10 m were selected at three different topographical positions on a dune (windward, top, and leeward).

Root Distribution

An individual Ao of similar height and crown width was selected at each site, and the soil was dug away until roots throughout the soil profile were exposed. The aboveground and underground morphology were photographed. Then, the individual growth morphology and root distribution characteristics were plotted in Photoshop software. Simultaneously, the numbers of coarse roots (root diameter $\Phi \geq 5$ mm), medium roots (2 mm $\leq \Phi < 5$ mm), and fine roots ($\Phi < 2$ mm) were counted at 10 cm intervals to the bottom of the soil profile. Then, the root density was calculated for each interval in soil the profile as below “samples collection” section.

Sample Collection

Soil, plant, and rainwater samples were collected once a month from May to September, which was the growing season in 2019. Soil samples were collected beneath marked Aos in fixed plots using a 10-cm-diameter auger at 10 cm intervals from 0 to 20 cm and at 20-cm intervals from 20 to 120 cm. One part of a soil sample was oven-dried to determine soil water content (SWC). Another portion was quickly placed in 20-ml screw-cap glass vials sealed with parafilm. Simultaneously, soil samples were collected in the same soil layers, placed in ziplock bags and returned to the laboratory to analyze soil particle size composition by using a Matersizer 3,000 (Malvern Ltd., WR14 1XZ, United Kingdom). Three replicates of all soil water and isotope samples were collected. Three individuals from the three plots were randomly chosen for plant sampling on each sampling date (12 May, 11 June, 12 July, 12 August, and 15 September). Three- to 5-cm-long branch sections were cut with clippers. The phloem tissue was removed to avoid isotopic fractionation of xylem water and contamination by isotopic enrichment (Dawson, 1996). Then, the sections were immediately placed in airtight vials and sealed with a screw-lid and parafilm to avoid evaporation. Soil and plant xylem isotopic samples were stored in a car refrigerator for transport to the laboratory where they were stored at −18°C until extraction. Water in xylem and soil samples was extracted using a fully automatic vacuum condensation extraction system (LI-2100 Pro, LICA United Technology Limited, Beijing, China). The extraction rate of water from samples was >98%.

The rainwater collector was constructed with a 10-cm-diameter funnel connected to a glass bottle. A plastic ball was placed on the funnel to prevent evaporation (Yang et al., 2015). All precipitation samples were transferred to clean polyethylene bottles (30 ml) and then sealed with parafilm.

The depth of the interdune water table in the study area ranged from 1.5 to 5.0 m. Therefore, a soil auger was used to collect groundwater in the shallow water table at 1.5 m on the sampling dates. Then, immediately, a self-made long spoon was used to collect the groundwater and place it in airtight vials, which were sealed with parafilm to avoid evaporation. Precipitation and groundwater samples were filtered using a 0.22-μm filter and then refrigerated at 4°C until stable isotope analysis.

Data Analyses

The $\delta^{18}O$ and $\delta^{2}H$ in xylem water, soil water, and precipitation (0.5–1.5 ml) were measured by an Isotopic Ratio Infrared Spectroscopy (IRIS) system (Model DLT-100; Los Gatos Research, Mountain View, CA, United States). Previous studies report that hydrogen offsets occur and persist in semi-arid (Dawson and Ehleringer, 1991), saline (Ellsworth and Williams, 2007), and mild oceanic climate (Barbeta et al., 2019) environments. However, the reasons for the hydrogen fractionation remain unclear, and two explanations have been proposed. It proposes that hydrogen fractionation is related to the mode of water absorption by roots (Ellsworth and Williams, 2007), whereas Barbeta et al. (2019) suggested that it is mainly related to the heterogeneity of soil water signals and plant tissues in temperate deciduous trees. Both agree that fractionation in ^{2}H is much stronger than that in ^{18}O and that ^{18}O therefore provides more satisfactory results. Thus, in this study, only oxygen isotopes ($\delta^{18}O$) were used to determine the sources of plant water. The stable isotopic composition was expressed as follows:

$$\delta^{18}O = \left(R_{sample}/R_{s\tan dard} - 1\right) \times 1000‰$$

where R_{sample} and $R_{standard}$ represent the molar abundance ratios ($^{18}O/^{16}O$, $^{2}H/^{1}H$) of the sample and the standard (Vienna Standard Mean Ocean Water for O and H), respectively. The Iso-Source model (http://www.epa.gov/wed/pages/models/stable-Isotopes/isosource/isosource.htm) was used to quantify the proportion of water uptake from each water source based on the mass balance of the isotope that was introduced, as detailed by Phillips and Gregg (2003).

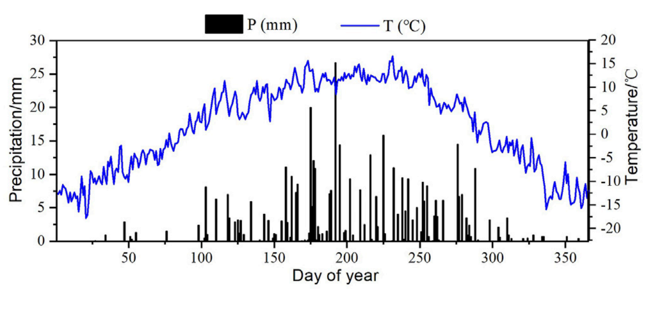

FIGURE 1 | Seasonal variation in precipitation and temperature in 2019.

For Ao growing in sand, the soil profile was subdivided into three potential water sources, the source increment was set at 1%, and the mass balance tolerance was set at 0.1%. The calculated results are reported as the distribution (e.g., maximum and minimum) of feasible solutions and the mean on each sampling date. The isotopic composition of each soil water layer was determined by the SWC-weighted mean approach (Snyder and Williams, 2003; Liu et al., 2015). According toWu et al. (2016b), the shallow soil layer was from 0 to 20 cm, the middle soil layer from 20 to 60 cm, and the deep soil layer from 60 to 150 cm.

One-way ANOVA combined with Tukey’s least significant difference test was applied to detect differences in plant water source from shallow, middle, and deep soil layers in different seasons. The significance level of the statistical analyses was set at 0.05. The statistical analyses were performed using the SPSS 20.0 software (SPSS Inc., Chicago, IL, United States).

TABLE 1 | Soil particle size (%) of different soil layers.

Position	Soil layers/cm	Clay	Silt	Very fine sand	Fine sand	Medium sand	Coarse sand	Very coarse sand
Windward	0–20	0.44 (0.19)	6.32 (1.60)	14.87 (3.56)	37.17 (5.33)	29.63 (2.91)	10.44 (6.35)	1.12 (1.41)
	20–60	0.27 (0.02)	3.96 (0.91)	15.11 (4.98)	44.87 (1.87)	30.29 (6.12)	5.29 (1.36)	0.10 (0.14)
	60–150	0.23 (0.02)	4.04 (0.26)	20.87 (1.37)	52.24 (1.08)	21.14 (1.62)	0.89 (0.55)	0.39 (0.33)
Top	0–20	0.29 (0.24)	5.74 (3.97)	10.43 (1.95)	46.43 (3.01)	34.94 (2.71)	2.10 (0.33)	0.05 (0.08)
	20–60	0.22 (0.00)	3.28 (0.02)	9.16 (1.31)	44.67 (1.36)	38.09 (2.30)	4.58 (0.36)	0.00 (0.00)
	60–150	0.33 (0.12)	3.08 (0.15)	8.56 (1.45)	44.46 (3.29)	39.03 (1.99)	4.00 (3.03)	0.30 (0.26)
Leeward	0–20	0.36 (0.09)	5.32 (0.98)	9.83 (2.49)	43.66 (2.49)	37.64 (4.87)	3.19 (1.17)	0.00 (0.00)
	20–60	0.32 (0.00)	2.99 (0.27)	7.31 (1.58)	44.81 (1.20)	41.67 (2.59)	2.90 (0.45)	0.00 (0.00)
	60–150	0.34 (0.09)	3.46 (0.66)	8.30 (1.44)	44.48 (3.37)	40.26 (4.13)	2.91 (1.93)	0.16 (0.27)

Note: data means average (standard error). The surface sediments of study sites contain all types of particle size, shown as clay (d < 0.005 mm), silt (0.005–0.05 mm), very fine sand (0.05–0.1 mm), fine sand (0.1–0.25 mm), medium sand (0.25–0.5 mm), coarse sand (0.5–1 mm), and very coarse sand (1–2 mm).

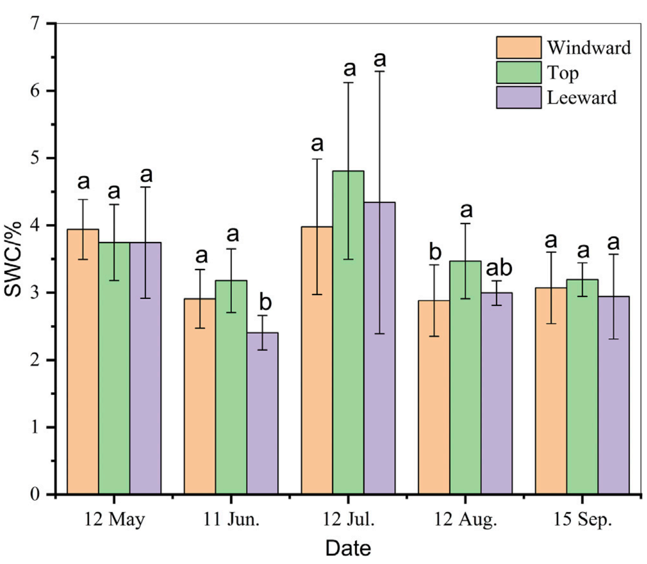

FIGURE 2 | Seasonal variation in soil water content (SWC, %) beneath *Artemisia ordosica* (Ao) in positions with different dune geomorphology. The same letter means that there is no significant difference between different positions of dune ($p > 0.05$), whereas different letters refer to significant differences between micro-landforms in dune ($p < 0.05$).

RESULTS

Environmental Factors

The study area had a semi-arid climate with low annual average temperature and low rainfall that was affected by the unique topography, altitude, and atmospheric circulation. Seasonally, precipitation in summer and autumn was relatively abundant, whereas it was relatively rare in winter and spring (**Figure 1**). In 2019, precipitation was 434.90 mm, with 77% occurring during the growing season from May to September, and the mean temperature was 1.65°C.

The deposits on the natural fixed dune were primarily composed of fine (45.08 ± 4.40%) and medium (34.56 ± 7.30%) sand. Clay and very coarse sand contents in the dune were negligible. In the windward position, fine sand includes very fine sand increased and coarse sand decreased as soil depth increased, whereas in the top and leeward dune positions, no changes occurred with the increase in depth (**Table 1**). Overall, windward deposits were finer than those at top and leeward positions, with significantly more very fine sand ($p = 0.000$). There was more medium sand at the leeward position than at the windward and top of dune positions ($p = 0.000$), whereas the contribution of coarse sand was greater in the shallow soil layer (20 cm depth) in the windward position than in the other two positions ($p = 0.000$).

With changes in the season, the SWC of different geomorphological positions changed significantly (**Figure 2**). The highest average SWC (3.68 ± 0.67%) was at the top of the dune, but it was not significantly different from that on windward (3.36 ± 0.56%) and leeward (3.29 ± 0.76%) slopes during the growing season ($p > 0.05$). The highest SWC at all sites was in July, whereas the lowest was either in June or August, with similar values.

Individual Features at Positions With Different Dune Geomorphology

Plant height, crown width, and coverage at the top of dune were greater than those on windward and leeward slopes (**Figure 3**). The height of Ao at the top of the dune (32.90 ± 12.94 cm) was significantly greater than that leeward ($p = 0.048$) but was not different from that windward ($p = 0.482$). The same trend was observed for N–S length of crown. The largest coverage of Ao was at the top of the dune (38.86 ± 1.03%), followed closely by that of plants windward (38.78 ± 0.68%) without significant difference, whereas the coverage of leeward plants was only 15.52 ± 0.46%. Nevertheless, the highest density was windward, followed by that at the top and leeward.

The root system of windward Ao was distributed to the 220 cm soil depth, whereas that of Ao at the top of the dune was distributed to 20 cm and that of leeward Ao was distributed to 50 cm (**Figure 4**). The roots were concentrated in the upper 20 cm at all sites. Although the tap root of windward Ao extended to 220 cm, most roots were distributed in the top 90 cm. In the top 20 cm, windward Ao had 41.67% fine roots, 35.83% medium roots, and 22.50% coarse roots. Coarse roots decreased in middle soil layers (20–60 cm), whereas the

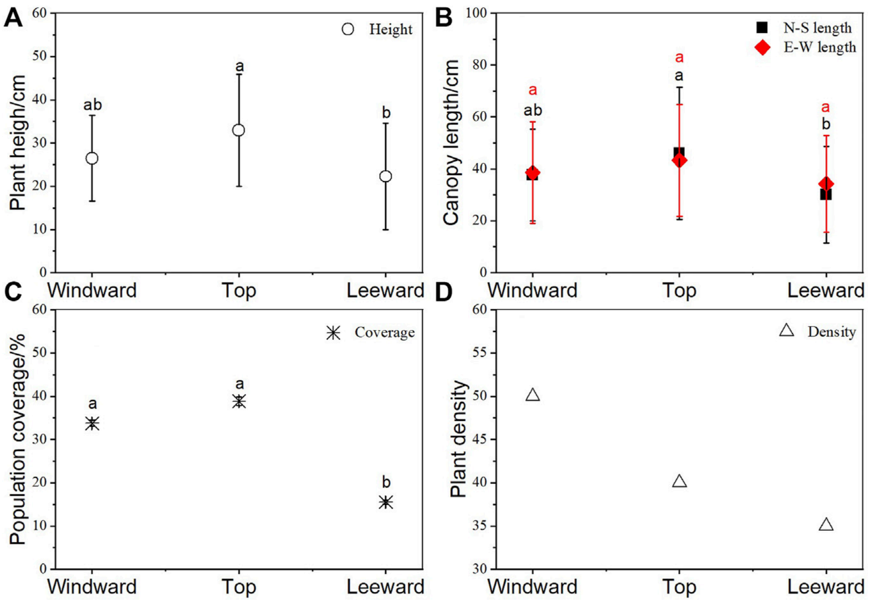

FIGURE 3 | *Artemisia ordosica* (Ao) growth features in positions with different dune geomorphology. **(A)** Height, **(B)** crown width of different orientation, **(C)** coverage, and **(D)** density. The same letter means that there is no significant difference between different positions of dune (p > 0.05), whereas different letters refer to significant differences between micro-landforms in dune (p < 0.05).

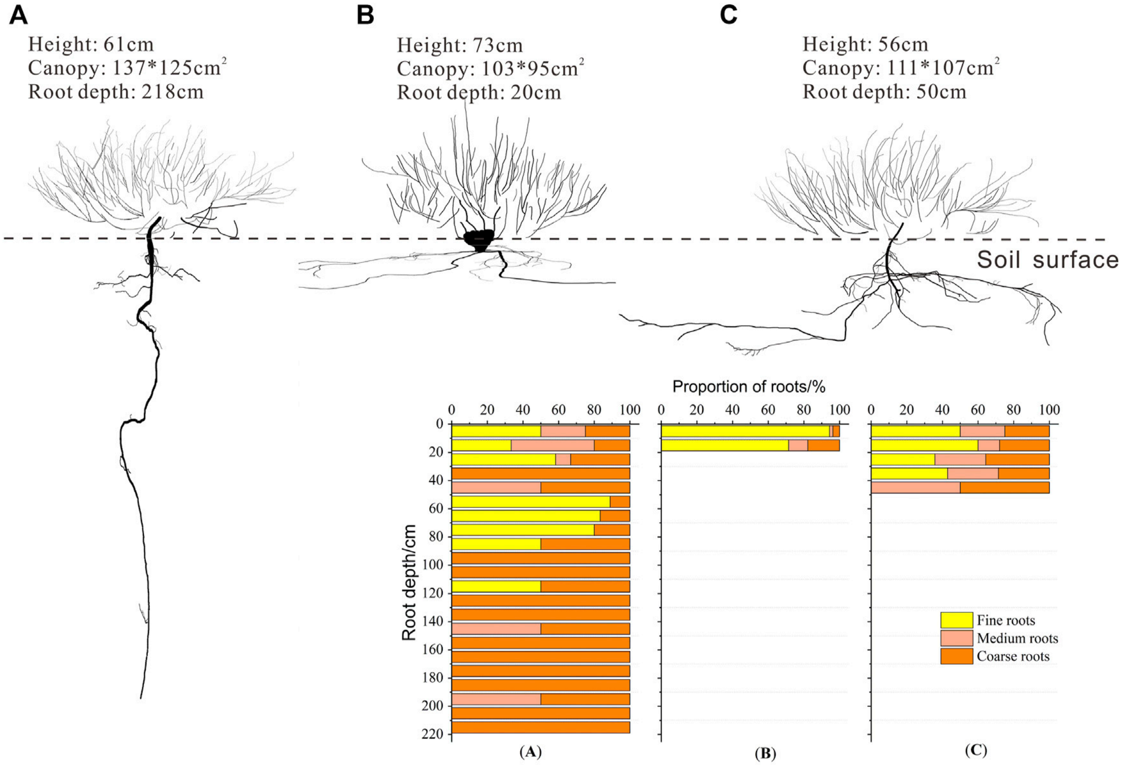

FIGURE 4 | Root distribution of *Artemisia ordosica* (Ao) in positions with different dune geomorphology. **(A)** Windward, **(B)** top of the dune, and **(C)** leeward.

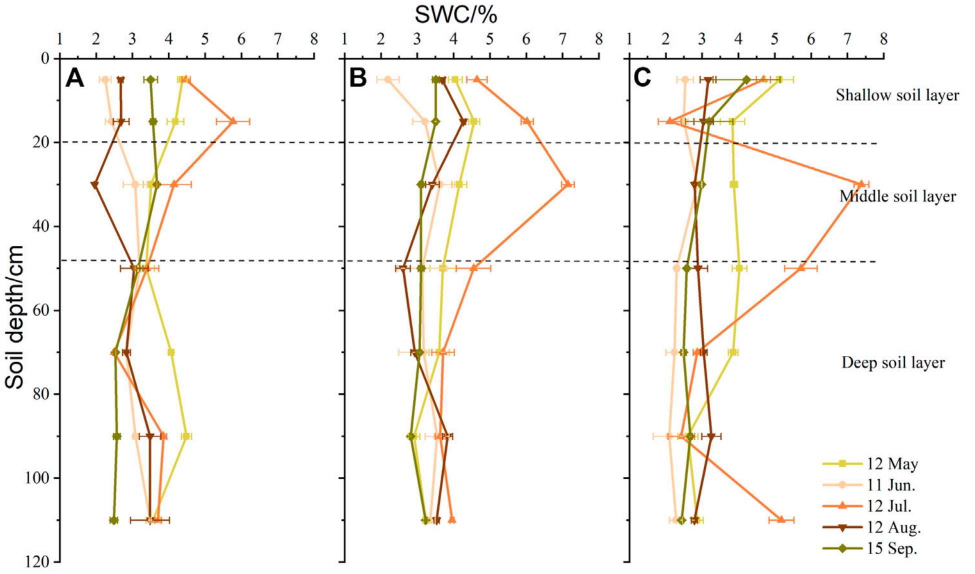

FIGURE 5 | Vertical variation in soil water content (SWC, %) in positions with different dune geomorphology. **(A)** Windward, **(B)** top of the dune, and **(C)** leeward.

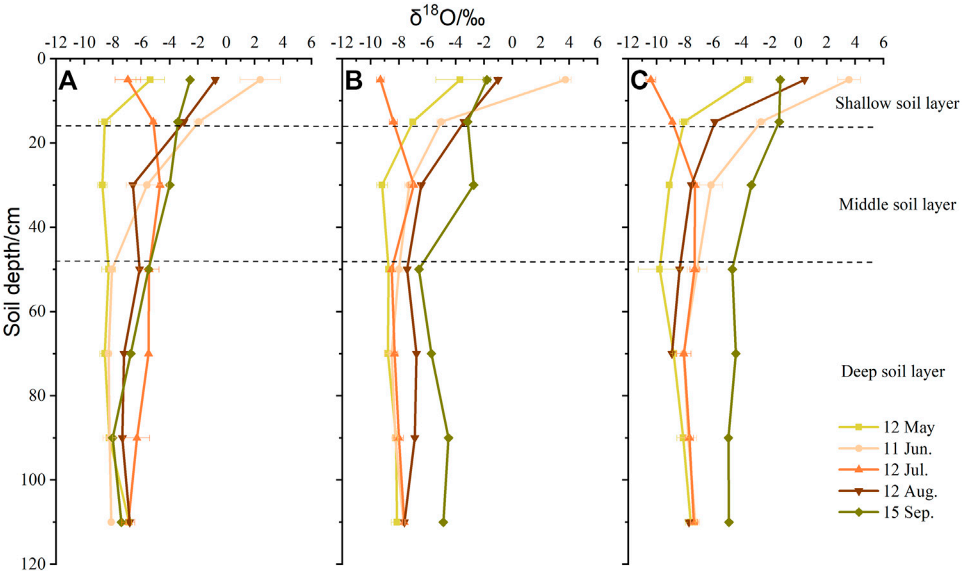

FIGURE 6 | Vertical variation in soil water $\delta^{18}O$ values in positions with different dune geomorphology. **(A)** Windward, **(B)** top of the dune, and **(C)** leeward.

highest density of fine roots was in deep soil layers (60–120 cm). The roots of Ao at the top of the dune were primarily in the shallow soil layer and were composed primarily of fine roots (82.88%). Fine roots of leeward Ao were distributed in the upper 40 cm.

Vertical Variation in Soil Water Content and Isotope Composition

As shown in **Figure 5**, SWC fluctuated as soil depth increased, with the surface 20 cm particularly affected by precipitation and evaporation. The highest SWC windward (3.59 ± 1.14%) and at the top of dune (3.97 ± 0.97%) was in the top 20 cm, whereas the highest SWC leeward (3.74 ± 1.66%) was in the middle soil layer (40–60 cm). The causes for this phenomenon were the large fluctuations in SWC because of the highest rainfall in July, which resulted in different levels of soil moisture at different topographic positions and under different cover conditions. However, there was no change in SWC in deep soil layers during the growing season. Compared with the upper 20 cm, the SWC was lower below 60 cm in all study sites.

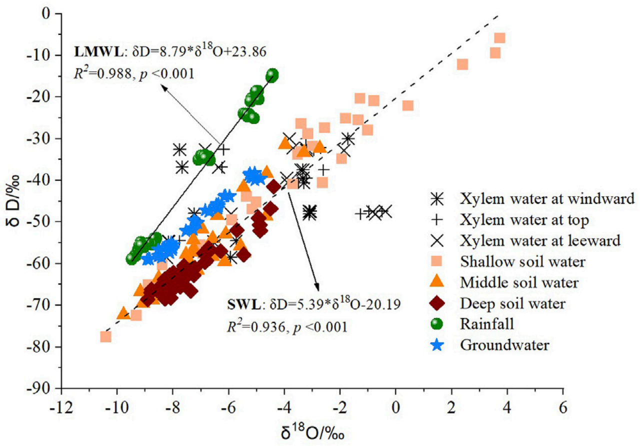

FIGURE 7 | Linear regression of δD and δ^{18}O values in different water pools in the study site.

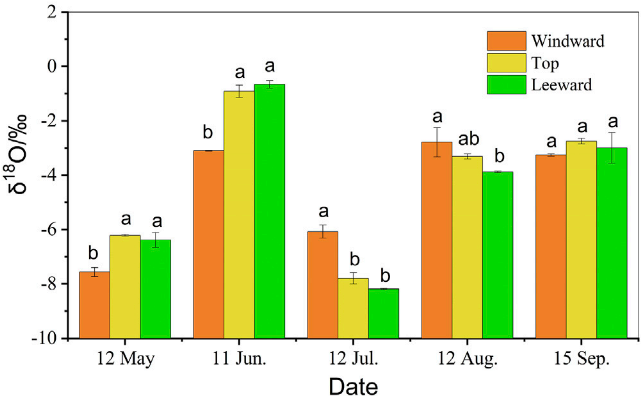

FIGURE 8 | Seasonal variation in δ^{18}O xylem water of *Artemisia ordosica* (Ao) in positions with different dune geomorphology. The same letter means that there is no significant difference between different positions of dune ($p >$ 0.05), whereas different letters refer to significant differences between micro-landforms in dune ($p < 0.05$).

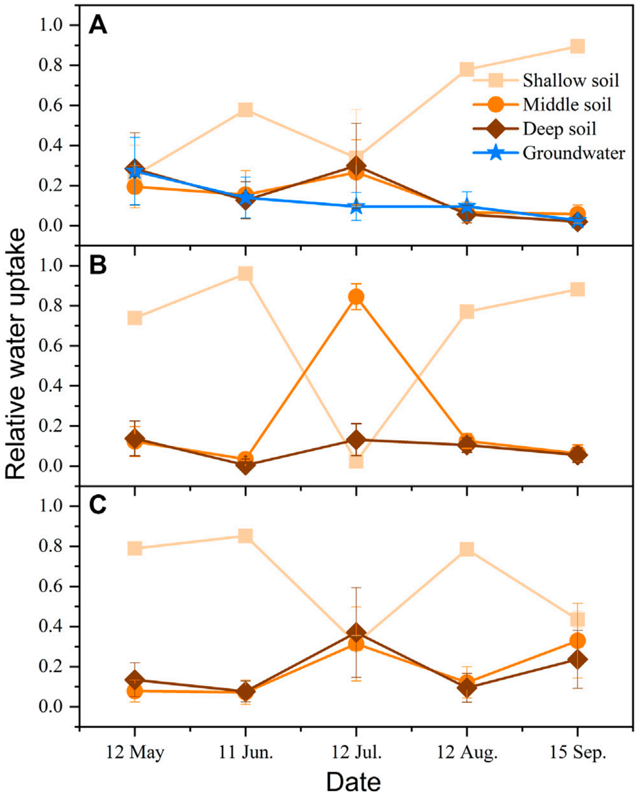

FIGURE 9 | Relative water uptake of *Artemisia ordosica* (Ao) at positions with different dune geomorphology. **(A)** Windward, **(B)** top of the dune, and **(C)** leeward.

Nevertheless, the vertical changes in oxygen isotope values in soil water were different from those of SWC (**Figure 6**). Except for increases in δ^{18}O values with increasing soil depth at all sites in July, the variation in soil water oxygen isotope values was the same in the other seasons and decreased as soil depth increased. There were the strong fluctuations in values that were concentrated in shallow soil layers. Windward, the soil water δ^{18}O value ranged from −8.56 ± 0.42‰ to 2.40 ± 1.42‰ in the upper 20 cm. In the same soil layer, values ranged from −7.01 ± 0.22‰ to 3.74 ± 0.40‰ at the top of dune, whereas the largest range was leeward, from −10.39 ± 0.34‰ to 3.58 ± 0.80‰. In the middle soil layers, soil water oxygen isotope values decreased in all sites.

Seasonal Variation in Isotope Composition of Xylem Water

The global meteoric water line (GMWL, $\delta D = 8\delta^{18}O + 10$) indicates the connection between different water pools in the water cycle (Craig, 1961). From **Figure 7**, both slope and intercept of the local meteoric water line (LMWL, $\delta D = 8.79\delta^{18}O + 23.86$) are greater than that of GMWL. Simultaneously, the soil evaporation line (SWL, $\delta D = 5.39\delta^{18}O - 20.19$) was to the lower right of the LMWL (**Figure 7**). The lower slope indicated that evaporation fractionation effects in the soil surface affected δD and δ^{18}O enrichment in soil water. In addition, the δD and δ^{18}O values in xylem water of individuals were distributed around those of soil water and groundwater, which indicated that the plants primarily take up soil water from different depths and the groundwater.

The δ^{18}O of Ao twig water at positions with different dune geomorphology showed seasonal variation ($p < 0.05$), with the highest value (enriched) in June and the lowest (depleted) in July (**Figure 8**). At the beginning of the growing season (May), the δ^{18}O values of Ao at the top of the dune and on the leeward slope were greater than those on the windward slope ($p < 0.05$). However, in the middle of growing season (July), there was greater enrichment on the windward slope ($p < 0.05$). At the end of the growing season (September), there was no significant difference among the different topographical positions ($p > 0.05$). Overall, the δ^{18}O value of Ao twig water on the top of the dune

(−4.05 ± 0.70‰) was higher than that on leeward (−4.42 ± 0.71‰) and windward (−4.56 ± 0.52‰) slopes.

Seasonal Variation in Contributions to Water Uptake

At the same topographical position, Ao obtained water from different sources in different seasons (**Figure 9**). At windward, Ao used four potential water pools in May, and the relative water uptake was in the range from 0.19 to 0.28, which represent the portion of water obtained from each of the four pools. However, plants were not likely to use groundwater in future growing seasons, because they shifted use to large amounts of the three soil water pools in the middle of the growing season and to shallow soil water (0.90) at the end of the growing season. Plants used only three layers of soil water at the top of the dune and leeward. At the top of the dune, Ao absorbed shallow soil water at the beginning and the end of the growing season but absorbed soil water from middle layers in July. Nevertheless, Ao leeward first used shallow soil water in the growing season and then used shallow soil water as well as middle soil water in the following months. Overall, Ao used shallow soil water the most, and its water uptake pattern was consistent with the root distribution at positions with different dune geomorphology.

In the same growing season, Ao exploited different water pools in different topographical positions. Early in the growing season, Ao at the top of the dune and leeward relied on shallow soil water as the main water source, whereas windward Ao used three layers of soil water as well as groundwater for uptake. In the summer, Ao on the top of the dune switched and used 0.85 of middle soil water, whereas those windward and leeward absorbed soil water from three layers of soil. However, shallow soil water was the main water source at all sites at the end of the growing season. Overall, Ao at the top of the dune and leeward tended to use the upper 60 cm of soil water during the entire growing season, whereas windward Ao used all potential water sources at the beginning of the growing season.

DISCUSSION

Potential Causes for Different Soil Water Contents in Positions With Different Dune Geomorphology

The SWC at the top and on windward and leeward slopes of the sand dune was not significantly different during the growing season in 2019 ($p > 0.05$). The SWC is easily affected by topography, soil texture, and vegetation (Hawley et al., 1983; Famiglietti et al., 1998), with slope often the most important factor affecting spatial changes in SWC. For example, the SWC in areas with steeper slopes is generally lower than that in areas with more gentle slopes (Famiglietti et al., 1998). Therefore, theoretically, the SWC on the top of the dune should be higher than that on windward and leeward slopes, which is consistent with the results in this study. On the natural fixed dune, soil particle sizes at different topographic positions were not significantly different ($p > 0.05$, **Table 1**). Nevertheless, the proportions of coarse sand and medium sand on the windward slope were greater than those on the leeward slope and at the top of the dune. In the relation between SWC and soil texture, SWC is positively correlated with the content of clay particles and negatively correlated with the content of coarse sand (Pan and Wang, 2009). In addition, vegetation height and coverage affect the distribution of soil moisture (Famiglietti et al., 2008). As shown in **Figure 3**, the height and crown width of individuals at the top of the dune were greater than those on windward and leeward slopes, which was consistent with the distribution of SWC. Pan et al. (2015) observed similar results in arid desert in northern China.

Soil moisture is one factor that limits growth of vegetation in the study area (Lu et al., 2012). The interdune groundwater level was 1.0–1.5 m on the windward side of the study dune; hence, the individuals on the windward slope could possibly absorb groundwater. However, the dune height was above 7 m, and as a result, plants at the top and on the leeward slope of dune likely had difficulty accessing groundwater. Precipitation is the first water source available for desert plants and determines the survival of plants in arid and water-limited environments (Schwinning et al., 2004). In deserts, fluctuations in precipitation during the growing season can be reflected in seasonal changes in soil moisture, as shown in **Figure 2** for this study (Porporato et al., 2002). In addition, initial soil moisture content, vegetation transpiration, and soil evaporation also affect the seasonal distribution of SWC (Hawley et al., 1983; Berndtsson et al., 1996; Pan and Wang, 2009; Shen et al., 2015). In this study, the ground surface quickly thawed to replenish soil moisture as temperatures gradually increased in May. At that stage, plants began to germinate, and because seedling soil water consumption and transpiration were relatively weak and soil surface evaporation was low, the SWC remained relatively high. Then, as plants began to grow in June, consumption exceeded replenishment by rainfall, and the SWC decreased immediately. In July, which had the most precipitation of the year, SWC was also the highest of the entire growing season. Although precipitation remained relatively high in August, SWC reached the second lowest value because plant transpiration consumed much of the soil water and the highest evaporation occurred at the soil surface. In September, SWC increased as precipitation and evapotranspiration and soil water use decreased. Overall, the seasonal variation in SWC beneath Ao was similar at the positions with different dune geomorphology.

The vertical distribution of SWC is affected by soil type, precipitation, topographic factors, land cover, and root distribution (Hawley et al., 1983; Pan et al., 2015; Yu et al., 2016). The distribution of SWC in study site was influenced by the distribution of roots, soil particle size, and vegetation cover at the different topographic positions. In uplands in an arid climate in a previous study, shallow infiltration led to shallow rooting (Fan et al., 2017). The infiltration depth of precipitation in the study area is within the top 40 cm of soil (Lu et al., 2013), which is consistent with the results in **Figures 5A–C**. The SWC at the concentrated layer of a root system is relatively low (Yu et al., 2013; Yu and Jia, 2014). As shown in **Figure 4**, relatively few fine roots were distributed in the top 20 cm on the windward slope; whereas fine roots were primarily concentrated in the surface 20 cm at the top and on the leeward slope of the dune. In addition, the root–shoot ratio of Ao on the windward slope was much larger (1.00) than that of Ao at the top (0.40) and on the leeward slope (0.36). The aboveground portion of plants was also larger. Therefore, SWC on the windward slope was significantly lower than that in other positions in July. Moreover, the canopy, height, coverage, and density of Ao on the leeward slope were lower than those on the windward slope and at the top (**Figure 3**), which might cause evaporation to be greater than that at the other two sites. In addition, coarse soil particles on the leeward slope likely led to poor water holding capacity at the soil surface, resulting in greater infiltration to the middle and deep soil layers. Under the influence of multiple factors, the surface SWC was relatively low and the middle layer SWC was relatively high on the leeward slope.

Water Use Patterns at Positions with Different Dune Geomorphology

Seasonal variation occurred in the water sources of plants, which indicated that Ao absorbed water from different pools at different stages in the growing season (**Figure 9**). In general, the seasonal variation in water sources used by plants is determined by two factors: the distribution of plant root systems and seasonal variations in hydrological conditions (Zencich et al., 2002; Asbjornsen et al., 2008; Pan et al., 2020). In spring (May), Ao at the top and on the leeward slope absorbed more than 0.70 of shallow soil water, whereas Ao windward used water from three soil layers and groundwater because the contribution of shallow soil water was from 0.19 to 0.28. This result might be because the leeward slope soil contained more coarse sand, which led to a shallow distribution of roots that used a large amount of shallow soil water. As shown in **Figures 2** and **5**, the shallow soil water at the top of the dune and on the leeward slope was sufficient to support plant growth in the spring, whereas windward individuals had the largest amount and hence needed more water to germinate at the beginning of the growing season. In July, Ao on the top of the dune switched and used 0.85 of middle soil water, whereas water was absorbed from three soil layers soil on windward (0.26–0.33) and leeward (0.31–0.37) slopes. This water uptake pattern seemed inconsistent with the root distribution shown in **Figure 4** of individuals dug outside of the sampled plot. However, where soil moisture is available, root activity rather than root presence can be a reliable indicator of actual water uptake dynamics in arid and semi-arid environments (Ehleringer and Dawson, 1992; Tiemuerbieke et al., 2018). It is most likely because of a trade-off between the activity of shallow and deep roots (Williams and Ehleringer, 2000; Martin-Gomez et al., 2015; Wang et al., 2019; Zhou et al., 2019). In addition, as shown in **Figure 5**, the highest SWC value was at 20–40 cm in July, which was consistent with the water uptake layer. The water uptake pattern of Ao in the summer was driven by SWC, consistent with other studies in the deserts of northern China (Pan et al., 2020). At the end of the growing season, all individuals used shallow soil water as the main water source, because SWC decreased as soil depth increased in September. Thus, the Ao at different topographic positions used different pools as the water source in different parts of the growing season, which was related to SWC, precipitation, and the activity of root systems under the influence of micro-topography. Overall, Ao likely used the upper 20 cm of soil water at all dune sites during the growing season.

The Impact of Climate and Topography on Root

The root zone water storage is the core of hydrological models as it controls the partitioning of available water for plant use (Gao et al., 2014). In this study, the root zone was different in three sites for same species (**Figure 4**). At the windward slope, the root zone was extending to more than 200 cm depth, whereas only 20 cm depth on the top of and 50 cm depth at the leeward slope. The ability of root zone water storage is controlled by root zone storage capacity S_R (Gentine et al., 2012), which accounts for the volume of water accessible to roots (Gao et al., 2014), and determines the maximum amount of soil moisture potentially available for vegetation transpiration (Wang-Erlandsson et al., 2016). Gao et al. (2014) showed that vegetation in arid catchments requires a higher S_R to store more water, which are mainly controlled by atmospheric moisture supply, canopy demand dynamics, and seasonality of precipitation. In semi-arid alpine desert, precipitation was concentrated in the summer so that vegetation could use sufficient water during the vigorous growth period to obtain the necessary soil water volume by lateral or vertical growth to adapt their root zones (Schenk, 2005). In addition, S_R estimates implicitly capture the root density that is active in water uptake more than root zone depth. Thus, in next step, we should take more attention on the factors affected on root zone water storage capacity because it emphasizes the role of co-evolution of vegetation and hydrology and understands the hydrological response of revegetation individuals.

Besides, topography is often the dominant driver of water movement caused by prevailing hydraulic gradients (Gao et al., 2018) and rooting depth (Fan et al., 2017). Plant rooting depth affects ecosystem resilience to environmental stress such as drought (Fan et al., 2017). Roots are highly adaptive to local soil environments, which was approved by soil particle size distribution. In study sites, windward has the coarse sand in the surface 20 cm depth, whereas more very fine sand in the other two sites (**Table 1**), which was prone to precipitation infiltration and downward growth of roots approved by Fan et al. (2017). In water-limited environment, roots connect soil water or groundwater to the atmosphere, thus influencing the local hydrologic cycle and climate.

It was warmer and increased precipitation in northern Tibetan Plateau in recent years. However, different types of vegetation exhibited different sensitivities to climatic change, which were attributed to the different initial conditions and changes in climatic factors among the types of vegetation (Shen et al., 2014; Wang et al., 2015). Previous studies show that water availability had stronger effects on aboveground net primary productivity (Wang et al., 2022), whereas increased precipitation could increase soil moisture in alpine meadow ecosystem (Shen et al., 2015; Yu et al., 2019). In alpine deserts, shrubs on dunes mainly use soil water at different depths (Jia et al., 2012; Wu et al., 2016b). Warm temperatures are beneficial because they increase the water use efficiency of alpine plants, and humidity favors higher surface SWC and promotes the maximum use of shallow soil water by plants growing in sand. The effects of stress on sand-fixing shrubs promote the benign development of sandy ecosystems. Therefore, in future research, under the background of warming and humidification, the other focus will be on the water use patterns of different types of artificial sand-fixing plants under different planting modes.

CONCLUSION

In this study, the stable isotopes of $\delta^{18}O$ and δD were used to analyze the variability in water sources of the native species Ao during the growing season in an alpine semi-arid desert. Although the species has high cold and drought tolerance in alpine environments and also an ability to adjust to water sources at different depths, soil water primarily recharged by precipitation is the critical factor controlling its survival and growth. Ao primarily depended on water from upper soil layers in the early growing season, except for those windward. Whereas in July, with the highest rainfall and SWC, plants likely used water in middle soil layers at all topographic positions on the dune. At the end of the growing season, the use shallow soil water became predominant again. Overall, Ao used shallow soil water the most, and its water uptake pattern was consistent with the root distribution at positions with different dune geomorphology. The results of this study indicate that the micro-landforms of sand dunes affect vegetation growth not only through aeolian activities and soil properties but also through plant water use.

DATA AVAILABILITY STATEMENT

The raw data supporting the conclusion of this article will be made available by the authors, without undue reservation.

AUTHOR CONTRIBUTIONS

HaW finished the data curation and formal analysis and wrote the original draft. LT played a guiding role in conceptualizing the field experiment, review, and editing the manuscript. HZ and HuW assisted in data analysis and sample collection. YY helped editing and reviewing the manuscript.

FUNDING

This research was funded by Natural Science Foundation of China (41961017), Qinghai Three Rivers Ecological Protection and Construction Phase II (2018-S-1), Science and Technology Project of Qinghai Province (2018-NK-A3), and State Key Laboratory of Earth Surface Processes and Resource Ecology (2020-KF-06).

ACKNOWLEDGMENTS

We thank Huade Guan for his help in data analysis and Qiaoyu Wang for her kind assistance in field experiments for this study.

REFERENCES

Asbjornsen, H., Shepherd, G., Helmers, M., and Mora, G. (2008). Seasonal Patterns in Depth of Water Uptake under Contrasting Annual and Perennial Systems in the Corn Belt Region of the Midwestern U.S. *Plant Soil* 308, 69–92. doi:10.1007/s11104-008-9607-3

Barbeta, A., Jones, S. P., Clavé, L., Wingate, L., Gimeno, T. E., Fréjaville, B., et al. (2019). Unexplained Hydrogen Isotope Offsets Complicate the Identification and Quantification of Tree Water Sources in a Riparian forest. *Hydrol. Earth Syst. Sci.* 23, 2129–2146. doi:10.5194/hess-23-2129-2019

Berndtsson, R., Nodomi, K., Yasuda, H., Persson, T., Chen, H., and Jinno, K. (1996). Soil Water and Temperature Patterns in an Arid Desert Dune Sand. *J. Hydrol.* 185, 20. doi:10.1016/0022-1694(95)02987-7

Beyer, M., Kühnhammer, K., and Dubbert, M. (2020). *In Situ* measurements of Soil and Plant Water Isotopes: a Review of Approaches, Practical Considerations and a Vision for the Future. *Hydrol. Earth Syst. Sci.* 24, 4413–4440. doi:10.5194/hess-24-4413-2020

Craig, H. (1961). Isotopic Variations in Meteoric Waters. *Science* 133, 1702–1703. doi:10.1126/science.133.3465.1702

Cui, B.-L., and Li, X.-Y. (2015). Stable Isotopes Reveal Sources of Precipitation in the Qinghai Lake Basin of the Northeastern Tibetan Plateau. *Sci. Total Environ.* 527-528, 26–37. doi:10.1016/j.scitotenv.2015.04.105

Dai, Y., Zheng, X.-J., Tang, L.-S., and Li, Y. (2014). Stable Oxygen Isotopes Reveal Distinct Water Use Patterns of Two Haloxylon Species in the Gurbantonggut Desert. *Plant Soil* 389, 73–87. doi:10.1007/s11104-014-2342-z

Dawson, T. E. (1996). Determining Water Use by Trees and Forests from Isotopic, Energy Balance and Transpiration Analyses: the Roles of Tree Size and Hydraulic Lift. *Tree Physiol.* 16, 263–272. doi:10.1093/treephys/16.1-2.263

Dawson, T. E., and Ehleringer, J. R. (1991). Streamside Trees that Do Not Use Stream Water. *Nature* 350, 3. doi:10.1038/350335a0

Dawson, T. E., and Pate, J. S. (1996). Seasonal Water Uptake and Movement in Root Systems of Australian Phraeatophytic Plants of Dimorphic Root Morphology: a Stable Isotope Investigation. *Oecologia* 107, 13–20. doi:10.1007/BF00582230

Ehleringer, J. R., and Dawson, T. E. (1992). Water Uptake by Plants: Perspectives from Stable Isotope Composition. *Ptant, Cel Environ.* 15, 10. doi:10.1111/j.1365-3040.1992.tb01657.x

Ehleringer, J. R., Phillips, S. L., Schuster, W. S., and Sandquist, D. R. (1991). Differential Utilization of Summer rains by Desert Plants. *Oecologia* 88, 430–434. doi:10.1007/BF00317589

Ellsworth, P. Z., and Williams, D. G. (2007). Hydrogen Isotope Fractionation during Water Uptake by Woody Xerophytes. *Plant Soil* 291, 93–107. doi:10.1007/s11104-006-9177-1

Famiglietti, J. S., Ryu, D., Berg, A. A., Rodell, M., and Jackson, T. J. (2008). Field Observations of Soil Moisture Variability across Scales. *Water Resour. Res.* 44. doi:10.1029/2006wr005804

Famiglietti, J. S., Rudnicki, J. W., and Rodell, M. (1998). Variability in Surface Moisture Content along a Hillslope Transect: Rattlesnake Hill, Texas. *J. Hydrol.* 210, 259–281. doi:10.1016/s0022-1694(98)00187-5

Fan, Y., Miguez-Macho, G., Jobbágy, E. G., Jackson, R. B., and Otero-Casal, C. (2017). Hydrologic Regulation of Plant Rooting Depth. *Proc. Natl. Acad. Sci. USA* 114, 10572–10577. doi:10.1073/pnas.1712381114

Gao, H., Hrachowitz, M., Schymanski, S. J., Fenicia, F., Sriwongsitanon, N., and Savenije, H. H. G. (2014). Climate Controls How Ecosystems Size the Root Zone Storage Capacity at Catchment Scale. *Geophys. Res. Lett.* 41, 7916–7923. doi:10.1002/2014gl061668

Gao, H. K., Birkel, C., Hrachowitz, M., Tetzlaff, D., Soulsby, C., and Savenije, H. H. G. (2018). A Simple Topography-Driven and Calibration-free Runoff Generation Module. *Hydrol. Earth Syst. Sci.* 23, 787–809. doi:10.5194/hess-23-787-2019

Gentine, P., D'odorico, P., Lintner, B. R., Sivandran, G., and Salvucci, G. (2012). Interdependence of Climate, Soil, and Vegetation as Constrained by the Budyko Curve. *Geophys. Res. Lett.* 39. doi:10.1029/2012gl053492

Hasselquist, N. J., Allen, M. F., and Santiago, L. S. (2010). Water Relations of evergreen and Drought-Deciduous Trees along a Seasonally Dry Tropical forest Chronosequence. *Oecologia* 164, 881–890. doi:10.1007/s00442-010-1725-y

Hawley, M. E., Jackson, T. J., and Mccuen, R. H. (1983). Surface Soil Moisture Variation on Small Agricultural Watersheds. *J. Hydrol.* 62, 22. doi:10.1016/0022-1694(83)90102-6

Jia, Z., Zhu, Y., and Liu, L. (2012). Different Water Use Strategies of Juvenile and Adult Caragana Intermedia Plantations in the Gonghe Basin, Tibet Plateau. *PLoS One* 7, e45902. doi:10.1371/journal.pone.0045902

Li, W., Shi, W., Wang, G., Han, X., and Li, Z. (2004). Analysis on Moisture Niche Fitness and Interspecific Coexistence of Artificial forest Plants in Shapotou Area. *Acta Botanic Boreal -Occidentalia Sinica* 24 (3), 384–391.

Liu, B., Zhao, W., Liu, Z., Yang, Y., Luo, W., Zhou, H., et al. (2015). Changes in Species Diversity, Aboveground Biomass, and Vegetation Cover along an Afforestation Successional Gradient in a Semiarid Desert Steppe of China. *Ecol. Eng.* 81, 301–311. doi:10.1016/j.ecoleng.2015.04.014

Lu, R., Tang, Q., and Sang, Y. (2012). Dynamic Changes of Soil Moisture in Different Dunes of Ketu Sand Land in Qinghai Lake Basin. *Res. Soil Water Conservation* 19 (2), 111–115.

Lu, R., Tang, Q., Wei, D., and Zhang, D. (2013). Rainwater Infiltration at Dunes under Various Rainfall Events in sandy Land to the East of Qinghai Lake. *J. Desert Res.* 33 (3), 797–803. doi:10.7522/j.issn.1000-694X.2013.00114

Martin-Gomez, P., Barbeta, A., Voltas, J., Peñuelas, J., Dennis, K., Palacio, S., et al. (2015). Isotope-ratio Infrared Spectroscopy: a Reliable Tool for the Investigation of Plant-Water Sources? *New Phytol.* 207, 914–927. doi:10.1111/nph.13376

McCole, A. A., and Stern, L. A. (2007). Seasonal Water Use Patterns of Juniperus Ashei on the Edwards Plateau, Texas, Based on Stable Isotopes in Water. *J. Hydrol.* 342, 238–248. doi:10.1016/j.jhydrol.2007.05.024

Pan, Y.-X., and Wang, X.-P. (2009). Factors Controlling the Spatial Variability of Surface Soil Moisture within Revegetated-Stabilized Desert Ecosystems of the Tengger Desert, Northern China. *Hydrol. Process.* 23, 1591–1601. doi:10.1002/hyp.7287

Pan, Y.-X., Wang, X.-P., Ma, X.-Z., Zhang, Y.-F., and Hu, R. (2020). The Stable Isotopic Composition Variation Characteristics of Desert Plants and Water Sources in an Artificial Revegetation Ecosystem in Northwest China. *Catena* 189, 104499. doi:10.1016/j.catena.2020.104499

Pan, Y.-X., Wang, X.-P., Zhang, Y.-F., and Hu, R. (2015). Spatio-temporal Variability of Root Zone Soil Moisture in Artificially Revegetated and Natural Ecosystems at an Arid Desert Area, NW China. *Ecol. Eng.* 79, 100–112. doi:10.1016/j.ecoleng.2015.04.019

Phillips, D. L., and Gregg, J. W. (2003). Source Partitioning Using Stable Isotopes: Coping with Too many Sources. *Oecologia* 136, 261–269. doi:10.1007/s00442-003-1218-3

Porporato, A., D'odorico, P., Laio, F., Ridolfi, L., and Rodriguez-Iturbe, I. (2002). Ecohydrology of Water-Controlled Ecosystems. *Adv. Water Resour.* 25, 14. doi:10.1016/s0309-1708(02)00058-1

Schenk, J. H. (2005). Vertical Vegetation Structure below Ground: Scaling from Root to Globe. *Prog. Bot.* 66, 341–373. doi:10.1007/3-540-27043-4_14

Schwinning, S., Sala, O. E., Loik, M. E., and Ehleringer, J. R. (2004). Thresholds, Memory, and Seasonality: Understanding Pulse Dynamics in Arid/semi-Arid Ecosystems. *Oecologia* 141, 191–193. doi:10.1007/s00442-004-1683-3

Shen, Z.-X., Li, Y.-L., and Fu, G. (2015). Response of Soil Respiration to Short-Term Experimental Warming and Precipitation Pulses over the Growing Season in an alpine Meadow on the Northern Tibet. *Appl. Soil Ecol.* 90, 35–40. doi:10.1016/j.apsoil.2015.01.015

Shen, Z., Fu, G., Yu, C., Sun, W., and Zhang, X. (2014). Relationship between the Growing Season Maximum Enhanced Vegetation Index and Climatic Factors on the Tibetan Plateau. *Remote Sensing* 6, 6765–6789. doi:10.3390/rs6086765

Snyder, K. A., and Williams, D. G. (2003). Defoliation Alters Water Uptake by Deep and Shallow Roots of Prosopis Velutina (Velvet Mesquite). *Funct. Ecol.* 17, 12. doi:10.1046/j.1365-2435.2003.00739.x

Song, L., Zhu, J., Li, M., and Yu, Z. (2014). Water Utilization of Pinus Sylvestris Var. Mongolica in a Sparse wood Grassland in the Semiarid sandy Region of Northeast China. *Trees* 28, 971–982. doi:10.1007/s00468-014-1010-5

Song, L., Zhu, J., Li, M., and Zhang, J. (2016). Water Use Patterns of Pinus Sylvestris Var. Mongolica Trees of Different Ages in a Semiarid sandy Lands of Northeast China. *Environ. Exp. Bot.* 129, 94–107. doi:10.1016/j.envexpbot.2016.02.006

Sun, J., Hou, G., Liu, M., Fu, G., Zhan, T., Zhou, H., et al. (2019). Effects of Climatic and Grazing Changes on Desertification of alpine Grasslands, Northern Tibet. *Ecol. Indicators* 107, 105647. doi:10.1016/j.ecolind.2019.105647

Szymczak, S., Barth, J., Bendix, J., Huneau, F., Garel, E., Häusser, M., et al. (2020). First Indications of Seasonal and Spatial Variations of Water Sources in pine Trees along an Elevation Gradient in a Mediterranean Ecosystem Derived from δ18O. *Chem. Geology.* 549, 119695. doi:10.1016/j.chemgeo.2020.119695

Tian, L., Wu, W., Zhang, D., and Yu, Y. (2020). Airflow Field Around Hippophae Rhamnoides in Alpine Semi-arid Desert. *Land* 9, 140. doi:10.3390/land9050140

Tian, L., Wu, W., Zhou, X., Zhang, D., Yu, Y., Wang, H., et al. (2019). The Ecosystem Effects of Sand-Binding Shrub Hippophae Rhamnoides in Alpine Semi-arid Desert in the Northeastern Qinghai-Tibet Plateau. *Land* 8, 183. doi:10.3390/land8120183

Tiemuerbieke, B., Min, X.-J., Zang, Y.-X., Xing, P., Ma, J.-Y., and Sun, W. (2018). Water Use Patterns of Co-occurring C3 and C4 Shrubs in the Gurbantonggut Desert in Northwestern China. *Sci. Total Environ.* 634, 341–354. doi:10.1016/j.scitotenv.2018.03.307

Wang, J., Fu, B., Lu, N., Wang, S., and Zhang, L. (2019). Water Use Characteristics of Native and Exotic Shrub Species in the Semi-arid Loess Plateau Using an Isotope Technique. *Agric. Ecosyst. Environ.* 276, 55–63. doi:10.1016/j.agee.2019.02.015

Wang, J. W., Li, M., Yu, C. Q., and Fu, G. (2022). The Change in Environmental Variables Linked to Climate Change Has a Stronger Effect on Aboveground Net Primary Productivity Than Does Phenological Change in Alpine Grasslands. *Front. Plant Sci.* 12. doi:10.3389/fpls.2021.798633

Wang, S.-H., Sun, W., Li, S.-W., Shen, Z.-X., and Fu, G. (2015). Interannual Variation of the Growing Season Maximum Normalized Difference Vegetation Index, MNDVI, and its Relationship with Climatic Factors on the Tibetan Plateau. *Polish J. Ecol.* 63, 424–439. doi:10.3161/15052249pje2015.63.3.012

Wang-Erlandsson, L., Bastiaanssen, W. G. M., Gao, H. K., Jägermeyr, J., Senay, G. B., Van Dijk, A. I. J. M., et al. (2016). Global Root Zone Storage Capacity from Satellite-Based Evaporation. *Hydrol. Earth Syst. Sci.* 20, 23. doi:10.5194/hess-20-1459-2016

Williams, D. G., and Ehleringer, J. R. (2000). Intra- and Interspecific Variation for Summer Precipitation Use in Pinyon–Juniper Woodlands. *Ecol. Monogr.* 70, 21. doi:10.2307/2657185

Wu, H., Li, J., Li, X.-Y., He, B., Liu, J., Jiang, Z., et al. (2018). Contrasting Response of Coexisting Plant's Water-Use Patterns to Experimental Precipitation Manipulation in an alpine Grassland Community of Qinghai Lake Watershed, China. *PLoS One* 13, e0194242. doi:10.1371/journal.pone.0194242

Wu, H., Li, X.-Y., Jiang, Z., Chen, H., Zhang, C., and Xiao, X. (2016b). Contrasting Water Use Pattern of Introduced and Native Plants in an alpine Desert Ecosystem, Northeast Qinghai-Tibet Plateau, China. *Sci. Total Environ.* 542, 182–191. doi:10.1016/j.scitotenv.2015.10.121

Wu, H., Li, X.-Y., Li, J., Zhang, C., He, B., Zhang, S., et al. (2019a). Age-related Water Uptake Patterns of alpine Plantation Shrubs in Reforestation Region of Qinghai-Tibetan Plateau Based on Stable Isotopes. *Ecohydrology* 12, e2049. doi:10.1002/eco.2049

Wu, H., Li, X. Y., Li, J., Jiang, Z., Chen, H., Ma, Y., et al. (2016a). Differential Soil Moisture Pulse Uptake by Coexisting Plants in an alpine Achnatherum Splendens Grassland Community. *Environ. Earth Sci.* 75, 914. doi:10.1007/s12665-016-5694-2

Wu, W., Zhang, D., Tian, L., Zhang, M., and Zhou, X. (2019c). Features of Artificial Plant Communications from the East Sand Region of the Qinghai Lake over the Last 10 Years. *Acta Ecologica Sinica* 39, 13. doi:10.5846/stxb201712292353

Wu, Y., Zhou, H., Zheng, X.-J., Li, Y., and Tang, L.-S. (2014). Seasonal Changes in the Water Use Strategies of Three Co-occurring Desert Shrubs. *Hydrol. Process.* 28, 6265–6275. doi:10.1002/hyp.10114

Xu, G.-Q., Li, Y., and Xu, H. (2011). Seasonal Variation in Plant Hydraulic Traits of Two Co-occurring Desert Shrubs, Tamarix Ramosissima and Haloxylon Ammodendron, with Different Rooting Patterns. *Ecol. Res.* 26, 1071–1080. doi:10.1007/s11284-011-0858-8

Xu, G., and Li, Y. (2009). Roots Distribution of Three Desert Shrubs and Their Response to Precipitation under Co-occurring Conditions. *Acta Ecologica Sinica* 29, 8. doi:10.1016/j.chnaes.2009.07.004

Xu, H., and Li, Y. (2006). Water-use Strategy of Three central Asian Desert Shrubs and Their Responses to Rain Pulse Events. *Plant Soil* 285, 5–17. doi:10.1007/s11104-005-5108-9

Yang, B., Wen, X., and Sun, X. (2015). Seasonal Variations in Depth of Water Uptake for a Subtropical Coniferous Plantation Subjected to Drought in an East Asian Monsoon Region. *Agric. For. Meteorology* 201, 218–228. doi:10.1016/j.agrformet.2014.11.020

Yu, C.-Q., Wang, J.-W., Shen, Z.-X., and Fu, G. (2019). Effects of Experimental Warming and Increased Precipitation on Soil Respiration in an alpine Meadow in the Northern Tibetan Plateau. *Sci. Total Environ.* 647, 1490–1497. doi:10.1016/j.scitotenv.2018.08.111

Yu, T., Feng, Q., Si, J., Xi, H., Li, Z., and Chen, A. (2013). Hydraulic Redistribution of Soil Water by Roots of Two Desert Riparian Phreatophytes in Northwest China's Extremely Arid Region. *Plant Soil* 372, 297–308. doi:10.1007/s11104-013-1727-8

Yu, Y., and Jia, Z. Q. (2014). Changes in Soil Organic Carbon and Nitrogen Capacities of Salix Cheilophila Schneid along a Revegetation Chronosequence in Semi-arid Degraded sandy Land of the Gonghe Basin, Tibet Plateau. *Solid Earth* 5, 1045–1054. doi:10.5194/se-5-1045-2014

Yu, Y., Loiskandl, W., Kaul, H.-P., Himmelbauer, M., Wei, W., Chen, L., et al. (2016). Estimation of Runoff Mitigation by Morphologically Different Cover Crop Root Systems. *J. Hydrol.* 538, 667–676. doi:10.1016/j.jhydrol.2016.04.060

Zencich, S. J., Froend, R. H., Turner, J. V., and Gailitis, V. (2002). Influence of Groundwater Depth on the Seasonal Sources of Water Accessed by Banksia Tree Species on a Shallow, sandy Coastal Aquifer. *Oecologia* 131, 8–19. doi:10.1007/s00442-001-0855-7

Zhang, C., Li, X., Wu, H., Wang, P., Wang, Y., Wu, X., et al. (2017). Differences in Water-Use Strategies along an Aridity Gradient between Two Coexisting Desert Shrubs (Reaumuria Soongorica and Nitraria Sphaerocarpa): Isotopic Approaches with Physiological Evidence. *Plant Soil* 419, 169–187. doi:10.1007/s11104-017-3332-8

Zhang, J., Han, H., Lei, Y., Yang, W., Li, H., Yang, D., et al. (2012). Correlations Between Distribution Characteristics of Artemisia ordosica Root System and Soil Moisture Under Different Fixation Stage of Sand Dunes. *Journal of Southwest Forestry University* 32(6), 1–5. doi:10.3969/j.issn.2095-1914.2012.06.001

Zhou, H., Zhao, W., He, Z., Yan, J., and Zhang, G. (2019). Variation in Depth of Water Uptake for Pinus Sylvestris Var. Mongolica along a Precipitation Gradient in sandy Regions. *J. Hydrol.* 577, 123921. doi:10.1016/j.jhydrol.2019.123921

Zhou, H., Zhao, W., and Zhang, G. (2017). Varying Water Utilization of Haloxylon Ammodendron Plantations in a Desert-Oasis Ecotone. *Hydrol. Process.* 31, 825–835. doi:10.1002/hyp.11060

Zong, N., and Fu, G. (2021). Variations in Species and Function Diversity of Soil Fungal Community along a Desertification Gradient in an alpine Steppe. *Ecol. Indicators* 131, 108197. doi:10.1016/j.ecolind.2021.108197

Conflict of Interest: The authors declare that the research was conducted in the absence of any commercial or financial relationships that could be construed as a potential conflict of interest.

The handling editor is currently co-organizing a Research Topic with one of the authors YY and confirms the absence of any other collaboration.

Frontiers in
Earth Science

Investigates the processes operating within the major spheres of our planet

Advances our understanding across the earth sciences, providing a theoretical background for better use of our planet's resources and equipping us to face major environmental challenges.

Discover the latest Research Topics

See more →

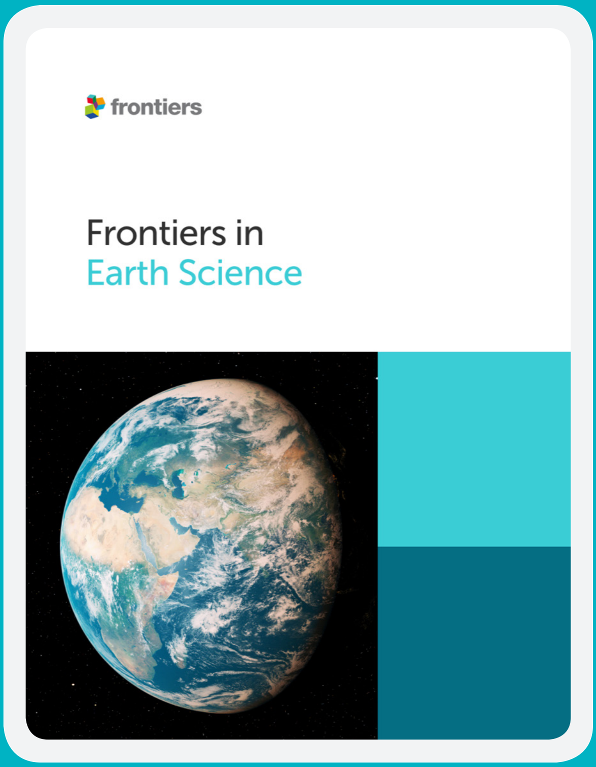
frontiers

Frontiers in
Earth Science

Frontiers

Avenue du Tribunal-Fédéral 34
1005 Lausanne, Switzerland
frontiersin.org

Contact us

+41 (0)21 510 17 00
frontiersin.org/about/contact